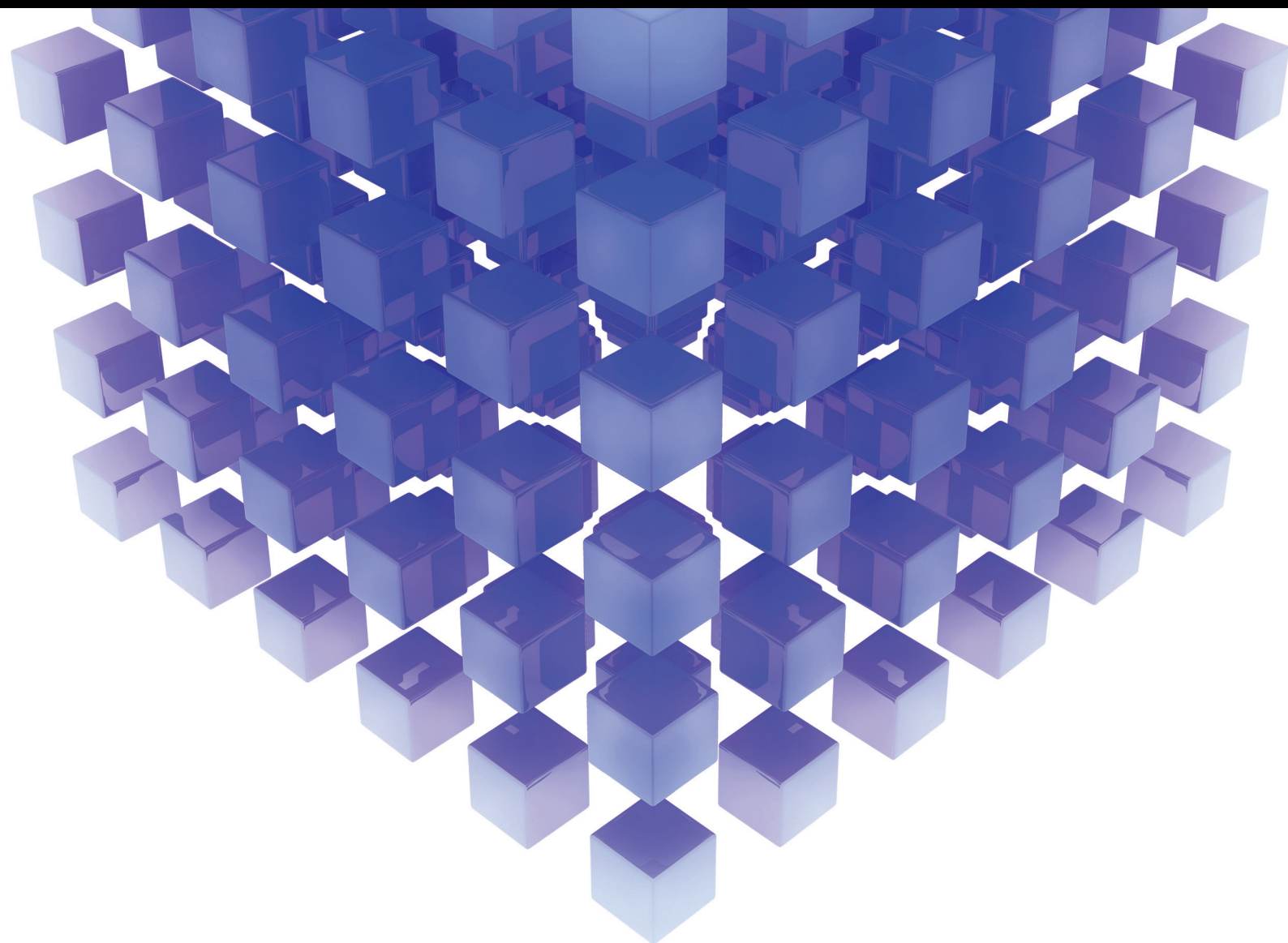


Mathematical Problems in Engineering

# Advanced Observer-Based Control for Benchmark Control Problems: From Mathematical Modeling to Control Design

Lead Guest Editor: Olfa Boubaker

Guest Editors: Mihai Lungu, Binoy K. Roy, and Luis J. Yebra





---

**Advanced Observer-Based Control for  
Benchmark Control Problems: From  
Mathematical Modeling to Control Design**

Mathematical Problems in Engineering

---

**Advanced Observer-Based Control for  
Benchmark Control Problems: From  
Mathematical Modeling to Control Design**

Lead Guest Editor: Olfa Boubaker

Guest Editors: Mihai Lungu, Binoy K. Roy, and Luis J. Yebra



---

Copyright © 2018 Hindawi. All rights reserved.

This is a special issue published in “Mathematical Problems in Engineering.” All articles are open access articles distributed under the Creative Commons Attribution License, which permits unrestricted use, distribution, and reproduction in any medium, provided the original work is properly cited.

## Editorial Board

- Mohamed Abd El Aziz, Egypt  
AITOUCHE Abdelouhab, France  
Leonardo Acho, Spain  
José A. Acosta, Spain  
Daniela Addressi, Italy  
Paolo Adesso, Italy  
Claudia Adduce, Italy  
Ramesh Agarwal, USA  
Francesco Aggogeri, Italy  
Juan C. Agüero, Australia  
Ricardo Aguilar-Lopez, Mexico  
Tarek Ahmed-Ali, France  
Elias Aifantis, USA  
Muhammad N. Akram, Norway  
Guido Ala, Italy  
Andrea Alaimo, Italy  
Reza Alam, USA  
Nicholas Alexander, UK  
Salvatore Alfonzetti, Italy  
Mohammad D. Aliyu, Canada  
Juan A. Almendral, Spain  
José Domingo Álvarez, Spain  
Cláudio Alves, Portugal  
J. P. Amezcua-Sanchez, Mexico  
Lionel Amodeo, France  
Sebastian Anita, Romania  
Renata Archetti, Italy  
Felice Arena, Italy  
Sabri Arik, Turkey  
Francesco Aristodemo, Italy  
Fausto Arpino, Italy  
Alessandro Arsie, USA  
Edoardo Artioli, Italy  
Fumihiko Ashida, Japan  
Farhad Aslani, Australia  
Mohsen Asle Zaem, USA  
Romain Aubry, USA  
Matteo Aureli, USA  
Richard I. Avery, USA  
Viktor Avrutin, Germany  
Francesco Aymerich, Italy  
T. P. Azevedo Perdicoulis, Portugal  
Sajad Azizi, Belgium  
Michele Baccocchi, Italy
- Seungik Baek, USA  
Adil Bagirov, Australia  
Khaled Bahlali, France  
Laurent Bako, France  
Pedro Balaguer, Spain  
Stefan Balint, Romania  
Ines Tejado Balsera, Spain  
Alfonso Banos, Spain  
Jerzy Baranowski, Poland  
Roberto Baratti, Italy  
Andrzej Bartoszewicz, Poland  
David Bassir, France  
Chiara Bedon, Italy  
Azeddine Beghdadi, France  
Denis Benasciutti, Italy  
Ivano Benedetti, Italy  
Rosa M. Benito, Spain  
Elena Benvenuti, Italy  
Giovanni Berselli, Italy  
Giorgio Besagni, Italy  
Michele Betti, Italy  
Jean-Charles Beugnot, France  
Pietro Bia, Italy  
Carlo Bianca, France  
Simone Bianco, Italy  
Vincenzo Bianco, Italy  
Vittorio Bianco, Italy  
Gennaro N. Bifulco, Italy  
David Bigaud, France  
Antonio Bilotta, Italy  
Paul Bogdan, USA  
Guido Bolognesi, UK  
Rodolfo Bontempo, Italy  
Alberto Borboni, Italy  
Paolo Boscariol, Italy  
Daniela Boso, Italy  
Guillermo Botella-Juan, Spain  
Boulaïd Boulkroune, Belgium  
Fabio Bovenga, Italy  
Francesco Braghin, Italy  
Ricardo Branco, Portugal  
Maurizio Brocchini, Italy  
Julien Bruchon, France  
Matteo Bruggi, Italy
- Michele Brun, Italy  
Vasilis Burganos, Greece  
Tito Busani, USA  
Raquel Caballero-Águila, Spain  
Filippo Cacace, Italy  
Pierfrancesco Cacciola, UK  
Salvatore Caddemi, Italy  
Roberto Caldelli, Italy  
Alberto Campagnolo, Italy  
Eric Campos-Canton, Mexico  
Marko Canadija, Croatia  
Salvatore Cannella, Italy  
Francesco Cannizzaro, Italy  
Javier Cara, Spain  
Ana Carpio, Spain  
Caterina Casavola, Italy  
Sara Casciati, Italy  
Federica Caselli, Italy  
Carmen Castillo, Spain  
Inmaculada T. Castro, Spain  
Miguel Castro, Portugal  
Giuseppe Catalanotti, UK  
Nicola Caterino, Italy  
Alberto Cavallo, Italy  
Gabriele Cazzulani, Italy  
Luis Cea, Spain  
Song Cen, China  
Miguel Cerrolaza, Venezuela  
M. Chadli, France  
Gregory Chagnon, France  
Ludovic Chamoin, France  
Ching-Ter Chang, Taiwan  
Qing Chang, USA  
Michael J. Chappell, UK  
Kacem Chehdi, France  
Peter N. Cheimets, USA  
Xinkai Chen, Japan  
Luca Chiapponi, Italy  
Francisco Chicano, Spain  
Nicholas Chileshe, Australia  
Adrian Chmielewski, Poland  
Ioannis T. Christou, Greece  
Hung-Yuan Chung, Taiwan  
Simone Cinquemani, Italy

Roberto G. Citarella, Italy  
Joaquim Ciurana, Spain  
John D. Clayton, USA  
Francesco Clementi, Italy  
Piero Colajanni, Italy  
Giuseppina Colicchio, Italy  
Vassilios Constantoudis, Greece  
Enrico Conte, Italy  
Francesco Conte, Italy  
Alessandro Contento, USA  
Mario Cools, Belgium  
José A. Correia, Portugal  
Jean-Pierre Corriou, France  
J.-C. Cortés, Spain  
Carlo Cosentino, Italy  
Paolo Crippa, Italy  
Andrea Crivellini, Italy  
Frederico R. B. Cruz, Brazil  
Erik Cuevas, Mexico  
Maria C. Cunha, Portugal  
Peter Dabnichki, Australia  
Luca D'Acerno, Italy  
Weizhong Dai, USA  
Andrea Dall'Asta, Italy  
P. Damodaran, USA  
Bhabani S. Dandapat, India  
Farhang Daneshmand, Canada  
Giuseppe D'Aniello, Italy  
Sergey Dashkovskiy, Germany  
Fabio De Angelis, Italy  
Samuele De Bartolo, Italy  
Abílio De Jesus, Portugal  
Pietro De Lellis, Italy  
Alessandro De Luca, Italy  
Stefano de Miranda, Italy  
Filippo de Monte, Italy  
Michael Defoort, France  
Alessandro Della Corte, Italy  
Xavier Delorme, France  
Laurent Dewasme, Belgium  
Angelo Di Egidio, Italy  
Roberta Di Pace, Italy  
Ramón I. Diego, Spain  
Yannis Dimakopoulos, Greece  
Zhengtao Ding, UK  
M. Djemai, France  
Alexandre B. Dolgui, France

Georgios Dounias, Greece  
Florent Duchaine, France  
George S. Dulikravich, USA  
Bogdan Dumitrescu, Romania  
Horst Ecker, Austria  
Saeed Eftekhari Azam, USA  
Ahmed El Hajjaji, France  
Antonio Elipe, Spain  
Fouad Erchiqui, Canada  
Anders Eriksson, Sweden  
R. Emre Erkmen, Australia  
G. Espinosa-Paredes, Mexico  
Leandro F. F. Miguel, Brazil  
Andrea L. Facci, Italy  
Giacomo Falcucci, Italy  
Giovanni Falsone, Italy  
Hua Fan, China  
Nicholas Fantuzzi, Italy  
Yann Favennec, France  
Fiorenzo A. Fazzolari, UK  
Giuseppe Fedele, Italy  
Roberto Fedele, Italy  
Arturo J. Fernández, Spain  
Jesus M. Fernandez Oro, Spain  
Massimiliano Ferraioli, Italy  
Massimiliano Ferrara, Italy  
Francesco Ferrise, Italy  
Eric Feulvarch, France  
Barak Fishbain, Israel  
S. Douwe Flapper, Netherlands  
Thierry Floquet, France  
Eric Florentin, France  
Alessandro Formisano, Italy  
Francesco Franco, Italy  
Elisa Francomano, Italy  
Tomonari Furukawa, USA  
Juan C. G. Prada, Spain  
Mohamed Gadala, Canada  
Matteo Gaeta, Italy  
Mauro Gaggero, Italy  
Zoran Gajic, USA  
Erez Gal, Israel  
Jaime Gallardo-Alvarado, Mexico  
Ugo Galvanetto, Italy  
Akemi Gálvez, Spain  
Rita Gamberini, Italy  
Maria L. Gandarias, Spain

Arman Ganji, Canada  
Zhiwei Gao, UK  
Zhong-Ke Gao, China  
Giovanni Garcea, Italy  
Luis Rodolfo Garcia Carrillo, USA  
Jose M. Garcia-Aznar, Spain  
Akhil Garg, China  
Alessandro Gasparetto, Italy  
Oleg V. Gendelman, Israel  
Stylianos Georgantzinou, Greece  
Fotios Georgiades, UK  
Mergen H. Ghayesh, Australia  
Georgios I. Giannopoulos, Greece  
Agathoklis Giaralis, UK  
Pablo Gil, Spain  
Anna M. Gil-Lafuente, Spain  
Ivan Giorgio, Italy  
Gaetano Giunta, Luxembourg  
Alessio Gizzi, Italy  
Jefferson L.M.A. Gomes, UK  
Emilio Gómez-Déniz, Spain  
Antonio M. Gonçalves de Lima, Brazil  
David González, Spain  
Chris Goodrich, USA  
Rama S. R. Gorla, USA  
Kannan Govindan, Denmark  
Antoine Grall, France  
George A. Gravvanis, Greece  
Fabrizio Greco, Italy  
David Greiner, Spain  
Simonetta Grilli, Italy  
Jason Gu, Canada  
Federico Guarracino, Italy  
Michele Guida, Italy  
Zhaoxia Guo, China  
José L. Guzmán, Spain  
Quang Phuc Ha, Australia  
Petr Hájek, Czech Republic  
Weimin Han, USA  
Zhen-Lai Han, China  
Thomas Hanne, Switzerland  
Mohammad Amin Hariri-Ardebili, USA  
Xiao-Qiao He, China  
Luca Heltai, Italy  
Nicolae Herisanu, Romania  
Alfredo G. Hernández-Díaz, Spain  
M.I. Herreros, Spain

Eckhard Hitzer, Japan  
 Paul Honeine, France  
 Jaromir Horacek, Czech Republic  
 Muneo Hori, Japan  
 András Horváth, Italy  
 S. Hassan Hosseinnia, Netherlands  
 Gordon Huang, Canada  
 Sajid Hussain, Canada  
 Asier Ibeas, Spain  
 Orest V. Iftime, Netherlands  
 Przemyslaw Ignaciuk, Poland  
 Giacomo Innocenti, Italy  
 Emilio Insfran Pelozo, Spain  
 Alessio Ishizaka, UK  
 Nazrul Islam, USA  
 Benoit Lung, France  
 Benjamin Ivorra, Spain  
 Payman Jalali, Finland  
 Mahdi Jalili, Australia  
 Łukasz Jankowski, Poland  
 Samuel N. Jator, USA  
 Juan C. Jauregui-Correa, Mexico  
 Reza Jazar, Australia  
 Khalide Jbilou, France  
 Piotr Jędrzejowicz, Poland  
 Isabel S. Jesus, Portugal  
 Linni Jian, China  
 Bin Jiang, China  
 Zhongping Jiang, USA  
 Emilio Jiménez Macías, Spain  
 Ningde Jin, China  
 Xiaoliang Jin, USA  
 Liang Jing, Canada  
 Dylan F. Jones, UK  
 Palle E. Jorgensen, USA  
 Vyacheslav Kalashnikov, Mexico  
 Tamas Kalmar-Nagy, Hungary  
 Tomasz Kapitaniak, Poland  
 Julius Kaplunov, UK  
 Haranath Kar, India  
 Konstantinos Karamanos, Belgium  
 Krzysztof Kecik, Poland  
 Jean-Pierre Kenne, Canada  
 Chaudry M. Khaliq, South Africa  
 Do Wan Kim, Republic of Korea  
 Nam-Il Kim, Republic of Korea  
 Jan Koci, Czech Republic  
 Ioannis Kostavelis, Greece  
 Sotiris B. Kotsiantis, Greece  
 Manfred Krafczyk, Germany  
 Frederic Kratz, France  
 Petr Krysl, USA  
 Krzysztof S. Kulpa, Poland  
 Shailesh I. Kundalwal, India  
 Jurgen Kurths, Germany  
 Cedrick A. K. Kwuimy, USA  
 Kyandoghere Kyamakya, Austria  
 Davide La Torre, Italy  
 Risto Lahdelma, Finland  
 Hak-Keung Lam, UK  
 Giovanni Lancioni, Italy  
 Jimmy Lauber, France  
 Antonino Laudani, Italy  
 Hervé Laurent, France  
 Aimé Lay-Ekuakille, Italy  
 Nicolas J. Leconte, France  
 Dimitri Lefebvre, France  
 Eric Lefevre, France  
 Marek Lefik, Poland  
 Yaguo Lei, China  
 Kauko Leiviskä, Finland  
 Thibault Lemaire, France  
 Roman Lewandowski, Poland  
 Chen-Feng Li, China  
 Jian Li, USA  
 En-Qiang Lin, USA  
 Zhiyun Lin, China  
 Peide Liu, China  
 Peter Liu, Taiwan  
 Wanquan Liu, Australia  
 Bonifacio Llamazares, Spain  
 Alessandro Lo Schiavo, Italy  
 Jean Jacques Loiseau, France  
 Francesco Lolli, Italy  
 Paolo Lonetti, Italy  
 Sandro Longo, Italy  
 António M. Lopes, Portugal  
 Sebastian López, Spain  
 Pablo Lopez-Crespo, Spain  
 Luis M. López-Ochoa, Spain  
 Ezequiel López-Rubio, Spain  
 Vassilios C. Loukopoulos, Greece  
 Jose A. Lozano-Galant, Spain  
 haiyan Lu, Australia  
 Gabriel Luque, Spain  
 Valentin Lychagin, Norway  
 Antonio Madeo, Italy  
 José María Maestre, Spain  
 Alessandro Magnani, Italy  
 Fazal M. Mahomed, South Africa  
 Noureddine Manamanni, France  
 Paolo Manfredi, Italy  
 Didier Maquin, France  
 Giuseppe Carlo Marano, Italy  
 Damijan Markovic, France  
 Francesco Marotti de Sciarra, Italy  
 Rui Cunha Marques, Portugal  
 Luis Martínez, Spain  
 Rodrigo Martinez-Bejar, Spain  
 Guiomar Martín-Herrán, Spain  
 Denizar Cruz Martins, Brazil  
 Benoit Marx, France  
 Elio Masciari, Italy  
 Franck Massa, France  
 Paolo Massioni, France  
 Alessandro Mauro, Italy  
 Fabio Mazza, Italy  
 Laura Mazzola, Italy  
 Driss Mehdi, France  
 Roderick Melnik, Canada  
 Pasquale Memmolo, Italy  
 Xiangyu Meng, USA  
 Jose Merodio, Spain  
 Alessio Merola, Italy  
 Mahmoud Mesbah, Iran  
 Luciano Mescia, Italy  
 Laurent Mevel, France  
 Mariusz Michta, Poland  
 Aki Mikkola, Finland  
 Giovanni Minafò, Italy  
 Hiroyuki Mino, Japan  
 Pablo Mira, Spain  
 Dimitrios Mitsotakis, New Zealand  
 Vito Mocella, Italy  
 Sara Montagna, Italy  
 Roberto Montanini, Italy  
 Francisco J. Montáns, Spain  
 Luiz H. A. Monteiro, Brazil  
 Gisele Mophou, France  
 Rafael Morales, Spain  
 Marco Morandini, Italy

Javier Moreno-Valenzuela, Mexico  
Simone Morganti, Italy  
Caroline Mota, Brazil  
Aziz Moukrim, France  
Dimitris Mourtzis, Greece  
Emiliano Mucchi, Italy  
Josefa Mula, Spain  
Jose J. Muñoz, Spain  
Giuseppe Muscolino, Italy  
Marco Mussetta, Italy  
Hakim Naceur, France  
Alessandro Naddeo, Italy  
Hassane Naji, France  
Mariko Nakano-Miyatake, Mexico  
Keivan Navaie, UK  
AMA Neves, Portugal  
Luís C. Neves, UK  
Dong Ngoduy, New Zealand  
Nhon Nguyen-Thanh, Singapore  
Tatsushi Nishi, Japan  
Xesús Nogueira, Spain  
Ben T. Nohara, Japan  
Mohammed Nouari, France  
Mustapha Nourelfath, Canada  
Włodzimierz Ogryczak, Poland  
Roger Ohayon, France  
Krzysztof Okarma, Poland  
Mitsuhiro Okayasu, Japan  
Alberto Olivares, Spain  
Enrique Onieva, Spain  
Calogero Orlando, Italy  
Alejandro Ortega-Moñux, Spain  
Sergio Ortobelli, Italy  
Naohisa Otsuka, Japan  
Erika Ottaviano, Italy  
Pawel Packo, Poland  
Arturo Pagano, Italy  
Alkis S. Paipetis, Greece  
Roberto Palma, Spain  
Alessandro Palmeri, UK  
Pasquale Palumbo, Italy  
Jürgen Pannek, Germany  
Elena Panteley, France  
Achille Paolone, Italy  
George A. Papakostas, Greece  
Xosé M. Pardo, Spain  
Vicente Parra-Vega, Mexico  
Manuel Pastor, Spain  
Petr Páta, Czech Republic  
Pubudu N. Pathirana, Australia  
Surajit Kumar Paul, India  
Sitek Paweł, Poland  
Luis Payá, Spain  
Alexander Paz, Australia  
Igor Pažanin, Croatia  
Libor Pekař, Czech Republic  
Francesco Pellicano, Italy  
Marcello Pellicciari, Italy  
Haipeng Peng, China  
Mingshu Peng, China  
Zhengbiao Peng, Australia  
Zhi-ke Peng, China  
Marzio Pennisi, Italy  
Maria Patrizia Pera, Italy  
Matjaz Perc, Slovenia  
A. M. Bastos Pereira, Portugal  
Ricardo Perera, Spain  
Francesco Pesavento, Italy  
Ivo Petras, Slovakia  
Francesco Petrini, Italy  
Lukasz Pieczonka, Poland  
Dario Piga, Switzerland  
Paulo M. Pimenta, Brazil  
Antonina Pirrotta, Italy  
Marco Pizzarelli, Italy  
Vicent Pla, Spain  
Javier Plaza, Spain  
Kemal Polat, Turkey  
Dragan Poljak, Croatia  
Jorge Pomares, Spain  
Sébastien Poncet, Canada  
Volodymyr Ponomaryov, Mexico  
Jean-Christophe Ponsart, France  
Mauro Pontani, Italy  
Cornelio Posadas-Castillo, Mexico  
Francesc Pozo, Spain  
Christopher Pretty, New Zealand  
Luca Pugi, Italy  
Krzysztof Puszynski, Poland  
Giuseppe Quaranta, Italy  
Vitomir Racic, Italy  
Jose Ragot, France  
Carlo Rainieri, Italy  
K. Ramamani Rajagopal, USA  
Ali Ramazani, USA  
Higinio Ramos, Spain  
Alain Rassinoux, France  
S.S. Ravindran, USA  
Alessandro Reali, Italy  
Jose A. Reinoso, Spain  
Oscar Reinoso, Spain  
Fabrizio Renno, Italy  
Nidhal Rezg, France  
Ricardo Riaza, Spain  
Francesco Riganti-Fulginei, Italy  
Gerasimos Rigatos, Greece  
Francesco Ripamonti, Italy  
Jorge Rivera, Mexico  
Eugenio Roanes-Lozano, Spain  
Bruno G. M. Robert, France  
Ana Maria A. C. Rocha, Portugal  
José Rodellar, Spain  
Luigi Rodino, Italy  
Rosana Rodríguez López, Spain  
Ignacio Rojas, Spain  
Alessandra Romolo, Italy  
Debasish Roy, India  
Gianluigi Rozza, Italy  
Jose de Jesus Rubio, Mexico  
Rubén Ruiz, Spain  
Antonio Ruiz-Cortes, Spain  
Ivan D. Rukhlenko, Australia  
Mazen Saad, France  
Kishin Sadarangani, Spain  
Andrés Sáez, Spain  
Mehrddad Saif, Canada  
John S. Sakellariou, Greece  
Salvatore Salamone, USA  
Vicente Salas, Spain  
Jose Vicente Salcedo, Spain  
Nunzio Salerno, Italy  
Miguel A. Salido, Spain  
Roque J. Saltarén, Spain  
Alessandro Salvini, Italy  
Sylwester Samborski, Poland  
Ramon Sancibrian, Spain  
Giuseppe Sanfilippo, Italy  
Miguel A. F. Sanjuan, Spain  
Vittorio Sansalone, France  
José A. Sanz-Herrera, Spain  
Nickolas S. Sapidis, Greece

E. J. Sapountzakis, Greece  
Luis Saucedo-Mora, Spain  
Marcelo A. Savi, Brazil  
Andrey V. Savkin, Australia  
Roberta Sburlati, Italy  
Gustavo Scaglia, Argentina  
Thomas Schuster, Germany  
Oliver Schütze, Mexico  
Lotfi Senhadji, France  
Junwon Seo, USA  
Joan Serra-Sagrsta, Spain  
Gerardo Severino, Italy  
Ruben Sevilla, UK  
Stefano Sfarra, Italy  
Mohamed Shaat, Egypt  
Mostafa S. Shadloo, France  
Leonid Shaikhet, Israel  
Hassan M. Shanechi, USA  
Bo Shen, Germany  
Suzanne M. Shontz, USA  
Babak Shotorban, USA  
Zhan Shu, UK  
Nuno Simões, Portugal  
Christos H. Skiadas, Greece  
Konstantina Skouri, Greece  
Neale R. Smith, Mexico  
Bogdan Smolka, Poland  
Delfim Soares Jr., Brazil  
Alba Sofi, Italy  
Francesco Soldovieri, Italy  
Raffaele Solimene, Italy  
Jussi Sopenan, Finland  
Marco Spadini, Italy  
Bernardo Spagnolo, Italy  
Paolo Spagnolo, Italy  
Ruben Specogna, Italy  
Vasilios Spitas, Greece  
Sri Sridharan, USA  
Ivanka Stamova, USA  
Rafał Stanisławski, Poland  
Florin Stoican, Romania  
Salvatore Strano, Italy  
Yakov Strelniker, Israel  
Guang-Yong Sun, China  
Ning Sun, China  
Sergey A. Suslov, Australia  
Thomas Svensson, Sweden

Andrzej Swierniak, Poland  
Andras Szekrenyes, Hungary  
Kumar K. Tamma, USA  
Yang Tang, Germany  
Hafez Tari, USA  
Alessandro Tasora, Italy  
Sergio Teggi, Italy  
Ana C. Teodoro, Portugal  
Alexander Timokha, Norway  
Gisella Tomasini, Italy  
Francesco Tornabene, Italy  
Antonio Tornambe, Italy  
Javier Martinez Torres, Spain  
Mariano Torrisi, Italy  
George Tsiatas, Greece  
Antonios Tsourdos, UK  
Federica Tubino, Italy  
Nerio Tullini, Italy  
Andrea Tundis, Italy  
Emilio Turco, Italy  
Vladimir Turetsky, Israel  
Mustafa Tutar, Spain  
Ilhan Tuzcu, USA  
Efstratios Tzirtzilakis, Greece  
Filippo Ubertini, Italy  
Francesco Ubertini, Italy  
Mohammad Uddin, Australia  
Hassan Ugail, UK  
Giuseppe Vairo, Italy  
Eusebio Valero, Spain  
Pandian Vasant, Malaysia  
Marcello Vasta, Italy  
Carlos-Renato Vázquez, Mexico  
Miguel E. Vázquez-Méndez, Spain  
Josep Vehi, Spain  
Martin Velasco Villa, Mexico  
K. C. Veluvolu, Republic of Korea  
Fons J. Verbeek, Netherlands  
Franck J. Vernerey, USA  
Georgios Veronis, USA  
Vincenzo Vespi, Italy  
Renato Vidoni, Italy  
V. Vijayaraghavan, Australia  
Anna Vila, Spain  
Rafael J. Villanueva, Spain  
Francisco R. Villatoro, Spain  
Uchechukwu E. Vincent, UK

Gareth A. Vio, Australia  
Francesca Vipiana, Italy  
Stanislav Vitek, Czech Republic  
Thuc P. Vo, UK  
Jan Vorel, Czech Republic  
Michael Vynnycky, Sweden  
Hao Wang, USA  
Liliang Wang, UK  
Shuming Wang, China  
Yongqi Wang, Germany  
Roman Wan-Wendner, Austria  
Jaroslaw Wąs, Poland  
P.H. Wen, UK  
Waldemar T. Wójcik, Poland  
Changzhi Wu, Australia  
Desheng D. Wu, Sweden  
Hong-Yu Wu, USA  
Yuqiang Wu, China  
Michalis Xenos, Greece  
Guangming Xie, China  
Xue-Jun Xie, China  
Gen Q. Xu, China  
Hang Xu, China  
Joseph J. Yame, France  
Xinggang Yan, UK  
Jixiang Yang, Canada  
Mijia Yang, USA  
Yongheng Yang, Denmark  
Luis J. Yebra, Spain  
Peng-Yeng Yin, Taiwan  
Qin Yuming, China  
Elena Zaitseva, Slovakia  
Arkadiusz Zak, Poland  
Daniel Zaldivar, Mexico  
Francesco Zammori, Italy  
Vittorio Zampoli, Italy  
Rafał Zdunek, Poland  
Ibrahim Zeid, USA  
Huaguang Zhang, China  
Kai Zhang, China  
Qingling Zhang, China  
Xianming Zhang, Australia  
Xuping Zhang, Denmark  
Zhao Zhang, China  
Yifan Zhao, UK  
Jian G. Zhou, UK  
Quanxin Zhu, China



---

Mustapha Zidi, France  
Gaetano Zizzo, Italy

Zhixiang Zou, Germany  
Maria do Rosário de Pinho, Portugal

# Contents

## **Advanced Observer-Based Control for Benchmark Control Problems: From Mathematical Modeling to Control Design**

Olfa Boubaker , Mihai Lungu , Binoy K. Roy, and Luis J. Yebra 

Editorial (2 pages), Article ID 2161456, Volume 2018 (2018)

## **Speed Control for a Marine Diesel Engine Based on the Combined Linear-Nonlinear Active Disturbance Rejection Control**

Runzhi Wang , Xuemin Li , Jiguang Zhang, Jian Zhang, Wenhui Li, Yufei Liu , Wenjie Fu , and Xiuzhen Ma

Research Article (18 pages), Article ID 7641862, Volume 2018 (2018)

## **Discontinuous High-Gain Observer in a Robust Control UAV Quadrotor: Real-Time Application for Watershed Monitoring**

A. E. Rodríguez-Mata, G. Flores, A. H. Martínez-Vásquez, Z. D. Mora-Felix, R. Castro-Linares , and L. E. Amabilis-Sosa 

Research Article (10 pages), Article ID 4940360, Volume 2018 (2018)

## **Full and Reduced-Order Unknown Input Observer Design for Linear Time-Delay Systems with Multiple Delays**

Seifeddine Ben Warrad, Olfa Boubaker , Mihai Lungu , and Saleh Mobayen

Research Article (13 pages), Article ID 1745734, Volume 2018 (2018)

## **An Optimal Identification of the Input-Output Disturbances in Linear Dynamic Systems by the Use of the Exact Observation of the State**

Jędrzej Byrski  and Witold Byrski 

Research Article (15 pages), Article ID 8048567, Volume 2018 (2018)

## **Sensorless Control for Joint Drive Unit of Lower Extremity Exoskeleton with Cascade Feedback Observer**

Pei Pei , Zhongcai Pei, Zhengqiang Shi, Zhiyong Tang , and Yang Li

Research Article (11 pages), Article ID 3029514, Volume 2018 (2018)

## **A New Direct Speed Estimation and Control of the Induction Machine Benchmark: Design and Experimental Validation**

Ali Hmidet , Rachid Dhifaoui , and Othman Hasnaoui

Research Article (10 pages), Article ID 9215459, Volume 2018 (2018)

## **A Finite-Time Disturbance Observer Based Full-Order Terminal Sliding-Mode Controller for Manned Submersible with Disturbances**

Xing Fang  and Fei Liu 

Research Article (11 pages), Article ID 1307308, Volume 2018 (2018)

## **Attitude Controller Design with State Constraints for Kinetic Kill Vehicle Based on Barrier Lyapunov Function**

Tao Zhang , Jiong Li, Huaji Wang , ChuHan Xiao, and Wanqi Li

Research Article (15 pages), Article ID 4397548, Volume 2018 (2018)

## **Unknown Inputs Nonlinear Observer for an Activated Sludge Process**

Feten Smida , Taoufik Ladhari , Salim Hadj Saïd, and Faouzi M'sahli

Research Article (12 pages), Article ID 1382914, Volume 2018 (2018)

## Editorial

# Advanced Observer-Based Control for Benchmark Control Problems: From Mathematical Modeling to Control Design

Olfa Boubaker <sup>1</sup>, Mihai Lungu <sup>2</sup>, Binoy K. Roy,<sup>3</sup> and Luis J. Yebra <sup>4</sup>

<sup>1</sup>University of Carthage, National Institute of Applied Sciences and Technology, Tunis, Tunisia

<sup>2</sup>University of Craiova, Craiova, Romania

<sup>3</sup>NIT Silchar, Assam, India

<sup>4</sup>Platforma Solar de Almeria, Almeria, Spain

Correspondence should be addressed to Olfa Boubaker; [olfa.boubaker@insat.rnu.tn](mailto:olfa.boubaker@insat.rnu.tn)

Received 12 December 2018; Accepted 12 December 2018; Published 27 December 2018

Copyright © 2018 Olfa Boubaker et al. This is an open access article distributed under the Creative Commons Attribution License, which permits unrestricted use, distribution, and reproduction in any medium, provided the original work is properly cited.

In the field of control theory, several benchmark systems of high interest exist in the literature and are frequently used as fundamental systems for testing emerging control algorithms. In spite of their simple structure, such systems have the richest dynamics and still refer to challenging control problems.

On the other hand, despite being a relatively old subject in control theory, observer-based control design has regained much interest in the last few years due to its significant potential to solve many engineering problems. The non exact knowledge of systems dynamics, non availability of state measurements, and the presence of uncertainties and perturbations could justify such attention. The separation principle of the controller-observer design is at the heart of this challenging problem in relation to rather conflicting requirements such as stability, performance, and robustness.

The first objective of this special issue is to bring the attention of the scientific community to the importance of mathematical modeling in the field of control systems. Our purpose is also to draw a state of the art of the available benchmarks in this field by focusing on the ability of their mathematical models to solve many complex control problems. These benchmarks include the following engineering applications: industrial applications: rotary drilling system, stirring reactor with heat exchanger, distillation column, chemical reactor, three-tank process, four-tank process, and so on; mechanical applications: mass-spring-damper system, bouncing ball, TORA system, hard-disk drive system, magnetic levitation system, and so on; robotic applications: cart

inverted pendulum, Furuta pendulum, reaction wheel pendulum, beam-and-ball, two-link flexible manipulator, and so on; automotive applications: vehicle dynamics system, diesel engine system, battery model, and so on; flight dynamics applications: VTOL aircraft, HL-20 vehicle, 747 Jet aircraft, and so on.

The second objective of this special issue is to propose advanced observer-based control mathematical methods in relation to the latest engineering problems.

A total of 41 papers were submitted for consideration of the special issue and only 9 papers were accepted for publication. Thus, the acceptance rate is less than 22%. Different types of observers are proposed especially where various benchmark systems are considered to implement the proposed observer-based controllers.

In “A Finite-Time Disturbance Observer Based Full-Order Terminal Sliding-Mode Controller for Manned Submersible with Disturbances” by X. Fang and F. Liu, a full-order terminal sliding-mode controller based on the finite-time disturbance observer for the “JIAOLONG” manned submersible with lumped disturbances is proposed. The closed-loop system stability analysis is given by Lyapunov theory. The simulation results demonstrate the satisfactory tracking performance and excellent disturbance rejection capability.

In “Unknown Inputs Nonlinear Observer for an Activated Sludge Process” by F. Smida et al., the authors have proposed a cascaded high gain unknown inputs nonlinear observer for an activated sludge process. The proposed

observer not only estimates the ammonia and substrate concentration (unmeasurable states) but also reconstructs the influent ammonia and the influent substrate concentration (unknown inputs). The simulation results are validated with experimental data.

S. Ben Warrad et al. have proposed full and reduced order unknown input observers for a class of linear time-delay systems with multiple delays in their paper titled “Full and Reduced-Order Unknown Input Observer Design for Linear Time-Delay Systems with Multiple Delays”. The existence conditions of the two observers are given. The proposed concepts are validated via simulation results using the quadruple-tank benchmark.

In “Sensorless Control for Joint Drive Unit of Lower Extremity Exoskeleton with Cascade Feedback Observer” by P. Pei et al., a cascade feedback observer consists of integral-switching-function sliding mode observer and an adaptive FIR filter is presented. The stability condition of the observer is obtained using Lyapunov theory. Simulations and experiments are carried out to verify its validity.

The paper titled “Attitude Controller Design with State Constraints for Kinetic Kill Vehicle Based on Barrier Lyapunov Function” is submitted by T. Zhang et al. In their paper, a nonlinear disturbance observer is designed for estimation and compensation of uncertainties and disturbances. An adaptive attitude controller is designed for Kinetic Kill Vehicle combining Barrier Lyapunov function with sliding mode controller. Numerical simulations validate that the proposed method can achieve state constraints, pseudolinear operation, and high accuracy.

In “Discontinuous High-Gain Observer in a Robust Control UAV Quadrotor: Real-Time Application for Watershed Monitoring” by A. E. Rodríguez-Mata et al., a high-gain observer based on a discontinuous technique is presented. The high-gain observer estimates external disturbances such as wind and parameter uncertainties. This observer is used to design a robust control algorithm for a quadrotor UAV attitude dynamics to monitor a watershed in real time. Lyapunov stability theory is used during the design. The simulation and experimental results validate the nonlinear observer performance and robustness of the approach under windy conditions.

R. Wang et al. have presented their paper on “Speed Control for a Marine Diesel Engine Based on the Combined Linear-Nonlinear Active Disturbance Rejection Control”. A compound control scheme with linear and nonlinear active disturbance rejection controllers along with their switching policy is proposed to control the speed of a marine diesel engine. Linear and nonlinear extended state observers are also used. The simulation results demonstrate that the proposed control scheme has prominent control effects under both the speed tracking mode and the condition with different types and levels of load disturbance.

In “An Optimal Identification of the Input-Output Disturbances in Linear Dynamic Systems by the Use of the Exact Observation of the State” by J. Byrski and W. Byrski, a technique is presented for the estimation of unknown disturbance signals acting in the input and output measurements

of a dynamic linear system. Two different integral type state observers are used in parallel for this purpose.

In “A New Direct Speed Estimation and Control of the Induction Machine Benchmark: Design and Experimental Validation” by A. Hmidet et al., a sensorless speed control technique of an induction machine is presented. The speed is estimated based on the measured current and voltage of the stator. Experimental results show that the proposed approach has interesting capabilities to conduct induction motor in real time operation with good accuracy.

## Conflicts of Interest

The editors declare that they have no conflicts of interest regarding the publication of this special issue.

## Acknowledgments

The editors would like to express their gratefulness to all authors of the special issue for their valuable contributions and to all reviewers for their helpful and professional efforts to provide precious effective comments and feedback. We hope this special issue offers a wide-ranging and timely view of the area of design of observers and observer-based controllers, which will generate stimulation for further academic research and industrial applications.

*Olfa Boubaker  
Mihai Lungu  
Binoy K. Roy  
Luis J. Yebra*

## Research Article

# Speed Control for a Marine Diesel Engine Based on the Combined Linear-Nonlinear Active Disturbance Rejection Control

Runzhi Wang <sup>1</sup>, Xuemin Li <sup>1</sup>, Jiguang Zhang,<sup>2</sup> Jian Zhang,<sup>1</sup> Wenhui Li,<sup>1</sup> Yufei Liu <sup>1</sup>, Wenjie Fu <sup>1</sup> and Xiuzhen Ma<sup>1</sup>

<sup>1</sup>College of Power and Energy Engineering, Harbin Engineering University, Harbin 150001, China

<sup>2</sup>China State Shipbuilding Corporation Limited, Beijing 100048, China

Correspondence should be addressed to Xuemin Li; [lxm@hrbeu.edu.cn](mailto:lxm@hrbeu.edu.cn)

Received 23 July 2018; Revised 11 November 2018; Accepted 28 November 2018; Published 13 December 2018

Academic Editor: Luis J. Yebra

Copyright © 2018 Runzhi Wang et al. This is an open access article distributed under the Creative Commons Attribution License, which permits unrestricted use, distribution, and reproduction in any medium, provided the original work is properly cited.

In this paper, a compound control scheme with linear active disturbance rejection control (LADRC) and nonlinear active disturbance rejection control (NLADRC) is designed to stabilize the speed control system of the marine engine. To deal with the high nonlinearity and the complex disturbance and noise conditions in marine engines, the advantages of both LADRC and NLADRC are employed. As the extended state observer (ESO) is affected severely by the inherent characteristics (cyclic speed fluctuation, cylinder-to-cylinder deviations, etc.) of the reciprocating engines, a cycle-detailed hybrid nonlinear engine model is adopted to analyze the impact of such characteristics. Hence, the controller can be evaluated based on the modified engine model to achieve more reliable performance. Considering the mentioned natural properties in reciprocating engines, the parameters of linear ESO (LESO), nonlinear ESO (NLESO), and the switching strategy between LADRC and NLADRC are designed. Finally, various comparative simulations are carried out to show the effectiveness of the proposed control scheme and the superiority of switching strategy. The simulation results demonstrate that the proposed control scheme has prominent control effects both under the speed tracking mode and the condition with different types and levels of load disturbance. This study also reveals that when ADRC related approaches are employed to the reciprocating engine, the impact of the inherent characteristics of such engine on the ESO should be considered well.

## 1. Introduction

Compared with the aviation, rail, and automobile transport, shipping is known as the most energy efficient and environmental friendly classical mode of transport [1]. The energy generated by marine diesel engines is widely used in the domain of ship propulsion [2–5]. In such application, speed control for the marine main engine becomes a crucial task.

On the one hand, the engine speed should be regulated effectively over all working points of the engine. Otherwise, the oscillation of engine speed would lead to abnormal operating conditions [4], which decreases the service life of engines and even results in premature failure of the transmission system in case of severe speed fluctuation [6]. Moreover, sustained overspeed will cause irreversible

damage to the marine main engine [7]. On the other, an excellent speed controller can help the engine keep good power performance under its complex operation conditions, thus reducing the fuel consumption and emission [8, 9] and releasing partial burden of the engine control unit (ECU) from the increasingly strict diesel emission regulations.

The main task of marine engine speed control comprises tracking the target speed fast and maintaining the engine speed steady in the presence of the intrinsic instabilities and disturbances coupled with the fast and dynamic changes of external environment, load, and operation conditions [7].

Historically, various different strategies have been adopted on the speed regulation for marine main engines, such as traditional PID [10], sliding mode control (SMC) [3],  $H_\infty$  control [11], fuzzy control [7], and model predictive

control (MPC) [12]. Although these control strategies have been attempted to provide feasible ways to deal with the marine engine speed control issue, most of them have corresponding drawbacks. For instance, the parameters in classical PID need to be readjusted when the engine operation deviates further from the calibrated situation caused by the changing of external condition; the chattering phenomenon in SMC is hard to be eliminated; the control effect of  $H_\infty$  and fuzzy methods is limited because the operation condition of the marine engine varies widely; and the implementation of MPC is complex and with considerable high cost.

So far, speed regulation for diesel engines remains to be a challengeable mission due to the fact that diesel engines are inherently high nonlinear, and their load disturbance is harsh and unpredictable. In fact, the load disturbance not only varies with the operation condition but also is affected strongly by numerous other external aspects, such as the marine weather and the sea surface condition [3, 13]. In the moderate sea conditions, the load disturbance is mainly caused by ocean current. However, when a ship navigates in extreme seas, partial or whole, the propeller disk would emerge from the water. Hence, different levels of change in propeller torque might exist and would result in a large fluctuation in marine engine speed [14].

Focusing on the mentioned sophisticated load disturbance, active disturbance rejection control (ADRC) has been applied to the marine engine speed control because of its considerable control effect in dealing with the system with uncertain disturbances. It has been proved by enormous practical applications in extensive industrial domains, such as in [15–18], that ADRC has strong robustness towards parameters variations, disturbances, and noises. In the field of marine main engine, for instance, in [19], a nonlinear active disturbance rejection controller was designed for a MAN B&W large low-speed diesel engine via a simplified transfer function engine model. In [20], a combined controller based on cerebellar model articulation controller (CMAC) and ADRC was presented to control the engine speed on a simplified empirical diesel engine model coupled with the model of propeller and hull dynamics.

However, in most of the previous articles concerning marine engine speed control, the controllers were only evaluated by using simple engine models. The impact of the intrinsic characteristic of the engine speed on the control effect of these controllers has been ignored. In terms of the reciprocating engine, engine speed is naturally cyclic fluctuation due to the existence of the in-cylinder discrete torque generation [21, 22]. The periodic instant speed signal in the crank-angle (CA) domain is cyclic but aperiodic in the time domain as the engine speed varies [23]. The inherent speed fluctuation would be more serious when affected by cylinder-to-cylinder and cycle-to-cycle differences in torque production [21, 24]. Furthermore, the deviations in engine speed caused by imbalance working in cylinders are characterized as periodic disturbances in the CA domain [21] rather than the general time domain, which has been proved as a difficulty for asymptotic tracking and disturbance rejection

[23]. In this study, it is found that this phenomenon has a significant impact on the performance of the ESO.

In general, it is reported that the mean value engine model (MVEM) is sufficient for controller design [25, 26]. But for some control algorithms it can be summed up from previous articles that it is hard to guarantee the objectivity when designing a speed controller for the reciprocating engine, because of the existence of these ignored characteristics in engine speed. For example, as for SMC, there are papers researched the application by testing MVEM or else simplified engine model, and the results are found to be satisfactory [3, 27]. Nevertheless, when the similar methods were tested on a more complex engine model or a real engine, the results turned out to be less ideal. In [28, 29], the oscillation in speed caused by the coupling of chattering phenomenon in SMC and the inherent speed fluctuation in reciprocating engine cannot be alleviated easily, and the oscillation of control input is also apparent [27]. Likewise, this is also an inevitable impact for the controller based on ADRC as the control performance of ADRC is affected by noise and disturbance [17, 30].

It should be pointed out that the mentioned issue has not drawn any attention when the ADRC method is applied on the engine speed regulation, whereas its impact can be observed in related articles. In [8], a linear ADRC (LADRC) framework was adopted to compensate the total disturbance for idle speed control in a diesel engine. Although the control performance for sudden load disturbances has been improved effectively, the steady-state speed variation is obviously larger than it in the commercial controller where PID method is employed. As far as the authors know, there is no analysis about the reason therein.

As mentioned above, the noise and disturbance are extremely complex and uncertain in marine engines, and the type and extent of the disturbance are various. Moreover, the performance of ESO is also affected by the natural speed fluctuation. Single LADRC or nonlinear ADRC (NLADRC) may not guarantee control performance over the whole work conditions. In [31], a systemic analysis of the characteristics of LADRC and NLADRC is provided. Normally, NLADRC outperforms LADRC, but when the level of the total noise and disturbance turns to a certain degree, the performance of NLADRC will decrease sharply [31]. It is summarized that by combining LADRC and NLADRC, it leads to a better method called LADRC/NLADRC switching control (SADRC), which keeps the merits of both methods. Better control performance can be obtained when the total disturbance and noise are complicated, and their amplitudes change widely. This kind of control strategy has not been tested in marine engine speed control domain which suffered from the mentioned sophisticated load disturbance, noise, and the inherent speed fluctuation.

Motivated by the previous research and the challenges stated above, a speed controller that employs the SADRC scheme is designed to deal with the complex noise and disturbance in the marine engine. Considering the analysis above about the inadequacy in the validation of the previous ADRC based controllers for the diesel engine speed control via MVEMs or simpler engine models, a more detailed engine

model is adopted, which can exhibit the inherent speed fluctuation. Aiming at the special features of the engine speed, the parameters for the proposed controller are adjusted via analyzing the impact of the inherent speed fluctuation on the performance of ESO. Finally, in order to show the superiority of the proposed scheme, comparisons between the proposed control scheme and other controllers are carried out under speed tracking mode and various external load disturbance conditions.

The rest of this paper is organized as follows. A cycle-detailed hybrid nonlinear engine model is presented in Section 2, and the detailed differences between the proposed engine model and the classic MVEM are compared. In Section 3, the SADRC algorithm for engine speed control is described. And the impact of the inherent speed fluctuation on the performance of ESO is studied, based on which the parameters in the proposed controller are designed. Section 4 exhibits the control performance of the proposed controller by comparing with LADRC, NLADRC, and PID controller. In Section 5, the conclusion is summarized about the whole work in this study, and a research direction for further work is discussed.

## 2. The Cycle-Detailed Hybrid Nonlinear Engine Model

In this study, the idea in [22, 32] is employed to modify the common MVEM. By doing such, the advantages in the MVEM are kept; meanwhile, the inherent speed fluctuation caused by the discrete torque generation and cyclic deviations among cylinders can be simulated without making the engine model more complex and harder to be executed in computation. Figure 1 demonstrates the thermodynamic volumes for the marine engine. The engine model is composed of five parts which are the intake and exhaust manifold, cylinders, intercooler, and turbocharger. In this paper, only the discrete torque generation process and the final crankshaft dynamic are provided. Else contents of the engine model, such as engine cycle delays, intake and exhaust manifold, intercooler, turbocharger, can refer to the authors' previous work [5].

*2.1. The Discrete Torque Generation Process.* The CA signal  $\varphi$  is calculated by

$$\varphi = \text{mod} \left( \int 6n_e dt, 720 \right), \quad (1)$$

where  $n_e$  is engine speed and operator "mod" represents modulus.

Such CA signal is used to decide the timing sequence for the in-cylinder process. For the individual cylinder, the discrete torque generation mechanism and the in-cylinder evolution process can be shown in the form of finite-state machines (FSMs) [22, 32]. Figure 2 shows that the indicated torque is produced only within the phases "C" to "E". Assuming the indicated torque is sustained unchanged during such phase, the mean indicated torque value in the whole working cycle can be replaced by the mean indicated torque during the process from "C" to "E".

Moreover, to simulate the imbalance working ability among cylinders, a factor  $\xi_i$  is defined, which denotes the cylinder-by-cylinder variation of the cylinder  $i$ . As a result, the gross indicated torque  $M_{ig}^i$  for the cylinder  $i$  is shown as follows

$$M_{ig}^i = P_{duration} \frac{30 \cdot W_f^i \cdot q_{HV} \cdot \eta_{ig}^i}{\pi \cdot n_e} \frac{720}{N_c \cdot \varphi_f} \xi_i, \quad (2)$$

$$P_{duration} = \begin{cases} 1 & (i-1) \frac{360}{N_c} < \varphi < (i-1) \frac{360}{N_c} + \varphi_f \\ 0 & \text{otherwise,} \end{cases} \quad (3)$$

$$\eta_{ig}^i = f(n_e, \lambda^i), \quad (4)$$

where  $P_{duration}$  is pulse function,  $W_f^i$  is the fuel mass flow rate of the cylinder  $i$ ,  $q_{HV}$  is the low calorific value of diesel,  $\eta_{ig}^i$  represents the indicated efficiency of the cylinder  $i$ , which can be defined as a function between the engine speed and air to fuel ratio (AFR) (defined as  $\lambda^i$  for the cylinder  $i$ ),  $\varphi_f$  means the lasting angle of the expansion phase, and  $N_c$  is the number of cylinders.

The mass fuel flow of the cylinder  $i$ ,  $W_f^i$ , can be calculated by

$$W_f^i = \frac{n_e \cdot N_c \cdot m_f}{120} \cdot 10^{-6}, \quad (5)$$

where  $m_f$  is the control input (fuel injection quality per stroke per cylinder).

The total gross indicated torque  $M_{ig}$  is

$$M_{ig} = \sum_1^{N_c} M_{ig}^i. \quad (6)$$

*2.2. Engine Rotational Dynamic.* Combing the indicated torque from all cylinders, the engine rotational dynamic equation can be described by

$$\begin{aligned} J_e \frac{dn_e}{dt} \\ = \frac{30}{\pi} \left( M_{ig} - (M_p + M_f + M_{load} + M_{wave} + M_{noise}) \right), \end{aligned} \quad (7)$$

where  $J_e$  is the total rotary inertia,  $M_p$  is the pumping torque,  $M_f$  is the friction torque,  $M_{load}$  means the load torque,  $M_{wave}$  represents the load disturbance from wave, and  $M_{noise}$  is the total bounded disturbance.

For more information about the engine model and the mentioned symbols, refer to [5].

*2.3. The Comparison between the Cycle-Detailed Hybrid Nonlinear Engine Model and the MVEM.* Under the same control parameters (a PID controller), noise condition, and tested

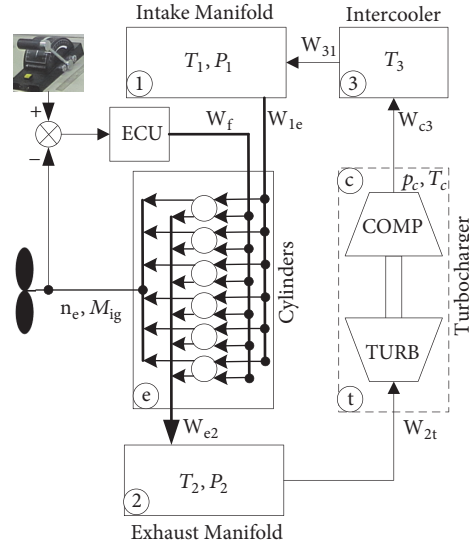


FIGURE 1: Schematic diagram of the marine diesel engine for propulsion.

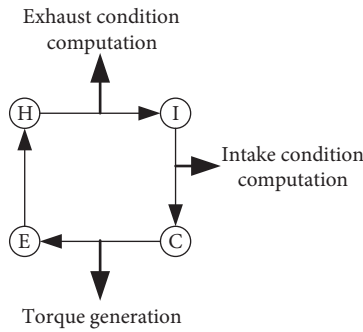


FIGURE 2: In-cylinder evolution process (where “I” represents intake process, “C” compression process, “E” expansion process, and “H” exhaust process).

process, the individual cylinder indicated torque waveform of the hybrid engine model can be demonstrated in Figure 3(a). The comparisons of the total indicated torque and the engine speed for both engine models are shown in Figures 3(b) and 3(c), respectively. The right side of Figure 3 denotes the enlarged plots for the corresponding compared variables within around one engine working cycle.

Figure 3(a) shows the pulse indicated torque in individual cylinder. It can clearly illustrate the discrete torque generation process. Meanwhile, it can be known from Figure 3(b) that the mean effect of the total indicated torque in the proposed engine model is almost the same in MVEM. It can be observed from Figure 3(c) that the inherent speed fluctuation can be modeled in the proposed engine model. The engine speed fluctuation (instant and average speed) in the engine model is significantly larger than that in the MVEM. And the control effect in the proposed engine model is inferior to that in the MVEM. Note that the MVEM has been verified in authors’ previous research [3]. It can be noticed from

Figure 3(c) that the speed responses in the two models are the same in overall, which can be believed as the verification of the proposed model in this study.

### 3. Controller Design

**3.1. Basic Description of the ADRC.** It was proved in previous papers, such as [8, 19, 20], that second-order or even first-order ADRC is suitable to the engine speed control by some corresponding simplifications. To improve the speed control accuracy, we decide to adopt second-order ADRC, although the engine rotational dynamic model Equation (7) is first-order. On one hand, having the engine system with inevitable delay (such as turbocharge lag and cyclic combustion delay), the first-order ADRC would not guarantee control performance in some working conditions. On the other, the second-order ADRC has better adaptability and disturbance prediction ability [33], which will improve the control performance in the case of sophisticated working conditions for marine diesel engines. In order to show clearly the advantage of the using second-order ADRC, Figure 4 gives the control performance comparison between them. It is obvious that the overshoot, settling time, and the steady-state speed fluctuation in the former are larger than those in the latter.

Taking the derivative of both sides of (7), we can get

$$\dot{n}_e = \frac{30}{\pi J_e} \dot{M}_{ig} - f(n_e, \dot{n}_e, \lambda^i, \omega(t)) \quad (8)$$

where  $\dot{n}_e$  is the derivate of engine speed  $n_e$ ,  $\omega(t)$  means the unknown disturbance and unmodeled dynamics,  $f(n_e, \dot{n}_e, \lambda^i, \omega(t)) = 30(\dot{M}_p + \dot{M}_f + \dot{M}_{load} + \dot{M}_{noise} + \dot{M}_{wave})/\pi J_e$ ,

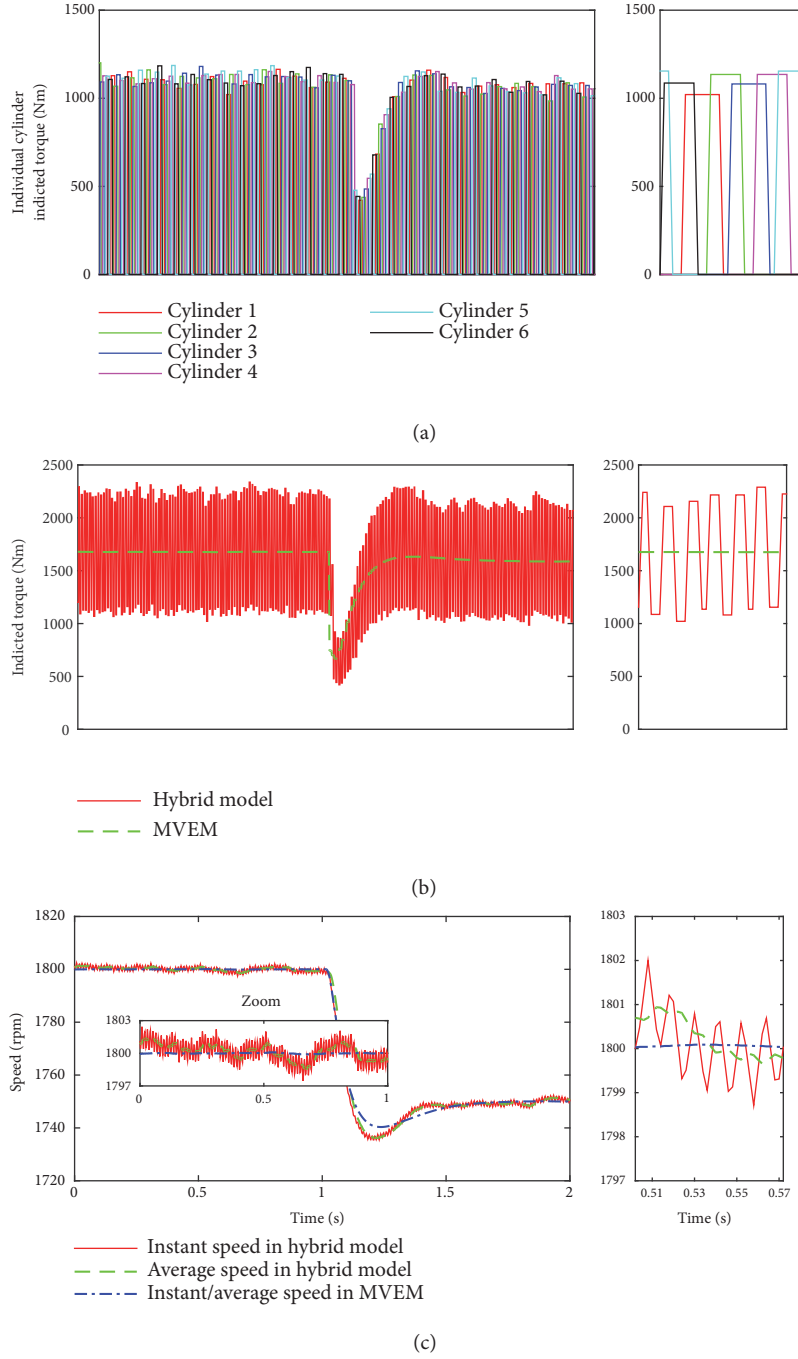


FIGURE 3: The comparisons of both engine models. (a) Individual cylinder indicated torque in the proposed engine model. (b) Total indicated torque of both engine models. (c) The speed responses of both engine models.

is an unknown and time-varying function, and  $\dot{M}_{ig}$  can be written as

$$\dot{M}_{ig} = \sum_1^{N_c} \dot{M}_{ig}^i = K \cdot g(n_e, \dot{n}_e, \lambda^i) \cdot \dot{m}_f \quad (9)$$

where  $K = (180q_{HV}\xi_i/\pi\varphi_F I_e)10^{-6}$ ,  $g(n_e, \dot{n}_e, \lambda^i) \cdot \dot{m}_f = \sum_1^{N_c} (d(P_{duration}(n_e) \cdot \eta_{ig}^i(n_e, \lambda^i) \cdot \dot{m}_f)/dt)$  is a nonlinear

time-varying function and  $\dot{m}_f$  is an intermediate variable without practical significance.

Combining (8) and (9), a new second-order dynamic model for engine speed can be constructed as follows

$$\begin{aligned} \ddot{n}_e &= K \cdot g(n_e, \dot{n}_e, \lambda^i) \cdot \dot{m}_f - f(n_e, \dot{n}_e, \lambda^i, \omega(t)) \\ &= b(t) \cdot \dot{m}_f - f(n_e, \dot{n}_e, \lambda^i, \omega(t)), \end{aligned} \quad (10)$$

where  $b(t) = (30K \cdot g(n_e, \dot{n}_e, \lambda^i) \cdot \dot{m}_f)/\pi J_e m_f$ .

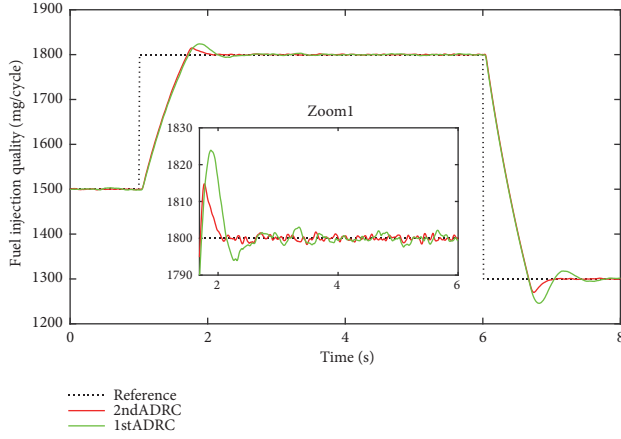


FIGURE 4: The control performance comparison between first-order and second-order ADRC.

Defining  $x_1 = n_e$ ,  $x_2 = \dot{n}_e$ ,  $x_3 = f(n_e, \dot{n}_e, \lambda^i, \omega(t))$ ,  $u = m_f$ , (10) can be rewritten in the form of state-space as follows

$$\begin{aligned} \dot{x}_1 &= x_2 \\ \dot{x}_2 &= b(t)u - x_3 \\ \dot{x}_3 &= \dot{f}(n_e, \dot{n}_e, \lambda^i, \omega(t)) \\ y &= x_1 \end{aligned} \quad (11)$$

where  $x_3$  represents the nonlinear dynamics of the engine, including the total lumped disturbance.

Hence, focusing on the state-space Equation (11), we study the second-order ADRC for diesel engine speed control in this study. According to [34], a general third-order ESO for the second-order system Equation (11) can be given as

$$\begin{aligned} e(k) &= z_1(k) - y \\ z_1(k+1) &= z_1(k) + h(z_2(k) - \beta_{01}\varphi_1(e(k))) \\ z_2(k+1) &= z_2(k) \\ &\quad + h(b_0u(k) + z_3(k) - \beta_{02}\varphi_2(e(k))) \\ z_3(k+1) &= z_3(k) - h\beta_{03}\varphi_3(e(k)) \end{aligned} \quad (12)$$

where  $y$  is the system output,  $h$  is step size,  $u(k)$  is the control input at instant  $k$ ,  $b_0$  is the control gain,  $\beta_{0i}$  ( $i=1,2,3$ ) are the gains of observer,  $z_1(k)$  and  $z_2(k)$  are the estimation of the system states at the instant  $k$ ,  $z_3(k)$  is the estimation of the total disturbance at the instant  $k$ , and  $\varphi_i(e(k))$  ( $i=1,2,3$ ) are nonlinear functions, which can be defined as

$$\begin{aligned} \varphi_i(e(k)) &= fal(e(k), \alpha_i, \delta) \\ &= \begin{cases} \frac{e(k)}{\delta^{1-\alpha_i}} & |e(k)| \leq \delta \\ |e(k)|^{\alpha_i} \operatorname{sgn}(e(k)) & |e(k)| > \delta \end{cases} \end{aligned} \quad (13)$$

where  $\alpha_i$  and  $\delta$  can be decided in advance; some recommended values are summed up in Han's research [35]. When

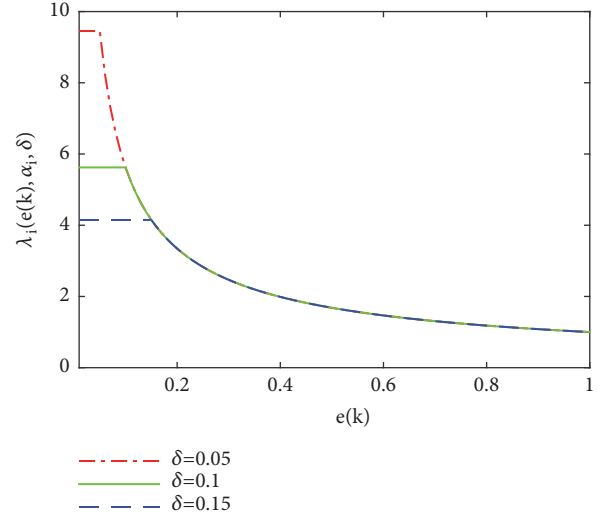


FIGURE 5: Demonstration of the function  $\lambda_i(e(k), \alpha_i, \delta)$  when  $\alpha = 0.25$ .

$\alpha_i < 1$ , this function can represent the characteristic of “small error, big gain; big error, small gain”. When  $\alpha_i = 1$ , it becomes a linear function.

To show clearly the effect of “small error, big gain; big error, small gain”, according to [31], function  $fal(e(k), \alpha_i, \delta)$  can be rewritten as

$$\begin{aligned} fal(e(k), \alpha_i, \delta) &= \frac{fal(e(k), \alpha_i, \delta)}{e(k)} e(k) \\ &= \lambda_i(e(k), \alpha_i, \delta) e(k) \end{aligned} \quad (14)$$

For instance,  $\alpha = 0.25$ , and taking  $\delta$  as 0.05, 0.1, and 0.15, respectively, a set of curves for  $\lambda_i(e(k), \alpha_i, \delta)$  can be obtained in Figure 5.

Hence, state error feedback control law can be defined as

$$\begin{aligned} e_1 &= v_1(k) - z_1(k) \\ e_2 &= v_2(k) - z_2(k) \\ u_0 &= \beta_1 fal(e_1, \alpha_i, \delta) + \beta_2 fal(e_2, \alpha'_i, \delta') \end{aligned} \quad (15)$$

where  $v_1(k)$  and  $v_2(k)$  are the set-points and their differential at the sampling instant  $k$ , respectively, and  $\beta_1$  and  $\beta_2$  are the control gains, which can be considered as nonlinear or linear control law based on the value of  $\alpha'_i$ .

In this study, to reduce both the amplification effect of noise and the burden of parameters tuning, we adopt linear control law. Hence, the state error feedback control law can be written as

$$u_0 = \beta_1 e_1 + \beta_2 e_2 \quad (16)$$

Considering the disturbance compensation, the control input can be given as

$$u(k) = u_0 - \frac{z_3(k)}{b_0} \quad (17)$$

**3.2. Scheme of SADRC for Marine Engine Speed Control.** As the state error feedback control law is chosen to be linear, the switching scheme for SADRC refers to the shift between the linear ESO (LESO) and the nonlinear ESO (NLESO).

Motivated by [31], the switch process depends on the value of  $e(k)$ . We do not consider the transition time as another shift condition as in [31]. Hence, only a specific value  $e_m$  should be decided, thus the shift between LESO and NLESO can be completed. To be specific, in the case of  $|e(k)| < e_m$ , NLESO works; otherwise, LESO takes the place of it. The method for selecting  $e_m$  proposed in [31] cannot be used directly in this study. The reason will be explained after introducing the parameters tuning of ESO (see Remark 2).

Given the input saturation of the actuator, the input signal for ESO diverges from the original control input, which causes the inaccurate estimation of the total disturbance in ESO. As shown in [36] and the references therein, a simple solution is to replace the control input for ESO by the saturated value of actuator.

To sum up, we can get the SADRC controller for marine engine speed control as illustrated in Figure 6.

**3.3. Parameters Tuning of the SADRC for Marine Engine Speed Control.** The parameters tuning in ADRC are sophisticated as there are multiple parameters that need to be adjusted, especially for NLADRC. Gao proposed a tuning method based on observer bandwidth for LADRC [30]. The parameters of LESO can be chosen as

$$\begin{aligned}\beta_{01} &= 3\omega_o, \\ \beta_{02} &= 3\omega_o^2, \end{aligned} \quad (18)$$

$$\begin{aligned}\beta_{03} &= \omega_o^3, \\ \omega_o &= 5\sim 10\omega_c, \end{aligned} \quad (19)$$

where  $\omega_o$  denotes the bandwidth of observer, which has a relationship with the control bandwidth  $\omega_c$ .

The determination of  $\omega_c$  can be found in [37], and it can be calculated by

$$\omega_c = \frac{10}{t_s^*} \quad (20)$$

where  $t_s^*$  denotes the desired setting time, which can be obtained by practical demand.

Initially, in this study, for the target engine, according to its response time (referring to Figure 4, the settling time for the acceleration and deceleration processes is within the range from 1s to 2s), the desired setting time is set to be 2s, i.e.,  $t_s^* \approx 2s$ . The choice of  $t_s^*$  should consider the limitation of the engine, including the mechanical safety and emission; for example, to obtain small  $t_s^*$ , the engine needs to run with quick speedup procedure, which would cause incomplete combustion or even damage to engine. Then we can get  $\omega_c = 5$  by (20). Choosing  $\omega_o = 8\omega_c = 40$ , the parameters in LESO can be obtained with the method of (18). Thus, we have  $\beta_{01} = 120$ ,  $\beta_{02} = 4800$ ,  $\beta_{03} = 64000$ . Note that the variations among cylinders have not been considered firstly, i.e., the factor  $\xi_i = 1$ .

On the basis of the initial parameters of LESO, the proper control parameters of linear error state feedback (LESF) are decided via trial-and-error approach in the proposed engine model. During such process, we follow some fundamentals: the delay in disturbance estimation depends on  $\beta_{03}$ , the bigger  $\beta_{03}$ , the less delay, but oversize  $\beta_{03}$  leads to oscillation; meanwhile, the control performance can be improved to a certain degree by adjusting  $\beta_{01}$  and  $\beta_{02}$  coordinately. Finally, we get the proper parameters for LESO:  $\beta_{01} = 200$ ,  $\beta_{02} = 10000$ ,  $\beta_{03} = 60000$ , and parameters for LESF:  $\beta_1 = 4.5$ ,  $\beta_2 = 0.15$ ,  $b_0 = 500$ . The control effect will be given in next section.

As for NLADRC, in [31], empirical formulas are summarized for the parameters design in NLESO. They can be decided as follows

$$\begin{aligned}\beta'_{01} &= 3\omega_o, \\ \beta'_{02} &= \frac{3\omega_o^2}{5}, \\ \beta'_{03} &= \frac{\omega_o^3}{9}. \end{aligned} \quad (21)$$

*Remark 1.* It is not possible to get feasible parameters to keep stability by (21) in this study. To get suitable parameters for NLESO, the impact of the inherent characteristics of the engine (such as speed fluctuation) on the performance of the ESO needs to be analyzed. But firstly, some parameters can be decided as  $\alpha_1 = 1$ ,  $\alpha_2 = 0.5$ ,  $\alpha_3 = 0.25$  by common previous experience [35].

Meanwhile, to illustrate the necessity of taking into account the inherent speed fluctuation while designing ADRC related controller for engine speed control, the estimation performances of the ESO between the proposed engine model and the MVEM are compared in detail. We find it easier to get the parameters of LESO in MVEM. The values calculated directly from (18) are adequate, i.e.,  $\beta_{01} = 120$ ,  $\beta_{02} = 4800$ ,  $\beta_{03} = 64000$ . Moreover, the parameters for LESO in the MVEM have a wider range than those in the proposed engine model.

The tracking curves of LESO state  $z_1$  and  $z_2$  for both engine models are shown in Figure 7. The tracking performance for  $z_3$  is not given for the total disturbance is unknown. Note that the noise condition is the same in both engine models. Moreover, the sampling and control time are designed to be 0.01s ( $h = 0.01$ ) in both engine models.

It can be observed from Figure 7 that  $z_1$  and  $z_2$  can appropriately track the system states. However, significant differences can be seen between the tracking curves of the two engine models. In the proposed engine model, the bound of the distribution of the tracking error  $e(k)$  is  $[-1.5, 1.5]$ , and most of  $e(k)$  distributes in the range  $[-1.0, 1.0]$ , whereas there is an order of magnitude difference for the corresponding values in the MVEM. Also, the changing frequency of these variables is apparently different in the two engine models. It is higher in the MVEM. The main reason is that the speed or torque changing is cycle based in the proposed engine model, while it is time based in the MVEM. From Figure 7 (c1), (c2),

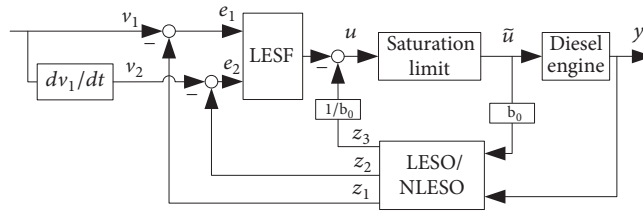


FIGURE 6: Basic control structure diagram of the SADRC method for marine engine speed control.

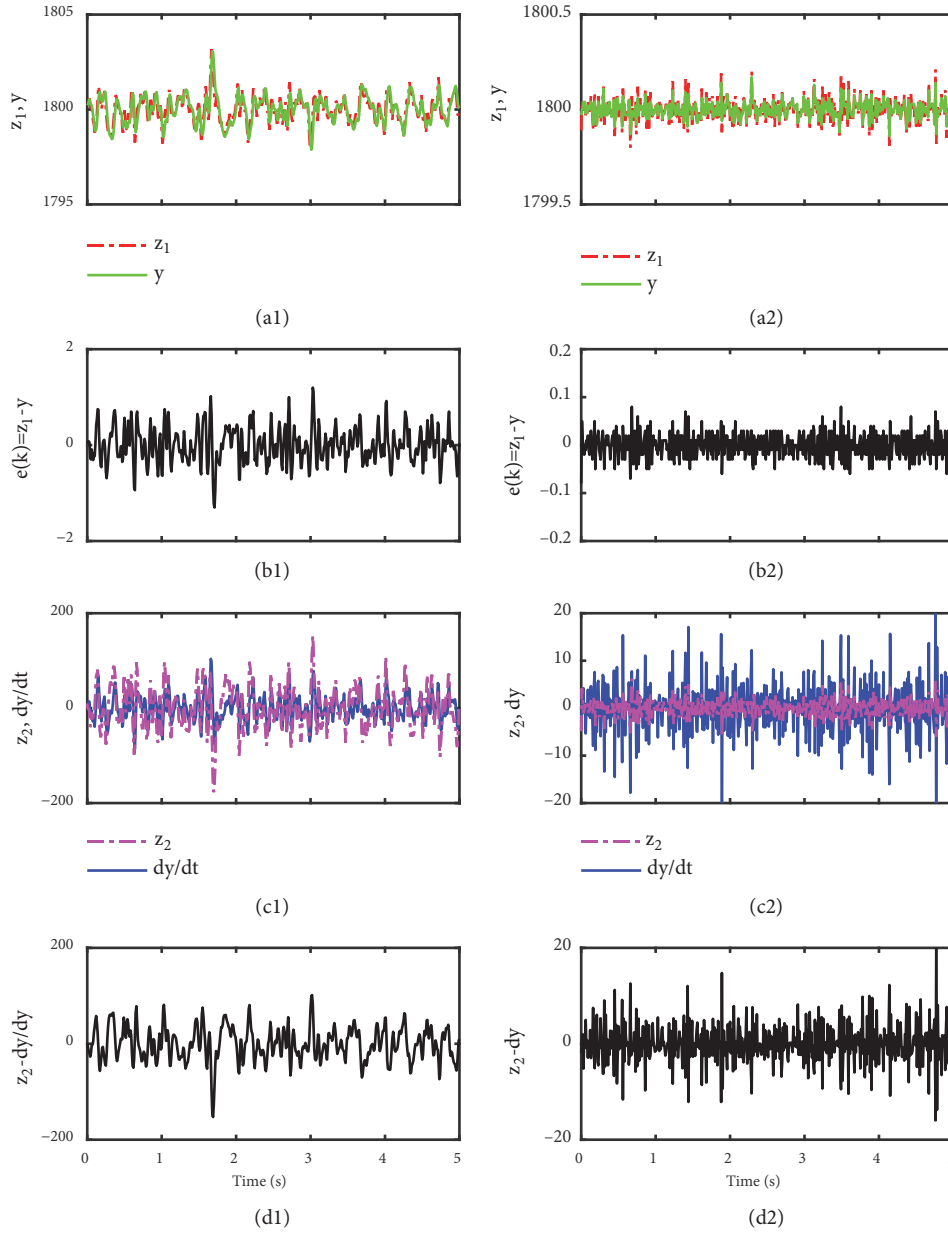


FIGURE 7: The tracking condition of the LESO state under different engine models. (a1) The tracking curves of  $z_1$  and  $y$  in the proposed engine model. (b1) The error between  $z_1$  and  $y$  in the proposed engine model. (c1) The tracking curves of  $z_2$  and  $dy/dt$  in the proposed engine model. (d1) The error between  $z_2$  and  $dy/dt$  in the proposed engine model. (a2), (b2), (c2), and (d2) represent the corresponding variables in the MVEM, respectively.

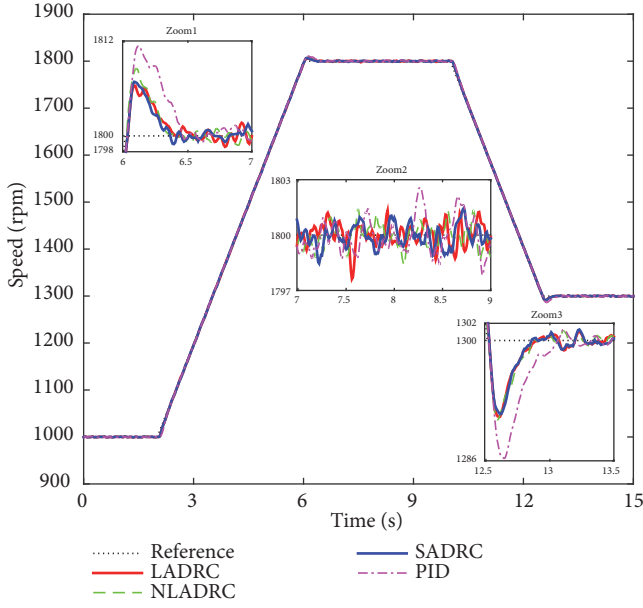


FIGURE 8: The comparisons of speed tracking performance.

we know that the estimated differential  $z_2$  is more smooth than the time-derivative of  $y$  ( $dy/dt$ ). This means that the LESO can effectively filter the disturbed time-derivative of  $y$  then lessen the noise effect on the control performance in the MVEM. On the contrary, this effect is not obvious or weak in the proposed engine model.

Since the tracking performance can hardly be improved by tuning the parameters of LESO in this study, it can be concluded that the performance of ESO (including LESO and NLESO) is limited by the inherent property in speed fluctuation, and the distribution of  $e(k)$  mentioned above is a kind of inherent property in reciprocating engines. This is different with other references, such as in [30, 31, 38, 39], where the tracking error  $e(k)$  is with a very small distribution range under steady-state. This property cannot be eliminated in the reciprocating engine. Furthermore, in a real engine, when  $e(k)$  is affected by the coupled effect of the inherent speed fluctuation and other noise and disturbance, the actual  $e(k)$  would far exceed the bound  $[-1.0, 1.0]$  inevitably. As a result, the estimating capacity of NLESO would deteriorate sharply, due to the fact shown in Figure 5 that the equivalent gain  $\lambda_i(e(k), \alpha_i, \delta) < 1$  when  $e(k) > 1$ .

*Remark 2.* Under the background mentioned above, an enlightenment is got for designing the parameters  $\beta'_{01}, \beta'_{02}, \beta'_{03}, \delta'$  in NLESO and  $e_m$  in SADRC. The basic rule is to avoid excessively amplifying the inherent property in speed fluctuation when  $e(k) < 1$ , which requires that the nonlinear gains maintain with relatively small value while  $e(k) < 1$ . Therefore,  $\delta'$  is chosen to be 0.1 to limit the maximum in gains. Then  $\beta'_{01}, \beta'_{02}, \beta'_{03}$  are regulated by reducing the corresponding value in obtained  $\beta_{01}, \beta_{02}, \beta_{03}$  (for LESO). Eventually, the proper parameters for NLESO can be determined as  $\beta'_{01} = 150, \beta'_{02} = 1200, \beta'_{03} = 5800$ . The switching condition is chosen as  $e_m = 1$ , it means that,

on the one hand, the advantage in NLESO is kept when  $e(k) < 1$ , and, on the other, LESO can avoid the performance degrading in NLESO when  $e(k) > 1$ . The choice of  $e_m$  is based on the characteristics in engine rather than the recommended value in [31]. The rationality to choose  $e_m = 1$  as the switching condition also was mentioned in [40].

## 4. Simulation and Analysis

*4.1. Engine Speed Tracking Performance.* As it is exhibited in Figure 8, to simulate the real acceleration and deceleration processes in a marine diesel engine for propulsion, ramp references are adopted. And four controllers (LADRC, NLADRC, SADRC, and PID) are compared to prove the superiority of the proposed method. The control parameters of the classical PID are well tuned by trail-and-error scheme with the consideration of wind-up scheme. Note that the load torque is normalized during these processes, and noise load is set as banded white noise with a basic constant 200 N·m. Besides, the cylinder-by-cylinder variation degree is designed as  $[\xi_1, \xi_2, \xi_3, \xi_4, \xi_5, \xi_6]^T = [1.0, 0.95, 1.0, 0.95, 0.95, 1.0]^T$ . Although the control parameters in the comparative controllers are obtained under the condition that there is no variation between cylinders, it is reasonable and necessary to assess the control effect under the imbalance cylinder condition. Because the imbalance cylinder working ability would occur and be different with its original condition when the controller was designed due to varying dynamics and ageing of components of the fuel injection system [41].

From Figure 8: Zoom1 and Zoom3, it can be observed that in both the acceleration and deceleration processes, LADRC, NLADRC, and SADRC are better than PID in terms of the control performance in overshoot and settling time. Moreover, LADRC and SADRC present slight advantage in overshoot when compared with NLADRC. As shown in Figure 8: Zoom2, the steady-state speed fluctuation in NLADRC and SARDC is obviously smaller than that in LADRC, followed by PID. When synthetically considering the control effects in overshoot and steady-state speed fluctuation, it is apparent that SADRC is the best one during the speed tracking process.

*4.2. Anti-Interference Ability under Mutation Load Disturbances.* As mentioned in the section above, when the ship voyages in the sea, the load torque is affected by wave. The load conditions become complex for marine engine. Especially, when sea waves make the partial or total propeller out of water surface then drop into water again, the load of engine would change violently. Under the same simulation condition as mentioned above, we design three different mutation loads to validate the proposed control scheme.

As displayed in Figure 9(a), when the mutation load is large (100% full load), the speed variations and settling time in LADRC and SADRC are obviously smaller than those in NLADRC and PID. Unexpectedly, the settling time in NLADRC is the longest; it is even far inferior to that in the classical PID. When the mutation load becomes to medium degree (60% full load), as shown in Figure 9(b),

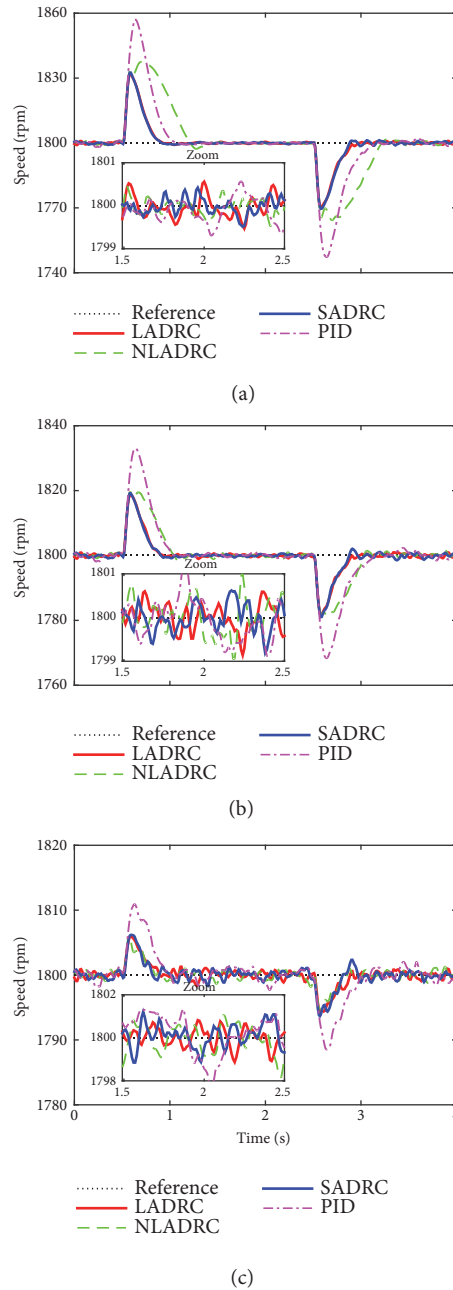


FIGURE 9: The speed responses under different levels of mutation load. (a) 100% full load. (b) 60% full load. (c) 20% full load.

the speed variations in LADRC, NLADRC, and SADRC are similar. Although the settling time in NLADRC catches up with that in PID, it is still not as good as that in the LADRC and SADRC. When the mutation load is small (20% full load), seen in Figure 9(c), both the speed variations and settling time in LADRC, NLADRC, and SADRC are almost the same. To understand well the impact of the extents of the load changing on the control performance of the comparative controllers, the estimate error of ESOs is compared in Figure 10. When the extents of load changing are larger (100% and 60% full load), the tracking error  $e(k)$  in ESOs is far beyond the bound  $[-1, 1]$  (see Figure 10, (a1, a2,

a3, b1, b2, b3)), which results in performance deterioration for NLESO. This is the reason why the NLADRC shows bad control performance in such conditions. On the contrary, when the load change is smaller (20% full load), the tracking error  $e(k)$  in ESOs is similar and within the bound  $[-1, 1]$  (see Figure 10, (c1, c2, c3)); as a result, the speed deviation and settling time during such processes for the ADRC related controllers are almost the same.

Besides, the control effects of the steady states after unloading different loads (during the time from 1.5s to 2.5s) are enlarged in the corresponding subplot in Figure 9. It can be observed that only SADRC can consistently maintain the

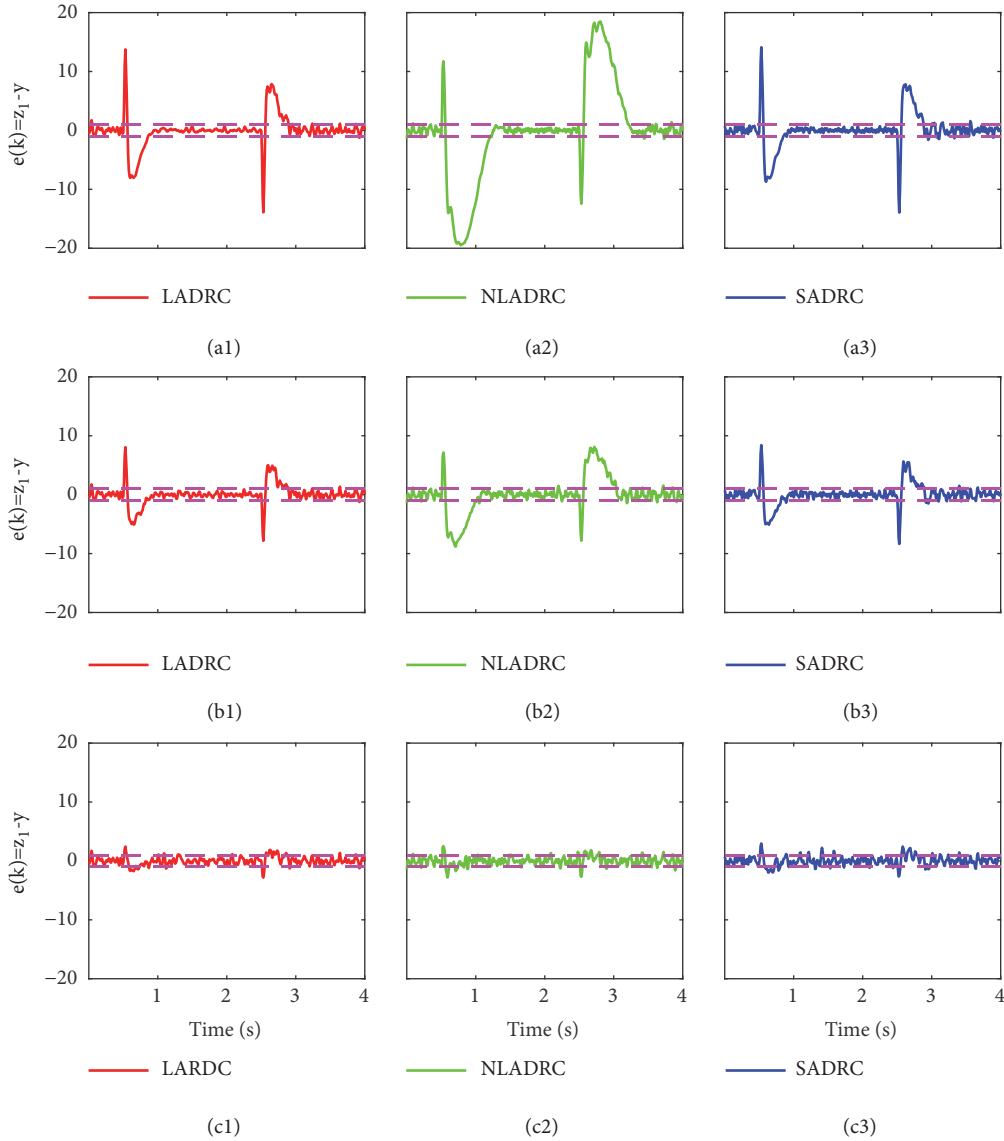


FIGURE 10: The tracking error  $e(k)$  in ESOs under different levels of mutation load. (a1, a2, a3) 100% full load. (b1, b2, b3) 60% full load. (c1, c2, c3) 20% full load.

smallest speed fluctuation. To distinguish more clearly the control effect of the controllers under steady-state, the criteria in integral absolute error ( $IAE$ ) of the system output and the total variation ( $TV$ ) of the control signal are calculated. The  $TV$  index represents the manipulated input usage, which can be computed by (22), and detailed information can be found in [42–44].

$$TV = \sum_{i=1}^{\infty} |u_{i+1} - u_i|, \quad (22)$$

where  $[u_1, u_2, \dots, u_i, \dots]$  represents the discretized control input  $u$ .

Hence, a more detailed comparison in the criteria of  $IAE$  and  $TV$  for the three mentioned steady states is manifested in Table 1. It can be seen that the value of  $IAE$  in SADRC is

significantly smaller than that in another three controllers, which means SADRC has better adaptability under steady-state after different levels of sudden load changing. As for the  $TV$  values, PID has less values in all the compared cases, which means that the control signal in PID is more smooth (as shown in Figure 11). From Figure 11, it can be observed that the control input in LADRC and SADRC adapts more quickly. On the one hand, it is similar to the explanation in [8] that faster antidisturbance ability is achieved by regulating the control input (fuel injection quality) quickly. On the other hand, it is also a drawback if high frequency oscillation with large amplitude occurs in control input. The existence of the inherent speed fluctuation and the imbalance working ability among cylinders are the main reason of such oscillation. From Table 1, we also know that, compared with LADRC, after unloading a larger load (100% and 60% full load), the

TABLE 1: The criteria of IAE and TV for different controllers after different mutation load processes.

	<b>After unloading 100% full load</b>			<b>After unloading 60% full load</b>			<b>After unloading 20% full load</b>		
	LADRC	NLADRC	PID	LADRC	NLADRC	PID	LADRC	NLADRC	PID
IAE	0.193	0.148	0.241	0.241	0.330	0.222	0.350	0.546	0.808
TV	65.3	59.5	12.1	96.7	88.2	90.9	141.5	140.6	31.1

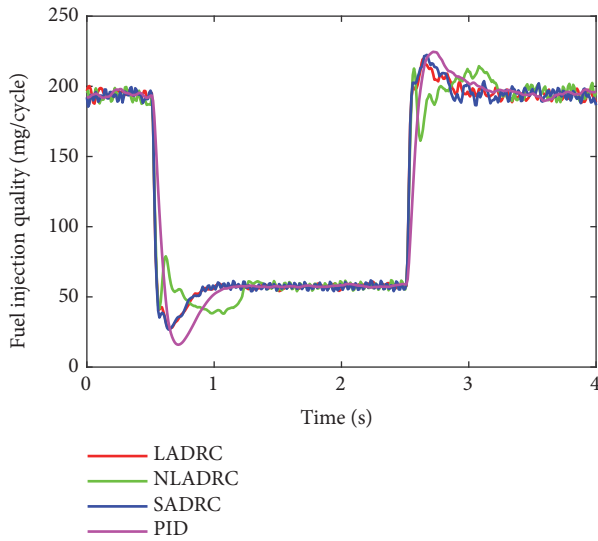


FIGURE 11: The comparison of control signal for the four controllers under mutation load (change 100% full load) condition.

$TV$  values in SADRC have a reduction of about 10% to 6%. When after unloading a smaller load (20% full load), such reduction is unapparent. The reason is that the estimate error  $e(k)$  starts to exceed the bound  $[-1, 1]$  (as shown in Figure 10 (c1, c2, c3), during the time from 1.5s to 2.5s), resulting in the performance deterioration in NLESO. This is also the reason why the  $IAE$  value in NLADRC gets larger than that in LADRC and SADRC after unloading 20% full load.

In overall, SADRC maintains the same speed deviation as LADRC under load changing process, but smaller speed fluctuation and less oscillation in control signal under the steady-state after unloading process. Compared with NLADRC, SADRC has less settling time when the level of sudden load change is large and less speed fluctuation under steady-state after unloading. It can be concluded that SADRC has evident superiority to deal with the different degrees of sudden load change.

**4.3. Anti-Interference Ability under Wave Load Disturbances.** The wave load disturbance is another typical inevitable perturbation for marine engine. Considering the value of normalized load torque at 1800 rpm, three sine waves with different amplitudes are designed to represent different intensities of the wave load; the amplitudes are 100 N·m, 200 N·m, and 300 N·m, respectively. And the frequency is set to be 0.2 Hz.

Figure 12 gives the speed responses of the four controllers under the three different wave load disturbances. Intuitively, the speed fluctuation in PID is the largest among them. To show clearly the control performance in these controllers, the comparison in the indexes of  $IAE$  and  $TV$  are given in Table 2. When wave load is smaller (amplitude is 100 N·m or 200 N·m), the values of  $IAE$  for SADRC are the smallest among the four controllers. Inversely, the  $IAE$  values of the LADRC show significant disadvantage when wave load is larger than 100 N·m. Note that when wave amplitude is

300 N·m, the wave load disturbance reaches to a limiting case compared with the normalized load torque at 1800 rpm; hence, it can be concluded that the SADRC has the best performance in the index of  $IAE$  under different levels of possible wave disturbance. As for the index in  $TV$ , compared with the ADRC related controllers, the PID controller gains the smallest values. One reason is as mentioned above that the ADRC related controllers can react faster to the load disturbance, leading to the oscillation in control signal. By combing the NLADRC and LADRC, the  $TV$  values in SADRC have been reduced by 13%, 8%, and 10% under the three cases, respectively. From Figure 13, we know that, under different levels of wave load, the tracking error  $e(k)$  in ESOs exceeds the bound  $[-1, 1]$ , especially when wave load is larger. With the switching scheme, the SADRC can combine the use of NLADRC and LADRC to obtain better control performance when the tracking error  $e(k)$  in ESOs changes with the disturbance load. It can be regarded as an adaptation ability for SADRC.

## 5. Conclusions and Future Work

Among the previous ADRC related articles on the marine engine speed control, the impact of the intrinsic characteristics of the reciprocating engine on the control effect of ADRC is ignored. One important intention of this paper is to design an ADRC based controller for marine diesel engine with the consideration of the mentioned characteristics. To this end, a cycle-detailed hybrid nonlinear engine model which can simulate the inherent speed fluctuation is employed to evaluate the ADRC based controller.

Single LADRC or NLADRC is not enough to keep good control effect due to the strong nonlinearity, complex disturbance, and the extra inherent speed fluctuation in marine engines. The compound of LADRC and NLADRC is introduced to keep the merits of both methods. On the basis of the proposed engine model, the impact of the inherent speed fluctuation on the performance of the ESO is analyzed. Then the control parameters are adjusted with the consideration of such features for the proposed controller by modifying the previous approaches in the references. The proposed scheme is compared with LADRC, NLADRC, and well-tuned conventional PID via numerical simulations. The results indicate that the SADRC controller gains the advantages of both LADRC and NLADRC. It provides better control effect in speed tracking and also has preponderance in keeping better control performance under different levels of both mutation disturbance and wave disturbance. However, we also find that the control input oscillation in ADRC related controllers is stronger than that in PID under the proposed engine model.

As it is found that, for ADRC related approaches, the existence of inherent speed fluctuation and cylinder variations in reciprocating engines would affect its control performance, making the parameters tuning difficult and causing the oscillation in control input, our future work will be focused on studying the method to improve the control performance of ADRC for engine speed control and alleviate such oscillation. One possible way would be making use of filter method

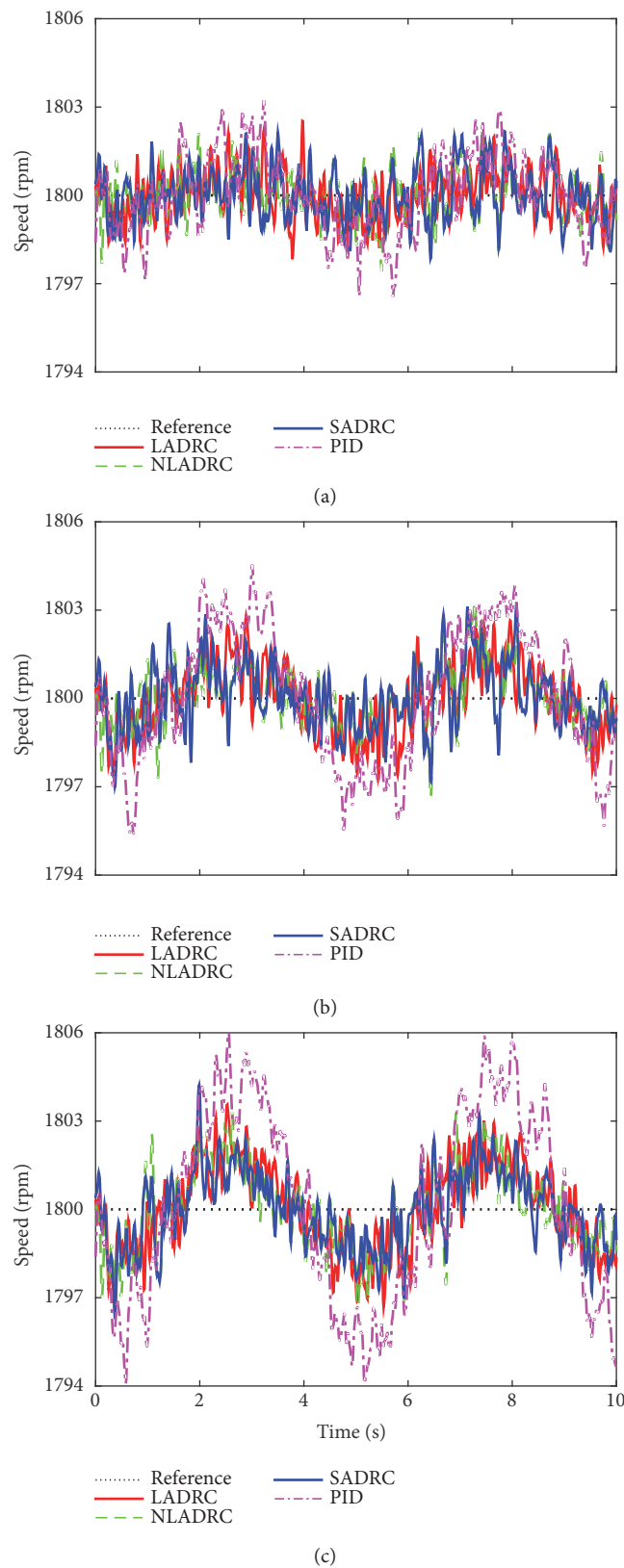


FIGURE 12: The speed responses under different levels of wave load. (a) Wave amplitude is 100 N·m. (b) Wave amplitude is 200 N·m. (c) Wave amplitude is 300 N·m.

TABLE 2: The indexes of IAE and TV for different controllers during different wave load conditions.

	Wave amplitude: 100 N·m			Wave amplitude: 200 N·m			Wave amplitude: 300 N·m					
	LADRC	NLADRC	SADRC	PID	LADRC	NLADRC	SADRC	PID	LADRC	NLADRC	SADRC	PID
IAE	6.2	6.4	5.9	11.3	9.3	8.0	7.9	20.1	12.8	10.3	10.4	28.1
TV	1546.2	1425.9	1349.1	379.5	1540.5	1431.2	1416.4	391.8	1612.5	1464.9	1444.4	469.9

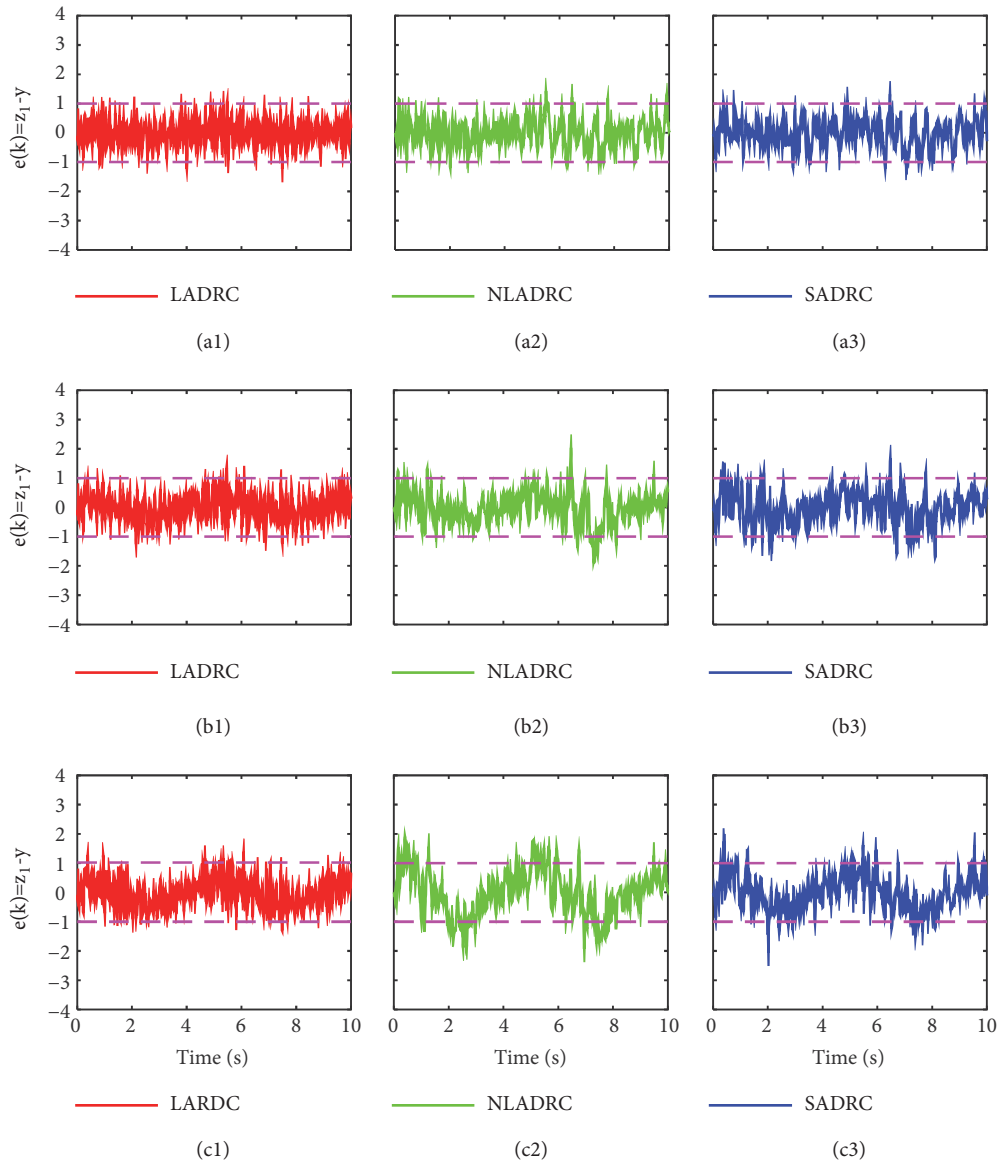


FIGURE 13: The tracking error  $e(k)$  in ESOs under different levels of wave load. (a1, a2, a3) Wave amplitude: 100 N-m. (b1, b2, b3) Wave amplitude: 200 N-m. (c1, c2, c3) Wave amplitude: 300 N-m.

[45, 46]. The proposed method needs to be further verified on the real engine bench as well.

## Data Availability

No data were used to support this study.

## Conflicts of Interest

The authors declare no conflicts of interest.

## References

- [1] F. Di Natale and C. Carotenuto, "Particulate matter in marine diesel engines exhausts: Emissions and control strategies," *Transportation Research Part D: Transport and Environment*, vol. 40, pp. 166–191, 2015.
- [2] N. Larbi and J. Bessrouer, "Measurement and simulation of pollutant emissions from marine diesel combustion engine and their reduction by water injection," *Advances in Engineering Software*, vol. 41, no. 6, pp. 898–906, 2010.
- [3] X. Li, Q. Ahmed, and G. Rizzoni, "Nonlinear robust control of marine diesel engine," *Journal of Marine Engineering Technology*, vol. 16, no. 1, p. 10, 2017.
- [4] Y. Guo, W. Li, S. Yu et al., "Diesel engine torsional vibration control coupling with speed control system," *Mechanical Systems and Signal Processing*, vol. 94, pp. 1–13, 2017.
- [5] R. Wang, X. Li, Y. Liu, W. Fu, S. Liu, and X. Ma, "Multiple Model Predictive Functional Control for Marine Diesel Engine," *Mathematical Problems in Engineering*, vol. 2018, Article ID 3252653, 20 pages, 2018.

- [6] J. Wei, A. Zhang, D. Qin et al., "A coupling dynamics analysis method for a multistage planetary gear system," *Mechanism and Machine Theory*, vol. 110, pp. 27–49, 2017.
- [7] C. Lynch, H. Hagrass, and V. Callaghan, "Using uncertainty bounds in the design of an embedded real-time type-2 neuro-fuzzy speed controller for marine diesel engines," in *Proceedings of the IEEE International Conference on Fuzzy Systems*, pp. 1446–1453, Vancouver, Canada, July 2006.
- [8] E. Kang, S. Hong, and M. Sunwoo, "Idle speed controller based on active disturbance rejection control in diesel engines," *International Journal of Automotive Technology*, vol. 17, no. 6, pp. 937–945, 2016.
- [9] Z. Ye, "Modeling, identification, design, and implementation of nonlinear automotive idle speed control systems—an overview," *IEEE Transactions on Systems, Man, and Cybernetics, Part C: Applications and Reviews*, vol. 37, no. 6, pp. 1137–1151, 2007.
- [10] N. I. Xiros, "PID marine engine speed regulation under full load conditions for sensitivity  $H_{\infty}$ -norm specifications against propeller disturbance," *Journal of Marine Engineering and Technology*, vol. 3, no. 2, pp. 3–11, 2004.
- [11] G. Papalambrou and N. P. Kyrtatos, " $H_{\infty}$  robust control of marine diesel engine equipped with power-take-in system," in *Proceedings of the 11th IFAC Symposium on Control in Transportation Systems, CTS2006*, pp. 591–596, Netherlands, August 2006.
- [12] T. Broomhead, C. Manzie, P. Hield, R. Shekhar, and M. Brear, "Economic model predictive control and applications for diesel generators," *IEEE Transactions on Control Systems Technology*, vol. 25, no. 2, pp. 388–400, 2017.
- [13] Y. Yuan, M. Zhang, Y. Chen, and X. Mao, "Multi-sliding surface control for the speed regulation system of ship diesel engines," *Transactions of the Institute of Measurement and Control*, vol. 40, no. 1, pp. 22–34, 2018.
- [14] O. Bondarenko and M. Kashiwagi, "Statistical consideration of propeller load fluctuation at racing condition in irregular waves," *Journal of Marine Science and Technology*, vol. 16, no. 4, pp. 402–410, 2011.
- [15] S. Li and Z. Liu, "Adaptive speed control for permanent-magnet synchronous motor system with variations of load inertia," *IEEE Transactions on Industrial Electronics*, vol. 56, no. 8, pp. 3050–3059, 2009.
- [16] H. P. Wang, D. Zheng, and Y. Tian, "High pressure common rail injection system modeling and control," *ISA Transactions*, vol. 63, pp. 265–273, 2016.
- [17] S. Li and J. Li, "Output Predictor-Based Active Disturbance Rejection Control for a Wind Energy Conversion System with PMSG," *IEEE Access*, vol. 5, pp. 5205–5214, 2017.
- [18] Q. Zheng and Z. Gao, "Active disturbance rejection control: some recent experimental and industrial case studies," *Control Theory and Technology*, vol. 16, no. 4, pp. 301–313, 2018.
- [19] W. Pan, H. Xiao, Y. Han, C. Wang, and G. Yang, "Nonlinear active disturbance rejection controller research of main engine for ship," in *Proceedings of the 2010 8th World Congress on Intelligent Control and Automation, WCICA 2010*, pp. 4978–4981, China, July 2010.
- [20] H.-D. Hua, N. Ma, J. Ma, and X.-Y. Zhu, "Robust intelligent control design for marine diesel engine," *Journal of Shanghai Jiaotong University (Science)*, vol. 18, no. 6, pp. 660–666, 2013.
- [21] A. W. Osburn and M. A. Franchek, "Reducing engine idle speed deviations using the internal model principle," *Journal of Dynamic Systems, Measurement, and Control*, vol. 128, no. 4, pp. 869–877, 2006.
- [22] A. Balluchi, L. Benvenuti, M. D. D. I. Benedetto, S. Member, C. Pinello, and A. Luigi, "Automotive engine control and hybrid systems: Challenges and opportunities," *Proceedings of the IEEE*, vol. 88, no. 7, pp. 888–911, 2000.
- [23] Z. Sun, "Tracking or rejecting rotational-angle dependent signals using time varying repetitive control," in *Proceedings of the 2004 American Control Conference (AAC)*, pp. 144–149, USA, July 2004.
- [24] P. Li, T. Shen, and D. Liu, "Idle speed performance improvement via torque balancing control in ignition-event scale for SI engines with multi-cylinders," *International Journal of Engine Research*, vol. 13, no. 1, pp. 65–76, 2012.
- [25] J. Karlsson and J. Fredriksson, "Cylinder-by-Cylinder Engine Models Vs Mean Value Engine Models for Use in Powertrain Control Applications," in *Proceedings of the International Congress & Exposition*.
- [26] A. Balluchi, L. Benvenuti, L. Berardi et al., "Engine idle speed control via maximal safe set computation in the crank-angle domain," in *Proceedings of the 2002 IEEE International Symposium on Industrial Electronics, ISIE 2002*, pp. 618–622, Italy, July 2002.
- [27] X. Li and S. Yurkovich, "Sliding mode control of delayed systems with application to engine idle speed control," *IEEE Transactions on Control Systems Technology*, vol. 9, no. 6, pp. 802–810, 2001.
- [28] K. B. Goh, S. K. Spurgeon, and N. B. Jones, "Higher-order sliding mode control of a diesel generator set," *Proceedings of the Institution of Mechanical Engineers, Part I: Journal of Systems and Control Engineering*, vol. 217, no. 3, pp. 229–241, 2003.
- [29] Tossaporn Chamsai, Piyoros Jirawattana, and Thana Radpukdee, "Robust Adaptive PID Controller for a Class of Uncertain Nonlinear Systems: An Application for Speed Tracking Control of an SI Engine," *Mathematical Problems in Engineering*, vol. 2015, Article ID 510738, 12 pages, 2015.
- [30] Z. Gao, "Scaling and bandwidth-parameterization based controller tuning," in *Proceedings of the American Control Conference*, pp. 4989–4996, Denver, Colo, USA, June 2003.
- [31] J. Li, Y. Xia, X. Qi, and Z. Gao, "On the Necessity, Scheme, and Basis of the Linear-Nonlinear Switching in Active Disturbance Rejection Control," *IEEE Transactions on Industrial Electronics*, vol. 64, no. 2, pp. 1425–1435, 2017.
- [32] E. De Santis, M. D. Di Benedetto, and G. Pola, "Digital idle speed control of automotive engines: a safety problem for hybrid systems," *Nonlinear Analysis. Theory, Methods & Applications. An International Multidisciplinary Journal*, vol. 65, no. 9, pp. 1705–1724, 2006.
- [33] C. Yang, X. Yang, and Y. Shardt, "An ADRC-Based Control Strategy for FRT Improvement of Wind Power Generation with a Doubly-Fed Induction Generator," *Energies*, vol. 11, no. 5, p. 1150, 2018.
- [34] J. Q. Han, "From PID to active disturbance rejection control," *IEEE Transactions on Industrial Electronics*, vol. 56, no. 3, pp. 900–906, 2009.
- [35] J. Han, *Active disturbance rejection control technique—the technique for estimating and compensating the uncertainties*, National Defense Industry Press, Beijing, China, 2008.
- [36] Y. Q. Wang, G. Ren, and J. D. Zhang, "Anti-windup schemes for nonlinear active disturbance rejection control in marine steam turbine," *Journal of Marine Science and Technology-Taiwan*, vol. 24, no. 1, pp. 47–53, Feb 2016.
- [37] X. Chen, D. H. Li, Z. Q. Gao, and C. F. Wang, "Tuning method for second-order active disturbance rejection control,"

- in *Proceedings of the 30th Chinese Control Conference*, pp. 6322–6327, Yantai, China, 2011.
- [38] Y. Huang and W. Xue, “Active disturbance rejection control: methodology and theoretical analysis,” *ISA Transactions*<sup>®</sup>, vol. 53, no. 4, pp. 963–976, 2014.
- [39] Y. X. Su, C. H. Zheng, and B. Y. Duan, “Automatic disturbances rejection controller for precise motion control of permanent-magnet synchronous motors,” *IEEE Transactions on Industrial Electronics*, vol. 52, no. 3, pp. 814–823, 2005.
- [40] J. Li, X.-H. Qi, Y.-Q. Xia, and Z.-Q. Gao, “On linear/nonlinear active disturbance rejection switching control,” *Zidonghua Xuebao/Acta Automatica Sinica*, vol. 42, no. 2, pp. 202–212, 2016.
- [41] F. Östman and H. T. Toivonen, “Adaptive cylinder balancing of internal combustion engines,” *IEEE Transactions on Control Systems Technology*, vol. 19, no. 4, pp. 782–791, 2011.
- [42] S. Skogestad, “Simple analytic rules for model reduction and PID controller tuning,” *Journal of Process Control*, vol. 13, no. 4, pp. 291–309, 2003.
- [43] M. Huba and I. Bélai, “Limits of a simplified controller design based on integral plus dead time models,” *Proceedings of the Institution of Mechanical Engineers, Part I: Journal of Systems and Control Engineering*, 2018.
- [44] M. Huba, “Performance measures, performance limits and optimal PI control for the IPDT plant,” *Journal of Process Control*, vol. 23, no. 4, pp. 500–515, 2013.
- [45] M. Huba and D. Vrančič, “Comparing filtered PI, PID and PIDDD 2 control for the FOTD plants,” *IFAC-PapersOnLine*, vol. 51, no. 4, pp. 954–959, 2018.
- [46] M. Huba, P. Bistak, T. Huba, and D. Vrancic, “Comparing filtered PID and smith predictor control of a thermal plant,” in *Proceedings of the 19th International Conference on Electrical Drives and Power Electronics, EDPE 2017*, pp. 324–329, Croatia, October 2017.

## Research Article

# Discontinuous High-Gain Observer in a Robust Control UAV Quadrotor: Real-Time Application for Watershed Monitoring

A. E. Rodríguez-Mata,<sup>1,2</sup> G. Flores,<sup>3</sup> A. H. Martínez-Vásquez,<sup>4</sup> Z. D. Mora-Felix,<sup>2</sup>  
R. Castro-Linares ,<sup>4</sup> and L. E. Amabilis-Sosa <sup>1,2</sup>

<sup>1</sup>CONACyT-Tecnológico Nacional de México, Culiacán, CP 80220, Mexico

<sup>2</sup>Tecnológico Nacional de México, Culiacán, CP 80220, Mexico

<sup>3</sup>Center for Research in Optics, León, Guanajuato, CP 37150, Mexico

<sup>4</sup>CINVESTAV, Department of Electrical Engineering, Mexico City, CP 07360, Mexico

Correspondence should be addressed to L. E. Amabilis-Sosa; leoamabilis@yahoo.com.mx

Received 10 July 2018; Revised 31 October 2018; Accepted 4 November 2018; Published 27 November 2018

Guest Editor: Binoy K. Roy

Copyright © 2018 A. E. Rodríguez-Mata et al. This is an open access article distributed under the Creative Commons Attribution License, which permits unrestricted use, distribution, and reproduction in any medium, provided the original work is properly cited.

A control algorithm that is robust with respect to wind disturbances for a quadrotor UAV attitude dynamics is presented. The proposed approach consists of a high-gain observer based on a discontinuous technique. Such an algorithm is embedded on board the quadrotor. The high-gain observer estimates external disturbances such as wind and parameter uncertainties, and a control algorithm is designed to compensate these undesired effects. The observer design is based on Lyapunov stability theory; simulation results and experiments validate the nonlinear observer performance and robustness of the approach under windy conditions. Also, a photogrammetry survey was carried out to develop Digital Elevation Models in order to experimentally demonstrate the effectiveness of our approach. The accuracy of such models was compared and the performance improvement is demonstrated.

## 1. Introduction

The research area of Unmanned Aerial Vehicles (UAVs or drones) has observed a rapid growth in the last decade. This is due to the ability of UAVs to effectively perform a wide range of applications at low cost and safely manage human resources. Nowadays, drones are being used in several outdoors missions including monitoring, agricultural services, mapping and photographing, battle damage assessment, border interdiction prevention, among others [1, 2]. In order to accomplish the aforementioned applications, it is required to guarantee a stable flight of the UAV by means of control algorithms.

*1.1. State of the Art of Robust Controllers for UAVs.* Several works propose control algorithms for UAVs to counteract wind effects within the limits of the UAV flight envelope. In [3], the authors employ an extended state observer to estimate aerodynamic disturbances for an UAV coaxial-rotor; such an approach was only tested in simulations. In [4],

the authors propose a Terminal Sliding Mode Control for position stabilization of a quadrotor. Such a controller does not estimate any disturbance; however the robustness of the controller relies on the properties of sliding mode closed-loop system. Reference [5] presents a robust adaptive altitude control on  $SO(3)$ ; the authors present some experimental results of a test bench where a quadrotor is attached to a bar limiting their movements. In [6], a controller with a disturbance observer is designed to stabilize the rotational error dynamics of a fixed-wing morphing UAV. Reference [7] solved the problem of guidance of a fixed-wing UAV under wind disturbances using a kinematic model based on Serret-Frenet framework. The authors assume that wind disturbances are quasiconstant; simulation results demonstrate the effectiveness of their results. On the other hand, control schemes are proposed with an accurate system model where the uncertainties of the system are not considered. For instance, in [8] a nonlinear disturbance observer is designed to solve the problem of disturbance estimation for dynamical systems based on the relationship between disturbance and

output. Several works have demonstrated that the use of robust high-gain observers interconnected with controllers ameliorates the system robustness [9]. As one can see in some of the aforementioned works, under certain conditions and assumptions, observers are capable of estimating certain system disturbances such as wind gusts effects. Such an approach is investigated in this paper.

**1.2. State of the Art of Observers and Control.** From control theory perspective, some authors have shown that the use of state observers interconnected with controllers provides robustness to the closed-loop system [9, 10]. In this regard, sliding mode and high-gain observers have been an effective approach in handling disturbances and modeling uncertainties in different types of systems. More recent research of nonlinear systems based on dynamical transformations to obtain an unknown parameter canonical representation are presented in [11, 12]. Adaptive observers for linear systems with a parameter adaptation algorithm has been presented in [13, 14]. Both state and disturbances are estimated for MIMO linear systems assuming that detectability and persistently exciting (PE) hold in [15–18]. As an alternative to the adaptive approach, various robust techniques have been considered. The most relevant are the sliding mode technique investigated in [15, 19, 20]. Regarding the use of some of the above-mentioned theoretic schemes in UAVs, we can cite [21], where a PID control technique to maintain a UAV in hover under intense turbulent environments is presented. Also, [22] proposes a design and implementation of a simple but effective feed-forward controller for wind gust compensation. Such an approach provides a stable and accurate flight under windy conditions. In [23, 24] some robust altitude controllers have been proposed for miniature quadrotors; however such studies are carried out in controlled environments.

**1.3. State of the Art of Environmental Studies Using Drones.** One of the drone applications is in the area of photography applied to environmental studies of rivers and watersheds, which allow the estimation of the main morphometric features of these environmental systems such as volume, surface, length, depth, among others [25, 26]. Environmental factors such as wind gusts affect the quality of data acquisition (photographs) during the construction of high resolution Digital Elevation Models (DEM). These models are used to study the terrain elevations and to model the hydrodynamics and water quality of waterbodies [27]. From this point of view, it is important to obtain reliable data to ensure the accuracy of such models. During a photogrammetry survey, DEMs accuracy can be affected by drone angle movements produced by wind, causing a distortion in the photographs. By the aforementioned discussion it is required to compensate wind gust by an intelligent control algorithm. This work deals with such a problem.

**1.4. Contribution.** We present a control and estimation algorithm to estimate and compensate uncertainties and external disturbances in a quadrotor attitude control. This algorithm is based on a sliding mode high-gain observer. Once we obtain

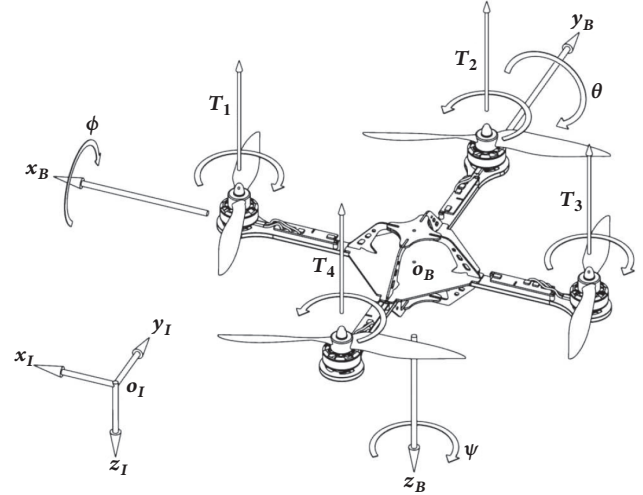


FIGURE 1: Quadrotor: body and inertial coordinates used for modeling.

a disturbance estimate, it is used to compensate the effects caused by the original disturbance. The main goal of the algorithm consists of maintaining the quadrotor aircraft in hovering flight through a disturbance compensation generated by wind gusts. The performance of the overall system is evaluated at simulation level and with real-time experiments.

**1.5. Paper Organization.** The remainder of this paper is organized as follows: Section 2 describes the quadrotor dynamical model; also in such section the problem formulation is presented. Section 3 shows the controller design process and describes how the nonlinear observer is developed; also the overall closed-loop system stability is shown. Section 4 presents simulations results obtained with the presented approach, and also the effectiveness of this technique is evaluated through real-time experiments with a quadrotor UAV. Finally, Section 5 gives a brief conclusion of the nonlinear disturbance observer algorithm.

## 2. Modeling and Problem Statement

Consider the quadrotor system depicted at Figure 1. The quadrotor is modeled as a rigid body where its full dynamics is represented in terms of rotational and translational dynamics as follows [28]:

$$\Sigma_1 : \{ m\ddot{\xi} = -ge_{z_I} + Ru \quad (1)$$

$$\Sigma_2 : \{ \mathbb{J}\dot{\eta} = -C(\eta, \dot{\eta})\dot{\eta} + \tau \quad (2)$$

where the position and attitude dynamics of the quadrotor are given by subsystem  $\Sigma_1$  and  $\Sigma_2$ , respectively;  $\xi = (x, y, z)^\top$  and  $\dot{\xi} = (v_x, v_y, v_z)^\top$  are the position and velocity of the aircraft relative to the inertial frame  $\mathbb{I} = (x_I, y_I, z_I)$ .  $R \in SO(3)$  is the rotational matrix representing the quadrotor attitude in the body coordinate frame  $\mathbb{B} = (x_B, y_B, z_B)$  with respect to  $\mathbb{I}$ ; the matrix  $R$  is a function of the Euler angles given by the vector  $\eta = (\phi, \theta, \psi)^\top$ ;  $u \in \mathbb{R}^3$  and  $\tau \in \mathbb{R}^3$  are the force and

torque vectors applied at the center of mass of the MAV;  $J \in \mathbb{R}^3$  is the inertia matrix in the body frame  $\mathbb{B}$ ;  $m$  is the mass of the body; and  $ge_{z_1}$  is the gravitational force, where  $e_{z_1} = (0, 0, 1)^T$  is a unit vector;  $C(\eta, \dot{\eta})$  is the Coriolis matrix which contains the gyroscopic and centrifugal terms associated with the Euler angles dependence;  $\mathbb{J}$  acts as the inertia matrix for the aircraft rotational kinetic energy expressed in terms of the Euler angles and is given by [29]

$$\mathbb{J} = \mathbb{J}(\eta) = W_\eta^T J W_\eta \quad (3)$$

where  $W_\eta$  is defined as

$$W_\eta = \begin{bmatrix} -\sin\theta & 0 & 1 \\ \cos\theta \sin\phi & \cos\phi & 0 \\ \cos\theta \cos\phi & -\sin\phi & 0 \end{bmatrix}. \quad (4)$$

Let us consider system  $\Sigma_2$ . Based on the results of [28], we propose the following perturbed attitude model:

$$\bar{\Sigma}_2 : \{\dot{\eta} = \mathbb{J}^{-1}(\tau - C(\eta, \dot{\eta})\dot{\eta}) = u + \delta_\eta(t)\} \quad (5)$$

where

$$\delta_\eta(t) = \begin{pmatrix} \delta_{\eta,\psi}(t) \\ \delta_{\eta,\theta}(t) \\ \delta_{\eta,\phi}(t) \end{pmatrix}, \quad (6)$$

$$u(t) = \begin{pmatrix} u_{\phi(t)} \\ u_{\theta(t)} \\ u_{\psi(t)} \end{pmatrix}$$

is the vector of unknown disturbances caused by wind gusts and unmodeled dynamics including Coriolis terms and  $u(t)$  is the control input. Equation (5) can be written in a scalar form as

$$\begin{aligned} \dot{\eta}_{1,\phi} &= \eta_{2,\phi} \\ \dot{\eta}_{2,\phi} &= u_\phi + \delta_{\eta,\phi}(t) \\ \dot{\eta}_{1,\theta} &= \eta_{2,\theta} \\ \dot{\eta}_{2,\theta} &= u_\theta + \delta_{\eta,\theta}(t) \\ \dot{\eta}_{1,\psi} &= \eta_{2,\psi} \\ \dot{\eta}_{2,\psi} &= u_\psi + \delta_{\eta,\psi}(t) \end{aligned} \quad (7)$$

where  $\eta_1 = \eta$  and  $\eta_2 = \dot{\eta}_1$ . The aforementioned system can be rewritten in one general equation in order to estimate each component of the vector  $\delta_{\eta,i}(t)$ . With  $i = \phi, \theta, \psi$ , the equation can be expressed as

$$\begin{aligned} \dot{\eta}_{1,i} &= \eta_{2,i} \\ \dot{\eta}_{2,i} &= u_i(t) + \delta_{\eta,i}. \end{aligned} \quad (8)$$

This model can be seen as a sum of a linear and a nonlinear part (given by disturbance  $\delta_{\eta,i}(t)$ ). This characteristic allows us to propose a control with active disturbance

rejection by means of sliding mode observers. This will be discussed in the next section. Now let  $x = (\eta_{1,i}, \eta_{2,i})^T \in \mathbb{R}^2$ ,  $y = \eta_{1,i}$ . Also denote  $\delta_{\eta,i}(t) = \delta_i$ , then system (8) can be expressed in a strict triangular form (i.e., the canonical observability form) as follows :

$$\begin{aligned} \dot{x} &= A_0 x + G(u_i + \delta_i) \\ y &= Cx \end{aligned} \quad (9)$$

where

$$\begin{aligned} A_0 &= \begin{pmatrix} 0 & 1 \\ 0 & 0 \end{pmatrix}, \\ G &= \begin{pmatrix} 0 \\ 1 \end{pmatrix}, \\ C &= (1 \ 0) \end{aligned} \quad (10)$$

Then, the problem is to design a controller to stabilize system (9) based on the following assumptions.

*Assumption 1.* The inverse of  $\mathbb{J}$  exists.

*Assumption 2.* Disturbance  $\delta_i$  is bounded.

*Assumption 3.* Angular position and velocity  $(\dot{\eta}_i, \eta_i)$  are supposed to be known, since those variables can be measured by available quadrotor sensors.

### 3. Control Design Based on a Robust Discontinuous Observer

In this section, a nonlinear control for the quadrotor attitude, particularly of system (9), is designed. This control scheme makes use of the residual sliding mode high-gain observer. A scheme of the observed-based control is depicted in Figure 2.

*3.1. Observer Design.* The high-gain observer is described by

$$\begin{aligned} \dot{\hat{x}} &= A_o \hat{x} + G(u + \hat{\delta}_i) - S_\infty^{-1} C^T C e_o \\ \dot{\hat{\delta}}_i &= -\Omega(h) \text{sign}(e_o) \end{aligned} \quad (11)$$

where  $\Omega(h) = f(h^n \dots h) \text{sup}(e_o)$  is scalar and positive function with  $f(h^n \dots h)$  a function of degree  $n$  with positive high gain  $h$ ;  $e_o = \hat{x} - x$  is the state estimation error;  $\text{sup}(e_o) = \|e_o\| \in \mathbb{R}$ , and  $S_\infty \in \mathbb{R}^{2 \times 2}$  is a positive definite symmetric matrix which is the solution of  $0 = -hS_\infty - A_o^T S_\infty - S_\infty A_o + C^T C$  (in the sense of [30]); and  $\tilde{\delta}_i = \hat{\delta}_i - \delta_i$  is the disturbance estimation error.

Then, the following assumptions for the observer design are considered [9, 31, 32].

*Assumption 4.* The disturbance estimation error  $\tilde{\delta}_i$  satisfies  $\|\tilde{\delta}_i\| \leq a_4 \|e_o\| \forall a_4 > 0$ , where  $a_4$  is the constant of Lipschitz with respect to the angular position.

*Assumption 5.* The first time derivative of the estimation error satisfies  $\|\dot{\tilde{\delta}}_i\| \leq \text{sup}(\dot{\delta}_i)$ .

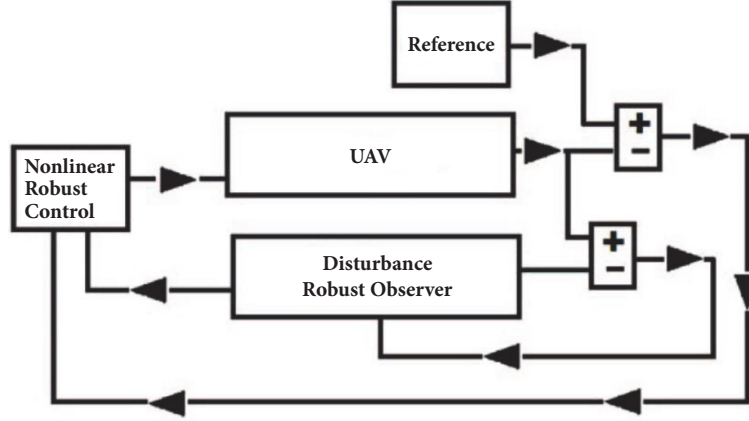


FIGURE 2: Nonlinear robust control strategy scheme.

*Assumption 6.* The maximal eigenvalue of the matrix  $S_{\infty}$ , denoted as  $\lambda_{\max}(S_{\infty})$ , is a function  $f(h)$  of grade  $n$ .

*Remark 7.* It is not hard to verify that  $\lambda_{\max}(S_{\infty})$  satisfies  $\lambda_{\max}(S_{\infty}) = f(h)$ . For instance, in [30] a matrix  $S_{\infty}$  for a two dimensional case is considered, more precisely

$$S_{\infty} = \begin{bmatrix} h^{-1} & -h^{-2} \\ -h^{-2} & 2h^{-3} \end{bmatrix} \quad (12)$$

for which the following Jordan structure is used

$$J(S_{\infty}) = \begin{bmatrix} f_1(h) & 0 \\ 0 & f_2(h) \end{bmatrix} \quad (13)$$

where

$$\begin{aligned} f_1(h) &= h^2 - \left( (h^2 - 2h + 2)(h^2 + 2h + 2) \right)^{0.5} \\ &\quad + \frac{2}{(2h^3)}, \\ f_2(h) &= \left( (h^2 - 2h + 2)(h^2 + 2h + 2) \right)^{0.5} + h^2 \\ &\quad + \frac{2}{(2h^3)}. \end{aligned} \quad (14)$$

For instance, setting  $h = 10$  then  $f_2(h) > f_1(h)$  and  $\lambda_{\max}(S_{\infty}) = f_2(h)$  such that  $\lambda_{\max}(S_{\infty})$  is a function  $f(h)$  of a high gain  $h$ .

From system (9) and observer (11), the state estimation error dynamics takes the form

$$\dot{e}_0 = \Psi(h) e_0 + G\tilde{\delta} \quad (15)$$

where  $\Psi(h) = A_0 - S_{\infty}^{-1}C^T C$ .

*Definition 8* (uniform ultimate boundedness [10]). The solution of (15) is uniformly ultimately bounded with ultimate bound  $b$  if there exist positive constant  $b, c$ , independent of

initial time  $t_0 \geq 0$  and  $\forall a \in (0, c)$ , there is  $T = T(a, b) > 0$  independent of  $t_0$ , such that

$$\begin{aligned} \|x(t_0)\| \leq a &\implies \\ \|x(t)\| \leq b, & \quad (16) \\ & \quad \forall t \geq t_0 + T \end{aligned}$$

The following result is stated for the ultimately bounded property of the state estimation error  $e_0$  dynamics (15).

**Theorem 9.** Let (11) be a residual sliding mode high-gain observer for system (9). Suppose Assumptions 4, 5, and 6 hold, then the state estimation error  $e_0$  is ultimately bounded in the presence of the disturbance and uncertainty  $\delta_i$  for all  $h > 1$ .

*Proof.* Consider a candidate Lyapunov function given by

$$V(e_0, \tilde{\delta}) = e_0^T S_{\infty} e_0 + \alpha_i \tilde{\delta}^2 \quad (17)$$

and the time derivative of  $V(e_0, \tilde{\delta})$  along the trajectories of  $e_0$  and  $\tilde{\delta}$  takes the form

$$\begin{aligned} \dot{V} &= e_0^T \left( \Psi(h)^T S_{\infty} + S_{\infty} \Psi(h) \right) e_0 \\ &\quad + 2\tilde{\delta} \left( G^T S_{\infty} e_0 + \alpha_i \dot{\tilde{\delta}} \right). \end{aligned} \quad (18)$$

Since  $0 = -hS_{\infty} - A_0^T S_{\infty} - S_{\infty} A_0 + C^T C$  holds,  $\dot{V}$  can be written as

$$\begin{aligned} \dot{V} &= -he_0^T S_{\infty} e_0 - e_0^T C^T C e_0 \\ &\quad + 2\tilde{\delta} \left( G^T S_{\infty} e_0 + \alpha_i \dot{\tilde{\delta}} + \alpha_i \delta \right). \end{aligned} \quad (19)$$

Substituting the disturbance estimation dynamics  $\dot{\tilde{\delta}} = \alpha_i \Omega(h) \text{sign}(e_0)$   $\delta$  is a positive constant such that

$$\|\alpha_i \Omega(h) \text{sign}(e_0)\| \leq \alpha_i \Omega(h) \quad (20)$$

following the procedure of [30] with  $e_o^T C^T C e_o$  bounded  $\dot{V}$  can be expressed as

$$\begin{aligned} \dot{V} \leq & -h \|e_o\|^2 \|S_{\infty}\| \\ & + 2 \|\bar{\delta}\| \left( \|G\| \|S_{\infty}\| \|e_o\| - \alpha_i \Omega(h) + \|\delta\| \right). \end{aligned} \quad (21)$$

After some computations, the last equation is reduced to

$$\begin{aligned} \dot{V} \leq & -a_1(h) \|e_o\|^2 \\ & + 2 \|\bar{\delta}\| \left( \alpha_i f(h^n \dots h) \|e_o\| - \alpha_i \Omega(h) + \|\delta\| \right) \end{aligned} \quad (22)$$

where  $a_1(h) = hf(h^n \dots h)$  and  $\|G\| \|S_{\infty}\| = \alpha_i f(h^n \dots h)$ . Due to the properties of matrix  $S_{\infty}$  (see Remark 7), it can be argued that  $\|S_{\infty}\| \leq \lambda_{\max}(S_{\infty})$ , where  $\lambda_{\max}(S_{\infty}) = f(h^n \dots h)$  denotes the maximal eigenvalue of the matrix  $S_{\infty}$ . Then if  $\Omega(h) = f(h^n \dots h) \|e_o\|$  holds, the Lyapunov function derivative is

$$\dot{V}(\cdot) \leq -a_1(h) \|e_o\|^2 + 2 \|\bar{\delta}\| \|\delta\|. \quad (23)$$

From Assumptions 5 and 4, it can be finally written:

$$\dot{V} \leq -a_1(h) \|e_o\| \left( \|e_o\| - 2 \frac{a_4 \sup(\delta)}{a_1(h)} \right). \quad (24)$$

Then,  $\dot{V} < 0$  for  $a_1(h) \gg a_4 \sup(\delta)$  and system (15) is ultimately bounded in the sense of [10] in a ball  $B_{e_o} \triangleq \{\|e_o\| \in \mathbb{R}^n : \|e_o\| < z(h)\} \forall z(h) = 2(a_4 \sup(\delta)/a_1(h))$ .  $\square$

**3.2. Control Design.** Now, consider second equation of (8)

$$\dot{\eta}_{2,i} = u_i(t) + \delta_{\eta,i}. \quad (25)$$

Let  $r$  be a reference vector which can be the zero vector in the case of hover and define the following tracking control error:

$$e_c = r - \eta_2. \quad (26)$$

Then the following robust control law is proposed:

$$u_i(t) = -K e_c + \hat{\delta}_i \quad (27)$$

**Theorem 10.** Let (27) be a robust control for (25). The tracking error will converge to zero if  $K$  is a Hurwitz matrix.

*Proof.* By substituting the control law (27) on derivative of (26)

$$\dot{e}_c = -K e_c + \hat{\delta}_i - \delta_i = -K e_c + \alpha(t) \quad (28)$$

since  $\hat{\delta}_i = \delta_i + \alpha \forall \|\delta_i\| \gg \|\alpha\|$  when  $h \gg 4\lambda_{\max}(\Gamma)$  where  $\Gamma$  is an diagonal positive matrix.  $K$  is Hurwitz by hypotheses and design, then  $V(t) = e_c^T P e_c$ , where  $K^T P + P K = -Q$  holds such that

$$\dot{V} \leq -\lambda_{\max}(Q) \|e_c\| \left( \|e_c\| - \frac{\sup(\alpha(t))}{\lambda_{\max}(Q)} \right). \quad (29)$$

The matrix  $K$  is chosen such that  $\dot{V}(\cdot) < 0$  for  $\lambda_{\max}(Q) \gg \sup(\alpha(t))$  and system (28) is ultimately bounded in a ball given by

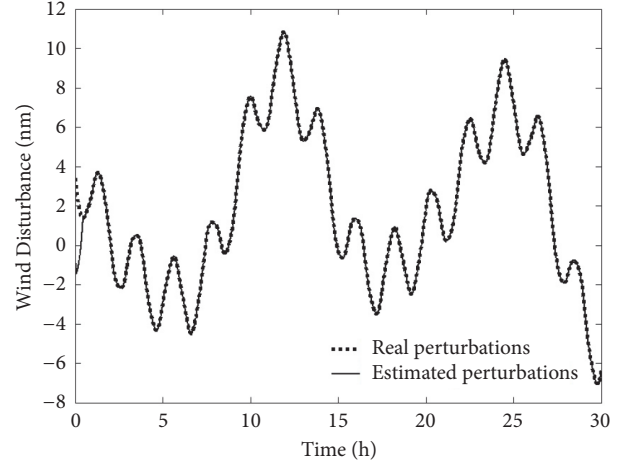


FIGURE 3: Disturbance and disturbance estimation signal of the quadrotor.

$$B_{e_c} \triangleq \{\|e_c\| \in \mathbb{R}^n : \|e_o\| < z_c(h)\}$$

$$\forall z_c(h) = \frac{\sup(\alpha(t))}{\lambda_{\max}(Q)}. \quad (30)$$

$\square$

A complete algorithm was developed based on the disturbance observer and the control law designed above. The closed-loop system together with disturbance observer is given by

$$\dot{\hat{x}} = A_o \hat{x} + G(u + \hat{\delta}_i) - S_{\infty}^{-1} C^T C e_o$$

$$\dot{\hat{\delta}}_i = -\Omega(h) \text{sign}(e_o) \quad (31)$$

$$u_i = -K e_c + \hat{\delta}_i$$

where  $\Omega(h) = f(h^n \dots h) \sup(e_o)$  and observer and control errors are defined as  $e_c = r - x_2$ ,  $e_o = \hat{x} - x$ , respectively.

## 4. Experiments

In this section simulation results of the theoretical development are given. Also, the control law proposed in (31) was applied in a photogrammetry survey. Such results are reported in this section.

**4.1. Numerical Results.** The quadrotor mathematical model is simulated taken into account the following parameters. The function  $\delta_i$  is generated by a Dryden wind model [33]) with high gain  $h = 30$  as follows:

$$v_w(t) = v_w^0 + \sum_{i=1}^n a_i \sin(v_i t + \varphi_i) \quad (32)$$

where  $v_i$  and  $\varphi_i$  are selected randomly and  $v_w^0$  is a wind static vector. Such a signal and its estimate are shown at Figure 3.



FIGURE 4: Quadrotor used and built for the development of DEM.

**4.2. Real Experiments.** In order to evaluate the performance of the control technique provided by the algorithm shown in (31), a photogrammetric survey was carried out in the Tamazula River basin, a river of great importance in the northeastern region of Mexico. Given that the central region of Sinaloa in Mexico is characterized by a very strong agricultural activity, an effective water resource management is vital to achieve good agricultural yields. In this region, the use of satellite images to calculate and estimate the water volumes, total mass flows, and waterbodies quality prediction is common. Photogrammetry survey was carried out at an altitude of 80 m and 32 C, with an average humidity of 35% and wind velocity average of 22 km/hr. During the data collection, different flight campaigns were carried out in the same area and route with the objective of evaluating the effect of the controller on the quality of Digital Elevation Models (DEM) of the basin. A comparison between the DEMs obtained with and without algorithm (31) was carried out, considering scenarios with real wind gusts average of 20 km/hr. A small quadrotor aircraft was used with a Futaba 2.4GHz FASST radio system for transmitting the control signals. A picture of the quadrotor is depicted in Figure 4. The quadrotor position  $(x, y, z)^T$  and the attitude  $(\theta, \phi, \psi)^T$  were measured in real time. 224 Sample points were used for the construction of a Digital Elevation Model of a river basin as part of a strategy for an efficiency water resource management. A Pixhawk autopilot with a GPS module sensor was programmed with the control and estimation algorithms. The benefits of the Pixhawk system include integrated multi-threading and a Unix/Linux-like programming environment for real-time applications.

The disturbance generated due to the wind gust was estimated in the roll and pitch angles, during a real-time flight and taking the location of the photographs as the reference points (see Figures 5 and 6). Note that the disturbance estimation is achieved in real-time flight.

In Figure 7, the position error in the  $x$ -axis and  $y$ -axis is shown in real wind conditions. It can be observed that the maximum error without disturbance compensation was approximately 5 m. Then, when the observer is activated, the position error is around  $\pm 1m$ , which is reasonable due to the

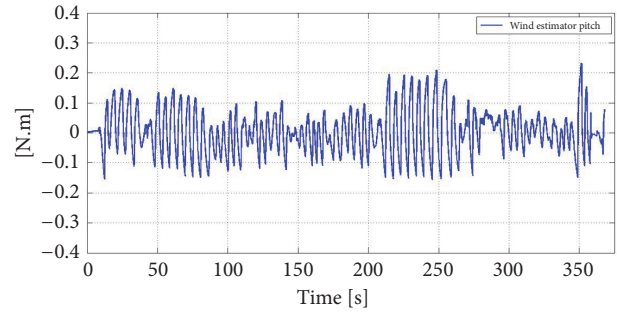


FIGURE 5: Disturbance and disturbance estimation signal in the pitch angle  $\theta$  during real-time flight.

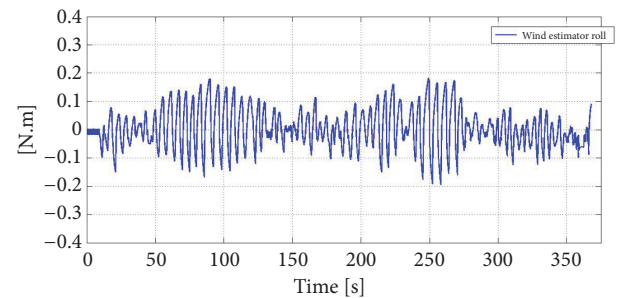


FIGURE 6: Disturbance and disturbance estimation signal in the roll angle  $\phi$  during real-time flight.

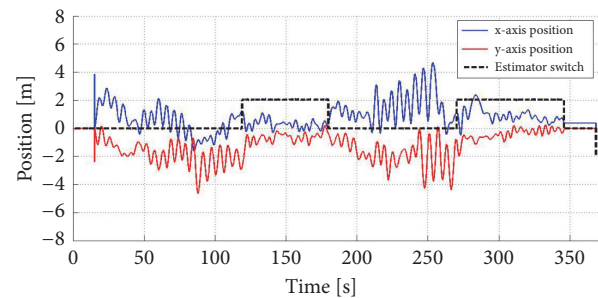


FIGURE 7: Quadrotor position in real conditions with and without compensation of wind gust disturbances.

error of the GPS sensor which is around 1 m. It can be seen at Figures 8 and 9 that, by reducing the unknown effect of wind and other distortions in attitude dynamics, it is also considering indirectly disturbances in position. This is due to the fact that the quadrotor is an underactuated system.

Figure 8 shows the position in the  $x$ - $y$  plane of the quadrotor without compensation. This signal is obtained from a GPS sensor. The reference is at the point  $(0,0)$  for a hover-flight mode. Note that the quadrotor is moving around the reference point, due to wind gusts of 20 m/s approximately. The quadrotor is shifted from the reference. Figure 9 shows the position with disturbance compensation. The attitude control law keeps the quadrotor around the reference. If Figures 10 and 11 are compared, the error is about 7 m in the first case and the error is about 1.3 m in the second case.

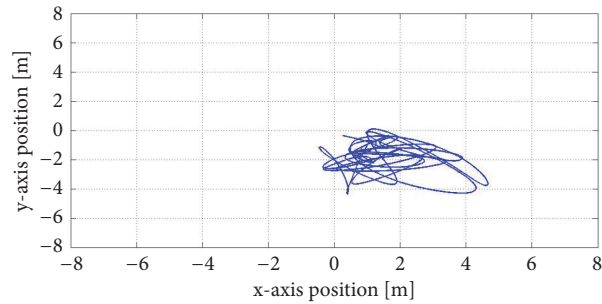


FIGURE 8: Quadrotor position in real-time flight without disturbance compensation.

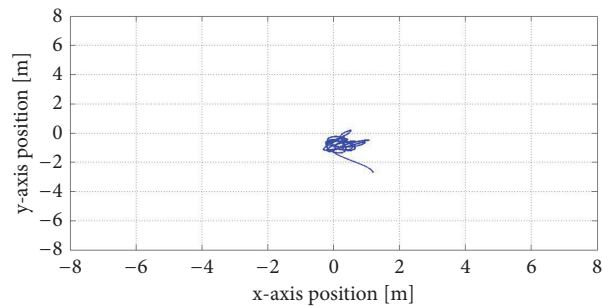


FIGURE 9: Quadrotor position in real-time flight with disturbance compensation.

Once the data was collected, the process of building the DEM was carried out using the free-Software OpenDronemap and Quantum GIS. Control points were obtained by using a fixed GNSS reference with a LEICAGR10 receiver and LEIARI0 NONE antenna on the coordinates Latitude 24 47' 42.30742" N and Longitude 107 24' 45.34764" W. These control points were used to measure the accuracy of the DEM. Photographic distortions can be observed due to the effect of the wind gusts. This situation generated an inaccuracy in the elevation of the river area and the DEM obtained was distorted. The robust control with disturbance rejection allowed better estimation of basin elevations. This algorithm improved the DEM in an average of 53% with respect to control points. The application of this control law supports the development of DEMs for water resources management and may be applied to other photogrammetric surveys. The proposed tool would also increase the quality of photographs and decrease flight surveys in further Digital Elevation Models.

## 5. Conclusions

In this paper a new algorithm for disturbance rejection and control of a quadrotor system is presented. This algorithm is easy tunable and programmable on a Pixhawk autopilot. The control is composed by a residual observer based on sliding modes plus a control that uses the observer solution to compensate for unknown disturbances. This approach is mathematical proved through Lyapunov stability analysis and in numerical and real-time experiments. In such experiments the use of the proposed controller improved the accuracy of the DEM of a river basin located in Sinaloa Mexico, with

respect to the classic PID controller. In particular, this work obtained a higher resolution DEM, which it is used for water resources management.

As future work it remains to investigate

- (i) robust controllers for position and attitude disturbances in which every disturbance in uncoupled one of each other;
- (ii) application of this approach to fixed-wing aircraft.

## Data Availability

The data related to Pixhawk support for Embedded Coder and Matlab and Simulink used to support the findings of this study were supplied by Instituto Tecnológico de Culiacán under license and so cannot be made freely available. Request for access to these data should be made to PhD. Rodríguez Mata by arodriguez@itculiacan.edu.mxst.

## Conflicts of Interest

The authors declare no conflicts of interest.

## Acknowledgments

The authors acknowledge National Council of Science and Technology in Mexico (CONACYT) for supporting this research work in the call for 2014 Young Researcher Grants (Cátedras para Jóvenes Investigadores 2014 Ref. 2572) and for 2014 Scientific Development Projects to Address National Problems Grants (Proyectos de Desarrollo Científico para Atender Problemas Nacionales 2014 Ref. 248517). Also the

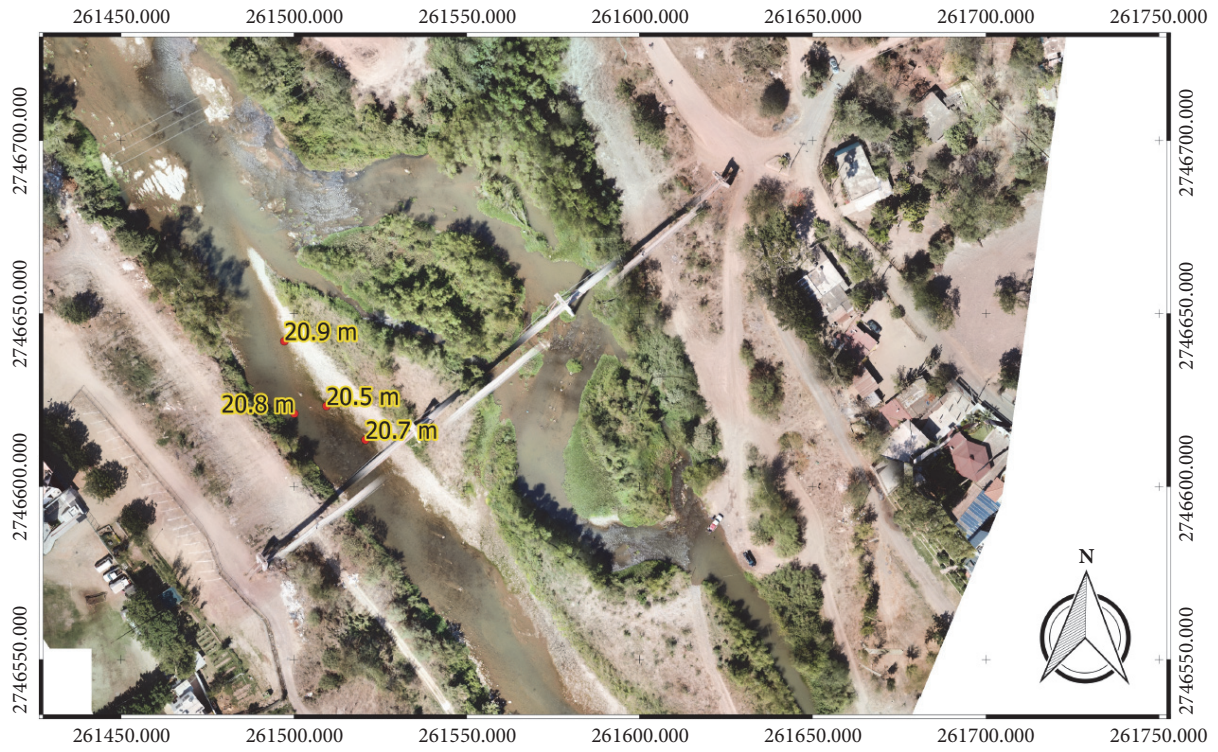


FIGURE 10: Digital elevation model of Tamazula River basin using a common PID controller.

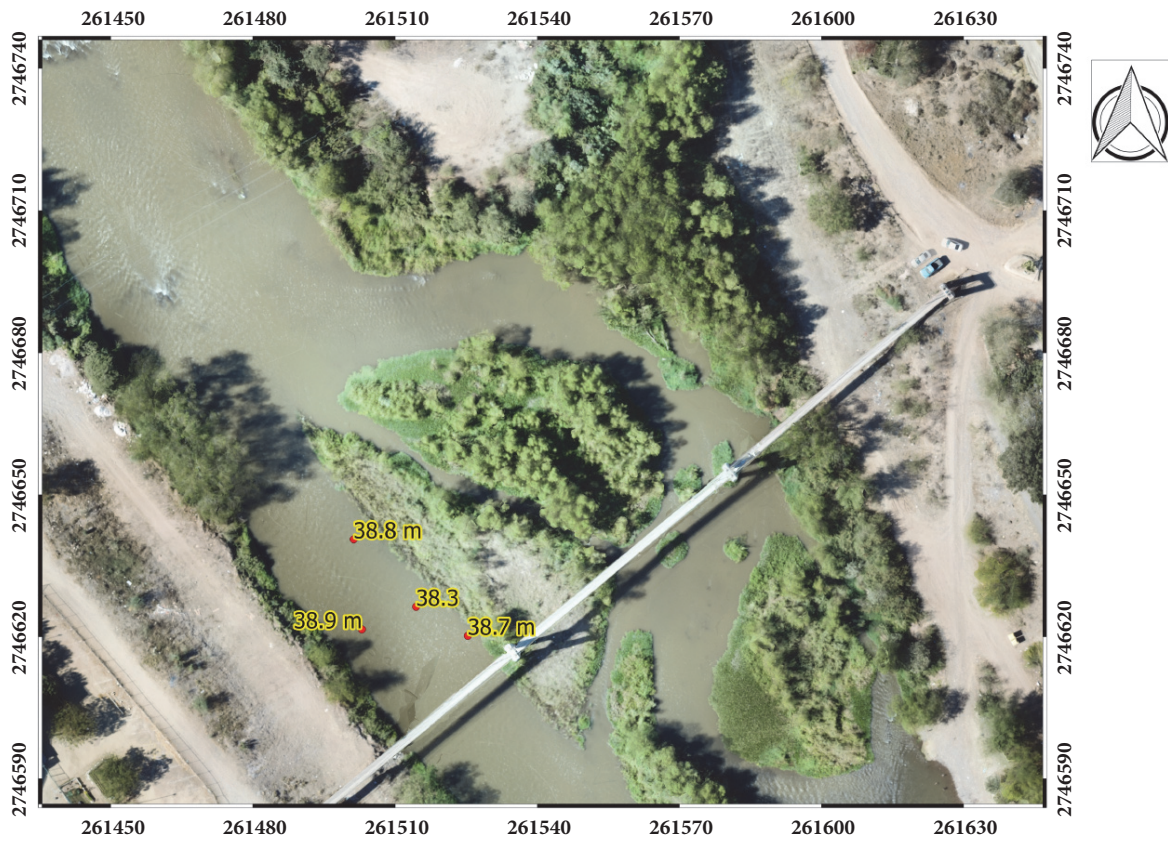


FIGURE 11: Digital elevation model of the Tamazula River basin using the robust controller proposed in this paper.

authors acknowledge National Council of Science and Technology in Mexico (CONACYT) for supporting this research through the FORDECYT-CONACYT program under Agreement 00000000292399. This work is supported by National Laboratory of Vision Optics of the National Council of Science and Technology in Mexico (CONACYT) (Agreement no. 293411).

## References

- [1] G. Flores and R. Lozano, "Lyapunov-based controller using singular perturbation theory: An application on a mini-UAV," in *Proceedings of the 2013 1st American Control Conference, ACC 2013*, pp. 1596–1601, Washington, DC, USA, June 2013.
- [2] G. Flores and R. Lozano, "Lyapunov-based controller using singular perturbation theory: An application on a mini-UAV," in *Proceedings of the 2013 American Control Conference (ACC)*, pp. 1596–1601, Washington, DC, June 2013.
- [3] M. R. Mokhtari, A. C. Braham, and B. Cherki, "Extended state observer based control for coaxial-rotor UAV," *ISA Transactions*, vol. 61, pp. 1–14, 2016.
- [4] J.-J. Xiong and G.-B. Zhang, "Global fast dynamic terminal sliding mode control for a quadrotor UAV," *ISA Transactions*, vol. 66, pp. 233–240, 2017.
- [5] T. Lee, "Robust adaptive attitude tracking on SO(3) with an application to a quadrotor UAV," *IEEE Transactions on Control Systems Technology*, vol. 21, no. 5, pp. 1924–1930, 2013.
- [6] L. Wang and J. Su, "Disturbance rejection control of a morphing UAV," in *Proceedings of the 2013 1st American Control Conference, ACC 2013*, pp. 4307–4312, USA, June 2013.
- [7] I. Sarras and H. Siguerdidjane, "On the guidance of a UAV under unknown wind disturbances," in *Proceedings of the 2014 IEEE Conference on Control Applications, CCA 2014*, pp. 820–825, France, October 2014.
- [8] X. Chen, S. Komada, and T. Fukuda, "Design of a nonlinear disturbance observer," *IEEE Transactions on Industrial Electronics*, vol. 47, no. 2, pp. 429–437, 2000.
- [9] A. E. Rodríguez-Mata, I. González-Hernández, J. G. Rangel-Peraza, S. Salazar, and R. L. Leal, "Wind-gust compensation algorithm based on high-gain Residual observer to control a Quadrotor aircraft: Real-time verification task at fixed point," *International Journal of Control, Automation, and Systems*, vol. 16, no. 2, pp. 856–866, 2018.
- [10] H. K. Khalil, *Nonlinear Systems*, Prentice Hall, New York, NY, USA, 2002.
- [11] N. Sydney, B. Smyth, and D. A. Paley, "Dynamic control of autonomous Quadrotor flight in an estimated wind field," in *Proceedings of the 52nd IEEE Conference on Decision and Control, CDC 2013*, pp. 3609–3616, Italy, December 2013.
- [12] Q. Zhang, "Adaptive observer for multiple-input-multiple-output (MIMO) linear time-varying systems," *IEEE Transactions on Automatic Control*, vol. 47, no. 3, pp. 525–529, 2002.
- [13] G. Bastin and M. R. Gevers, "Stable adaptive observers for nonlinear time-varying systems," *Institute of Electrical and Electronics Engineers Transactions on Automatic Control*, vol. 33, no. 7, pp. 650–658, 1988.
- [14] M. Farza, M. M'Saad, T. Ménard, M. L. Fall, O. Gehan, and E. Pigeon, "Simple cascade observer for a class of nonlinear systems with long output delays," *Institute of Electrical and Electronics Engineers Transactions on Automatic Control*, vol. 60, no. 12, pp. 3338–3343, 2015.
- [15] L. Fridman, Y. Shtessel, C. Edwards, and X.-G. Yan, "Higher-order sliding-mode observer for state estimation and input reconstruction in nonlinear systems," *International Journal of Robust and Nonlinear Control*, vol. 18, no. 4–5, pp. 399–412, 2008.
- [16] R. Marino and P. Tomei, "Adaptive observers with arbitrary exponential rate of convergence for nonlinear systems," *Institute of Electrical and Electronics Engineers Transactions on Automatic Control*, vol. 40, no. 7, pp. 1300–1304, 1995.
- [17] A. Maouche, M. M'Saad, B. Bensaker, and M. Farza, "High gain adaptive observer design for sensorless state and parameter estimation of induction motors," *International Journal of Control, Automation, and Systems*, vol. 13, no. 5, pp. 1106–1117, 2015.
- [18] O. H. Gonzalez, T. Menard, M. Farza, C. M. A. Zaragoza, and G. V. G. Ramirez, "Continuous-discrete time observer for a class of state affine nonlinear systems: application to an induction motor," *International Journal of Sciences and Techniques of Automatic control & Computer Engineering (IJ-STA)*, vol. 10, no. 1, pp. 2072–2078, 2016.
- [19] D. Efimov and L. Fridman, "Global sliding-mode observer with adjusted gains for locally Lipschitz systems," *Automatica*, vol. 47, no. 3, pp. 565–570, 2011.
- [20] F. J. Bejarano and L. Fridman, "High order sliding mode observer for linear systems with unbounded unknown inputs," *International Journal of Control*, vol. 83, no. 9, pp. 1920–1929, 2010.
- [21] A. Ryan and J. K. Hedrick, "A mode-switching path planner for UAV-assisted search and rescue," in *Proceedings of the 44th IEEE Conference on Decision and Control, and the European Control Conference (CDC-ECC '05)*, pp. 1471–1476, December 2005.
- [22] D. Cabecinhas, R. Cunha, and C. Silvestre, "A nonlinear quadrotor trajectory tracking controller with disturbance rejection," *Control Engineering Practice*, vol. 26, no. 1, pp. 1–10, 2014.
- [23] G. Flores, L. Garcia Carrillo, G. Sanahuja, and R. Lozano, "PID switching control for a highway estimation and tracking applied on a convertible mini-UAV," in *Proceedings of the 2012 IEEE 51st Annual Conference on Decision and Control (CDC)*, pp. 3110–3115, Maui, HI, USA, December 2012.
- [24] G. Besancon, J. de Leon-Morales, and O. Huerta-Guevara, "On adaptive observers for state affine systems," *International Journal of Control*, vol. 79, no. 6, pp. 581–591, 2006.
- [25] J. de Anda, G. Rangel-Peraza, O. Obregon et al., "The use of digital elevation models (dems) for bathymetry development in large tropical reservoirs," in *Bathymetry and Its Applications*, P. Blondel, Ed., pp. 105–118, IntechOpen, 2012.
- [26] A. M. Sawyer, G. B. Pasternack, H. J. Moir, and A. A. Fulton, "Riffle-pool maintenance and flow convergence routing observed on a large gravel-bed river," *Geomorphology*, vol. 114, no. 3, pp. 143–160, 2010.
- [27] J. G. Rangel-Peraza, J. De Anda, F. A. González-Farías, and M. Rode, "Sensitivity and uncertainty analysis on water quality modelling of Aguamilpa reservoir," *Journal of Limnology*, vol. 75, no. 51, pp. 81–92, 2013.
- [28] P. Castillo, R. Lozano, and A. Dzul, "Stabilization of a mini rotorcraft with four rotors: experimental implementation of linear and nonlinear control laws," *IEEE Control Systems Magazine*, vol. 25, no. 6, pp. 45–55, 2005.
- [29] R. W. Beard and T. W. McLain, *Small Unmanned Aircraft: Theory and Practice*, Princeton University Press, United Kingdom, 2012.
- [30] J.-P. Gauthier, H. Hammouri, and S. Othman, "A simple observer for nonlinear systems applications to bioreactors,"

*Institute of Electrical and Electronics Engineers Transactions on Automatic Control*, vol. 37, no. 6, pp. 875–880, 1992.

- [31] R. López-Gutiérrez, A. E. Rodríguez-Mata, S. Salazar, I. González-Hernández, and R. Lozano, “Robust quadrotor control: Attitude and altitude real-time results,” *Journal of Intelligent & Robotic Systems*, vol. 88, no. 2, pp. 299–312, 2017.
- [32] R. Lopez, I. Gonzalez-Hernandez, S. Salazar, A. E. Rodriguez, J. J. Ordaz, and A. Osorio, “Disturbance rejection for a Quadrotor aircraft through a robust control,” in *Proceedings of the 2015 International Conference on Unmanned Aircraft Systems (ICUAS)*, pp. 409–415, Denver, CO, USA, June 2015.
- [33] R. Baltaxe, “Air flow patterns in the lee of model windbreaks,” *Archiv für Meteorologie, Geophysik und Bioklimatologie Serie B*, vol. 15, no. 3, pp. 287–312, 1967.

## Research Article

# Full and Reduced-Order Unknown Input Observer Design for Linear Time-Delay Systems with Multiple Delays

Seifeddine Ben Warrad,<sup>1</sup> Olfa Boubaker ,<sup>1</sup> Mihai Lungu ,<sup>2</sup> and Saleh Mobayen<sup>3</sup>

<sup>1</sup>National Institute of Applied Sciences and Technology, Centre Urbain Nord, BP 676, 1080 Tunis Cedex, Tunisia

<sup>2</sup>University of Craiova, Faculty of Electrical Engineering, 107 Decebal Blvd., Craiova, Romania

<sup>3</sup>Advanced Control Systems Laboratory, Department of Electrical Engineering, University of Zanjan, University Blvd., 45371-38791 Zanjan, Iran

Correspondence should be addressed to Olfa Boubaker; [olfa.boubaker@insat.rnu.tn](mailto:olfa.boubaker@insat.rnu.tn)

Received 31 July 2018; Revised 2 November 2018; Accepted 11 November 2018; Published 26 November 2018

Academic Editor: Francesco Conte

Copyright © 2018 Seifeddine Ben Warrad et al. This is an open access article distributed under the Creative Commons Attribution License, which permits unrestricted use, distribution, and reproduction in any medium, provided the original work is properly cited.

In this work, we consider the design problem of a full-order and also reduced-order unknown input observers for a particular class of time-delay systems. Asymptotic stability and existence conditions for the designed observers are established. The quadruple-tank process is used as a benchmark to prove the efficiency of the proposed algorithms.

## 1. Introduction

Time delays emerge in many industrial applications such as hydraulic systems, automotive applications, and telecommunication networks [1–7]. Commonly, delays describe propagation phenomena, energy transfer, or data transmission. Furthermore, it is recognized that delays are the key sources of instability and poor dynamics [8]. Since the sixteen's century, the research theme of time-delay systems has concerned lots of interest and has been considered as one of the essential research areas in control theory for which many significant research works have been devoted. The topical survey [9] and the recent books [10–12] as well as their related references prove the richness and maturity of this field. Time delays can appear in either the state variables, control inputs, or measurement outputs and the negligence of time delays in the controller design can lead to undesirable dynamics such as oscillations, bifurcations, chaos dynamics, and instability [8]. In this trend, stabilization of linear systems with delays has obtained a huge interest (see, for example, recent works [13–15] and related references). As reported in [16], for stabilization of continuous linear systems subject to time delays, most research works only focus in systems with input delays and solve the problem in the absence of state delays. To the best of the authors' knowledge, few

research works have considered the stabilization problem with multiple delays in states and inputs where the problem is generally solved by assuming fully available state variables [1] or by resorting to output-feedback controllers [17]. The design problem of observer-based stabilization for systems with multiple delays in states and inputs is rarely solved [16, 18]. Until now, this issue of theoretical and practical importance has been remained a challenging problem for systems subject to unknown inputs, uncertainties, and input saturation.

In control theory, modeling and controlling benchmark systems is another fundamental issue. Such systems are considered as challenging control problems, yet, in spite of their uncomplicated arrangement. In this outline, several systems are commonly used in control theory for testing novel control algorithms. We can cite in this framework the three-tank process [19], mass-spring-damper system [20], bouncing ball [21], TORA system [22], hard-disk drive system [23], magnetic levitation system [24], cart-inverted pendulum [25], Furuta pendulum [26], reaction wheel pendulum [27], beam-and-ball [28], two-link flexible manipulator [29], and so on. In the same direction, the well-known quadruple-tank benchmark [30–36] has attracted many attention since it can show elementary notions in estimation and control theory, particularly performance limitation due to the

nonminimum-phase zeros and their output directions for multivariable systems. This system is composed of four coupled tanks, two pumps, and two valves [35]. Many research papers have been devoted to the problem of observer and controller design of this benchmark system without consideration of time delays [37–43] and to the best of our information, no researches have been investigated for unknown input observer design of time-delay quadruple-tank systems.

Motivated by the authors' early works for linear systems without delays [44], in this paper, we expand the problem of full-order unknown input observer (FOUIO) and *reduced-order unknown input observer* (ROUIO) design for linear systems with multiple time delays in states and inputs affected by unknown inputs. In this framework, it is important to note that a FOUIO is designed in [45–47] for linear systems with a single delay in the states and two delays in the inputs whereas another FOUIO is proposed in [48] for linear systems with a single delay in the states and a single delay in the inputs. For the last works, only the state information is used to design observers in open loops and to the best of our knowledge, there are no related works for which both the state vector and the input vectors are used to design the observer. Furthermore, in our best knowledge, there is not in the vast literature ROUIO design approach that attempts to solve such a problem.

The design procedures of both reduced-order and full-order observers are considered here. The key contributions of this work can be recapitulated as follows:

- (i) The designed observers' approaches do not require approximation of the infinite dimensional model of the delayed system in a lumped one as described in our previous works [45, 46].
- (ii) Different from [46] where only the state vector is used to construct observers in open loop, in this paper, we construct the novel observers by using both state and input vectors. The structure of the proposed observers allows us to introduce more observer gains that can accomplish better control performance.
- (iii) Different from the observer designed in [47] where the delayed system introduces a single delay in the states and a single delay in the inputs, in this paper, multiple time delays in the inputs are considered.

The rest of this paper is organized as follows: the problem statement is considered in Section 2. The full-order observer is designed in Section 3 whereas the reduced-order observer is developed in Section 4. Section 5 is devoted to the application of the proposed approaches to the quadruple-tank benchmark. Finally, conclusions are provided in Section 6.

## 2. Problem Statement

Consider a class of time-delay systems described by

$$\begin{aligned} \dot{x}(t) &= A_0x(t) + A_1x(t - \tau_0) + \sum_{i=0}^k (B_iu(t - \tau_{i+1})) \\ &\quad + Dd(t), \\ y(t) &= Cx(t), \end{aligned} \quad (1)$$

where  $x(t) \in \mathcal{R}^n$  is the state vector,  $u(t) \in \mathcal{R}^m$  is the input vector,  $d(t) \in \mathcal{R}^q$  is the unknown input vector, and  $y(t) \in \mathcal{R}^p$  is the output vector;  $A_0 \in \mathcal{R}^{n \times n}$ ,  $A_1 \in \mathcal{R}^{n \times n}$ ,  $B_i \in \mathcal{R}^{n \times m}$ ,  $C \in \mathcal{R}^{p \times n}$ , and  $D \in \mathcal{R}^{n \times q}$  are constant matrices with appropriate dimensions, while  $\tau_0$  and  $\tau_{i+1}$  for  $i=0, \dots, k$  are known and constant time delays.

The objective of this paper is to design two different approaches of unknown input observers (UIOs) for system (1):

- (1) An FOUIO is described by

$$\dot{\zeta}(t) = N\zeta(t) + Ly(t) + Jy(t - \tau_0) + \sum_{i=0}^k G_iu(t - \tau_{i+1}), \quad (2)$$

$$\hat{x}(t) = \zeta(t) - Ey(t),$$

where  $\zeta(t) \in \mathcal{R}^n$  and  $\hat{x}(t) \in \mathcal{R}^n$  are the observer state vector and the estimated state vector, respectively.  $N, L, J, E$ , and  $G_i$  ( $i=0, \dots, k$ ) are matrices of appropriate dimensions to be calculated such that  $\hat{x}(t)$  converges asymptotically to  $x(t)$  under the following assumptions: (A1)  $\text{rank}(D) = q$ ; (A2)  $\text{rank}(C) = p$ ; (A3) the pair  $(A_0, C)$  is observable (detectable).

- (2) An ROUIO is also designed in this paper for the estimation of the state vector  $x(t)$  by obtaining the estimation of the vector:  $\bar{\zeta}(t) = Fx(t)$ ,  $F \in \mathcal{R}^{s \times n}$ , where  $\bar{\zeta}(t) \in \mathcal{R}^s$  is the vector enclosing a part of the system's states or a combination of them. The dynamics of the ROUIO is

$$\begin{aligned} \hat{\bar{\zeta}}(t) &= \bar{N}\hat{\bar{\zeta}}(t) + \bar{L}y(t) + \bar{J}y(t - \tau_0) \\ &\quad + \sum_{i=0}^k \bar{G}_i u(t - \tau_{i+1}), \end{aligned} \quad (3)$$

$$\hat{x}(t) = H\hat{\bar{\zeta}}(t) + \bar{E}y(t),$$

where  $\hat{\bar{\zeta}}(t) \in \mathcal{R}^s$  and  $\hat{x}(t) \in \mathcal{R}^n$  are the observer state vector and estimated state vector, respectively.  $\bar{N} \in \mathcal{R}^{s \times s}$ ,  $\bar{L} \in \mathcal{R}^{s \times p}$ ,  $\bar{J} \in \mathcal{R}^{s \times p}$ ,  $\bar{G}_i \in \mathcal{R}^{s \times m}$  for  $(i = 0, \dots, k)$ ,  $H \in \mathcal{R}^{n \times s}$ ,  $\bar{E} \in \mathcal{R}^{n \times p}$ ,  $F \in \mathcal{R}^{s \times n}$  and  $Z \in \mathcal{R}^{s \times s}$  are matrices of appropriate dimensions to be calculated such that  $\hat{\bar{\zeta}}(t)$  and  $\hat{x}(t)$  converge asymptotically to  $\bar{\zeta}(t)$  and  $x(t)$ , respectively, under the assumptions as

(A4)  $\text{rank}(D) = q$ ; (A5)  $\text{rank}(C) = p$ ; (A6) the pair  $(A_0, C)$  is observable; (A7)  $n > s > p \geq q$ ; (A8)  $n = p + q$ .

*Remark 1.* For the design procedure of ROUIO, a particular form for the matrix  $C$  can be chosen as  $C = [C_1 \ 0_{p \times q}]$ , where  $C_1 \in \mathcal{R}^{p \times p}$  is a full rank (nonsingular) matrix. This is not restrictive as long as the matrix  $C$  is full row rank (conditions A2=A5), and there will always be an orthogonal transformation which leads to the equation  $y(t) = [C_1 \ 0]x(t)$ .

Either for the FOUIO (2) or the ROUIO (3), system (1) is controlled using the state-feedback controller as

$$u = K\hat{x}(t) \quad (4)$$

where  $K \in \mathcal{R}^{m \times n}$  is designed using one of the appropriate approaches for system (1), for example, the approach proposed in [1].

### 3. Design of the Full-Order Observer

**Theorem 2.** Consider system (1) with assumptions (A1-A3) presented above. The FOUIO (2) is convergent, i.e.,  $e(t) \rightarrow 0$  as  $t \rightarrow \infty$  with an arbitrary convergence rate for any  $x(0)$ ,  $d(t)$ , and  $u(t)$ , if there exists a positive-definite matrix  $R \in \mathcal{R}^{n \times n}$  verifying the matrix inequality

$$N^T R + RN < 0 \quad (5)$$

and if the matrix  $P = (I + EC) \in \mathcal{R}^{n \times n}$  fulfills the following conditions:

$$\begin{aligned} NP + LC - PA_0 &= 0, \\ JC - PA_1 &= 0 \\ G_i - PB_i &= 0 \quad \forall i = 0 \dots k, \\ PD &= 0. \end{aligned} \quad (6)$$

*Proof.* Define the observer reconstruction error vector as the difference between the estimated state  $\hat{x}(t)$  described by (2) and the state vector related to system (1) as

$$\begin{aligned} e(t) &= \hat{x}(t) - x(t) = \zeta(t) - x(t) - Ey(t) \\ &= \zeta(t) - (I + EC)x(t). \end{aligned} \quad (7)$$

Using (1) and (2), the dynamics of the estimation error becomes

$$\dot{e}(t) = \dot{\zeta}(t) - (I + EC)\dot{x}(t), \quad (8)$$

or

$$\begin{aligned} \dot{e}(t) &= Ne(t) + [N(I + EC) + LC - (I + EC)A_0]x(t) \\ &\quad + [JC - (I + EC)A_1]x(t - \tau_0) \\ &\quad + \sum_{i=0}^k [(G_i - (I + EC)B_i)u(t - \tau_{i+1})] \\ &\quad - (I + EC)Dd(t). \end{aligned} \quad (9)$$

Using  $P = I + EC$ , the error dynamics (9) is written in the following form:

$$\begin{aligned} \dot{e}(t) &= Ne(t) + (NP + LC - PA_0)x(t) \\ &\quad + (JC - PA_1)x(t - \tau_0) \\ &\quad + \sum_{i=0}^k ((G_i - PB_i)u(t - \tau_{i+1})) - PDd(t). \end{aligned} \quad (10)$$

If conditions (6) are satisfied, the error dynamics of the observer is expressed as  $\dot{e}(t) = Ne(t)$ . FOUIO's convergence is then achieved if the LMI (5) is verified.  $\square$

The determination of the matrices  $N$ ,  $L$ ,  $J$ , and  $P$  from the first, second, and fourth equations of (6) is a difficult task because we have to calculate four matrices by using only three equations. In order to use the well-known results obtained for the classical full-order observer without unknown inputs [2], by means of the notation

$$K_0 = L + NE, \quad (11)$$

the first term of (6) becomes

$$N = PA_0 - K_0C. \quad (12)$$

Now, using (11) and (12), the dynamics (2) can be written as

$$\begin{aligned} \dot{\zeta}(t) &= (PA_0 - K_0C)\zeta(t) + Ly(t) + Jy(t - \tau_0) \\ &\quad + \sum_{i=0}^k G_i u(t - \tau_{i+1}), \end{aligned} \quad (13)$$

$$\hat{x}(t) = \zeta(t) - Ey(t).$$

If the pair  $(PA_0, C)$  is not observable, the calculation of matrix  $K_0$  is made such that the observer is asymptotically stable if and only if  $(PA_0, C)$  is detectable [2]. By extending the approach from [2], we can conclude that the necessary and sufficient conditions to design a stable observer are given by the following theorem.

**Theorem 3** (see [2]). For system (1), the full-order observer (13) exists if and only if (1)  $\text{rank}(CD) = q$ ; (2)  $\text{rank} \begin{bmatrix} sI - PA_0 \\ C \end{bmatrix} = n$ ,  $(\forall)s \in \mathcal{L}$ ,  $\text{Re}(s) \geq 0$ .

*Proof.* The proof of the theorem is an extension of the approach from [2]. Because system (13) is in the form of a standard observer equation, then the matrix  $K_0$  can be calculated such that the observer (2) is asymptotically stable if and only if the pair  $(PA_0, C)$  is observable. In [2], it is proved that the above condition (2) is equivalent with the pair  $(PA_0, C)$ -observable or at least detectable (first existence condition of the full-order observer). The second constraint is the condition (1) from Theorem 3; bearing in mind the assumptions A1 and A2, as well as the dimensions of the matrices  $C$  and  $D$ , this condition is always fulfilled. Therefore, up to this point in the design of the unknown input observer, the only existence condition of FOUIO is related to the observability or at least detectability of the pair  $(PA_0, C)$ .  $\square$

To calculate  $N$ ,  $L$ ,  $J$ ,  $P$ ,  $G_0$ , and  $G_1$ , we partition matrices  $A_0$ ,  $A_1$ ,  $C$ ,  $N$ ,  $P$ ,  $L$ , and  $J$  as follows:

$$A_0 = \begin{bmatrix} A_{0(11)} & A_{0(12)} \\ A_{0(21)} & A_{0(22)} \end{bmatrix},$$

$$A_1 = \begin{bmatrix} A_{1(11)} & A_{1(12)} \\ A_{1(21)} & A_{1(22)} \end{bmatrix},$$

$$C^T = \begin{bmatrix} C_1^T \\ C_2^T \end{bmatrix},$$

$$N = \begin{bmatrix} N_{11} & N_{12} \\ N_{21} & N_{22} \end{bmatrix},$$

$$P = \begin{bmatrix} P_{11} & P_{12} \\ P_{21} & P_{22} \end{bmatrix},$$

$$\begin{aligned}
L &= \begin{bmatrix} L_1 \\ L_2 \end{bmatrix}, & C_1 &\in \mathcal{R}^{p \times (n-p)}, \\
J &= \begin{bmatrix} J_1 \\ J_2 \end{bmatrix}, & C_2 &\in \mathcal{R}^{p \times p}.
\end{aligned} \tag{14}$$

where

$$\begin{aligned}
A_0 &\in \mathcal{R}^{n \times n}, \\
A_{0(11)} &\in \mathcal{R}^{(n-p) \times (n-p)}, \\
A_{0(12)} &\in \mathcal{R}^{(n-p) \times p}, \\
A_{0(21)} &\in \mathcal{R}^{p \times (n-p)}, \\
A_{0(22)} &\in \mathcal{R}^{p \times p}, \\
A_1 &\in \mathcal{R}^{n \times n}, \\
A_{1(11)} &\in \mathcal{R}^{(n-p) \times (n-p)}, \\
A_{1(12)} &\in \mathcal{R}^{(n-p) \times p}, \\
A_{1(21)} &\in \mathcal{R}^{p \times (n-p)}, \\
A_{1(22)} &\in \mathcal{R}^{p \times p}, \\
N &\in \mathcal{R}^{n \times n}, \\
N_{11} &\in \mathcal{R}^{(n-p) \times (n-p)}, \\
N_{12} &\in \mathcal{R}^{(n-p) \times p}, \\
N_{21} &\in \mathcal{R}^{p \times (n-p)}, \\
N_{22} &\in \mathcal{R}^{p \times p}, \\
P &\in \mathcal{R}^{n \times n}, \\
P_{11} &\in \mathcal{R}^{(n-p) \times (n-p)}, \\
P_{12} &\in \mathcal{R}^{(n-p) \times p}, \\
P_{21} &\in \mathcal{R}^{p \times (n-p)}, \\
P_{22} &\in \mathcal{R}^{p \times p}, \\
L &\in \mathcal{R}^{n \times p}, \\
L_1 &\in \mathcal{R}^{(n-p) \times p}, \\
L_2 &\in \mathcal{R}^{p \times p}, \\
J &\in \mathcal{R}^{n \times p}, \\
J_1 &\in \mathcal{R}^{(n-p) \times p}, \\
J_2 &\in \mathcal{R}^{p \times p}, \\
C &\in \mathcal{R}^{p \times n},
\end{aligned}$$

The observer's design is concentrated into the following theorem.

**Theorem 4.** *If the rank conditions in Theorem 3 are satisfied, the UIO (2) can be designed for system (1) as follows:*

$$\begin{aligned}
E &= D(CD)^+ C, \\
P &= I_n - D(CD)^+ C, \\
G_i &= PB_i \quad (\text{for } k = 0 \cdots k), \\
J &= PA_1 C^+, \\
N & \\
&= \begin{bmatrix} N_{11} \left( F_{12} - (F_{11} - F_{12} P_{22}^{-1} P_{21}) (C_1 - C_2 P_{22}^{-1} P_{21})^+ C_2 \right) P_{22}^{-1} \\ N_{21} \left( F_{22} - (F_{21} - F_{22} P_{22}^{-1} P_{21}) (C_1 - C_2 P_{22}^{-1} P_{21})^+ C_2 \right) P_{22}^{-1} \end{bmatrix}, \\
L &= \begin{bmatrix} (F_{11} - F_{12} P_{22}^{-1} P_{21}) (C_1 - C_2 P_{22}^{-1} P_{21})^+ \\ (F_{21} - F_{22} P_{22}^{-1} P_{21}) (C_1 - C_2 P_{22}^{-1} P_{21})^+ \end{bmatrix},
\end{aligned} \tag{16}$$

where

$$\begin{aligned}
F_{11} &= P_{11} A_{0(11)} + P_{12} A_{0(21)} - N_{11} P_{11}, \\
F_{12} &= P_{11} A_{0(12)} + P_{12} A_{0(22)} - N_{11} P_{12}, \\
F_{21} &= P_{21} A_{0(11)} + P_{22} A_{0(21)} - N_{21} P_{11}, \\
F_{22} &= P_{21} A_{0(12)} + P_{22} A_{0(22)} - N_{21} P_{21},
\end{aligned} \tag{17}$$

while  $N_{11}$  and  $N_{21}$  are arbitrarily chosen;  $P_{22}$  should be a nonsingular matrix.

*Proof.* Since  $\text{rank}(CD) = q$ , i.e., the matrix  $(CD)$  has full column rank, we can use the pseudoinverse of  $(CD)$ , given by [17]:  $(CD)^+ = [(CD)^T(CD)]^{-1}(CD)^T$ . By means of this pseudoinverse matrix, we can solve the fourth equation of (6); one successively gets

$$\begin{aligned}
(I + EC)D = 0 &\iff D + ECD = 0 \iff E \\
&= -D(CD)^+.
\end{aligned} \tag{18}$$

Hence, one gets  $P = I_n + EC = I_n - D(CD)^+ C$ . Replacing  $P$  into the third equation of (6), we obtain  $G_i = PB_i = (I_n - D(CD)^+ C)B_i$ . Now, substituting (14) into the first equation of (6), we obtain

$$\begin{aligned}
&N_{11} P_{11} + N_{12} P_{21} + L_1 C_1 - P_{11} A_{0(11)} - P_{12} A_{0(21)} \\
&= 0_{(n-p) \times (n-p)}, \\
&N_{11} P_{12} + N_{12} P_{22} + L_1 C_2 - P_{11} A_{0(12)} - P_{12} A_{0(22)} \\
&= 0_{(n-p) \times p}, \\
&N_{21} P_{11} + N_{22} P_{21} + L_2 C_1 - P_{21} A_{0(11)} - P_{22} A_{0(21)} \\
&= 0_{p \times (n-p)},
\end{aligned}$$

$$\begin{aligned} & N_{21}P_{12} + N_{22}P_{22} + L_2C_2 - P_{21}A_{0(12)} - P_{22}A_{0(22)} \\ & = 0_{p \times p} \end{aligned} \quad (19)$$

By using (17), system (19) is divided into the following systems:

$$N_{12}P_{21} + L_1C_1 = F_{11}, \quad (20)$$

$$N_{12}P_{22} + L_1C_2 = F_{12},$$

$$N_{22}P_{22} + L_2C_2 = F_{22}, \quad (21)$$

$$N_{22}P_{21} + L_2C_1 = F_{21}.$$

Working in the hypothesis: the matrix  $(C_1 - C_2P_{22}^{-1}P_{21}) \in \mathcal{R}^{p \times (n-p)}$  is full column rank. By solving systems (20) and (21), we obtain

$$\begin{aligned} L_1 &= (F_{11} - F_{12}P_{22}^{-1}P_{21})(C_1 - C_2P_{22}^{-1}P_{21})^+, \\ L_2 &= (F_{21} - F_{22}P_{22}^{-1}P_{21})(C_1 - C_2P_{22}^{-1}P_{21})^+, \\ N_{12} &= (F_{12} \\ &\quad - (F_{11} - F_{12}P_{22}^{-1}P_{21})(C_1 - C_2P_{22}^{-1}P_{21})^+ C_2)P_{22}^{-1}, \\ N_{22} &= (F_{22} \\ &\quad - (F_{21} - F_{22}P_{22}^{-1}P_{21})(C_1 - C_2P_{22}^{-1}P_{21})^+ C_2)P_{22}^{-1}. \end{aligned} \quad (22)$$

Now, solving the second equation of (6), we get

$$J = PA_1C^+. \quad (23)$$

The unknown matrices of the FOUIO (2), i.e., N, L, J, P, and  $G_i$ , have been successfully determined with respect to the arbitrarily chosen matrices  $N_{11}$  and  $N_{21}$ . According to Theorem 2, the obtained matrix N should satisfy two constraints: (1) there exists a symmetric and positive-definite matrix  $R \in \mathcal{R}^{n \times n}$  which verifies the LMI (5), i.e., the matrix N is Hurwitz; (2) the pair  $(PA_0, C)$  is observable. If these two conditions are satisfied, the matrix N has been obtained properly, the dynamics of the observer error has an homogeneous form, and  $e(t) \rightarrow 0$  as  $t \rightarrow \infty$  with an arbitrary convergence rate for any  $x(0)$ ,  $d(t)$ , and  $u(t)$ . Otherwise, other matrices  $N_{11}$ ,  $N_{21}$  are chosen, the matrices from (17) are again calculated, and systems (20) and (21) are solved until the above presented constraints are fulfilled. In fact, no condition regarding the observability or detectability of the pairs  $(PA_0, C)$  is required in our design approach. Therefore, the unique existence condition of the observer is  $\text{rank}(CD) = q$ . The theorem's proof is now complete.  $\square$

The algorithm associated to the delay-dependent observer is summarized below.

*Algorithm 5.* Design of FOUIO

*Step 1.* Given system (1), verify the related assumptions A1-A3.

*Step 2.* If the existence conditions given in Theorem 3 hold, one calculates the generalized inverse matrix  $(CD)^+$  related to the matrix CD. By using it, one computes the matrix E by means of the first equation of (16); then, one computes the matrices P,  $G_0$ , and  $G_1$  with the second, third, and fourth equations of (16), respectively.

*Step 3.* One partitions the matrices  $A_0$ ,  $A_1$ , C, N, P, L, and J according to (14).

*Step 4.* Matrices  $N_{11}$  and  $N_{21}$  are arbitrarily chosen; the matrices from (17) are determined.

*Step 5.* One solves systems (20) and (21); after that, the matrices N, L, and J are built.

*Step 6.* Using the obtained matrix N, if the required constraints are satisfied, then (1) the matrix N is Hurwitz, i.e., there exists a symmetric and positive-definite matrix  $R \in \mathcal{R}^{n \times n}$  verifying the LMI (5); (2) the pair  $(PA_0, C)$  is observable or at least detectable; the matrix N has been obtained properly; otherwise, Steps 4–6 are repeated (in a “while” loop) until these conditions are fulfilled. Bearing in mind that there is no risk for infinite “while” loop, there can be concluded that the FOUIO's design algorithm has no existence conditions, being characterized by lack of a priori restrictions on the class of systems to be considered.

*Step 7.* The observer described by (2) is completely designed and the time history of the system's estimated states can be obtained.

#### 4. Design of the Reduced-Order Observer

**Theorem 6.** Consider the LTI multivariable system (1) with multiple delays under the five assumptions (A4-A8) presented above; the ROUIO (3) is asymptotically stable, if and only if there exist symmetric and positive-definite matrix  $\bar{R} \in \mathcal{R}^{s \times s}$  verifying the LMI:

$$\bar{N}^T \bar{R} + \bar{R} \bar{N} < 0, \quad (24)$$

with  $\bar{N} = Z^{-1}N$ , and if there exists a vector  $\bar{\zeta}(t) = Fx(t)$  such that the next conditions are satisfied:

$$\begin{aligned} \bar{N}F + \bar{L}C - ZFA_0 &= 0, \\ \bar{J}C - ZFA_1 &= 0, \\ \bar{G}_i - ZFB_i &= 0 \quad \forall i = 0 \dots k, \\ ZFD &= 0, \\ \bar{E}C + HF &= I_n; \end{aligned} \quad (25)$$

*Proof.* Define the observer error vector defined as the difference between the estimated vector  $\hat{\zeta}(t)$  described by (3) and the state vector related to system (1) as

$$\bar{e}(t) = \hat{\zeta}(t) - \bar{\zeta}(t) \quad (26)$$

Using (1), (3), and (4), the dynamics of the estimation error becomes

$$\begin{aligned} Z\dot{\tilde{e}}(t) &= \bar{N}\tilde{e}(t) + [\bar{N}F - ZFA_0 + \bar{L}C]x(t) \\ &+ [\bar{J}C - ZFA_1]x(t - \tau_0) \\ &+ \sum_{i=0}^k ([\bar{G}_i - ZFB_i]u(t - \tau_{i+1})) - ZFDd(t). \end{aligned} \quad (27)$$

If  $\bar{N}F + \bar{L}C - ZFA_0 = 0$ ,  $\bar{J}C - ZFA_1 = 0$ ,  $\bar{G}_i - ZFB_i = 0 \forall i = 0 \dots k$ ,  $ZFD = 0$  the error dynamics (27) can be written as

$$\dot{\tilde{e}}(t) = \bar{N}\tilde{e}(t), \quad (28)$$

where  $\bar{N} = Z^{-1}\bar{N}$ .

Let the state estimation error be defined as  $e_x(t) = \hat{x}(t) - x(t)$ . From (1) and (3), one obtains  $e_x(t) = (HF - I_n + \bar{E}C)x(t)$ . If  $HF - I_n + \bar{E}C = 0$ ,  $e_x(t) = 0$  for any  $x(t)$  results.

Furthermore, if condition (24) is satisfied then the observer's error dynamics (28) is asymptotically stable. Now, the proof of the Theorem 6 is complete.  $\square$

To compute the matrices  $F$ ,  $Z$ ,  $\bar{E}$ ,  $\bar{N}$ ,  $\bar{L}$ ,  $\bar{J}$ ,  $H$ ,  $\bar{G}_0$ , and  $\bar{G}_1$ , let us partition the matrices  $A_0$ ,  $A_1$ ,  $C$ ,  $\bar{N}$ ,  $H$ ,  $\bar{L}$ ,  $\bar{J}$ ,  $F$ ,  $Z$ , and  $D$  as follows:

$$\begin{aligned} A_0 &= \begin{bmatrix} A_{0(11)} & A_{0(12)} \\ A_{0(21)} & A_{0(22)} \end{bmatrix}, \\ A_1 &= \begin{bmatrix} A_{1(11)} & A_{1(12)} \\ A_{1(21)} & A_{1(22)} \end{bmatrix}, \\ C &= [C_1 \quad 0_{p \times q}] = [\bar{C}_1 \quad \bar{C}_2], \\ D &= \begin{bmatrix} D_1 \\ D_2 \end{bmatrix}, \\ \bar{N} &= \begin{bmatrix} \bar{N}_{11} & \bar{N}_{12} \\ \bar{N}_{21} & \bar{N}_{22} \end{bmatrix} = [\bar{N}_1 \quad \bar{N}_2], \\ H &= \begin{bmatrix} H_{11} & H_{12} \\ H_{21} & H_{22} \end{bmatrix}, \\ \bar{L} &= \begin{bmatrix} \bar{L}_1 \\ \bar{L}_2 \end{bmatrix}, \\ \bar{J} &= \begin{bmatrix} \bar{J}_1 \\ \bar{J}_2 \end{bmatrix}, \\ \bar{E} &= \begin{bmatrix} \bar{E}_1 \\ \bar{E}_2 \end{bmatrix}, \\ F &= \begin{bmatrix} F_{11} & F_{12} \\ F_{21} & F_{22} \end{bmatrix} = \begin{bmatrix} 0_{p \times q} & I_{p \times p} \\ 0_{(s-p) \times q} & 0_{(s-p) \times p} \end{bmatrix}, \\ Z &= \begin{bmatrix} Z_{11} & Z_{12} \\ Z_{21} & Z_{22} \end{bmatrix} = [Z_1 \quad Z_2], \end{aligned}$$

$$Z_1 = \begin{bmatrix} Z_{11} \\ Z_{21} \end{bmatrix},$$

$$Z_2 = \begin{bmatrix} Z_{12} \\ Z_{22} \end{bmatrix},$$

(29)

where

$$\begin{aligned} A_0 &\in \mathcal{R}^{n \times n}, \\ A_{0(11)} &\in \mathcal{R}^{q \times q}, \\ A_{0(12)} &\in \mathcal{R}^{q \times p}, \\ A_{0(21)} &\in \mathcal{R}^{p \times q}, \\ A_{0(22)} &\in \mathcal{R}^{p \times p}, \\ A_1 &\in \mathcal{R}^{n \times n}, \\ A_{1(11)} &\in \mathcal{R}^{q \times q}, \\ A_{1(12)} &\in \mathcal{R}^{q \times p}, \\ A_{1(21)} &\in \mathcal{R}^{p \times q}, \\ A_{1(22)} &\in \mathcal{R}^{p \times p}, \\ \bar{N} &\in \mathcal{R}^{s \times s}, \\ \bar{N}_{11} &\in \mathcal{R}^{q \times p}, \\ \bar{N}_{12} &\in \mathcal{R}^{q \times (s-p)}, \\ \bar{N}_{21} &\in \mathcal{R}^{(s-q) \times p}, \\ \bar{N}_{22} &\in \mathcal{R}^{(s-q) \times (s-p)}, \\ H &\in \mathcal{R}^{n \times s}, \\ H_{11} &\in \mathcal{R}^{q \times p}, \\ H_{12} &\in \mathcal{R}^{q \times (s-p)}, \\ H_{21} &\in \mathcal{R}^{p \times p}, \\ H_{22} &\in \mathcal{R}^{p \times (s-p)}, \\ \bar{L} &\in \mathcal{R}^{s \times p}, \\ \bar{L}_1 &\in \mathcal{R}^{q \times p}, \\ \bar{L}_2 &\in \mathcal{R}^{(s-q) \times p}, \\ \bar{J} &\in \mathcal{R}^{s \times p}, \\ \bar{J}_1 &\in \mathcal{R}^{q \times p}, \\ \bar{J}_2 &\in \mathcal{R}^{(s-q) \times p}, \\ \bar{E} &\in \mathcal{R}^{n \times p}, \end{aligned}$$

$$\begin{aligned}
 \bar{E}_1 &\in \mathcal{R}^{q \times p}, \\
 \bar{E}_2 &\in \mathcal{R}^{p \times p}, \\
 D &\in \mathcal{R}^{n \times q}, \\
 D_1 &\in \mathcal{R}^{q \times q}, \\
 D_2 &\in \mathcal{R}^{p \times q}, \\
 Z &\in \mathcal{R}^{s \times s}, \\
 Z_{11} &\in \mathcal{R}^{q \times p}, \\
 Z_{12} &\in \mathcal{R}^{q \times (s-p)}, \\
 Z_{21} &\in \mathcal{R}^{(s-q) \times p}, \\
 Z_{22} &\in \mathcal{R}^{(s-q) \times (s-p)}, \\
 Z_1 &\in \mathcal{R}^{s \times p}, \\
 Z_2 &\in \mathcal{R}^{s \times (s-p)}, \\
 \bar{N}_1 &\in \mathcal{R}^{s \times p}, \\
 \bar{N}_2 &\in \mathcal{R}^{s \times (s-p)}, \\
 C &\in \mathcal{R}^{p \times n}, \\
 C_1 &\in \mathcal{R}^{p \times p}, \\
 \bar{C}_1 &\in \mathcal{R}^{p \times q}, \\
 \bar{C}_2 &\in \mathcal{R}^{p \times p}.
 \end{aligned} \tag{30}$$

The ROUIO's design is concentrated into the following theorem.

**Theorem 7.** Consider the LTI multivariable (1) under the assumptions A4-A8; the ROUIO (3) is asymptotically stable if and only if the following conditions are satisfied: (1) there exists the matrix  $\bar{R} > 0$  verifying the LMI (24); (2) the matrices  $\bar{G}_0, \bar{G}_1, \bar{N}, \bar{L}, \bar{J}, \bar{E}$ , and  $H$  are given by

$$\begin{aligned}
 Z_1 &= I_{s \times p} - \bar{D}_2 (C_1 D_2)^+ C_1, \\
 \bar{G}_i &= [0_{s \times q} \quad Z_1] B_i \quad \forall i = 1 \dots k, \\
 \bar{N} &= [Z_1 (A_{0(14)} - A_{0(13)} \bar{C}_1^+ \bar{C}_2) \quad \bar{N}_2], \\
 \bar{L} &= Z_1 A_{0(21)} \bar{C}_1^+, \\
 \bar{J} &= (ZFA_1) C^+, \\
 \bar{E} &= \begin{bmatrix} \bar{C}_1^+ \\ I_p - \bar{C}_1 (C_1 \bar{C}_1)^+ C_1 \end{bmatrix}, \\
 H &= \begin{bmatrix} -\bar{C}_1^+ \bar{C}_2 & 0_{q \times (s-p)} \\ I_p - \bar{C}_2 + \bar{C}_1 (C_1 \bar{C}_1)^+ C_1 \bar{C}_2 & 0_{p \times (s-p)} \end{bmatrix},
 \end{aligned} \tag{31}$$

where the matrices  $Z_2 \in \mathcal{R}^{s \times (s-p)}$  and  $\bar{N}_2 \in \mathcal{R}^{s \times (s-p)}$  are arbitrarily chosen,  $\bar{C}_1 \in \mathcal{R}^{p \times q}$  and  $\bar{C}_2 \in \mathcal{R}^{p \times p}$  are submatrices of the matrix  $C$ , and  $\bar{D}_2 = I_{s \times p} D_2$ .

*Proof.* Using (29) and (30), the fourth equation of (25) becomes

$$Z_1 D_2 = 0_{s \times q}. \tag{32}$$

To compute the matrix  $Z_1$  from this equation, one can choose

$$Z_1 = I_{s \times p} + T_1 C_1, \tag{33}$$

with  $T_1 \in \mathcal{R}^{s \times p}$  an unknown matrix to be computed. With the notation  $\bar{D}_2 = I_{s \times p} D_2$ , one gets  $T_1 = -\bar{D}_2 (C_1 D_2)^+$ , where  $(C_1 D_2)^+$  is the generalized pseudoinverse of  $(C_1 D_2)$ , given by  $(C_1 D_2)^+ = [(C_1 D_2)^T (C_1 D_2)]^{-1} (C_1 D_2)^T$ . According to the assumption A5 and to the fact that the matrix  $C_1$  is full rank, we can conclude that  $\text{rank}(C_1 D_2) = q$ , and the generalized pseudoinverse of  $(C_1 D_2)$  can be always obtained.

Equation (33) can be then written as

$$Z_1 = I_{s \times p} - \bar{D}_2 (C_1 D_2)^+ C_1, \tag{34}$$

and the matrix  $Z_2 \in \mathcal{R}^{s \times (s-p)}$  is chosen arbitrarily.

Now, using the expression of the matrix  $Z$ , we obtain the matrices  $\bar{G}_i$  in the third equation of (25). We arbitrarily choose the matrices  $N_{12}$  and  $N_{22}$ ; as a consequence, the matrix  $\bar{N}_2$  is arbitrarily chosen. Using this as well as the form of matrix  $C$  given in (29) and (30), i.e.,  $C = [C_1 \quad 0_{p \times q}] = [\bar{C}_1 \quad \bar{C}_2]$ , the first equation (25) can be written in a form of matrix system as follows:

$$\begin{aligned}
 -Z_{11} A_{0(21)} + \bar{L}_1 \bar{C}_1 &= 0_{q \times q}, \\
 \bar{N}_{11} - Z_{11} A_{0(22)} + \bar{L}_1 \bar{C}_2 &= 0_{q \times p}, \\
 -Z_{21} A_{0(21)} + \bar{L}_2 \bar{C}_1 &= 0_{(s-q) \times q}, \\
 \bar{N}_{21} - Z_{21} A_{0(22)} + \bar{L}_2 \bar{C}_2 &= 0_{(s-q) \times p};
 \end{aligned} \tag{35}$$

by solving system (35), we obtain

$$\begin{aligned}
 \bar{N}_{11} &= Z_{11} (A_{0(22)} - A_{0(21)} \bar{C}_1^+ \bar{C}_2), \\
 \bar{L}_1 &= Z_{11} A_{0(21)} \bar{C}_1^+, \\
 \bar{N}_{21} &= Z_{21} (A_{0(22)} - A_{0(21)} \bar{C}_1^+ \bar{C}_2), \\
 \bar{L}_2 &= Z_{21} A_{0(21)} \bar{C}_1^+;
 \end{aligned} \tag{36}$$

bearing in mind the fact that  $q < p$ , it results that  $\bar{C}_1$  is a submatrix of the nonsingular matrix  $C_1$ ; from this, one deduces that  $\text{rank}(\bar{C}_1) = q$ , i.e.,  $\bar{C}_1$  is a full column rank matrix.

Now, solving the second equation of (25), we get

$$\bar{J} = (ZFA_1) C^+. \tag{37}$$

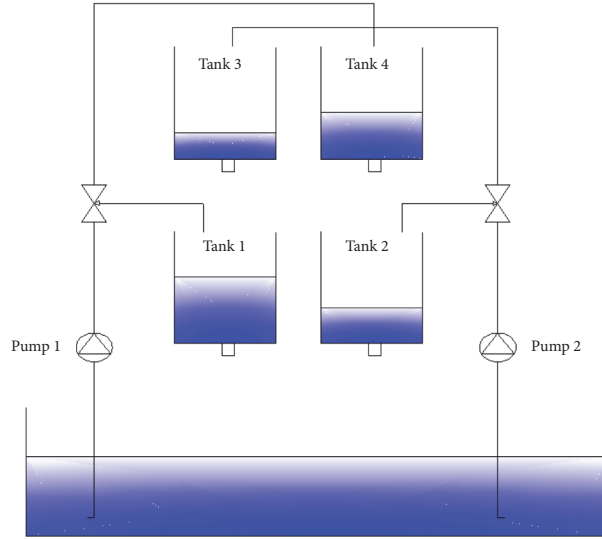


FIGURE 1: The quadruple-tank process.

Using (29) and (30), the sixth equation (25) can be transformed into a matrix system as

$$\begin{aligned} \bar{E}_1 \tilde{C}_1 &= I_q, \\ \bar{E}_1 \tilde{C}_2 + H_{11} &= 0_{q \times p}, \\ \bar{E}_2 \tilde{C}_1 &= 0_{p \times q}, \\ \bar{E}_2 \tilde{C}_2 + H_{21} &= I_p; \end{aligned} \quad (38)$$

from the first and second equations of (38), we obtain  $\bar{E}_1 = \tilde{C}_1^+$  and  $H_{11} = -\bar{E}_1 \tilde{C}_2 = -\tilde{C}_1^+ \tilde{C}_2$ . On the other hand, the matrix  $\bar{E}_2$  is calculated from the third equation of (35) as follows:

$$\bar{E}_2 = I_p + T_2 C_1, \quad (39)$$

where  $T_2 \in \mathcal{R}^{p \times p}$  is an unknown matrix to be computed. Because  $C_1 \in \mathcal{R}^{p \times p}$  is a nonsingular matrix and  $\text{rank}(\tilde{C}_1) = q$ , one gets  $\text{rank}(C_1 \tilde{C}_1) = q$ , i.e.,  $(C_1 \tilde{C}_1)$  is a full column rank matrix. Taking this into account, one successively gets  $T_2 = -\tilde{C}_1 (C_1 \tilde{C}_1)^+$  and  $\bar{E}_2 = I_p - \tilde{C}_1 (C_1 \tilde{C}_1)^+ C_1$ . From the fourth equation of system (38), we obtain  $H_{12} = I_p - \tilde{C}_2 + \tilde{C}_1 (C_1 \tilde{C}_1)^+ C_1 \tilde{C}_2$ ; by concatenation of the matrices  $\bar{E}_1, \bar{E}_2, H_{11}, H_{21}, H_{12} = 0_{q \times (s-p)}$  and  $H_{22} = 0_{p \times (s-p)}$ , the last two equations (31) result. Now, the proof of the Theorem 7 is complete.  $\square$

*Algorithm 8.* Design of the ROUIO.

*Step 1.* Given system (1), verify the five related assumptions A4-A8.

*Step 2.* The matrix  $F$  of from (29) is chosen; the matrices  $A_0, A_1, C, D, \bar{N}, H, \bar{L}, \bar{J}, \bar{E}$ , and  $Z$  are partitioned with (29) and (30). The matrices  $Z_{12}$  and  $Z_{22}$  and thus the matrix  $Z_2$  are

arbitrarily chosen; the matrices  $Z_1, \bar{G}_i \forall i = 1 \dots k$ , are obtained via (31).

*Step 3.* The matrices  $\bar{N}_{12}, \bar{N}_{22}$  and thus the matrix  $\bar{N}_2$  are arbitrarily chosen; by solving system (35) with respect to the matrices  $\bar{N}_{11}, \bar{N}_{21}, \bar{L}_1, \bar{L}_2$  or, directly, by means of (36), these four matrices are obtained; the matrices  $\bar{N}, \bar{J}$  and  $\bar{L}$  are then calculated with (31). Matrices  $\bar{E}$  and  $H$  are computed by solving system (38).

*Step 4.* Using the above calculated matrix  $\bar{N}$ , one checks if there exists a symmetric and positive-definite matrix  $\bar{R} \in \mathcal{R}^{n \times n}$  verifying the LMI (24); if so, the matrix  $\bar{N}$  has been properly obtained; otherwise, Steps 2-4 are repeated (in a "while" loop) until this condition is fulfilled.

*Step 5.* The observer described by (3) is completely designed and the time history of the system's estimated states can be obtained.

## 5. Numerical Simulation Results

*5.1. The Quadruple-Tank Process.* The quadruple-tank process is shown in Figure 1. It is composed of four connected tanks and two pumps that split water into two tanks [30, 31, 49]. The inlet flow of each tank is measured by an electromagnetic flow-meter and regulated by a pneumatic valve whereas the level of each tank  $h_i$  ( $i=1 \dots 4$ ) is measured by means of a pressure sensor. The process inputs are the input voltages of the pumps ( $\vartheta_1$  and  $\vartheta_2$ ) and the output variables are the tank levels  $y_1$  and  $y_2$ .

*5.2. The Quadruple-Tank Process Model.* For practical considerations, we assume that the operating regime of the process is well known that the quadruple-tank process is

affected by delays and that the transport delays are perfectly symmetric. In such a case, the model of the process can be written as case study of model (1) and can be described by [30]

$$\begin{aligned} \dot{x}(t) &= A_0 x(t) + A_1 x(t - \tau_1) + B_0 u(t - \tau_2) \\ &\quad + B_1 u(t - \tau_3) + Dd(t), \\ y(t) &= Cx(t), \end{aligned} \quad (40)$$

with  $x = [h_1 \ h_2 \ h_3 \ h_4]^T$  being the state vector,  $u = [\vartheta_1 \ \vartheta_2]^T$  being the input vector, and  $y = [y_1 \ y_2]^T$  being the output vector, respectively, and with

$$\begin{aligned} A_0 &= \begin{bmatrix} -\frac{a_1}{A_1} \sqrt{\frac{g}{2h_{10}}} & 0 & 0 & 0 \\ 0 & -\frac{a_2}{A_2} \sqrt{\frac{g}{2h_{20}}} & 0 & 0 \\ 0 & 0 & -\frac{a_3}{A_3} \sqrt{\frac{g}{2h_{30}}} & 0 \\ 0 & 0 & 0 & -\frac{a_4}{A_4} \sqrt{\frac{g}{2h_{40}}} \end{bmatrix}, \\ B_0 &= \begin{bmatrix} \frac{\gamma_1 k_1}{A_1} & 0 \\ 0 & \frac{\gamma_2 k_2}{A_2} \\ 0 & 0 \\ 0 & 0 \end{bmatrix}, \\ A_1 &= \begin{bmatrix} 0 & 0 & \frac{a_3}{A_1} \sqrt{\frac{g}{2h_{30}}} & 0 \\ 0 & 0 & 0 & \frac{a_4}{A_2} \sqrt{\frac{g}{2h_{40}}} \\ 0 & 0 & 0 & 0 \\ 0 & 0 & 0 & 0 \end{bmatrix}, \\ B_1 &= \begin{bmatrix} 0 & 0 \\ 0 & 0 \\ 0 & \frac{(1 - \gamma_2) k_2}{A_3} \\ \frac{(1 - \gamma_1) k_1}{A_4} & 0 \end{bmatrix}. \end{aligned} \quad (41)$$

Using the following numerical values

$$\begin{aligned} D_1 &= D_2 = D_3 = D_4 = 9.2 \text{ cm}, \\ A_1 &= A_2 = A_3 = A_4 = \pi \left( \frac{D_1}{2} \right)^2, \\ h_{\max} &= 50 \text{ cm}, \\ h_{i0} &= \frac{h_{\max}}{2} = 25 \text{ cm}, \\ g &= 981 \text{ cm} \cdot \text{s}^{-2}, \\ d_1 &= 0.2 \text{ cm}, \end{aligned}$$

$$a_1 = a_2 = \pi \left( \frac{d_1}{2} \right),$$

$$d_3 = 0.9,$$

$$a_3 = a_4 = \pi \left( \frac{d_3}{2} \right)^2,$$

$$k_1 = 7.39,$$

$$k_2 = 6.92,$$

(42)

the matrices from (1) are given by

$$\begin{aligned} A_0 &= \begin{bmatrix} -0.0021 & 0 & 0 & 0 \\ 0 & -0.0021 & 0 & 0 \\ 0 & 0 & -0.0424 & 0 \\ 0 & 0 & 0 & -0.0424 \end{bmatrix}, \\ B_0 &= \begin{bmatrix} 0.1113 \times \gamma_1 & 0 \\ 0 & 0.1042 \times \gamma_2 \\ 0 & 0 \\ 0 & 0 \end{bmatrix}, \\ A_1 &= \begin{bmatrix} 0 & 0 & 0.0424 & 0 \\ 0 & 0 & 0 & 0.0424 \\ 0 & 0 & 0 & 0 \\ 0 & 0 & 0 & 0 \end{bmatrix}, \\ B_1 &= \begin{bmatrix} 0 & 0 \\ 0 & 0 \\ 0 & (1 - \gamma_2) \times 0.1042 \\ (1 - \gamma_1) \times 0.1042 & 0 \end{bmatrix}. \end{aligned} \quad (43)$$

**5.3. Software Implementation of the Full-Order Observer.** For simulation results, the following numerical values are chosen:  $x(0) = [-4 \ 4 \ 6 \ -5]$ ,  $d(t) = 0.3 \sin(2\pi ft)$ ,  $D^T = \begin{bmatrix} 10 & 20 & -12 & 15 \\ -23 & 28 & 30 & -36 \end{bmatrix}$ ,  $\gamma_1 = 0.333$ ,  $\gamma_2 = 0.307$ ,  $\alpha = 0.4420$ , and  $\tau_1 = 5\text{s}$ ,  $\tau_2 = 3\text{s}$ ,  $\tau_3 = 4\text{s}$ . The control gain matrix is computed using the approach proposed in [1]

$$K = \begin{bmatrix} -0.1603 & -0.1765 & -0.0795 & -0.2073 \\ -0.1977 & -0.1579 & -0.2288 & -0.0772 \end{bmatrix} \quad (44)$$

For the FOUIO software implementation, one obtains

$$E = \begin{bmatrix} -1 & 0 \\ 0 & -1 \\ 1.264 & -0.032 \\ -1.54 & 0.02 \end{bmatrix},$$

$$\begin{aligned}
P &= \begin{bmatrix} 0 & 0 & 0 & 0 \\ 0 & 0 & 0 & 0 \\ 1.26 & -0.032 & 1 & 0 \\ -1.54 & -0.020 & 0 & 1 \end{bmatrix}, \\
G_0 &= \begin{bmatrix} 0 & 0 \\ 0 & 0 \\ 0.046 & -0.01 \\ -0.057 & 0.06 \end{bmatrix}, \\
G_1 &= \begin{bmatrix} 0 & 0 \\ 0 & 0 \\ 0 & 0.072 \\ 0.074 & 0 \end{bmatrix}, \\
N &= \begin{bmatrix} -1 & 0 & 0 & 0 \\ 0 & -1 & 0 & 0 \\ 1 & 1 & -0.0424 & 0 \\ 1 & 1 & 0 & -0.0424 \end{bmatrix}, \\
L &= \begin{bmatrix} 0 & 0 \\ 0 & 0 \\ -0.05 & -0.013 \\ -0.06 & 0.08 \end{bmatrix}, \\
J &= \begin{bmatrix} 0 & 0 \\ 0 & 0 \\ -0.043 & 0.095 \\ -0.025 & 0.017 \end{bmatrix}, \\
\bar{G}_0 &= \begin{bmatrix} 0 & 0 \\ 0.1 & 0 \\ 0 & 0.07 \end{bmatrix}, \\
\bar{G}_1 &= \begin{bmatrix} 0 & 0.072 \\ 0.074 & 0 \\ 0 & 0 \end{bmatrix}, \\
\bar{N} &= 10^{13} \begin{bmatrix} 0 & 0 & 2.945 \\ 0 & 0 & 0.46 \\ 0 & 0 & 0 \end{bmatrix}, \\
\bar{L} &= \begin{bmatrix} 0 & 0 \\ 0 & 0 \\ -0.05 & -0.013 \\ -0.06 & 0.08 \end{bmatrix}, \\
\bar{J} &= \begin{bmatrix} 0 & 0 \\ 0 & 0 \\ -0.043 & 0.095 \\ -0.025 & 0.017 \end{bmatrix}, \\
Z &= 10^{-14} \begin{bmatrix} 0.2220 & -0.0439 & 0.5255 \\ 0.1377 & 0.0111 & 0.8992 \\ 0 & 0 & 0.9452 \end{bmatrix}
\end{aligned} \tag{45}$$

*5.4. Software Implementation of the Reduced-Order Observer.* During the first step of the Algorithm 8, we find the matrices and vectors from (3). In this paper, the order is chosen as equal  $n=4$ ,  $m=2$ ,  $p=2$ ,  $q=2$ , and  $s=3$  and the constant time delays are chosen as  $\tau_1 = 5s$ ,  $\tau_2 = 2s$ , and  $\tau_3 = 4s$ . We obtain

$$\begin{aligned}
\bar{E} &= \begin{bmatrix} 1 & 0 \\ 0 & 1 \\ 0 & 0 \\ 0 & 0 \end{bmatrix}, \\
H &= \begin{bmatrix} 0 & 0 & 0 \\ 0 & 0 & 0 \\ 1 & 0 & 0 \\ 0 & 1 & 0 \end{bmatrix},
\end{aligned}$$

Figure 2 shows the effectiveness of two designed observers for the quadruple-process and their performances for which the variables  $x_1$  and  $x_2$  (variation of water levels in tanks 1 and 2) are measured and only the variables  $x_3$  and  $x_4$  (variation of water levels in tanks 3 and 4) are estimated. The effectiveness of two observers is proved by the superpose of the three curves.

## 6. Conclusion

This study considers the design of two approaches of UIOs for systems with multiple time-delays: a full-order delay-dependent UIO and a reduced-order delay-dependent UIO. The quadruple-tank process was used as a benchmark to prove the effectiveness of the new observer algorithms for the case study of multivariable nonminimum phase systems with multiple delays.

## Data Availability

The data used to support the findings of this study are included within the article.

## Conflicts of Interest

The authors declare that there are no conflicts of interest regarding the publication of this paper.

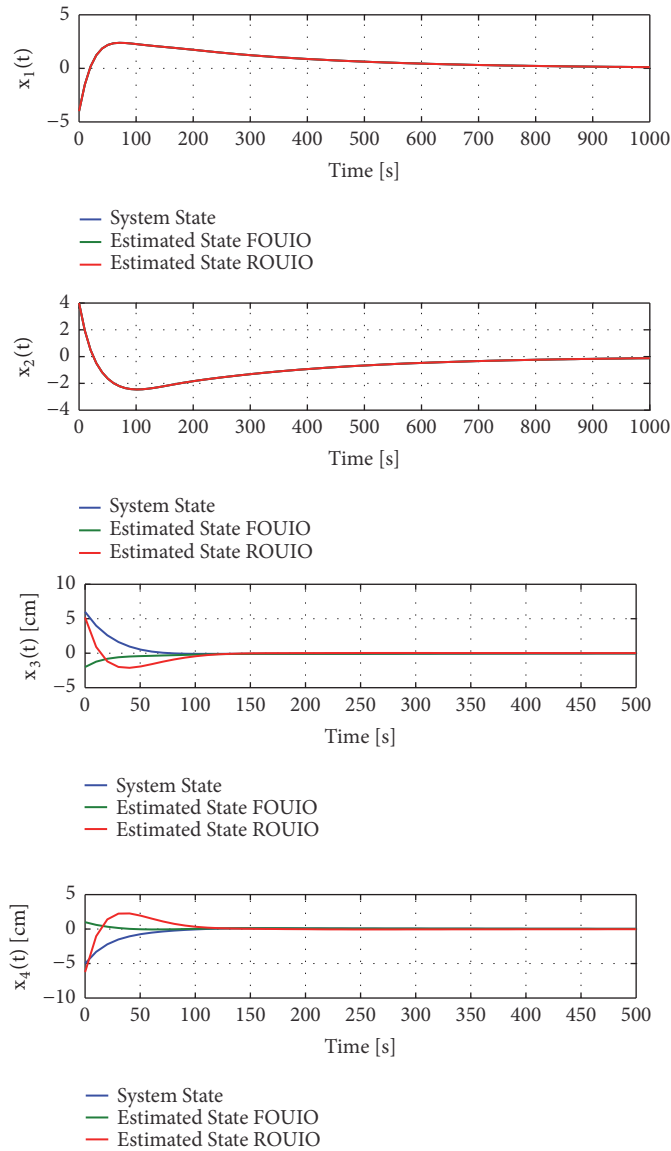


FIGURE 2: FOUIO and ROUIO of the quadruple-tank process.

**References**

- [1] F. El Haoussi, E. H. Tissir, F. Tadeo, and A. Hmamed, "Delay-dependent stabilisation of systems with time-delayed state and control: application to a quadruple-tank process," *International Journal of Systems Science*, vol. 42, no. 1, pp. 41–49, 2011.
- [2] M. Darouach, M. Zasadzinski, and S. J. Xu, "Full-order observers for linear systems with unknown inputs," *Institute of Electrical and Electronics Engineers Transactions on Automatic Control*, vol. 39, no. 3, pp. 606–609, 1994.
- [3] F. Zhang, S. Zong, X. Wang, and X. Ren, "An Expert PI Controller with Dead Time Compensation of Monitor AGC in Hot Strip Mill," *Mathematical Problems in Engineering*, vol. 2016, Article ID 3041538, 8 pages, 2016.
- [4] H. Li, X. Jing, and H. R. Karimi, "Output-feedback-based  $H_\infty$  control for vehicle suspension systems with control delay," *IEEE Transactions on Industrial Electronics*, vol. 61, no. 1, pp. 436–446, 2014.
- [5] R. Sanz, P. Garcia, Q.-C. Zhong, and P. Albertos, "Predictor-Based Control of a Class of Time-Delay Systems and Its Application to Quadrotors," *IEEE Transactions on Industrial Electronics*, vol. 64, no. 1, pp. 459–469, 2017.
- [6] S. Bououden, M. Chadli, L. Zhang, and T. Yang, "Constrained model predictive control for time-varying delay systems: Application to an active car suspension," *International Journal of Control, Automation, and Systems*, vol. 14, no. 1, pp. 51–58, 2016.
- [7] W. Cao, Z. Liu, Y. Chang, and A. Szumanowski, "Direct Yaw-Moment Control of All-Wheel-Independent-Drive Electric Vehicles with Network-Induced Delays through Parameter-Dependent Fuzzy SMC Approach," *Mathematical Problems in Engineering*, vol. 2017, Article ID 5170492, 15 pages, 2017.
- [8] O. Boubaker, V. E. Balas, A. Benzaouia, M. Chaabane, M. S. Mahmoud, and Q. Zhu, "Time-Delay Systems: Modeling, Analysis, Estimation, Control, and Synchronization," *Mathematical Problems in Engineering*, vol. 2017, Article ID 1398904, 3 pages, 2017.

- [9] M. S. Mahmoud, "Recent Progress in Stability and Stabilization of Systems with Time-Delays," *Mathematical Problems in Engineering*, vol. 2017, Article ID 7354654, 25 pages, 2017.
- [10] E. Fridman, *Introduction to Time-delay Systems: Analysis and Control*, Springer, Berlin, Germany, 2014.
- [11] B. Zhou, *Truncated predictor feedback for time-delay systems*, Springer, Berlin, Germany, 2014.
- [12] E. Witrant, E. Fridman, O. Sename, and L. Dugard, *Recent Results on Time-Delay Systems*, vol. 5, Springer International Publishing, 2016.
- [13] X.-M. Zhang, Q.-L. Han, A. Seuret, and F. Gouaisbaut, "An improved reciprocally convex inequality and an augmented Lyapunov-Krasovskii functional for stability of linear systems with time-varying delay," *Automatica*, vol. 84, pp. 221–226, 2017.
- [14] W. Qian, M. Yuan, L. Wang, X. Bu, and J. Yang, "Stabilization of systems with interval time-varying delay based on delay decomposing approach," *ISA Transactions*, vol. 70, 6 pages, 2017.
- [15] X. Cai, N. Bekiaris-Liberis, and M. Krstic, "Input-to-state stability and inverse optimality of linear time-varying-delay predictor feedbacks," *Institute of Electrical and Electronics Engineers Transactions on Automatic Control*, vol. 63, no. 1, pp. 233–240, 2018.
- [16] Q. Liu and B. Zhou, "Extended observer based feedback control of linear systems with both state and input delays," *Journal of The Franklin Institute*, vol. 354, no. 18, pp. 8232–8255, 2017.
- [17] W. Belhaj and O. Boubaker, "MIMO PI Controllers for LTI Systems with Multiple Time Delays Based on ILMIs and Sensitivity Functions," *Mathematical Problems in Engineering*, vol. 2017, Article ID 1241545, 25 pages, 2017.
- [18] B. Zhou, Q. Liu, and F. Mazenc, "Stabilization of linear systems with both input and state delays by observer-predictors," *Automatica*, vol. 83, pp. 368–377, 2017.
- [19] R. Dormido, H. Vargas, N. Duro et al., "Development of a web-based control laboratory for automation technicians: the three-tank system," *IEEE Transactions on Education*, vol. 51, no. 1, pp. 35–44, 2008.
- [20] S. Di Cairano, A. Bemporad, I. V. Kolmanovskiy, and D. Hrovat, "Model predictive control of magnetically actuated mass spring dampers for automotive applications," *International Journal of Control*, vol. 80, no. 11, pp. 1701–1716, 2007.
- [21] A. C. Luo and R. P. Han, "The dynamics of a bouncing ball with a sinusoidally vibrating table revisited," *Nonlinear Dynamics*, vol. 10, no. 1, pp. 1–18, 1996.
- [22] M. Jankovic, D. Fontaine, and P. V. Kokotović, "TORA example: cascade- and passivity-based control designs," *IEEE Transactions on Control Systems Technology*, vol. 4, no. 3, pp. 292–297, 1996.
- [23] B. M. Chen, T. H. Lee, and V. Venkataramanan, *Hard disk drive servo systems*, Springer, Berlin, Germany, 2002.
- [24] N. F. Al-Muthairi and M. Zribi, "Sliding mode control of a magnetic levitation system," *Mathematical Problems in Engineering*, vol. 2004, no. 2, pp. 93–107, 2004.
- [25] O. Boubaker and R. Iriarte, *The Inverted Pendulum in Control Theory and Robotics: From theory to new innovations*, Institution of Engineering and Technology, Stevenage, UK, 2017.
- [26] I. Fantoni and R. Lozano, "Stabilization of the Furuta pendulum around its homoclinic orbit," *International Journal of Control*, vol. 75, no. 6, pp. 390–398, 2002.
- [27] D. J. Block, K. J. Åström, and M. W. Spong, "The Reaction Wheel Pendulum," *Synthesis Lectures on Controls and Mechatronics*, vol. 1, no. 1, pp. 1–105, 2007.
- [28] F. Andreev, D. Auckly, S. Gosavi, L. Kapitanski, A. Kelkar, and W. White, "Matching linear systems, and the ball and beam," *Automatica*, vol. 38, no. 12, pp. 2147–2152, 2002.
- [29] F. Matsuno and Y. Sakawa, "Modeling and Quasi-Static Hybrid Position/Force Control of Constrained Planar Two-Link Flexible Manipulators," *IEEE Transactions on Robotics and Automation*, vol. 10, no. 3, pp. 287–297, 1994.
- [30] K. H. Johansson, "The quadruple-tank process: a multivariable laboratory process with an adjustable zero," *IEEE Transactions on Control Systems Technology*, vol. 8, no. 3, pp. 456–465, 2000.
- [31] K. H. Johansson, A. Horch, O. Wijk, and A. Hansson, "Teaching multivariable control using the quadruple-tank process," in *Proceedings of the The 38th IEEE Conference on Decision and Control (CDC)*, pp. 807–812, 1999.
- [32] K. H. Johansson and J. L. R. Nunes, "A multivariable laboratory process with an adjustable zero," in *Proceedings of the American Control Conference (ACC '98)*, pp. 2045–2049, 1998.
- [33] T. Roinila, M. Vilkkö, and A. Jaatinen, "Corrected Mathematical Model of Quadruple Tank Process," *IFAC Proceedings Volumes*, vol. 41, no. 2, pp. 11678–11683, 2008.
- [34] W. Belhaj and O. Boubaker, "On MIMO PID control of the quadruple-tank process via ILMIs approaches: minimum and non-minimum case studies," in *Proceedings of the 10th IFAC Symposium on Dynamics and Control of Process Systems (DYCOPS '13)*, pp. 481–486, Mumbai, India, 2013.
- [35] K. H. Johansson, "Interaction bounds in multivariable control systems," *Automatica*, vol. 38, no. 6, pp. 1045–1051, 2002.
- [36] I. Alvarado, D. Limon, W. García-Gabín, T. Alamo, and E. Camacho, "An Educational Plant Based on the Quadruple-Tank Process," *IFAC Proceedings Volumes*, vol. 39, no. 6, pp. 82–87, 2006.
- [37] S. H. Said and F. M. Sahli, "A set of observers design to a quadruple tank process," in *Proceedings of the 2008 IEEE International Conference on Control Applications (CCA) part of the IEEE Multi-Conference on Systems and Control*, pp. 954–959, San Antonio, TX, USA, 2008.
- [38] H. Gouta, S. H. Saïd, N. Barhoumi, and F. M'Sahli, "Generalized predictive control for a coupled four tank MIMO system using a continuous-discrete time observer," *ISA Transactions*, vol. 67, pp. 280–292, 2017.
- [39] C. Huang, E. Canuto, and C. Novara, "The four-tank control problem: Comparison of two disturbance rejection control solutions," *ISA Transactions*, vol. 71, pp. 252–271, 2017.
- [40] N. Xavier, B. Bandyopadhyay, and R. Schmid, "Robust non-overshooting tracking using continuous control for linear multivariable systems," *IET Control Theory & Applications*, vol. 12, no. 7, pp. 1006–1011, 2018.
- [41] H. Gouta, S. H. Said, and F. M'Sahli, "Observer-based Back-stepping liquid level controller for a quadruple tank process," in *Proceedings of the 16th International Conference on Sciences and Techniques of Automatic Control and Computer Engineering, STA 2015*, pp. 351–356, Tunisia, 2015.
- [42] F. Smida, S. H. Said, and F. M'Sahli, "Cascade unknown input observers applied to a quadruple tank process," in *Proceedings of the 2015 12th International Multi-Conference on Systems, Signals & Devices (SSD)*, pp. 1–6, Mahdia, Tunisia, 2015.
- [43] I. Manaa, N. Barhoumi, and F. M'Sahli, "Unknown inputs observers design for a class of nonlinear switched systems," *International Journal of Modelling, Identification and Control*, vol. 23, no. 1, pp. 45–54, 2015.

- [44] M. Lungu and R. Lungu, "Full-order observer design for linear systems with unknown inputs," *International Journal of Control*, vol. 85, no. 10, pp. 1602–1615, 2012.
- [45] S. Ben Warrad and O. Boubaker, "Robust observer for multiple time-delay systems with unknown inputs," in *Proceedings of the 16th International Conference on Sciences and Techniques of Automatic Control and Computer Engineering. (STA '15)*, pp. 859–864, Tunisia, 2015.
- [46] S. B. Warrad and O. Boubaker, "Full order unknown inputs observer for multiple time-delay systems," *International Journal On Smart Sensing and Intelligent Systems*, vol. 9, no. 4, pp. 1750–1775, 2016.
- [47] S. Ben Warrad and O. Boubaker, "Design of unknown input observers for linear systems with state and input delays," in *Proceedings of the 15th IEEE International Multi-Conference on Systems, Signals and Devices*, Hammamet, Tunisia, 2018.
- [48] S. Ben Warrad, O. Boubaker, M. Lungu, and Q. Zhu, "On unknown inputs observer design for linear systems with delays in states and inputs," in *New Trends in Observer-based Control: An Introduction to Design Approaches and Engineering Applications*, Elsevier Academic Press, 1st edition, 2019.
- [49] W. Belhaj and O. Boubaker, "Multivariable PID Control via LMIs: Performances Assessment," *International Journal on Smart Sensing & Intelligent Systems*, vol. 8, no. 4, pp. 1896–1916, 2015.

## Research Article

# An Optimal Identification of the Input-Output Disturbances in Linear Dynamic Systems by the Use of the Exact Observation of the State

Jędrzej Byrski <sup>1</sup> and Witold Byrski <sup>2</sup>

<sup>1</sup>Department of Applied Computer Science, AGH University of Science and Technology, Krakow, Poland

<sup>2</sup>Department of Automatic Control and Robotics, AGH University of Science and Technology, Krakow, Poland

Correspondence should be addressed to Jędrzej Byrski; [jbyrski@agh.edu.pl](mailto:jbyrski@agh.edu.pl)

Received 5 August 2018; Accepted 22 October 2018; Published 8 November 2018

Academic Editor: Luis J. Yebra

Copyright © 2018 Jędrzej Byrski and Witold Byrski. This is an open access article distributed under the Creative Commons Attribution License, which permits unrestricted use, distribution, and reproduction in any medium, provided the original work is properly cited.

A new methodology for the identification of the values of unknown disturbance signals acting in the input and output measurements of the dynamic linear system is presented. For the solution of this problem, the new idea of the use of two different state observers, which are working simultaneously in parallel, was elaborated. Special integral type observers are operating on the same finite time window of the width  $T$  and both can reconstruct the exact value of the vector state  $x(T)$  on the basis of input-output measurements in this interval  $[0, T]$ . If in the input-output signals the disturbances are absent (measurements of I/O signals are perfect) then both observers (although they are different) reconstruct the exact and the same state  $x(T)$ . However, if in the measurement signals the disturbances are present then these observers will reconstruct the different values of the final states  $x_1(T)=x(T)+e_1(T)$  and  $x_2(T)=x(T)+e_2(T)$ . It is because they have different norms and hence they generate different errors in both estimated states. Because of the disturbances, the real state  $x(T)$  is unknown, but it is easy to calculate the state difference:  $x_1(T)-x_2(T)=e_1(T)-e_2(T)$ . It occurs that, based on this difference, the values of all the disturbances acting during the control process can be identified. In the paper, the theory of the exact state observation and application of such observers in online mode is recalled. The new methodology for disturbances identification is presented.

## 1. Introduction

In the classic control theory and its applications, a common practice in the estimation of inaccessible for measurement state vector of a linear observable system is the use of Luenberger type asymptotic observers. D.G. Luenberger in [1] proposed the pole placement technique for calculation of the observer gain matrix. The structure of such an observer was derived directly from the differential form of the Kalman Filter, KF [2, 3]. Calculation of the optimal gain matrix in KF was based on the known stochastic properties of the disturbances and the least-squares estimation error approach. In both types of these estimators, their structures are given by ordinary linear differential equations. Hence under assumption that real initial state is unknown the solution of the estimation problem by the use of these observers could give only a state estimate, which tends to the real state

asymptotically and reaches them theoretically in infinity. Calculation of the current estimation error is impossible, because the real state is unknown.

Nowadays in many real-time control applications and fault detection, the finishing of the observation tasks in assumed and possibly short time  $T$  is an important requirement. The asymptotic state estimators may not be sufficient for this purpose. The power of the modern microcomputers makes the design of the other online observation algorithms possible. They reconstruct the value of the current state vector **exactly** in finite time  $T$ . The calculations are based on the finite time history of measurement samples of input and output. What is more, the width  $T > 0$  of the measurement window can be almost freely chosen.

The general theory of the exact reconstruction of the finite dimension state for linear systems in Hilbert spaces as well as the rules for designing of the exact state observers

with minimal norm was formulated and presented by W. Byrski and S. Fuksa in 1984 [4, 5]. This theory originates from the definition of the state observability and formulates the extension of the method presented in [6] with the use of functional analysis technique. The authors of [4, 5] proposed a deterministic approach to disturbances characterization and to the exact and optimal state observation for which the relations were formulated generally in function Hilbert spaces  $U, Y$ . Such type of the observer must have the structure of two linear continuous functionals. It is because based on two fragments of two continuous functions  $u$  and  $y$ , which are given on finite time interval  $T$ , the observer should calculate the real unknown vectors  $x(0)$  or  $x(T)$ , where  $x \in \mathbb{R}^n$ . On the other hand from the Riesz Representation Theorem it follows that every linear continuous functional in Hilbert space can be expressed as the inner product. Hence the structure of the observer must have a form of two inner products: one product of continuous output function  $y \in Y$  and special observation function  $G_1(\tau) \in Y$  and the second one with the input function  $u \in U$  and special observation function  $G_2(\tau) \in U$ . After the first observation interval  $[0, T]$  the observer reconstructs  $x(T)$  and next can also reconstruct the exact values of the state  $x(t)$  for  $\forall t > T$ , based on continuous moving window (in online mode). Choosing different input-output Hilbert spaces one can obtain different formulas for the finite state exact observers.

In engineering sciences, commonly used is the function space  $L^2[0, T]$ . This space is defined as a space of functions for which the second power is integrable in Lebesgue sense, on the interval  $[0, T]$ . The existence of such integral enables definition of the norm of the function as the square root of this integral. In many cases, it can represent the square root of the signal's energy. The space  $L^2[0, T]$  belongs to class of Hilbert spaces; hence the inner product of its two elements has the form of the integral operator.

The studies on the exact state observation were undertaken by various authors, although they may be considered as particular cases of the general theory of the exact state observation [4]. In 1966 J.D. Gilchrist [7] proposed mixed version of the exact state observation with the use of discrete measurement of the output signal and continuous measurements of the control. Similar approach was presented in [8–11]. In 1992 A. Medvedev and H.T. Toivonen in [12, 13] continued the study of such mixed types of state observers and called them “finite memory deadbeat observers.” Some other version of the finite memory deadbeat observer was also presented in [14]. However, all of the above observer's versions were based on standard least squares approach and are only subcases of the general form of the exact and optimal state observer.

As it was stated before, the exactness in reconstruction of the state is possible by the use of the exact state observers but only under assumption that no input-output noise or disturbances occur (i.e., in the case of perfect input-output measurements). Hence, in practical case of noisy measurements the use of the exact observers gives also a reconstruction error. In the most popular version of the exact observers it was assumed that the input function (control)

is perfectly known and for state calculation there is no need for its extra measurement. The last assumption however, in practical application, is not always proper because, e.g., the actuator and the control valve produce the system input signal and it may differ from the control signal  $u$ , which is generated by the computer (the number of impulses). From the general theory of the exact and optimal observation one can obtain the observer with minimal norm. It guarantees that, based on the perfect input-output measurements, the state  $x$  will be reconstructed exactly and for the measurements with bounded disturbances on  $y$  and  $u$  (disturbances with bounded norm, from unit balls) the norm of the state reconstruction error will be minimal.

In publications [4, 5] it was assumed that spaces  $Y$  and  $U$  are chosen as  $L^2[0, T]$ ; hence the inner product is represented by the integral operator. Therefore the name “integral observers” was also frequently used to underline its contrary type to differential structure of the Kalman Filter (LQF) or Luenberger observer [15–17]. Particularly important theorem of a closed loop stability with the use of the integral observer and linear quadratic regulator (LQR) was given in [4]. It was also proven that integral observer and LQR controller in closed loop create the dynamic system of the order  $n$ , and not  $2n$  like in linear quadratic Gaussian system (LQG=LQF+LQR).

The extended results of the online exact observation and application were presented in [15, 16, 18]. For instance in the paper [18], the integral observers with Expanding Window as well as Moving Window of Observation (sliding window) and their differential versions were given. In [16] the application of Moving Window Observer (MWO) and LQR to stabilization of distillation column was presented. In [19, 20] the authors presented the use of the double window exact state observer for detection and isolation of abrupt faults in system parameters.

The most important properties and features of the integral observers used for the exact reconstruction of the continuous state are

- (i) problem was formulated for Multi-Input Multi-Output (MIMO) continuous linear time invariant (LTI) systems given by the standard state matrix equation model,
- (ii) the state observer has integral description in space  $L^2[0, T]$  and can be used online (in interval  $[t-T, t]$ ),
- (iii) the possible existence of the disturbance in both the control  $u(t)$  and output  $y(t)$  signals is assumed,
- (iv) the optimal formulas of the observer are obtained by the minimization of its norm which is the function of assumed weighting coefficients,
- (v) the independence of the state observation from the initial conditions of the real state (unknown) occurs,
- (vi) fixed finite observation time interval  $[0, T]$  is used.

A brief explanation regarding the first point may be useful. The theory of the exact state observation in function space  $L^2[0, T]$  can use the idea of continuous functions and all the mathematical proofs as well as the final results relate

to continuous functions. However, of course for the real applications the term continuous measurements of such functions means that for computer calculations it is enough to have standard discrete measurements, although with frequency, according to Nyquist-Shannon sampling theorem. This establishes a sufficient condition for a sample rate that permits a discrete sequence of samples to capture all the information from a continuous-time signal of finite bandwidth. In that case numerical calculations of integrals, e.g., by Simpson's rule, will guarantee accuracy which will correspond to continuous version.

In this paper the quite new idea of the exact state observers application will be presented. Using two different exact state observers (with different norms) working simultaneously in parallel structure on the same time interval, it is possible to calculate the unknown values of some disturbances, which affect the input-output measurements. The calculation is possible either in the batch mode or in online observation version.

If in the input-output measurements the disturbances are absent (measurements of I/O signals are perfect), then two different observers reconstruct the exact and the same state  $x(T)$ . However, if in the measurement signals the disturbances are present ( $y+z_1$ ,  $u+z_2$ ) then the first observer reconstructs the value  $x_1(T)$  and the second  $x_2(T)$ . This is because the observers have different norms and in the case of disturbances they generate various errors  $e_1(T)$  and  $e_2(T)$ ; i.e., they generate the estimates  $x_1(T)=x(T)+e_1(T)$  and  $x_2(T)=x(T)+e_2(T)$ . The real undisturbed state  $x(T)$  is unknown, but it is easy to find the states difference  $\varepsilon(T) = x_1(T) - x_2(T) = e_1(T) - e_2(T)$ . It occurs that, based on this difference, the values of all the disturbances acting during the control process can be identified. In the next sections the first observer will be marked as the observer (a) and the second observer as the observer (b).

Such identification of disturbances cannot be performed using classical asymptotic state estimators like Kalman Filter, due to the unknown real value (even theoretical) of the state in both estimators. Such an approach, by the use of classical estimators (e.g., bank of Kalman Filters) for the disturbance isolation, was tested however in [21–23] with the use of “fault signatures” table. Other works [24–26] use disturbance distribution matrices and apply observers for diagnosis [27, 28].

In Section 2 we will start with a reminder of the theory of the exact state observation and the application of such observers in online mode.

## 2. The General and Optimal Form of the Exact Integral Observer in $L^2[0,T]$ Space

*2.1. The Existence Conditions of the Exact Observer.* Let a linear state observable MIMO system be given

$$\begin{aligned} \dot{x}(t) &= Ax(t) + Bu(t) \\ y(t) &= Cx(t) \end{aligned} \quad (1)$$

where  $x(t) \in \mathbb{R}^n$ ,  $u(t) \in \mathbb{R}^r$ , and  $y(t) \in \mathbb{R}^m$  for  $\forall t \geq 0$ ,  $m < n$ . Matrices  $A, B, C$  are of compatible dimensions.

Assume that we perfectly measure the control  $u$  and the output  $y$  on the interval  $[0, T]$ , where  $T$  is the fixed observation time.

Our purpose is to determine the state  $x(T)$ . We assume the following.

The state space  $X = \mathbb{R}^n$  (for state vectors), the output space  $Y = (L^2(0, T))^m$  (for output functions  $y \in Y$ ), and the control space  $U = (L^2(0, T))^r$  (for input functions,  $u \in U$ ). The output of the system (1) has the well-known form

$$y(t) = Ce^{-A(T-t)}x(T) - C \int_t^T e^{A(t-s)}Bu(s) ds \quad (2)$$

The general exact state observer should have the form of two inner products in  $L^2[0,T]$ :

$$x(T) = \int_0^T G_1(T, \tau) y(\tau) d\tau + \int_0^T G_2(T, \tau) u(\tau) d\tau \quad (3)$$

where the dimensions of matrices  $G_1(T, \tau)$  and  $G_2(T, \tau)$  are  $(n \times m)$  and  $(n \times r)$ , respectively. The elements of these matrices are functions of time  $\tau \in [0, T]$ . They are also functions of assumed observation time  $T$ . However in the sequel we will omit the first argument  $T$  in writing,  $G_1(\tau)$ ,  $G_2(\tau)$ .

For these assumptions, the general conditions for the observation matrices  $G_1, G_2$  should be determined, in such a manner that formula (3) could represent an accurate state observer. To this end, one must substitute (2) to (3). We obtain

$$\begin{aligned} x(T) &= \int_0^T G_1(T, \tau) Ce^{-A(T-\tau)} d\tau \cdot x(T) \\ &\quad - \int_0^T G_1(T, \tau) C \left[ \int_\tau^T e^{A(\tau-s)} Bu(s) ds \right] d\tau \\ &\quad + \int_0^T G_2(T, \tau) u(\tau) d\tau \end{aligned} \quad (4)$$

or after changing the order of integration in internal integral

$$\begin{aligned} x(T) &= \int_0^T G_1(T, \tau) Ce^{-A(T-\tau)} d\tau \cdot x(T) \\ &\quad - \int_0^T \left[ \int_0^s G_1(T, \tau) Ce^{A(\tau-s)} B d\tau \right] u(s) ds \\ &\quad + \int_0^T G_2(T, \tau) u(\tau) d\tau \end{aligned} \quad (5)$$

The left hand side of the above equation is equal to right hand side if and only if matrices  $G_1$  and  $G_2$  fulfill conditions

$$\int_0^T G_1(\tau) Ce^{-A(T-\tau)} d\tau = I, \quad (6)$$

where  $I$  is  $n \times n$  identity matrix and

$$G_2(\tau) = \int_0^\tau G_1(s) Ce^{-A(\tau-s)} B ds. \quad (7)$$

Equation (6) should be treated as the constraint for all possible observation matrices  $G_1(\tau)$  in (3). For the chosen

matrix  $G_1$ , the matrix  $G_2$  should fulfill the second constraint (7). For the observable linear system (1) there is infinite number of  $G_1, G_2$  matrix pairs which fulfill (6) and (7) and are matrices for exact observation in (3). Therefore, one can additionally assume some quality index and find the observer, which will fulfill the minimum of this index. A very reasonable quality index of observation is the observer's norm.

**2.2. Interpretation of the Observer Norm.** Any exact state observer perfectly reconstructs the state of the system (1) regardless of the initial or final conditions, if no disturbances occur in the input-output measurements. Otherwise, any exact state observer will reconstruct the state with some observation error. If the observer norm will be minimal, the norm of observation error will be also minimal (under some assumptions). Let us assume that in measurements  $y$  and  $u$  additive bounded norm disturbances occur,  $z_1 \in L^2[0, T]$ ,  $z_2 \in L^2[0, T]$ ,  $\|z_1\| \leq 1$ , and  $\|z_2\| \leq 1$ .

Then the state estimate is given by

$$\hat{x}(T) = \int_0^T G_1^o(y + z_1) d\tau + \int_0^T G_2^o(u + z_2) d\tau \quad (8)$$

Hence, the vector of the state reconstruction errors will have a value:

$$\varepsilon(T) = \int_0^T G_1^o(\tau) z_1(\tau) d\tau + \int_0^T G_2^o(\tau) z_2(\tau) d\tau. \quad (9)$$

We can estimate the norm of the error  $\|\varepsilon\|$  in the space  $L^2[0, T]$  assuming that disturbances are bounded and normalized to unit balls in  $L^2[0, T]$ ,  $\|z_1\| \leq 1$ , and  $\|z_2\| \leq 1$ . Inner product is denoted by  $\langle \bullet | \bullet \rangle$ .

$$\begin{aligned} \max_{(z_1, z_2)} \|\varepsilon\|_{R^n}^2 &= \max_{(z_1, z_2)} \|\langle G_1 | z_1 \rangle + \langle G_2 | z_2 \rangle\|_{R^n}^2 \\ &\leq 2 \left[ \|G_1\|_Y^2 + \|G_2\|_U^2 \right] = 2 \|(G_1, G_2)\|_{Y \times U}^2 \quad (10) \\ &= 2J \end{aligned}$$

Such assumed observer's norm  $J$  estimates maximal observation error in most pessimistic scenario. This min-max approach gives interpretation of the optimization task.

$$\min_{(G_1, G_2)} J = J^o \quad (11)$$

Obviously, an observer with a minimum norm still exactly reconstructs the state in the case of perfect and undisturbed input-output measurements.

**2.3. The Exact State Observer with Minimal Norm.** From continuity and linearity in (6) and (7), it follows that the set of all observers (pairs of matrices  $G_1, G_2$ ) is closed, linear manifold in the space  $Y^n \times U^n$

$$Y^n \times U^n = [L^2[0, T]]^{m \times n} \times [L^2[0, T]]^{r \times n}. \quad (12)$$

In this space one can introduce a seminorm of the observer like in (13):

$$\begin{aligned} \|(G_1, G_2)\|^2 &= \int_0^T \left[ \sum_{i=1}^n \alpha_i \sum_{j=1}^m (g_1^{ij}(\tau))^2 + \sum_{i=1}^n \beta_i \sum_{j=1}^r (g_2^{ij}(\tau))^2 \right] d\tau \quad (13) \\ &= J \end{aligned}$$

where  $g_1^{ij}(\tau), g_2^{ij}(\tau)$  are  $i$ -th row and  $j$ -th column elements of matrices  $G_1, G_2$  and  $\alpha_i, \beta_i$  are weighting coefficients for the whole  $i$ -th rows of corresponding matrices.

For simplification (without loss of generality) we will assume identity weighting coefficients  $\alpha_i = 1$ . The weight  $\beta$  may be interpreted as the relative norm of the possible disturbance  $z_2$ . The task of the optimization is minimization of the norm

$$J^o = \min_{(G_1, G_2)} J, \quad (14)$$

under constraints (6) and (7). The norm (13) of the observer is the function of observation time  $T$ .

Because of (6) the Lagrange functional is of the form

$$L = J + 2 \sum_{i=1}^n \left[ \left[ e_i^T - \left[ \langle g_1^i, h_1^1 \rangle, \dots, \langle g_1^i, h_1^n \rangle \right] \right] \cdot \lambda_i \right] \quad (15)$$

- (i) where  $e_i$  are basis vectors in  $R^n$  with one in  $i$ -th row,
- (ii)  $g_1^i$  denotes column vector which is transposition of  $i$ -th row of matrix  $G_1$ ,
- (iii)  $h_1^i$  denotes  $i$ -th column vector of matrix  $Ce^{-A(T-t)}$ ,
- (iv) the symbol  $\langle g_1^i, h_1^i \rangle$  stands for the integral inner products,
- (v)  $\lambda_i \in R^n$  are vectors of Lagrange multipliers.

From constraint (7) it follows that the squared norm  $J$  and hence Lagrange functional  $L$  are functions of matrix  $G_1$  rows  $g_1^i$ , only.

Hence from optimality condition  $\delta L / \delta g_1^i = 0$  after some calculation one can obtain the main formula

$$G_1^i(t) = - \int_t^T Ce^{A(t-\tau)} B G_2^i(\tau) d\tau \beta + Ce^{-A(T-t)} \lambda \quad (16)$$

- (i) where  $\beta$  is diagonal matrix with  $\beta_i$  elements,
- (ii)  $\lambda$  is Lagrange multipliers matrix with vector columns  $\lambda_i$ ,
- (iii) apostrophe ' denotes matrix transposition.

Transposition of (7) gives the result:

$$G_2^i(\tau) = \int_0^T B^i e^{-A(\tau-s)} C^i G_1^i(s) ds. \quad (17)$$

Equations (16) and (17) give the set of two integral equations, which can be solved. To this end let us notice that we

have some boundary relationships for rectangular matrices:

$$\begin{aligned} G_1'(T) &= C\lambda, \\ G_2(0) &= 0, \\ G_2(T) &= B. \end{aligned} \quad (18)$$

Let us introduce two square matrices  $P_1$  and  $P_2$  of  $[n \times n]$  dimension.

$$\begin{aligned} G_1'(t) &= CP_1'(t), \\ G_2'(t) &= BP_2'(t) \end{aligned} \quad (19)$$

Then one can obtain two new equations:

$$P_1'(t) = e^{-A(T-t)}\lambda - \int_t^T e^{A(t-\tau)}BBP_2'(\tau) d\tau \cdot \beta \quad (20)$$

$$P_2'(t) = \int_0^t e^{-A'(t-\tau)}C'CP_1'(\tau) d\tau \quad (21)$$

with boundary condition:

$$\begin{aligned} P_1'(T) &= \lambda, \\ P_2(0) &= 0, \\ P_2'(T) &= I. \end{aligned} \quad (22)$$

It is easy to see that (20) represent the solution of two differential equations.

$$\begin{aligned} \dot{P}_1'(t) &= AP_1'(t) + BBP_2'(t)\beta \\ \dot{P}_2'(t) &= C'CP_1'(t) - A'P_2'(t) \end{aligned} \quad (23)$$

with the above mentioned mixed boundary conditions.

Denote by  $p_1^i(t), p_2^i(t)$  the columns of matrices  $P_1'(t), P_2'(t)$ , and introduce fundamental matrices  $\Phi_i(t)$ , for  $i = 1, \dots, n$ .

$$\Phi_i(t) = e^{W_i t} = \begin{bmatrix} \Phi_{11}^i(t) & \Phi_{12}^i(t) \\ \Phi_{21}^i(t) & \Phi_{22}^i(t) \end{bmatrix} \quad (24)$$

$$\text{where } W_i = \begin{bmatrix} A & \beta_i BB \\ C'C & -A' \end{bmatrix}. \quad (25)$$

And under the condition  $p_2^i(0) = 0$ , we have the solution of (23) for  $2n$  dimensional problem:

$$\begin{aligned} \begin{bmatrix} p_1^i(t) \\ p_2^i(t) \end{bmatrix} &= \begin{bmatrix} \Phi_{11}^i(t) & \Phi_{12}^i(t) \\ \Phi_{21}^i(t) & \Phi_{22}^i(t) \end{bmatrix} \begin{bmatrix} p_1^i(0) \\ p_2^i(0) \end{bmatrix} \\ &= \begin{bmatrix} \Phi_{11}^i(t) & \Phi_{12}^i(t) \\ \Phi_{21}^i(t) & \Phi_{22}^i(t) \end{bmatrix} \begin{bmatrix} p_1^i(0) \\ 0 \end{bmatrix} \\ &= \begin{bmatrix} \Phi_{11}^i(t) & p_1^i(0) \\ \Phi_{21}^i(t) & p_1^i(0) \end{bmatrix} \end{aligned} \quad (26)$$

One can find initial conditions for  $p_1^i(0)$  by substitution (26) to the constraint (6).

$$\begin{aligned} \int_0^T e^{-A'(T-\tau)}C'C [\Phi_{11}^1(\tau)p_1^1(0), \dots, \Phi_{11}^n(\tau)p_1^n(0)] d\tau \\ = I \end{aligned} \quad (27)$$

Hence denote  $n$  different square matrices by  $M_i, i=1, \dots, n$ :

$$\begin{aligned} M_i &= \int_0^T e^{-A'(T-\tau)}C'C\Phi_{11}^i(\tau) d\tau \\ M_i^{-1} &= \left[ \int_0^T e^{A'\tau}C'C\Phi_{11}^i(\tau) d\tau \right]^{-1} e^{A'T}. \end{aligned} \quad (28)$$

$$\text{Then } M_i = \left[ \int_0^T \Phi_{11}^i(\tau) C'Ce^{A\tau} d\tau \right] e^{-AT},$$

$$\text{and } M_i^{-1} = e^{AT} \left[ \int_0^T \Phi_{11}^i(\tau) C'Ce^{A\tau} d\tau \right]^{-1}.$$

The initial conditions have the form

$$\begin{aligned} M_1 p_1^1(0) &= [1 \ 0 \ \dots \ 0]^T, \\ M_2 p_1^2(0) &= [0 \ 1 \ \dots \ 0]^T, \\ &\vdots \\ M_n p_1^n(0) &= [0 \ 0 \ \dots \ 1]^T. \end{aligned} \quad (29)$$

Finally, the solution for columns of matrices  $P_1'(t), P_2'(t)$  has the form

$$\begin{aligned} p_1^i(t) &= \Phi_{11}^i(t) [M_i']^{-1} e_i \\ p_2^i(t) &= \Phi_{21}^i(t) [M_i']^{-1} e_i \end{aligned} \quad (30)$$

where  $e_i$  are basis vectors in  $R^n$  with one on  $i$ -th row.

The vectors  $p_1^i(t), p_2^i(t)$  after transposition will form the rows of optimal matrices  $G_1^0(t)$  and  $G_2^0(t)$  according to equations

$$\begin{aligned} G_1^0(t) &= P_1(t)C', \\ G_2^0(t) &= P_2(t)B \end{aligned} \quad (31)$$

It is the most general optimal form of the exact state observer with minimal norm (13) and weighting coefficients  $\beta_i$ .

**2.4. Two Special Cases of Minimal Norm Observer.** Two cases will be considered:

- (a) The weighting coefficients  $\beta=I$  form unity matrix. This is reasonable case if in the measurements of the output  $y(t)$  and the input control  $u(t)$  the norms of the possible disturbances are the same.
- (b) The weighting coefficients  $\beta=0$ . This is reasonable case if in measurement of the control  $u(t)$  the disturbances are absent.

*The Solution to the Case (a).* For symmetric case  $\beta=I$ , the solution of the optimization task has simpler and more compact form than (30) and (31).

$$\begin{aligned} G_{1a}^o(T, \tau) &= M^{-1} \Phi_{11}'(\tau) C' \\ G_{2a}^o(T, \tau) &= M^{-1} \Phi_{21}'(\tau) B. \end{aligned} \quad (32)$$

All the matrices  $M_i$  are the same  $M=M_i$  and  $M^{-1}$  has the form

$$M = \left[ \int_0^T \Phi_{11}'(\tau) C' C e^{A\tau} d\tau \right] e^{-AT} \quad (33)$$

$$M^{-1} = e^{AT} \left[ \int_0^T \Phi_{11}'(\tau) C' C e^{A\tau} d\tau \right]^{-1} \quad (34)$$

Two submatrices  $\Phi_{11}(\tau)$ ,  $\Phi_{21}(\tau)$  of the fundamental matrix  $\Phi(\tau)$  are calculated from (35):

$$\begin{aligned} W &= \begin{bmatrix} A & BB' \\ C'C & -A' \end{bmatrix}, \\ \Phi(t) &= e^{Wt} = \begin{bmatrix} \Phi_{11}(t) & \Phi_{12}(t) \\ \Phi_{21}(t) & \Phi_{22}(t) \end{bmatrix} \end{aligned} \quad (35)$$

Then, matrices  $G$  (32) for the given observation time  $T$  can be calculated offline in interval  $[0, T]$  and applied online in optimal observer moving window [2].

*The Solution to the Case (b).* For the special values of weight factors  $\beta=0$ , one can obtain from (25) the special form of the exact state observer. It means that one can obtain this form of the observer (3) by minimization of simplified form of the norm (13) which corresponds only to the output  $y$  measurements. It is reasonable case if in the measurement of the control signal  $u(t)$  the disturbances are absent.

$$\|(G_{1b})\|^2 = \int_0^T \left[ \sum_{i=1}^n \sum_{j=1}^m (g_1^{ij}(\tau))^2 \right] d\tau. \quad (36)$$

Equation (23) takes the form

$$\dot{P}_1'(t) = AP_1'(t) \quad (37)$$

$$\dot{P}_2'(t) = C'CP_1'(t) - A'P_2'(t)$$

$$P_1'(T) = \lambda,$$

$$P_2(0) = 0, \quad (38)$$

$$P_2'(T) = I.$$

The solution for matrices  $P_1'(t)$ ,  $P_2'(t)$  has the form

$$\begin{bmatrix} P_1'(t) \\ P_2'(t) \end{bmatrix} = \begin{bmatrix} e^{At} & 0 \\ \Phi_{21}(t) & e^{-A't} \end{bmatrix} \begin{bmatrix} P_1'(0) \\ P_2'(0) \end{bmatrix} \quad (39)$$

$$= \begin{bmatrix} e^{At} & P_1'(0) \\ \Phi_{21}(t) & P_1'(0) \end{bmatrix}$$

$$P_1'(t) = e^{At} P_1'(0), \quad (40)$$

$$P_1(t) = P_1(0) e^{A't}$$

One can find the initial conditions in (40) by substitution of (40) to the constraint (6) remembering that

$$\int_0^T G_1(\tau) C e^{-A(T-\tau)} d\tau = I, \quad (41)$$

$$G_1(t) = P_1(t) C',$$

$$G_2(t) = P_2(t) B$$

Hence,

$$P_1(0) \int_0^T e^{A'\tau} C' C e^{A\tau} d\tau \cdot e^{-AT} = I$$

$$P_1(0) = e^{AT} \left[ \int_0^T e^{A'\tau} C' C e^{A\tau} d\tau \right]^{-1}. \quad (42)$$

$$P_1(t) = P_1(0) e^{A't} = e^{AT} \left[ \int_0^T e^{A'\tau} C' C e^{A\tau} d\tau \right]^{-1} \cdot e^{A't}$$

Let us assume that the square matrix  $M$  with symmetric Gram matrix  $M_G$  has a form as in (33)

$$M = \int_0^T e^{A'\tau} C' C e^{A\tau} d\tau \cdot e^{-AT} = M_G \cdot e^{-AT}$$

$$M^{-1} = e^{AT} M_G^{-1}, \quad (43)$$

$$[M^{-1}]' = M_G^{-1} e^{A'T}$$

Then  $P_1(0) = M^{-1}$  and  $P_1'(T) = \lambda = e^{AT} P_1'(0) = e^{AT} [M^{-1}]'$

$$P_1'(t) = e^{At} \cdot P_1'(0) = e^{At} \cdot [M^{-1}]' \quad (44)$$

For  $P_2(0) = 0$ , the solution for  $P_2$  from (37) and (44) is

$$\begin{aligned} P_2'(t) &= \int_0^t e^{-A'(t-\tau)} C' C P_1'(\tau) d\tau \\ &= \int_0^t e^{-A'(t-\tau)} C' C e^{A\tau} d\tau P_1'(0) \\ &= e^{-A't} \int_0^t e^{A'\tau} C' C e^{A\tau} d\tau [M^{-1}]' \end{aligned} \quad (45)$$

From the above the form of  $\Phi_{21}(t)$  in (39) is visible.

Finally we have the matrices P

$$\begin{aligned} P_1(t) &= M^{-1} e^{A't} = e^{AT} M_G^{-1} e^{A't} \\ P_2(t) &= M^{-1} \int_0^t e^{A'\tau} C' C e^{A\tau} d\tau \cdot e^{-At} \\ &= e^{AT} M_G^{-1} \int_0^t e^{A'\tau} C' C e^{A\tau} d\tau \cdot e^{-At} \end{aligned} \quad (46)$$

and we have the matrices  $G_1$  and  $G_2$  (marked finally as  $G_{1b}$ ,  $G_{2b}$ ) of the optimal observer for the case (b):

$$G_{1b}(t) = e^{AT} M_G^{-1} e^{A't} C', \quad (47)$$

$$G_{2b}(t) = e^{AT} M_G^{-1} \int_0^t e^{A'\tau} C' C e^{A\tau} d\tau \cdot e^{-At} B. \quad (48)$$

For the observation time  $T$ , these matrices can be calculated offline in interval  $[0, T]$  in as many samples as needed and then applied online in the observer moving window.

Interestingly, the same forms of  $G_1$ ,  $G_2$  as in (47), (48) can be obtained by using the easy and standard least squares approach, i.e., by the multiplying of both sides of the output equation (2) by the transposition of the appropriate matrix and integration of this equation on  $[0, T]$ .

$$\begin{aligned} &\int_0^T e^{-A'(T-t)} C' y(t) dt \\ &= \int_0^T e^{-A'(T-t)} C' C e^{-A(T-t)} dt \cdot x(T) \\ &\quad - \int_0^T \left[ e^{-A'(T-t)} C' C \int_t^T e^{A(t-s)} B u(s) ds \right] dt \end{aligned} \quad (49)$$

Then after changing the order of integration in internal integral we obtain the matrices  $G$  as in (47) and (48) and those of the form of the observer for the case (b):

$$x(T) = \int_0^T G_{1b}(\tau) y(\tau) d\tau + \int_0^T G_{2b}(\tau) u(\tau) d\tau. \quad (50)$$

It confirms the correctness of all the above derived formulas (47) and (48) and the general theory of the optimal observation (30), (31).

By the way, it means that the use of the above version of the observers in different applications of the exact state observers [12–14] may give the result, which is not in general the optimal observation solution, but only for the special observer norm (36).

In authors' research, it turned out that the norm (13) of the observer decreases to some small value with increasing of the observation time  $T$  and increases to infinity with decreasing of time  $T$  to zero, like in Figure 1.

$$\begin{aligned} \text{for } T \rightarrow \infty, \quad \|(G_1, G_2)\|(\infty) &\rightarrow \text{small value} \\ \text{for } T \rightarrow 0 \quad \text{the norm } \|(G_1, G_2)\|(0) &\rightarrow \infty, \end{aligned} \quad (51)$$

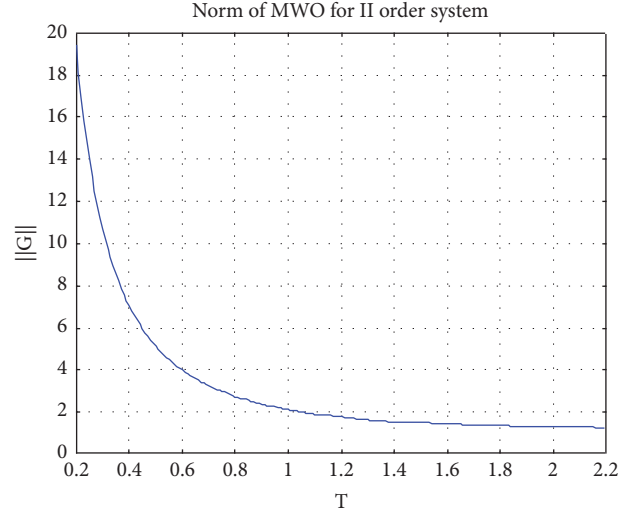


FIGURE 1: An exemplary shape of the norm, as the function of observation time  $T$ , for the second-order system.

### 3. Integral Observers in Online Mode as Moving Window Observers

Presented integral form of the exact observers given on finite time interval  $[0, T]$

$$x(T) = \int_0^T G_1(\tau) y(\tau) d\tau + \int_0^T G_2(\tau) u(\tau) d\tau \quad (52)$$

can be applied in online observation and in control systems.

To this end one can design the structure of Moving Window Observer (MWO). Equation (52) is valid for any linear time invariant (LTI) systems and for any fragment of measured functions  $y$  and  $u$  and hence for shifted input/output functions, also.

One can use two possible representations of MWSO at time  $t$ :

$$\begin{aligned} x(t) &= \int_0^T G_1(\tau) y(t - T + \tau) d\tau \\ &\quad + \int_0^T G_2(\tau) u(t - T + \tau) d\tau \end{aligned} \quad (53)$$

$$\begin{aligned} x(t) &= \int_{t-T}^t G_1(T - t + \tau) y(\tau) d\tau \\ &\quad + \int_{t-T}^t G_2(T - t + \tau) u(\tau) d\tau \end{aligned} \quad (54)$$

The form (54) represents moving window of width  $T$  shifted along time axis against measurements and after integrals calculations giving current and exact state  $x(t)$  for  $t \geq T$ . Such type of the observer has characteristic delay in starting of the observation connected with the first window for  $0 \leq t \leq T$ .

The matrices  $G_1$ ,  $G_2$  do not depend on current time  $t$  and can be calculated only once and offline in interval  $[0, T]$ . Then they may be stored in memory registers in as many samples as needed for accurate calculation of integrals, depending on discretization time of measurements of  $y$  and  $u$ .

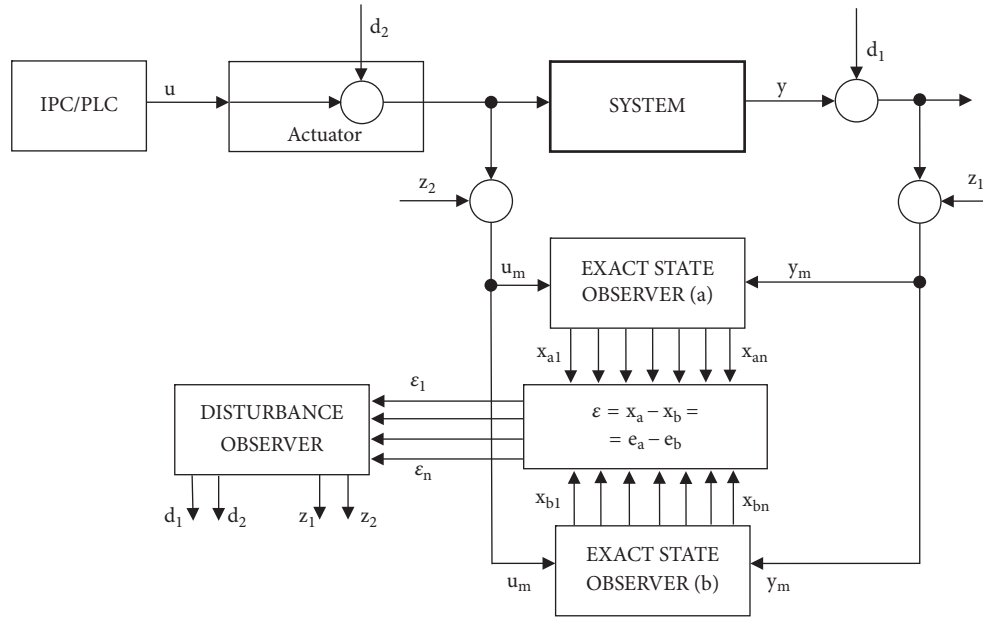


FIGURE 2: The system for reconstruction of disturbances.

Digital control equipment should have enough computation power for online calculation of thousands of multiplications and summations per second. For the nowadays industrial computers (IPC) this is no problem, let alone for those with digital signal processors (DSP).

During designing of the observer, the main problem is the right choice of the observation time  $T$ . The short interval  $T$  results in quick start of the online state reconstruction process and requires fewer calculations during the moving window mode but the observer is more highly sensitive to the disturbances (has the bigger norm). The longer time  $T$  results in bigger time delay in starting of observation and causes more calculations within the window but the observer is less sensitive to disturbances (has the smaller norm).

#### 4. The Main Idea of the Paper

Let a linear state observable system be given

$$\begin{aligned}\dot{x}(t) &= Ax(t) + Bu(t) \\ y(t) &= Cx(t)\end{aligned}\quad (55)$$

We will consider the case of Single Input–Single Output (SISO) system; however one can generalize the disturbances detection method to Multi-Input Multi-Output case. The system is of  $n$ -th order, the state  $x(t) \in \mathbb{R}^n$ , the control  $u(t) \in \mathbb{R}^1$ , and the output  $y(t) \in \mathbb{R}^1$ , for  $\forall t \geq 0$ . Matrices  $A$ ,  $B$ ,  $C$  are of compatible dimensions.

Assume that we perfectly measure the control  $u$  and the output  $y$  (without any disturbances) on the interval  $[0, T]$ , where  $T$  is the fixed observation time.

For the exact state observation, we will use simultaneously working two observers (a), (32), (33), (35) and (b), (47), (48).

Both observers reconstruct the exact state  $x_a(T) = x_b(T) = x(T)$ .

However, if during control process the disturbances  $d_2$  of the control and disturbances  $d_1$  of the output occur and the measurement noises occur (measurement disturbances on input-output  $z_2, z_1$ ), then we have a situation like in Figure 2.

Our purpose is to determine the state  $x_a(T) = x(T) + e_a(T)$ ,  $x_b(T) = x(T) + e_b(T)$  and the disturbance values  $d$  and  $z$ , based on the measurement signals  $y_m(t)$  and  $u_m(t)$ .

The equation of the disturbed system has the form

$$\begin{aligned}\dot{x}(t) &= Ax(t) + B[u(t) + d_2(t)] \\ y(t) &= Cx(t),\end{aligned}\quad (56)$$

and the reconstructed state is given by two equations, one from the observer (a) (the pair of matrices  $G_{1a}, G_{2a}$ ) and the second from the observer (b) (the pair of matrices  $G_{1b}, G_{2b}$ ). Both observers use for the state calculations the disturbed measurements,

$$\begin{aligned}y_m(t) &= y(t) + d_1(t) + z_1(t), \\ u_m(t) &= u(t) + d_2(t) + z_2(t)\end{aligned}\quad (57)$$

Control  $u(t) \in \mathbb{R}^1$ , the output  $y(t) \in \mathbb{R}^1$ , disturbances  $d_1(t) \in \mathbb{R}^1$ ,  $d_2(t) \in \mathbb{R}^1$ ,  $z_1(t) \in \mathbb{R}^1$ ,  $z_2(t) \in \mathbb{R}^1$ , for  $\forall t \geq 0$

The control signal  $u(t)$  is known, because it is generated by the deterministic control algorithm in industrial PC or Programmable Logic Controller (PLC).

The algorithm of disturbance detection is presented in Figure 2.

The reconstructed state  $x_a(T)$  by the observer (a):

$$\begin{aligned}x_a(T) &= \int_0^T G_{1a}(\tau) y_m(\tau) d\tau + \int_0^T G_{2a}(\tau) u_m(\tau) d\tau \\ &= \int_0^T G_{1a}(\tau) [y(\tau) + d_1(\tau) + z_1(\tau)] d\tau\end{aligned}$$

$$\begin{aligned}
 & + \int_0^T G_{2a}(\tau) [u(\tau) + d_2(\tau) + z_2(\tau)] d\tau \\
 & = x(T) + e_a(T)
 \end{aligned} \tag{58}$$

The reconstructed state  $x_b(T)$  by the observer (b):

$$\begin{aligned}
 x_b(T) &= \int_0^T G_{1b}(\tau) y_m(\tau) d\tau + \int_0^T G_{2b}(\tau) u_m(\tau) d\tau \\
 &= \int_0^T G_{1b}(\tau) [y(\tau) + d_1(\tau) + z_1(\tau)] d\tau \\
 & \quad + \int_0^T G_{2b}(\tau) [u(\tau) + d_2(\tau) + z_2(\tau)] d\tau \\
 &= x(T) + e_b(T)
 \end{aligned} \tag{59}$$

Taking into account the fact that the real state  $x(T)$  in (56) is given by

$$\begin{aligned}
 x(T) &= \int_0^T G_{1a}(\tau) y(\tau) d\tau \\
 & \quad + \int_0^T G_{2a}(\tau) [u(\tau) + d_2(\tau)] d\tau,
 \end{aligned} \tag{60}$$

as well as

$$\begin{aligned}
 x(T) &= \int_0^T G_{1b}(\tau) y(\tau) d\tau \\
 & \quad + \int_0^T G_{2b}(\tau) [u(\tau) + d_2(\tau)] d\tau,
 \end{aligned} \tag{61}$$

the difference of the estimated states (58), (59) gives the estimation error  $\varepsilon(T)$ .

$$\begin{aligned}
 \varepsilon(T) &= x_a(T) - x_b(T) \\
 &= \int_0^T [G_{1a}(\tau) - G_{1b}(\tau)] [d_1(\tau) + z_1(\tau)] d\tau \\
 & \quad + \int_0^T [G_{2a}(\tau) - G_{2b}(\tau)] [z_2(\tau)] d\tau
 \end{aligned} \tag{62}$$

$$\varepsilon(T) \in R^n.$$

*The Main Assumption.* Let us assume that the values of the disturbances  $d_1, z_1, d_2, z_2$  within the interval  $T$  are constant.

Such assumption is reasonable if the interval  $T$  is small.

Let us mark two vector-matrices  $[nx1]$  for each observer, with the second indexes, which mean the numbers (items) of the state vector elements.

$$\begin{aligned}
 (G_{1a}, G_{2a}) &= \left( \begin{array}{c} [G_{11,a}(\tau)] \\ \vdots \\ [G_{1n,a}(\tau)] \end{array}, \begin{array}{c} [G_{21,a}(\tau)] \\ \vdots \\ [G_{2n,a}(\tau)] \end{array} \right), \\
 (G_{1b}, G_{2b}) &= \left( \begin{array}{c} [G_{11,b}(\tau)] \\ \vdots \\ [G_{1n,b}(\tau)] \end{array}, \begin{array}{c} [G_{21,b}(\tau)] \\ \vdots \\ [G_{2n,b}(\tau)] \end{array} \right)
 \end{aligned} \tag{63}$$

Then, we have from (62) the main equation for the estimation error.

$$\begin{aligned}
 \varepsilon(T) &= \begin{bmatrix} \varepsilon_1(T) \\ \vdots \\ \varepsilon_n(T) \end{bmatrix} \\
 &= \begin{bmatrix} \int_0^T [G_{11,a}(\tau) - G_{11,b}(\tau)] d\tau \\ \vdots \\ \int_0^T [G_{1n,a}(\tau) - G_{1n,b}(\tau)] d\tau \end{bmatrix} [d_1 + z_1] \\
 & \quad + \begin{bmatrix} \int_0^T [G_{21,a}(\tau) - G_{21,b}(\tau)] d\tau \\ \vdots \\ \int_0^T [G_{2n,a}(\tau) - G_{2n,b}(\tau)] d\tau \end{bmatrix} [z_2],
 \end{aligned} \tag{64}$$

or in compact form with the constant matrix  $D [nx2]$ :

$$\begin{bmatrix} \varepsilon_1(T) \\ \vdots \\ \varepsilon_n(T) \end{bmatrix} = \begin{bmatrix} \int_0^T [G_{11,a}(\tau) - G_{11,b}(\tau)] d\tau, & \int_0^T [G_{21,a}(\tau) - G_{21,b}(\tau)] d\tau \\ \vdots & \vdots \\ \int_0^T [G_{1n,a}(\tau) - G_{1n,b}(\tau)] d\tau, & \int_0^T [G_{2n,a}(\tau) - G_{2n,b}(\tau)] d\tau \end{bmatrix} \begin{bmatrix} d_1 + z_1 \\ z_2 \end{bmatrix} \tag{65}$$

$$\varepsilon(T) = D \begin{bmatrix} d_1 + z_1 \\ z_2 \end{bmatrix} = D\Theta \tag{66}$$

In this equation the vector of estimation error  $\varepsilon(T) \in \mathbb{R}^n$  is known as well as the rectangular and constant matrix  $D [n \times 2]$ . The unknown vector  $\Theta$  of two real numbers represents the values of unknown disturbances  $\Theta \in \mathbb{R}^2$ . These values  $\Theta$  are valid for the entire interval  $T$ .

Hence, for the system's order  $n=2$ ,  $D$  is the square matrix,  $D[2 \times 2]$ , and for the equation  $\varepsilon(T) = D\theta$ , we have the single solution for the vector of disturbances  $\Theta$ :

$$\Theta = D^{-1} \varepsilon(T) \quad (67)$$

For  $n > 2$ , the matrix  $D$  is rectangular  $D[n \times 2]$  and by the least squares approach it is easy to find that the best solution of (66) is given by

$$\Theta = [D'D]^{-1} D' \varepsilon(T) \quad (68)$$

$$\Theta = \begin{bmatrix} d_1 + z_1 \\ z_2 \end{bmatrix} \quad (69)$$

Then, it is easy to find that the disturbance  $d_2$  is given by

$$d_2 = u_m(t) - u(t) - z_2. \quad (70)$$

It turned out that the separation of the disturbance sum  $d_1 + z_1$  at the time  $T$  and the exact calculation of the constant values  $d_1, z_1$  is not possible by this method (see Conclusions).

## 5. The Moving Window Disturbances Observer

All the above considerations were carried out, for the one observation window  $[0, T]$  (batch mode).

If we use the idea of the Moving Window State Observer (53) working in online mode,

$$\begin{aligned} x(t) = & \int_0^T G_1(\tau) y_m(t - T + \tau) d\tau \\ & + \int_0^T G_2(\tau) u_m(t - T + \tau) d\tau \end{aligned} \quad (71)$$

then using two MWSO, for reconstruction of  $x_1(t)$  and  $x_2(t)$ , one can also design the Moving Window Disturbances Observer, for the online identification of the disturbances for  $t > T$ .

We can have continuous equation for the online reconstruction of the disturbances:

$$\Theta(t) = [D'D]^{-1} D' \varepsilon(t) \quad (72)$$

where

$$\varepsilon(t) = x_a(t) - x_b(t) \quad (73)$$

and the values of  $x_a(t)$  and  $x_b(t)$  are reconstructed online by the observers of type (71). The constant rectangular matrix  $D [n \times 2]$  is the same as in (66):

$$D = \begin{bmatrix} \int_0^T [G_{11,a}(\tau) - G_{11,b}(\tau)] d\tau, & \int_0^T [G_{21,a}(\tau) - G_{21,b}(\tau)] d\tau \\ \vdots & \vdots \\ \int_0^T [G_{1n,a}(\tau) - G_{1n,b}(\tau)] d\tau, & \int_0^T [G_{2n,a}(\tau) - G_{2n,b}(\tau)] d\tau \end{bmatrix} \quad (74)$$

The real matrix  $D$  as well as  $[D'D]^{-1} D'$  should be calculated offline for a given interval  $T$  only once (based on (32), (47), and (48)) and used during online calculation. Of course in practice each element of the observer function matrices  $G_1(t)$  and  $G_2(t)$  calculated offline must be stored in computer memory within  $[0, T]$ , e.g., as 100 samples, with  $\Delta=0.1$  sec each ( $T=10$  sec). The same samples time must apply to I/O signal measurement. These measurements may be delivered in online mode and final calculation of the observers integrals is performed in real time numerically in the last window  $[t-T, t]$  for each  $t$ , i.e., in numerical version  $[i\Delta-T, i\Delta]$  for each  $i$  (with the use of the best integration procedure, e.g., with Simpson's rule).

There is no real-time computation problem with online calculation of such Moving Window Observer based on (71), (72), and (73). The not very new processor Pentium 4 can perform 3 GFLOPS (floating point operations per 1 sec), i.e., 3 mln FLOP/ 1 msec, while Pentium Core i7 5960X – can perform even 300 GFLOPS. Assuming that PLC cycle time is about 100 msec (sampling time of measurements), it means that during this time Pentium 4 can perform 300 mln FLOP. Two integrals in one observer with two integral windows  $T$ , each sampled, e.g., 1000 times, need 2000 multiplications (1000 multiplications of each element, e.g.,  $G_{11a}(t)y(t)$ , and 1000 multiplications of each element, e.g.,  $G_{21a}(t)u(t)$ ) as well as 2000 summation (simplest calculation of integrals based on trapezoid rules). Hence, two observer's integrals need 8000 floating point operations for single function element. If the SISO system is of order  $n=10$  then the disturbance reconstruction (detection) needs computation power 80 000 FLOP in each sample. This is 3% of Pentium 4 power ratio. The above theoretical and simplified estimation of the computational capabilities of standard PCs has been presented only to justify the applicability of the MWO in the real industrial processes and in online mode. All numerical experiments in this article were carried out in the Matlab/Simulink environment in which numerical integration procedures are performed with the Simpson algorithm.

## 6. Numerical Example

All the simulation data used to support the findings of this study are included within the article.

Assume that second-order system is given.

$$\begin{aligned} \dot{x}(t) &= \begin{bmatrix} 0 & 1 \\ 0 & 0 \end{bmatrix} x(t) + \begin{bmatrix} 0 \\ 1 \end{bmatrix} u(t) \\ y(t) &= [2 \ 0] x(t) \end{aligned} \quad (75)$$

For this simple system, all the exact observer calculations can be done analytically.

$$\begin{aligned} e^{At} &= \begin{bmatrix} 1 & t \\ 0 & 1 \end{bmatrix}; \\ e^{A't} &= \begin{bmatrix} 1 & 0 \\ t & 1 \end{bmatrix}; \end{aligned}$$

$$M_G = \int_0^T e^{A't} C' C e^{At} dt = \int_0^T \begin{bmatrix} 4 & 4t \\ 4t & 4t^2 \end{bmatrix} dt \quad (76)$$

We will derive the exact state  $x(T)$  optimal observer formula, for two cases of weighting coefficients  $\beta=1$  and  $\beta=0$ .

*The Case of the Observer (a), the Weighting Coefficients  $\beta = 1$ .* After some longer calculations, one can obtain that submatrices  $\Phi_{11}(t)$  and  $\Phi_{21}(t)$  from (35) have the form

$$\Phi_{11}(t)$$

$$\begin{aligned} &= \begin{bmatrix} \cosh t \cos t, & \frac{1}{2} (\sinh t \cos t + \cosh t \sin t) \\ \sinh t \cos t - \cosh t \sin t, & \cosh t \cos t \end{bmatrix} \\ \Phi_{21}(t) &= \begin{bmatrix} 2 (\sinh t \cos t + \cosh t \sin t), & 2 \sinh t \sin t \\ -2 \sinh t \sin t, & \sinh t \cos t - \cosh t \sin t \end{bmatrix} \end{aligned} \quad (77)$$

Matrices  $M$  and  $M^{-1}$  from (33) have the form

$$\begin{aligned} M &= \begin{bmatrix} 2 \sinh T \cos T + 2 \cosh T \sin T, & -2 \sinh T \sin T \\ 2 \sinh T \sin T, & \sinh T \cos T - \cosh T \sin T \end{bmatrix} \\ M^{-1} &= \frac{1}{2 \sinh^2 T - 2 \sin^2 T} \begin{bmatrix} \sinh T \cos T - \cosh T \sin T, & 2 \sinh T \sin T \\ -2 \sinh T \sin T, & 2 (\sinh T \cos T + \cosh T \sin T) \end{bmatrix} \end{aligned} \quad (78)$$

The optimal observer matrices (in this case vectors)  $G_{1a}(t)$  and  $G_{2a}(t)$  within the interval  $[0, T]$  have the final form as in (32) and are visible in Figure 3.

$$G_{1a}(t) = M^{-1} \begin{bmatrix} 2 \cos(t) \cosh(t) \\ \cos(t) \sinh(t) + \sin(t) \cosh(t) \end{bmatrix}, \quad (79)$$

$$G_{2a}(t) = M^{-1} \begin{bmatrix} -2 \sin(t) \sinh t \\ \cos(t) \sinh(t) - \sin(t) \cosh(t) \end{bmatrix}, \quad (80)$$

and the observer (a) is given by

$$\begin{aligned} \begin{bmatrix} x_{1,a}(T) \\ x_{2,a}(T) \end{bmatrix} &= \int_0^T \begin{bmatrix} G_{11,a}(\tau) \\ G_{12,a}(\tau) \end{bmatrix} y(\tau) d\tau \\ &+ \int_0^T \begin{bmatrix} G_{21,a}(\tau) \\ G_{22,a}(\tau) \end{bmatrix} u(\tau) d\tau. \end{aligned} \quad (81)$$

The norm (13) of this observer is a function of interval  $T$

$$\|(G_{1a}, G_{2a})\|(T) = \sqrt{\frac{3 \sinh(2T) + \sin(2T)}{4(\sinh^2(T) - \sin^2(T))}}, \quad (82)$$

and as a function of  $T$  it is presented in Figure 1.

*The Case of the Observer (b), the Weighting Coefficients  $\beta = 0$ .* For this simpler case, the observer matrices are as (47), (48):

$$M^{-1} = \frac{1}{2T^3} \begin{bmatrix} -T^2 & 3T \\ -3T & 6 \end{bmatrix} \quad (83)$$

$$G_{1b}(t) = \frac{1}{T^3} \begin{bmatrix} 3Tt - T^2 \\ 6t - 3T \end{bmatrix}; \quad (84)$$

$$G_{2b}(t) = \frac{1}{T^3} \begin{bmatrix} T^2 t^2 - Tt^3 \\ 3Tt^2 - 2t^3 \end{bmatrix};$$

The optimal observer matrices (in this case vectors)  $G_{1b}(t)$  and  $G_{2b}(t)$  within the interval  $[0, T]$  have the final form as in (47), (48) and are visible in Figure 4.

The norm (13) of this observer is also function of interval  $T$

$$\|(G_{1b}, G_{2b})\|(T) = \sqrt{\frac{T^6 + 39T^4 + 105T^2 + 315}{105T^3}} \quad (85)$$

$$\begin{aligned} \begin{bmatrix} x_{1b}(T) \\ x_{2b}(T) \end{bmatrix} &= \int_0^T \begin{bmatrix} G_{11,b}(\tau) \\ G_{12,b}(\tau) \end{bmatrix} y(\tau) d\tau \\ &+ \int_0^T \begin{bmatrix} G_{21,b}(\tau) \\ G_{22,b}(\tau) \end{bmatrix} u(\tau) d\tau. \end{aligned} \quad (86)$$

The matrix (74) has the form

$$D = \begin{bmatrix} \int_0^T [G_{11,a}(\tau) - G_{11,b}(\tau)] d\tau, & \int_0^T [G_{21,a}(\tau) - G_{21,b}(\tau)] d\tau \\ \int_0^T [G_{12,a}(\tau) - G_{12,b}(\tau)] d\tau, & \int_0^T [G_{22,a}(\tau) - G_{22,b}(\tau)] d\tau \end{bmatrix} \quad (87)$$

It is easy to calculate numerically all elements of matrix differences, e.g.,  $G_{11,a}(\tau) - G_{11,b}(\tau)$ , on  $[0, T]$  and then integrate them obtaining the all real matrix  $D$   $[2 \times 2]$ , and so the matrix  $[D D]^{-1} D$   $[2 \times 2]$ , which in this case is directly equal to the real matrix  $D^{-1}$   $[2 \times 2]$ .

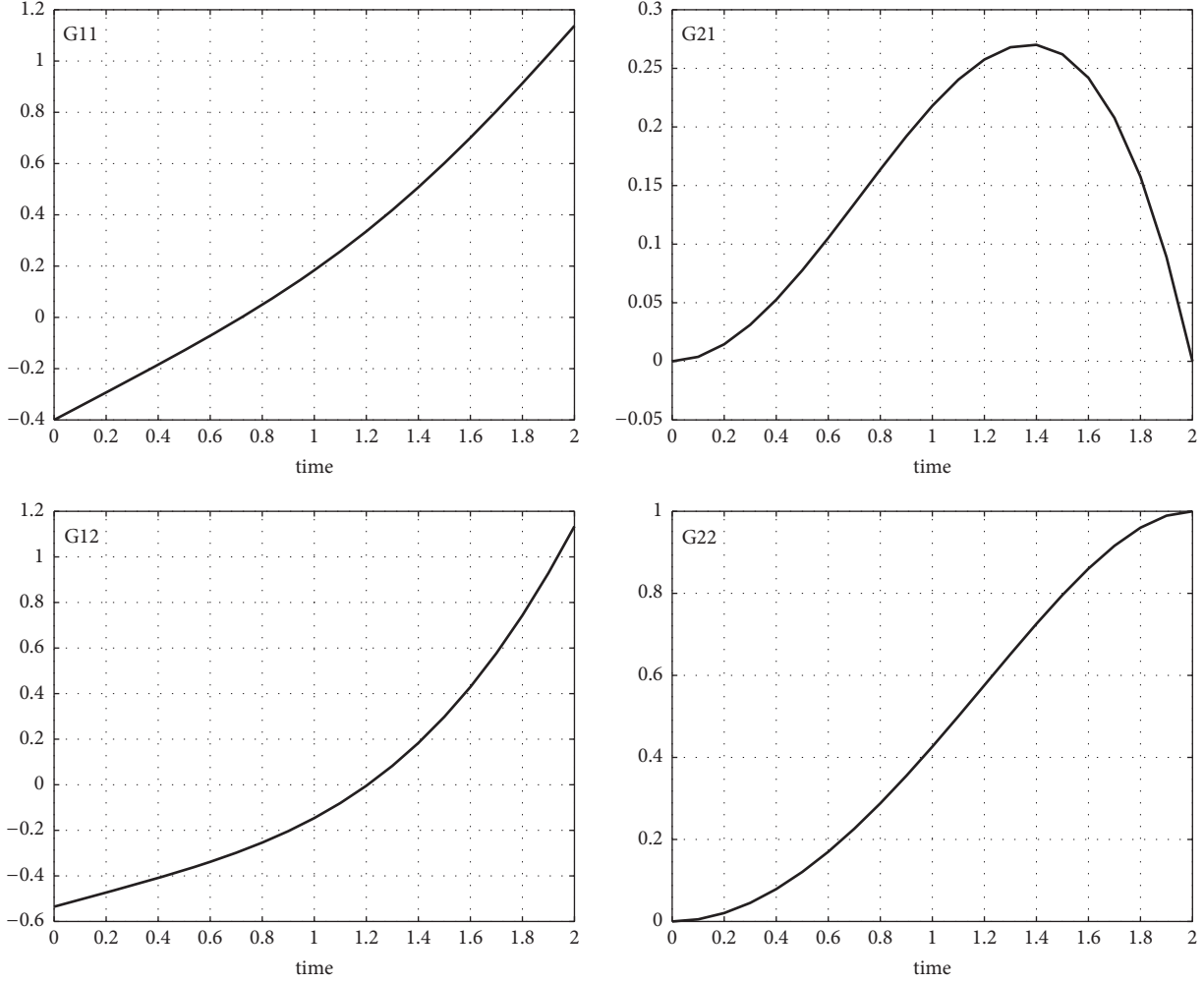


FIGURE 3: The shape of the matrix functions  $G_{11,a}$  and  $G_{12,a}$  as well as  $G_{21,a}$  and  $G_{22,a}$  of the observer (a), for  $T = 2$ .

The shapes of the integral functions (differences) in the matrix  $D$  are visible in Figure 5.

Assuming  $T=2$  and using (80) and (84) equations, one can calculate the real matrix  $D$  and  $\text{inv}(D)$  from (87),

$$D = \begin{bmatrix} 0.0005 & -0.0337 \\ 0.00153 & -0.0788 \end{bmatrix}, \quad (88)$$

$$D^{-1} = \begin{bmatrix} -6325,56 & 2709,57 \\ -123,11 & 40,06 \end{bmatrix},$$

Simulation of  $\varepsilon(T)$  using (58), (59) for some chosen  $u(t)$  as well as for some chosen constant disturbances has given value of the error

$$\varepsilon(2) = x_a(2) - x_b(2) = \begin{bmatrix} -0.0079 \\ -0.0182 \end{bmatrix}. \quad (89)$$

Hence, from (67)

$$\Theta = D^{-1} \varepsilon(2) = \begin{bmatrix} 1 \\ 0.25 \end{bmatrix} = \begin{bmatrix} d_1 + z_1 \\ z_2 \end{bmatrix}. \quad (90)$$

Assuming that  $z_1=z_2$ , we have  $d_1=0.75$ ,  $z_1=z_2=0.25$ . These values are the same as those assumed in simulation.

## 7. Conclusions

In the paper, the quite new methodology of identification of the unknown constant values of the disturbances acting in dynamical control system was presented. To this end, the theory and application of the exact state integral observers were used. The structure of the Moving Window Disturbance Observer, which consists of two MWO, is defined.

It is possible to identify exactly three values of disturbances  $d_1+z_1$ ,  $d_2$ ,  $z_2$ . However, there is also the possibility of identification of the disturbance  $d_1$  if we assume that constant values of the noises are the same;  $z_1=z_2$  (e.g., if the identified

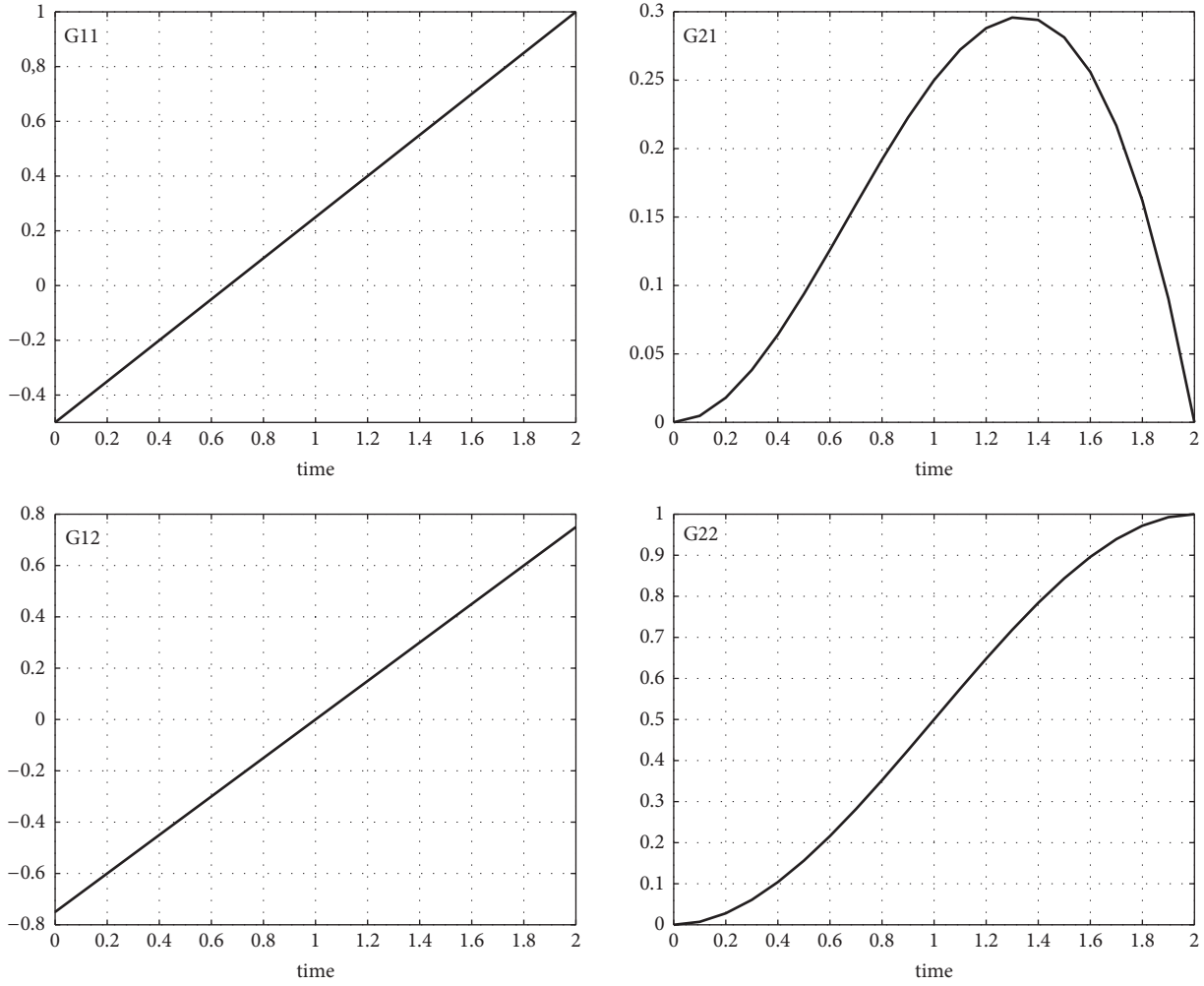


FIGURE 4: The shape of the matrix functions  $G_{11,b}$  and  $G_{12,b}$  as well as  $G_{21,b}$  and  $G_{22,b}$  of the observer (b), for  $T = 2$ .

value of  $z_2$  represents the mean value of the noise  $z_2(t)$  and the noise  $z_1(t)$  in the interval  $T$ ). Then

$$d_1 = (d_1 + z_1) - z_2. \tag{91}$$

For different signs of  $z_1$  and  $z_2$ , there is also possible estimation of the norm of  $\|d_1\|$ , if we assume that at least the norm of  $\|z_1\| = \|z_2\|$  in  $L^2[0, T]$  ( $z_2$  was calculated).

Because we know the value of  $d_1 + z_1$ , then we can calculate and estimate the norm  $\|d_1 + z_1\|$ ,

$$\|d_1 + z_1\| \leq \|d_1\| + \|z_1\|, \tag{92}$$

and estimate the norm of  $\|d_1\|$

$$\|d_1\| \geq \|d_1 + z_1\| - \|z_1\|. \tag{93}$$

If  $\|z_1\| = \|z_2\|$ , then for sure it is true that

$$\|d_1\| \geq \|d_1 + z_1\| - \|z_2\|. \tag{94}$$

Hence, because of the constant values of  $d_1, z_1, z_2$  we have

$$|d_1| = |d_1 + z_1| - |z_2| \tag{95}$$

or

$$|d_1| = |d_1 + z_1| + |z_2|. \tag{96}$$

In this paper the general conditions and formulas for the exact observers with minimal norm in  $L^2[0, T]$  spaces were recalled. In this problem, there is no need for the discussion about the convergence of the method. There is no differential equation (unlike in the Kalman Filter theory). All algorithms are based on integration operations on finite windows, and even for an unstable model, because, of the finite interval of the window, integrals cannot tend to infinity. With nondisturbed  $y$  and  $u$  measurements, the state of the unstable object will be still reconstructed exactly. In the case of disturbed measurements, there is an error in the reconstruction of the state, not due to the instability of the object, but due to measurement errors. Of course, one must assume that numerical Simpson procedures of integration are correct.

The numerical example (in Matlab/Simulink) confirms the correctness of this new method for the disturbance identification.

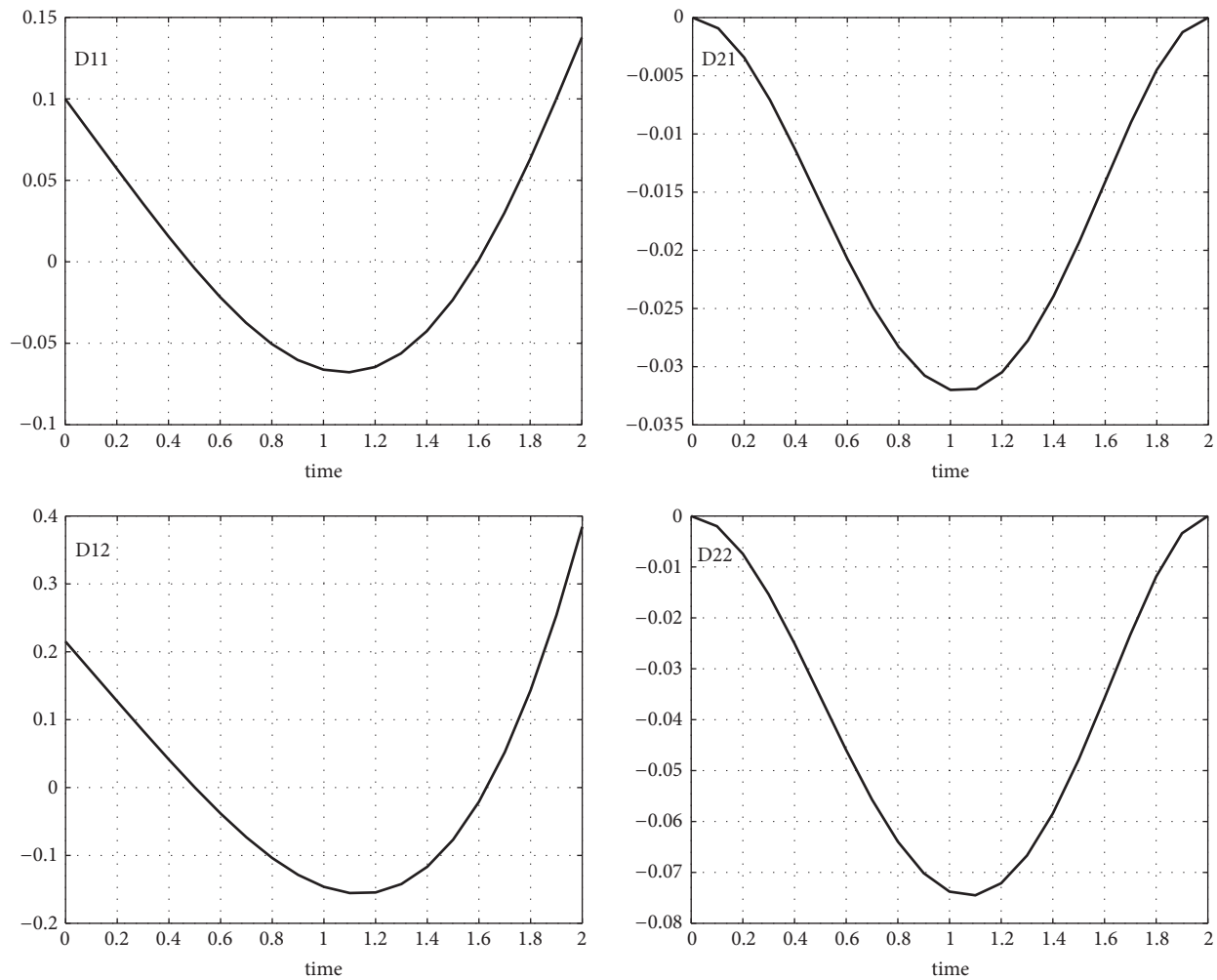


FIGURE 5: The shape of the integral functions  $D_{11}$ ,  $D_{12}$ ,  $D_{21}$ ,  $D_{22}$ .

## Data Availability

The data used to support the findings of this study are included within the article.

## Conflicts of Interest

The authors declare that they have no conflicts of interest.

## Acknowledgments

This work was supported by the scientific research funds from the Polish Ministry of Science and Higher Education within the AGH UST Agreements no 11.11.120.396 and 11.11.120.859.

## References

- [1] D. G. Luenberger, "Observers for Multivariable Systems," *IEEE Transactions on Automatic Control*, vol. 11, no. 2, pp. 190–197, 1966.
- [2] R. E. Kalman, "Contributions to the theory of optimal control," in *Proceedings of the Conf. on Ordinary Differential Equation*, vol. 5, Mexico City, 1959.
- [3] R. E. Kalman and R. S. Bucy, "New results in linear filtering and prediction theory," *Transactions of the ASME, Journal of Basic Engineering*, vol. 83, p. 95, 1961.
- [4] W. Byrski and S. Fuksa, "Optimal finite parameter observer. An application to synthesis of stabilizing feedback for a linear system," *Control and Cybernetics*, vol. 13, no. 1-2, pp. 73–83, 1984.
- [5] S. Fuksa and W. Byrski, "General Approach to Linear Optimal Estimator of Finite Number of Parameters," *IEEE Transactions on Automatic Control*, vol. 29, no. 5, pp. 470–472, 1984.
- [6] S. Rolewicz, "On optimal observability of linear systems with infinite-dimensional states," *Studia Mathematica*, vol. 44, pp. 411–416, 1972.
- [7] J. D. Gilchrist and J. D. Gilchrist, "n-Observability for Linear Systems," *IEEE Transactions on Automatic Control*, vol. 11, no. 3, pp. 388–395, 1966.
- [8] M. James, "Finite time observers and observability," in *Proceedings of the 29th IEEE Conference on Decision and Control*, vol. 2, pp. 770–771, Honolulu, HI, USA, 1990.
- [9] D. H. Chyung, "State variable reconstruction," *International Journal of Control*, vol. 39, no. 5, pp. 955–962, 1984.
- [10] F. Pourboghraat and D. H. Chyung, "Exact state-variable reconstruction of delay systems," *International Journal of Control*, vol. 44, no. 3, pp. 867–877, 1986.

- [11] M. Polities, "Exact state Reconstruction in deterministic digital control systems," Tech. Rep., NASA Technical Paper, 1987.
- [12] A. V. Medvedev and H. T. Toivonen, "Continuous finite-memory deadbeat observer," in *Proceedings of the American Control Conference*, p. 1800, 1992.
- [13] A. Medvedev, "Fault detection and isolation by functional continuous deadbeat observers," *International Journal of Control*, vol. 64, no. 3, pp. 425–439, 1996.
- [14] W. Nuninger, F. Kratz, and J. Ragot, "Finite Memory Generalised State Observer for failure Detection in Dynamic Systems," in *Proceedings of the IEEE Conf. on Decision & Control*, Tampa, USA, 1998.
- [15] W. Byrski, "Integral Description of the Optimal State Observers," in *Proceedings of the II European Control Conference*, vol. 4, p. 1832, Groningen, Netherlands, 1993.
- [16] W. Byrski, "Theory and Application of the Optimal Integral State Observers," in *Proceedings of the III European Control Conference. ECC'95*, p. 52, Roma, Italy, 1995.
- [17] W. Byrski and P. Kubik, "Integral Observer of Finite State in Heat Equation Approximated by ODE," in *Proceedings of the IFAC/IMACS Large Scale Systems Symposium LSS'98*, Patras Greece, 1998.
- [18] W. Byrski, "Optimal State Observers with Moving and Expanding Observation Window," in *Proceedings of the IASTED, XII Intern. Conference on Model. & Simul.*, p. 68, Innsbruck, Austria, 1993.
- [19] J. Byrski, *Finite memory algorithms for signal processing in the diagnosis of processes*, AGH UST Scientific Publishers, Krakow, Poland, 2016.
- [20] J. Byrski and W. Byrski, "A double window state observer for detection and isolation of abrupt changes in parameters," *International Journal of Applied Mathematics and Computer Science*, vol. 26, no. 3, 2016.
- [21] N. R. Clark, *Fault diagnosis in Dynamic Systems. Theory and Application*, Prentice Hall, 1989.
- [22] R. J. Patton, P. M. Frank, and N. R. Clark, *Fault diagnosis in Dynamic Systems. Theory and Application*, Prentice Hall, 1989.
- [23] R. J. Patton, P. M. Frank, and R. N. Clark, *Issues of Fault Diagnosis for Dynamic Systems*, Springer, 2000.
- [24] S.-K. Chang and P.-L. Hsu, "A novel design for the unknown input faults detection observer," *Control Theory and Advanced Technology*, vol. 10, no. 4, 1995.
- [25] S. Simani, C. Fantuzzi, and R. J. Patton, *Model-based Fault Diagnosis in Dynamic Systems Using Identification Techniques*, Springer, 2003.
- [26] J. Chen and R. J. Patton, *Robust Model-Based fault Diagnosis for Dynamic Systems*, Kluwer Academic Pub., 1999.
- [27] S. Sundaram and C. N. Hadjicostis, "Delayed observers for linear systems with unknown inputs," *IEEE Transactions on Automatic Control*, vol. 52, no. 2, pp. 334–339, 2007.
- [28] A. Hocine, D. Maquin, and J. Ragot, "Finite memory observer for switching systems: Application to diagnosis," in *Proceedings of the Workshop on Advanced Control and Diagnosis*, Karlsruhe, Germany, 2004.

## Research Article

# Sensorless Control for Joint Drive Unit of Lower Extremity Exoskeleton with Cascade Feedback Observer

Pei Pei <sup>1</sup>, Zhongcai Pei,<sup>1</sup> Zhengqiang Shi,<sup>2</sup> Zhiyong Tang <sup>1</sup> and Yang Li<sup>1</sup>

<sup>1</sup>School of Automation Science and Electrical Engineering, Beihang University, Beijing 100191, China

<sup>2</sup>Beijing Institute of Precise Mechatronic Controls, Beijing 100076, China

Correspondence should be addressed to Zhiyong Tang; zyt\_76@buaa.edu.cn

Received 13 July 2018; Revised 2 October 2018; Accepted 18 October 2018; Published 30 October 2018

Academic Editor: Luis J. Yebra

Copyright © 2018 Pei Pei et al. This is an open access article distributed under the Creative Commons Attribution License, which permits unrestricted use, distribution, and reproduction in any medium, provided the original work is properly cited.

In this paper, a sensorless control method for joint drive unit driven by BLDC motor of low extremity exoskeleton, cascade feedback observer identification method, is proposed. The cascade feedback observer identification method is based on improved Integral-Switching-Function Sliding-Mode-Observer (ISF-SMO) and adaptive FIR filter. The improved Integral-Switching-Function Sliding-Mode-Observer is used to identify the back-EMF of motor. The sliding mode surface redesigned according to Integral-Switching-Function (ISF) eliminates the inevitable chattering problem in conventional Sliding-Mode-Observer (SMO). The stability condition of Integral-Switching-Function Sliding-Mode-Observer is obtained with Lyapunov function. Meanwhile, considering the estimation error and system instability caused by the mismatch between the actual resistance value ( $R_s$ ) and the set resistance value, the LMS algorithm is used to estimate the resistance value online according to the structure of adaptive FIR filter. When system is running, the modified Integral-Switching-Function Sliding-Mode-Observer and adaptive FIR filter are used to modify the back-EMF and the resistance value by cascading feedback relation, and the modified back-EMF value is taken as the final output of the system. Because of considering the uncertainty of resistance caused by temperature variation, the robustness and stability of the cascade feedback observer can be improved. Meanwhile, higher estimation accuracy is obtained, and operation range of sensorless control is extended, which is suitable for motor in low speed region. Finally, the correctness and validity of the proposed method are verified by simulations and experiments.

## 1. Introduction

Brushless DC (BLDC) motor not only has the advantages of simple operation and reliable maintenance [1], but also has the advantages of simple control, high efficiency, and good performance of speed regulation as DC motor; therefore, it is widely used in aerospace, instrumentation, medical devices, robotics, and other fields. There are many examples of the use of BLDC motor as a power source in extremity exoskeleton systems, and some of them have achieved very successful results, such as HAL-5 [2], Lokomat [3], and Rewalk [4]. The correct commutation of BLDC motor based on rotor position information is needed in motor operation process, but the existence of position sensor has brought a series of disadvantages of BLDC motor application. The principle of highly integrated and high reliability should be followed in the design of extremity exoskeleton system; therefore, a

sensorless BLDC motor is selected in the design of the joint drive unit (Figure 1), which will be controlled by sensorless control technology.

At present, sensorless control methods for BLDC motor can be divided into two categories: one is based on machine anisotropy [5, 6] and the other is based on mathematical model of BLDC motor [7, 8]. Anisotropy-based methods acquire rotor position by injecting high frequency (HF) signals into motor, which is suitable for sensorless control of ultralow speed operation. However, the injection of HF signals will bring additional loss and greater torque ripple. Mathematical model based methods are used to calculate rotor position according to the position information contained in motor mathematical model, which is suitable for the sensorless control of the middle and high speed operation. Mathematical model based methods include model reference adaptive system (MRAS) method [9], sliding mode observer

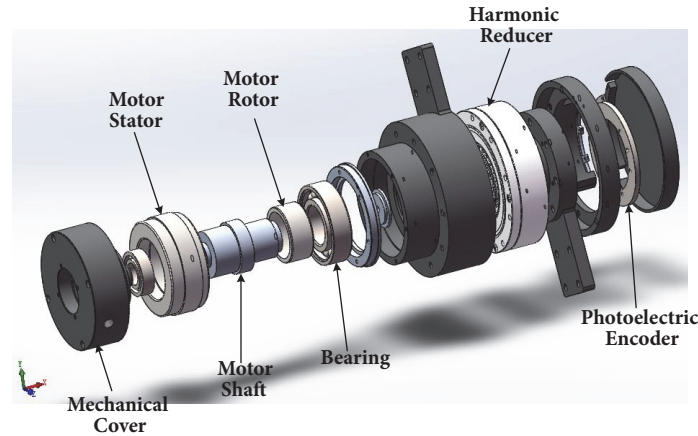


FIGURE 1: Joint drive unit.

(SMO) method [10, 11], Kalman filter method [12], and Luenberger observer [13]. Most of these methods obtain rotor position information by identifying back-EMF and usually use the zero-crossing of the nonconducted phase's back-EMF as the basis of motor commutation. The real commutation of motor is zero-crossing of phase's back-EMF adding a certain shift angle which is related to motor's speed directly, so the ideal commutation point cannot be obtained when a large fluctuation is in speed. This paper takes zero-crossings of the nonconducted line's back-EMF as the basis of motor commutation, which is corresponding to the commutation of Hall signal completely.

SMO methods are widely used in sensorless control of motor due to its simple structure and strong robustness to parameter variation. The first-order SMO as a kind of SMO is the most classical method to identify motor's back-EMF. However, there is chatting problem in the first-order SMO, which requires a low filter to filter the output single of observer, so there is phase lag of identification result. In [14], a mathematical method is used to compensate phase lag. In [15], a hyperbolic tangent function is used instead of symbolic function in SMO, which avoids phase lag brought by low pass filter. In view of the disadvantage of the first-order SMO, the second-order SMO and the improved observer based on the second-order SMO are used to identify motor's back-EMF. The second-order SMO is improved in [16]. In [17], considering the nonlinear effect of power inverter, an adaptive second-order SMO is designed, which reduces observation error effectively. A global fast terminal SMO based on linear SMO and fast terminal SMO is proposed in [18], which made full use of the advantages of linear SMO and fast terminal SMO.

The parameter  $R_s$  is contained in most of the identification results, which is not a constant in the process of motor operation due to the reasons of temperature rise and so on. So the estimation of the resistance value online plays an important role in sensorless control, especially in low speed region, where motor's back-EMF is relatively small compared to voltage drop. Mismatch between actual and set value of the resistance value may lead to rotor position and speed

estimation error and even system instability. The parameters identification of motor has been studied by many researchers. An online identification technique of the parameters which were needed to minimize power consumption in an application with PMSM was proposed in [19]. Two new parameters estimation methods for a single-phase induction machine (SPIM) were proposed in [20]. Besides, some researchers have combined the parameters identification of motor with no sensor control of sensor. In [21], a model reference adaptive algorithm based on adaptive fuzzy neural network was proposed, which could identify back-EMF very well in the case of motor parameter perturbations, but the control law designed by this method was too complex. Reference [8] proposed a two-stage high gain observer which could overcome the effect of parameter perturbation on system identification. In [22], an identification method which combined second-order sliding mode super-twisting algorithm (STA) and model reference adaptive system (MRAS) was proposed. By identifying the resistance value online, the influence of the uncertainty of resistance value on the system can be overcome and the speed working range of sensorless control was extended. In [23], the method of neural network was used to identify the resistance value according to the rotor position deviation, but the identification effect was greatly reduced under dynamic condition. A parallel estimation method of a super-twisting algorithm and second-order SMO is proposed in [24], which had overcome the influence of the uncertainty of resistance value and had achieved good results in low speed region.

Aiming at sensorless control of joint drive unit driven by BLDC motor of lower extremity exoskeleton system, a cascade feedback observer identification method based on improved ISF-SMO and adaptive FIR filter is proposed in this paper. Firstly, a novel ISF-SMO based on the improved ISF sliding mode control is designed, which can eliminate the chatting problem of the first-order SMO without low pass filter. The stability condition of ISF-SMO is obtained with Lyapunov function. In addition, LMS algorithm according to the structure model of adaptive FIR filter is used to identify the resistance value ( $R_s$ ) online instead of using

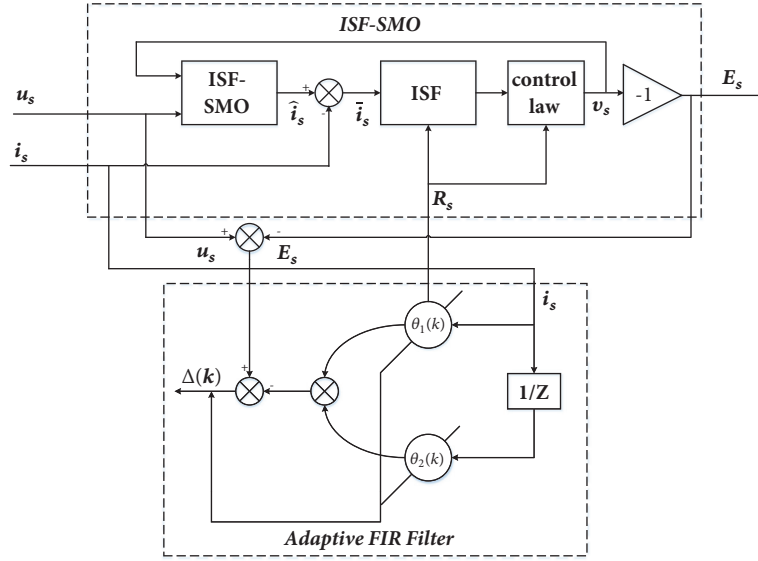


FIGURE 2: Schematic diagram of cascade feedback observer.

fixed value. Then, the robustness and identification accuracy of the system are improved. Furthermore, ISF-SMO and adaptive FIR filter constitute a cascade feedback observer identification system for sensorless control of BLDC motor. Finally, the correctness and effectiveness of the proposed cascade feedback observer identification method is verified by simulations and experiments.

## 2. Design of Cascade Feedback Observer

The cascade feedback observer system proposed in this paper includes two subsystems: ISF-SMO and adaptive FIR filter. When system is running, the two subsystems belong not only to parallel relationship, but to cascade feedback relationship as well. The schematic diagram of cascade feedback observer is shown in Figure 2. The input of cascade feedback observer is voltage and current, and the output is the estimated value of back-EMF. First of all, the ISF-SMO will identify line back-EMF based on the input line voltage and line current of the previous period. The line back-EMF is used as the input of the adaptive FIR filter identification system, and then the adaptive FIR filter identifies the equivalent value of resistance according to the line voltage, line current, and line back-EMF. The equivalent value of resistance is fed back to ISF-SMO identification system as the input. The ISF-SMO identifies the line back-EMF as the final output according to the values of line voltage, line current, and resistance. At the same time it is fed back to adaptive FIR filter identification system as the input. The two subsystems will be introduced in Sections 2.1 and 2.2, respectively.

**2.1. Integral-Switch-Function Sliding-Mode-Observer (ISF-SMO) Identification System.** Neglecting the influence of iron losses, eddy-current losses, and saturation effect, the mathematical model of Brushless DC motor can be described as

$$\begin{aligned} u_a &= R_s i_a + L_s \frac{di_a}{dt} + e_a + u_0 \\ u_b &= R_s i_b + L_s \frac{di_b}{dt} + e_b + u_0 \\ u_c &= R_s i_c + L_s \frac{di_c}{dt} + e_c + u_0, \end{aligned} \quad (1)$$

$$i_a + i_b + i_c = 0, \quad (2)$$

where  $u_a$ ,  $u_b$ , and  $u_c$  are phase's voltage of stator,  $i_a$ ,  $i_b$ , and  $i_c$  are phase's current of stator,  $e_a$ ,  $e_b$ , and  $e_c$  are phase's back-EMF of stator,  $R_s$  is resistance of stator, and  $L_s$  is equivalent inductance.

There is a certain phase shift angle between the zero-crossings of phase's back-EMF and the commutation point of Hall. However, the zero-crossings of line's back-EMF and the commutation point of the Hall signal are completely corresponding. Equations (1) and (2) can be translated into expressions of line voltage and line current as

$$\begin{aligned} u_{ab} &= R_s i_{ab} + L_s \frac{di_{ab}}{dt} + e_{ab} \\ u_{bc} &= R_s i_{bc} + L_s \frac{di_{bc}}{dt} + e_{bc} \\ u_{ca} &= R_s i_{ca} + L_s \frac{di_{ca}}{dt} + e_{ca}, \end{aligned} \quad (3)$$

$$i_{ab} + i_{bc} + i_{ca} = 0, \quad (4)$$

where  $u_{ab}$ ,  $u_{bc}$ , and  $u_{ca}$  are line's voltage of stator, and  $i_{ab}$ ,  $i_{bc}$ , and  $i_{ca}$  are line's current of stator.

The mathematical model of BLDC motor is simplified into two linear independent first-order current models in parallel. The space state equation can be expressed as follows:

$$\dot{X} = AX + B(U - E), \quad (5)$$

$$Y = CX, \quad (6)$$

where  $X = [x_1, x_2]^T = [i_{ab}, i_{bc}]^T$ ,  $U = [u_1, u_2]^T = [u_{ab}, u_{bc}]^T$  and  $E = [e_{ab}, e_{bc}]^T$ ,

$$A = \begin{bmatrix} -\frac{R_s}{L_s} & 0 \\ 0 & -\frac{R_s}{L_s} \end{bmatrix}, \quad (7)$$

$$B = \begin{bmatrix} -\frac{1}{L_s} & 0 \\ 0 & -\frac{1}{L_s} \end{bmatrix},$$

$$C = [1, 1]^T.$$

According to the state space equation of motor, an Integral-Switching-Function Sliding-Mode-Observer is designed as

$$\dot{\widehat{X}} = A\widehat{X} + B(U + V), \quad (8)$$

where  $\widehat{X} = [\widehat{i}_{ab}, \widehat{i}_{bc}]^T$  is the estimate of  $X$ ;  $V = [v_{ab}, v_{bc}]^T$  is the control law of SMO.

By subtracting (5) from (8), we can get state equation of state variable error as

$$\dot{\overline{X}} = A\overline{X} + B(V + E), \quad (9)$$

where  $\overline{X} = \widehat{X} - X$ .

The sliding mode surface of an Integral-Switching-Function Sliding-Mode-Observer is designed as

$$S = C \left( \overline{X} - BK \int \overline{X} dt \right), \quad (10)$$

where  $C$  is positive constant coefficient matrix;  $K$  is state feedback gain matrix.

When the system state is on the sliding mode surface,  $S = \dot{S} = 0$ , that is,

$$\dot{\overline{X}} = BK\overline{X}. \quad (11)$$

In this case, an ideal control effect can be obtained by adjusting  $K$  appropriately.

In order to identify the line's back-EMF of motor, the control law of the Integral-Switching-Function Sliding-Mode-Observer is needed. In this paper, the control law ( $V$ ) of ISF-SMO consists of two parts: equivalent control quantity ( $V_{eq}$ ) and switching control quantity ( $V_n$ ). Taking a line's current ( $i_{ab}$ ) as an example, the other two are similar. The control law ( $v$ ) of the ISF-SMO is designed as

$$V = V_{eq} + V_n$$

$$V_{eq} = R_s * \widehat{i}_s$$

$$V_n = \frac{1}{B} (\widehat{i}_s - A\widehat{i}_s) - K\widehat{i}_s + f \operatorname{sgn}(S), \quad (12)$$

where,  $f \geq |E|$ ;  $K$  is negative real number;  $S$  is sliding mode surface of ISF-SMO.

When the system moves on the sliding surface,  $\overline{i}_s = \widehat{i}_s = 0$ , then from (9) we obtain

$$E = -V. \quad (13)$$

According to (12), the identification result contains differential component  $\widehat{i}_s$ . In practical application, differentiator usually uses first-order differential signal, which is easy to introduce noise interference and then affect the identification accuracy. In this paper, a differential estimator is designed by using the second-order sliding mode algorithm to estimate the differential component ( $\widehat{i}_s$ ) in the identification result.

Define:  $\widehat{i}_s = e(t)$  and  $d\widehat{i}_s/dt = v_0(t)$ , then we can get

$$\overline{e}(t) = \widehat{e}(t) - e(t)$$

$$\dot{\overline{e}}(t) = \dot{\widehat{e}}(t) - v_0(t), \quad (14)$$

where  $\widehat{e}(t)$  is the estimator of  $e(t)$  and  $\overline{e}(t)$  is the estimating error.

The designed differential estimator is

$$\dot{\widehat{e}}(t) = v_0(t)$$

$$v_0(t) = -\lambda_0 * |\widehat{e}(t) - e(t)|^{1/2} * \operatorname{sgn}[\widehat{e}(t) - e(t)] + z \quad (15)$$

$$\dot{z} = -\lambda_1 * \operatorname{sgn}[\widehat{e}(t) - e(t)].$$

The convergence condition [25, 26] of differential estimator (15) is

$$\ddot{e}(t) < a$$

$$\lambda_1 > a$$

$$\lambda_0^2 \geq \frac{4a(\lambda_1 + a)}{(\lambda_1 - a)}, \quad (16)$$

where  $a$  is a positive constant. The controlled dynamics are affected by the choice of parameters  $\lambda_0$  and  $\lambda_1$ . The parameter tuning methods of  $\lambda_0$  and  $\lambda_1$  are similar to Ziegler-Nichols method used in PID parameter tuning. Meanwhile, the parameter tuning methods are based on the gain setting method of high order sliding mode control.

When the differential estimator converges, we can obtain

$$\widehat{i}_s = \frac{d\widehat{i}_s}{dt} = v_0(t). \quad (17)$$

The principle diagram of ISF-SMO is shown in Figure 2.

Then the stability of the improved ISF-SMO is analyzed with Lyapunov function.

Construct Lyapunov function as

$$V = \frac{1}{2} S^T S, \quad (18)$$

where  $S$  is the sliding mode surface of the ISF-SMO constructed by formula (10).

The differential of  $V$  is

$$\dot{V} = S^T \dot{S}, \quad (19)$$

$$\dot{S} = C\dot{\overline{X}} - CBK\overline{X}, \quad (20)$$

where  $\overline{X} = \widehat{X} - X$ ;  $\dot{\overline{X}} = \dot{\widehat{X}} - \dot{X}$ . Then (20) can be arranged as

$$\dot{S} = C \left( \dot{\widehat{X}} - \dot{X} \right) - CBK\overline{X}, \quad (21)$$

By substituting (5) with (21), we can get

$$\dot{S} = C\dot{\hat{X}} - C(AX + BU - BE) - CBK\bar{X}. \quad (22)$$

By substituting (12) with (22), we can get

$$\begin{aligned} \dot{S} &= C\dot{\hat{X}} - C \left\{ AX \right. \\ &\quad \left. + B \left[ \frac{1}{B} (\dot{\hat{X}} - A\hat{X}) - K\bar{X} + f \operatorname{sgn}(S) + \frac{A}{B}\bar{X} \right] \right. \\ &\quad \left. - BE \right\} - CBK\bar{X} \\ &= C\dot{\hat{X}} - C \left[ AX \right. \\ &\quad \left. + (\dot{\hat{X}} - A\hat{X} - BK\bar{X} + Bf \operatorname{sgn}(S) + A\bar{X}) - BE \right] \\ &\quad - CBK\bar{X} \\ &= C(-Bf \operatorname{sgn}(S) + BE). \end{aligned} \quad (23)$$

The derivation of the constructed Lyapunov function can be obtained by substituting (23) with (19):

$$\dot{V} = CB(-sf \operatorname{sgn}(S) + sE). \quad (24)$$

With the conditions for constructing ISF-SMO:  $f \geq |E|$ , we can obtain

$$\dot{V} = CB(-sf \operatorname{sgn}(S) + sE) = CB(-f|s| + sE) \leq 0. \quad (25)$$

Obviously, the reasonable selection of  $f$  can ensure that the control law of ISF-SMO satisfies the sliding mode arrival condition, and the stability of the SMO can be guaranteed.

It can be seen from (12) that the identification result of line's back-EMF contains parameter ( $R_s$ ), and its exact value will be identified online.

**2.2. Adaptive FIR Filter Identification System.** Equation (3) can be rewritten as

$$u_m = Ri_m + L \frac{di_m}{dt} + e_m; \quad (26)$$

$$u_m - e_m = R_m i_m + L_m \frac{di_m}{dt}. \quad (27)$$

The upper expression can be regarded as FIR filter with input ( $i_m$ ) and output ( $u_m - e_m$ ). After discretization we can get

$$u_m(k) - e_m(k) = \left( R + \frac{L}{\tau} \right) i_m(k) - \frac{L}{\tau} * i_m(k-1). \quad (28)$$

Define

$$\begin{aligned} y(k) &= u_m(k) - e_m(k) \\ \theta(k) &= \left[ R(k) - \frac{L(k)}{\tau}, -\frac{L(k)}{\tau} \right]^T \end{aligned} \quad (29)$$

$$x(k) = [i_m(k), i_m(k-1)]^T,$$

the output term ( $u_m(k) - e_m(k)$ ) from (19) can be estimated by FIR filter. Define  $\hat{y}(k)$  as estimated output of filter, we can get

$$\hat{y}(k) = \theta^T(k) x(k). \quad (30)$$

The estimated deviation can be expressed as

$$e(k) = y(k) - \hat{y}(k) = u_m(k) - e_m(k) - \hat{y}(k). \quad (31)$$

In the detection, if  $e(k)$  converge to 0, then  $\hat{y}(k)$  converge to  $y(k)$  which also means that several parameter values in the vector  $\theta(k)$  converge to the real parameters of system. The voltage and current values measured during the operation of system contain noise and the vector  $\theta(k)$  is time-varying. Adaptive filter is used to identify the parameters of three-phase winding in real time and online. The schematic diagram of adaptive FIR filter is shown in Figure 4.

In practice, variance is usually used as criterion and objective function. The mean square error of  $e(k)$  is

$$\begin{aligned} F(e(k)) &= E(e^2(k)) \\ &= E[y^2(k) - 2y(k)\hat{y}(k) + \hat{y}^2(k)]. \end{aligned} \quad (32)$$

By substituting (30) with (32), then we can get

$$\begin{aligned} F(e(k)) &= E[y^2(k) - 2y(k)\theta^T(k)x(k) \\ &\quad - \theta^T(k)x(k)x^T(k)\theta(k)] = E[y^2(k) \\ &\quad - 2E[y(k)\theta^T(k)x(k)] \\ &\quad + E[\theta^T(k)x(k)x^T(k)\theta(k)]]. \end{aligned} \quad (33)$$

Take  $\theta^T(k)$  as parameter vector, then (33) can be expressed as

$$\begin{aligned} F(e(k)) &= E[y^2(k)] - 2\theta^T(k)E[y(k)x(k)] \\ &\quad + \theta^T(k)E[x(k)x^T(k)]\theta(k) \\ &= E[y^2(k)] - 2\theta^T(k) * P + \theta^T(k) * R \\ &\quad * \theta(k), \end{aligned} \quad (34)$$

where  $P = E[y(k)x(k)]$  is the output signal vector associated with the input signal;  $R = E[x(k)x^T(k)]$  is the auto-correlation vector of the input signal. It can be deduced that the minimum value of (34) is obtained when its gradient to  $\theta(k)$  is 0, that is,

$$g_\theta = \frac{\partial F}{\partial \theta} = -2P + 2R\theta_0 = 0. \quad (35)$$

Then,

$$\theta_0 = R^{-1}P. \quad (36)$$

Equation (36) is the Wiener-Hopf equation [27]. If the solution of Wiener-Hopf equation exists, the parameter vector of the FIR filter can be found. The gradient descent method (the steepest descent method) is used to approximate the optimal solution vector. The gradient descent method takes the negative gradient direction as the search direction. The step size is smaller and the progress is slower with the gradient

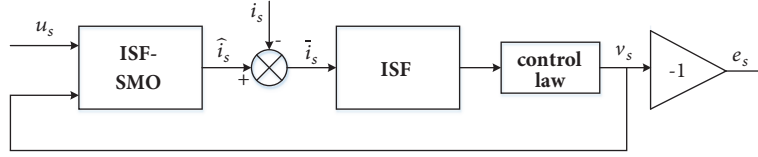


FIGURE 3: Schematic diagram of ISF-SMO.

descent method close to the target value. According to the principle of gradient descent method, the recursive formula of parameter vector can be expressed as

$$\theta_{k+1} = \theta_k - \mu \nabla F(e(k)), \quad (37)$$

where  $\mu$  represents the search step in gradient direction and the value of  $\mu$  determines the convergence rate of parameter vector. The gradient of variance function in (32) is

$$\nabla F(e(k)) = \nabla E(e^2(k)) = -E(e(k)x(k)). \quad (38)$$

By substituting (38) with (37), we can get

$$\theta_{k+1} = \theta_k + \mu E(e(k)x(k)). \quad (39)$$

Equation (39) is a recursive formula to find the optimal solution by using gradient descent method. In practical applications,  $E(e(k)x(k))$  is an unknown quantity and is difficult to be calculated by measurement, so it is usually replaced by the mean value of  $L$  sampling points, that is,

$$\hat{E}(e(k)x(k)) = \frac{1}{L} \sum_{l=0}^{L-1} [e(k-l)x(k-l)]. \quad (40)$$

For ease of calculation, set  $L=1$ , then (39) can be expressed as

$$\theta_{k+1} = \theta_k + \mu e(k)x(k). \quad (41)$$

Equation (41) is Least Mean Square (LMS) algorithm. And the convergence direction of (41) is the same as that of (37). The key to implement LMS algorithm is to determine  $\mu$ . When  $0 < \mu < 2/tr(R)$ , LMS algorithm is convergent, but  $R$  is unknown. For this reason, an approximate method is needed to determine the upper and lower limits of  $\mu$ . For stationary stochastic processes:

$$tr(R) = LE[x^2(k)], \quad (42)$$

where  $L$  is the dimension of input vector, then the range of  $\mu$  can be determined as

$$0 < \mu < \frac{2}{LE(x^2(k))}, \quad (43)$$

where  $E(x^2(k)) = (1/L) \sum_{l=0}^{L-1} x^2(k-l)$ . Then (43) can be transformed as

$$0 < \mu < \frac{2}{x^T(k)x(k)}. \quad (44)$$

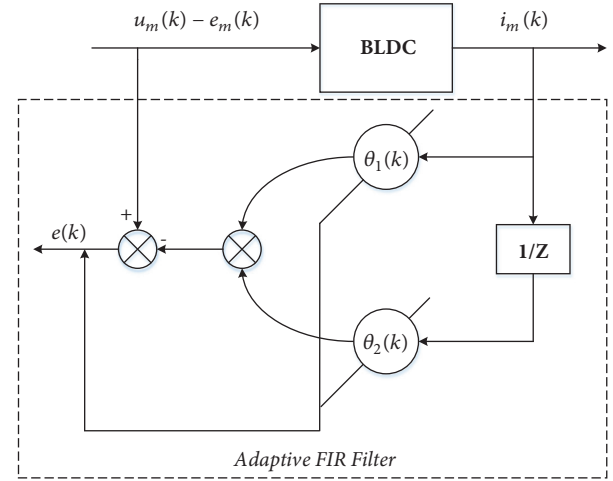


FIGURE 4: Schematic diagram of adaptive FIR filter.

Introduce normalized coefficient  $\beta$  ( $0 < \beta < 2$ ) and take  $\mu(k) = \beta/x^T(k)x(k) = \beta/\|x(k)\|$  to replace the fixed coefficient ( $\mu$ ), then the normalized LMS recursive algorithm is

$$\theta_{k+1} = \theta_k + \frac{\beta}{\|x(k)\|} e(k)x(k). \quad (45)$$

Compared with standard LMS algorithm, the normalized LMS algorithm has a variable correction gain ( $\mu(k)$ ), that is, the variable step size LMS algorithm.

As shown in (28), the resistance ( $R$ ) is related to line's current; however, the inductor ( $L$ ) is related to the differential of line's current. The value of the line's current can be measured directly in actual application, but its derivative cannot. That is to say, the identification results of resistance value ( $R$ ) with NLMS are more accurate. In this paper, only resistance values ( $R$ ) are identified, and the simulation results show that the variation of inductor value ( $L$ ) has little effect on the identification results of the line's back-EMF.

### 3. Simulation Results and Discussions

The system diagram of sensorless control of BLDC with cascade feedback observer identification method is shown in Figure 2. The model is built based on Matlab/Simulink. PID controller is applied for speed controller and current controller in this paper. The details of ISF-SMO and adaptive FIR filter are shown in Figures 3 and 4, respectively. Table 1 gives the main parameters of BLDC and control system.

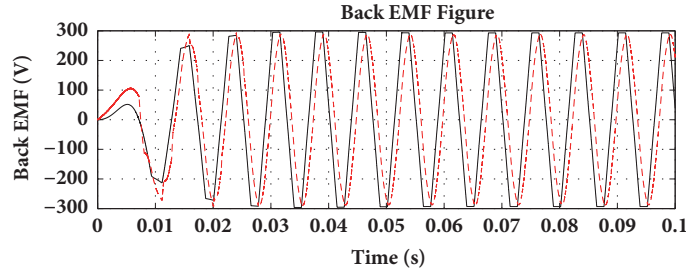


FIGURE 5: Identification result of conventional SMO.

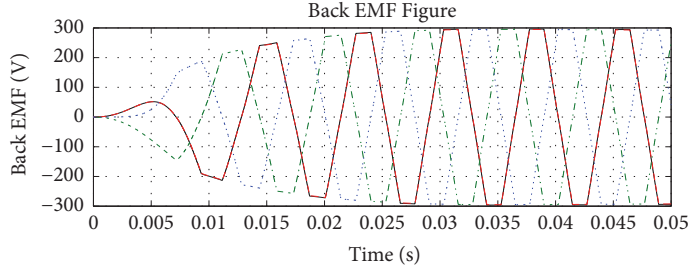


FIGURE 6: Identification result of ISF-SMO.

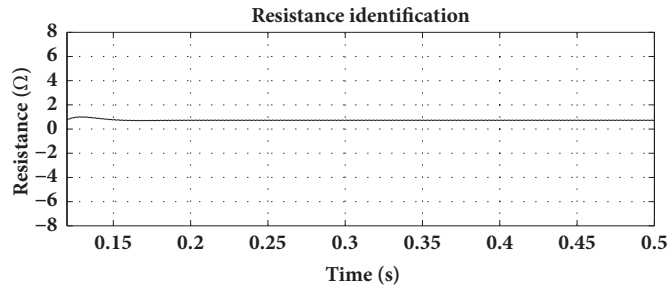

 FIGURE 7: Identification result of resistance value ( $R_s$ ).

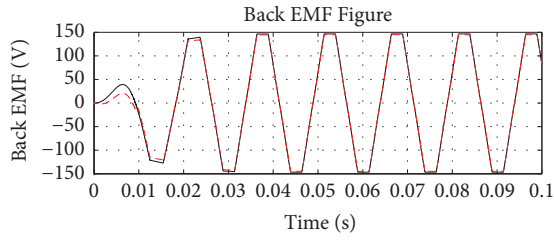
TABLE 1: Main parameters of simulation system.

Parameter	Value
$R_s$	$0.356\Omega$
$L$	$0.0083\text{H}$
$\psi_f$	$0.175\text{Wb}$
$J$	$0.0008\text{Kgm}^2$
$P_n$	6
$c$	30
$f$	0.5
$k$	-100
$\lambda_0$	20
$\lambda_1$	8

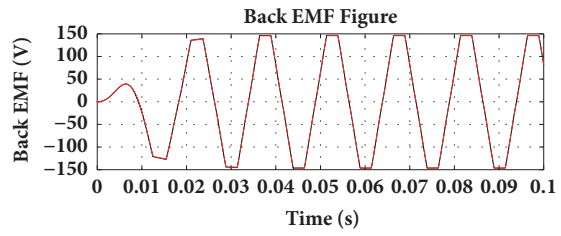
3.1. *Simulation Results of the Conventional SMO and ISF-SMO.* Both of the conventional first-order SMO and STASMO based sensorless control systems are constructed under continuous-time domain and the system bandwidth is the same. Simulation results of the conventional first-order SMO and ISF-SMO are shown in Figures 5 and 6,

respectively. Comparing these, the chattering problem is eliminated, but the result without phase lag of ISF-SMO is much better than the result with phase lag of conventional first-order SMO.

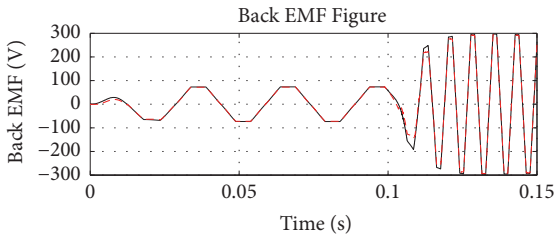
3.2. *Simulation Results of Cascade Feedback Observer and ISF-SMO.* In practical engineering, the resistance value will increase with the increase of temperature. In order to compare simulation result more clearly, we change the resistance value from  $0.356\Omega$  to  $0.712\Omega$ . In this case, the motor motion is speed step (from 0 to 1000 rpm). The identification result of resistance ( $R_s$ ) is shown is Figure 7. Simulation results are shown in Figure 8. In Figures 8(a), 8(c), 8(e), and 8(g), it is obvious that there is a large error when the resistance value changes with ISF-SMO control, especially at the time of acceleration stage, speed change stage, and load disturbance stage. In the real world, the problem will be exaggerated by discretization and measurement noises. Larger estimation error and even instability may occur. Therefore, online estimating of the resistance value is necessary in terms of estimation accuracy and system stability.



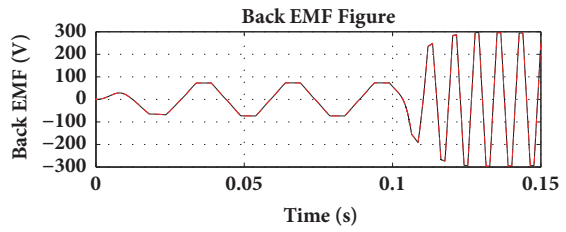
(a) Identification result of ISF-SMO when speed is 1000 rpm.



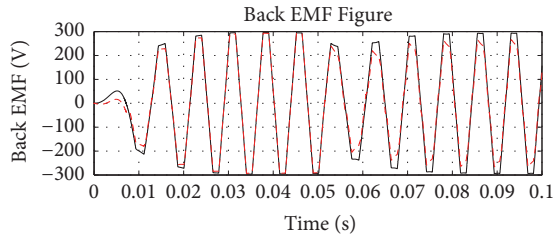
(b) Identification result of cascade feedback observer when speed is 1000 rpm.



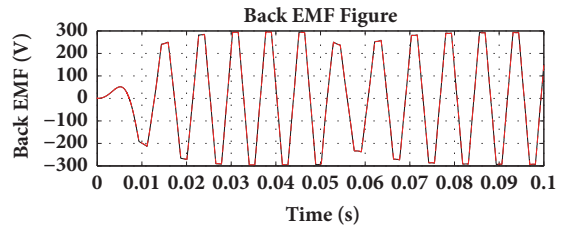
(c) Identification result of ISF-SMO when speed is from 500 rpm to 2000 rpm.



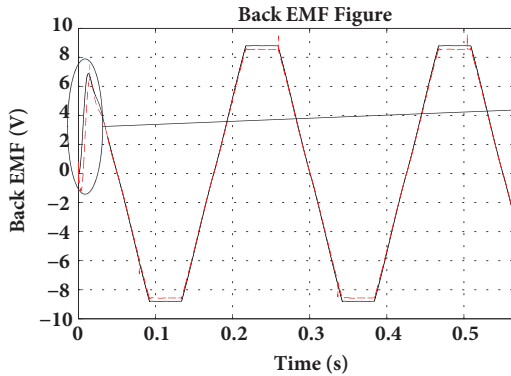
(d) Identification result of cascade feedback observer when speed is from 500 rpm to 2000 rpm.



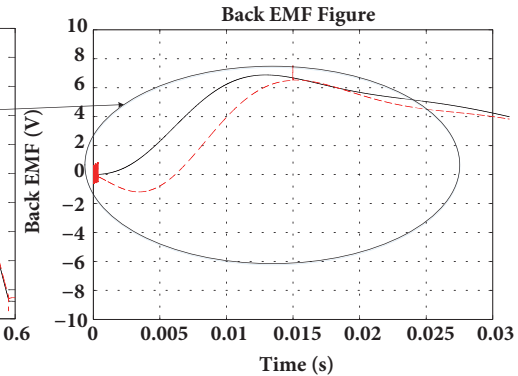
(e) Identification result of ISF-SMO when speed is 1000 rpm with load 10Nm at 0.05s.



(f) Identification result of cascade feedback observer when speed is 1000 rpm with load 10Nm at 0.05s.

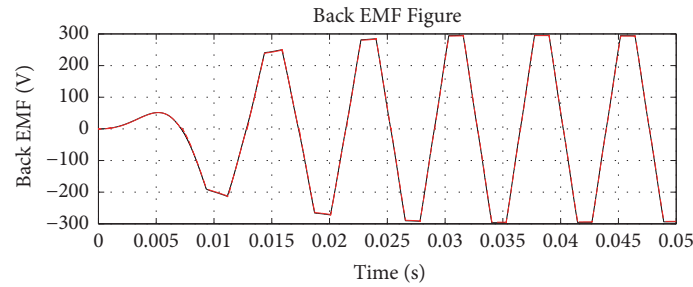


(g) Identification result of ISF-SMO when speed is 60 rpm.

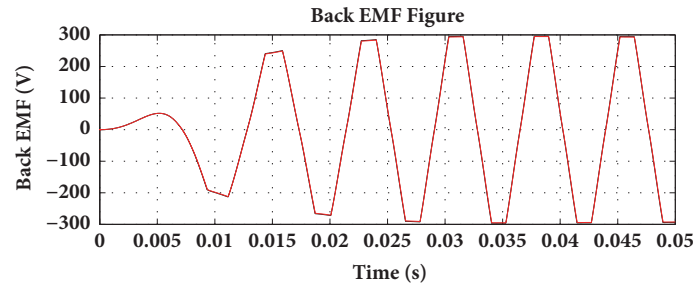


(h) Identification result of cascade feedback observer when speed is 60 rpm.

FIGURE 8: Compare simulation results of cascade feedback observer and ISF-SMO. (a), (c), (e), and (h) are the results of ISF-SMO, and (b), (d), (f), and (g) are the results of cascade feedback observer.



(a) Identification result of ISF-SMO when speed is 2000 rpm with inductance value of 0.0166H.



(b) Identification result of ISF-SMO when speed is 2000 rpm with inductance value of 0.0083H.

FIGURE 9: Compare simulation results of ISF-SMO with inductance value of 0.0166H and ISF-SMO with inductance value of 0.0083H. (a) is the result of ISF-SMO with inductance value of 0.0166H, and (b) is the result of ISF-SMO with inductance value of 0.0083H.

The simulation results of the cascade feedback observer identification method are shown in Figure 8. The system configuration is the same as that without the resistance value change. From Figures 8(b), 8(d), 8(f), and 8(h), it is obvious that the identification results are coinciding with reference EMF basically, even at the time of speed change stage and load disturbance stage. But at the acceleration stage of ultralow speed, there is some chattering.

From the discussion above, it can be concluded that the resistance variation has a great influence on estimation accuracy and robustness of the ISF-SMO. The effectiveness of online estimation of resistance value has been validated by simulations.

The influence of inductance variation on the ISF-SMO sensorless control system is also investigated. The simulation model is controlled by ISF-SMO based sensorless control method with the inductance value of 0.0166H (Figure 9(a)) and the inductance value of 0.0083H (Figure 9(b)), respectively. The simulation results are shown in Figure 9. It can be seen that inductance variation has little influence on estimation error, as shown in Figure 9. Because  $L_S(di_s/dt)$  is small at steady state, so the influence of inductance variation can be neglected.

#### 4. Experiment Results and Discussion

Before the structure design and processing completion of extremity exoskeleton, the effectiveness of sensorless control for joint drive unit of extremity exoskeleton with cascade feedback observer is verified on a semiphysical simulation test bench. The control system test bench is shown in

Figure 10. The control system mainly includes controller, motor control card, current sensor, voltage sensor, drive units, and BLDC.

In experimental results, the Hall signal identified by cascade feedback observer is output by DO. The phase voltage, phase current, actual Hall signal, and Hall signal identified by feedback observer can be measured by oscilloscope. The experimental results are shown in Figures 11–14. The oscilloscope interface contains phase voltage (cyan), phase current (pink), actual Hall signal (yellow), and Hall signal identified by cascade feedback observer (green). Figures 11–14 are the identification results at 2000 rpm, 4000 rpm, 5000 rpm, and 6000 rpm, respectively.

By comparing the actual Hall signal with Hall signal identified by cascade feedback observer, it can be found that their rising edge and descending edge are basically the same; that is, the correct commutation information which is used for BLDC commutation can be obtained by cascade feedback observer. The performance of proposed sensorless control method is verified by the experimental results.

#### 5. Conclusion

In this paper, the cascade feedback observer based on ISF-SMO and adaptive FIR filter is proposed, which will be used for sensorless control for joint drive unit of lower extremity exoskeleton. The chattering problem in conventional SMO is alleviated by designing an Integral-Switch-Function sliding mode surface based on the improved Integral-Switch-Function Sliding-Mode-Control. In the meantime, an online resistance value ( $R_S$ ) estimation method based on adaptive

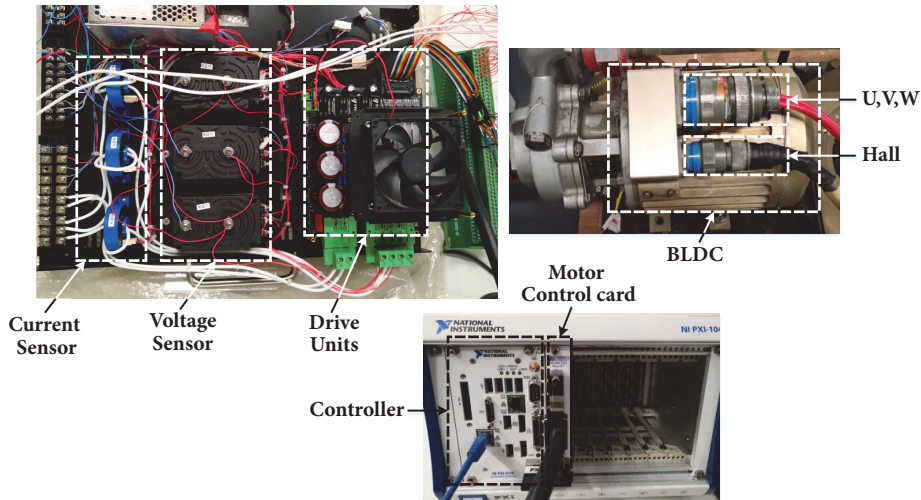


FIGURE 10: The control system test bench.

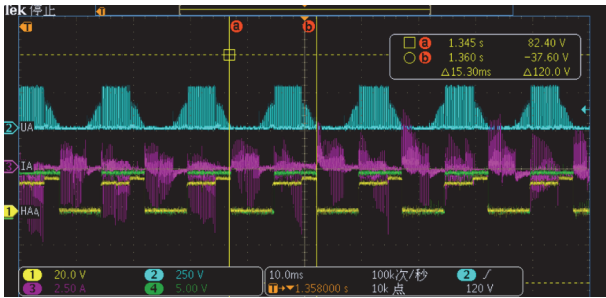


FIGURE 11: Experimental result of cascade feedback observer when speed is 2000 rpm.



FIGURE 13: Experimental result of cascade feedback observer when speed is 5000 rpm.



FIGURE 12: Experimental result of cascade feedback observer when speed is 4000 rpm.

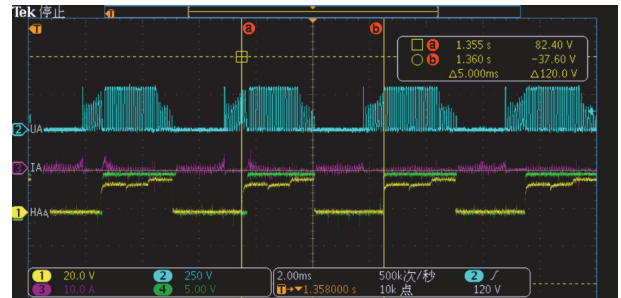


FIGURE 14: Experimental result of cascade feedback observer when speed is 6000 rpm.

FIR filter is utilized to obtain the accurate resistance value ( $R_S$ ), which improves the identification precision of back-EMF significantly, especially at the time of acceleration stage, speed change stage, and load disturbance stage. Simulations and experiments are carried out to verify its validation. The results show that the proposed cascade feedback observer can improve the stability and robustness of system. However, because the proposed cascade feedback observer is based on machine model, it is scarcely capable of operating at the

ultralow speed. In the future work, we will take a transitional scheme to solve this problem, such as high frequency injection method.

### Data Availability

The simulation model data and simulation result data used to support the findings of this study are available from the corresponding author upon request.

## Conflicts of Interest

The authors declare that there are no conflicts of interest regarding the publication of this paper.

## Acknowledgments

This work was supported by the Chinese National Science Foundation (no. 51075017). The authors would like to thank the anonymous reviewers for their valuable comments.

## References

- [1] R. Manikandan and R. Arulmozhiyal, "Intelligent position control of a vertical rotating single arm robot using BLDC servo drive," *Journal of Power Electronics*, vol. 16, no. 1, pp. 205–216, 2016.
- [2] Y. Sankai, "Leading edge of cybernics: robot suit HAL," in *Proceedings of the SICE-ICASE International Joint Conference*, pp. P-1–P-2, Busan, South Korea, October 2006.
- [3] B. Michaud, Y. Cherni, M. Begon, G. Girardin-Vignola, and P. Roussel, "A serious game for gait rehabilitation with the Lokomat," in *Proceedings of the 2017 International Conference on Virtual Rehabilitation, ICVR 2017*, Canada, June 2017.
- [4] E. Prassler and A. Baroncelli, "Team ReWalk Ranked First in the Cybathlon 2016 Exoskeleton Final [Industrial Activities]," *IEEE Robotics and Automation Magazine*, vol. 24, no. 4, pp. 8–10, 2017.
- [5] G. Wang, L. Yang, G. Zhang, X. Zhang, and D. Xu, "Comparative Investigation of Pseudorandom High-Frequency Signal Injection Schemes for Sensorless IPMSM Drives," *IEEE Transactions on Power Electronics*, vol. 32, no. 3, pp. 2123–2132, 2017.
- [6] D. Kim, Y.-C. Kwon, S.-K. Sul, J.-H. Kim, and R.-S. Yu, "Suppression of injection voltage disturbance for high-frequency square-wave injection sensorless drive with regulation of induced high-frequency current ripple," *IEEE Transactions on Industry Applications*, vol. 52, no. 1, pp. 302–312, 2016.
- [7] S. S. Alex and A. E. Daniel, "An Efficient Position Tracking Smoothing Algorithm for Sensorless Operation of Brushless DC Motor Drives," *Modelling and Simulation in Engineering*, vol. 2018, Article ID 4523416, 9 pages, 2018.
- [8] P. Mercorelli, "A Two-Stage Sliding-Mode High-Gain Observer to Reduce Uncertainties and Disturbances Effects for Sensorless Control in Automotive Applications," *IEEE Transactions on Industrial Electronics*, vol. 62, no. 9, pp. 5929–5940, 2015.
- [9] Y. Shi, K. Sun, L. Huang, and Y. Li, "Online identification of permanent magnet flux based on extended Kalman filter for IPMSM drive with position sensorless control," *IEEE Transactions on Industrial Electronics*, vol. 59, no. 11, pp. 4169–4178, 2012.
- [10] P. Mercorelli, "A two-stage augmented extended Kalman filter as an observer for sensorless valve control in camless internal combustion engines," *IEEE Transactions on Industrial Electronics*, vol. 59, no. 11, pp. 4236–4247, 2012.
- [11] T. Bernardes, V. F. Montagner, H. A. Grundling, and H. Pinheiro, "Discrete-time sliding mode observer for sensorless vector control of permanent magnet synchronous machine," *IEEE Transactions on Industrial Electronics*, vol. 61, no. 4, pp. 1679–1691, 2014.
- [12] Hong-Ru Li, Zhi-Bin Jiang, and Nan Kang, "Sliding Mode Disturbance Observer-Based Fractional Second-Order Non-singular Terminal Sliding Mode Control for PMSM Position Regulation System," *Mathematical Problems in Engineering*, vol. 2015, Article ID 370904, 14 pages, 2015.
- [13] P. Mercorelli, "A Motion-Sensorless Control for Intake Valves in Combustion Engines," *IEEE Transactions on Industrial Electronics*, vol. 64, no. 4, pp. 3402–3412, 2017.
- [14] O. Saadaoui, A. Khlaief, A. Chaari, and M. Boussak, "A new approach rotor speed estimation for PMSM based on sliding mode observer," in *Proceedings of the 15th International Conference on Sciences and Techniques of Automatic Control and Computer Engineering, STA 2014*, pp. 968–973, Tunisia, December 2014.
- [15] W. Hu and Y. Geng, "Model-free adaptive control of BLDCM based on improved sliding mode observer," *Journal of Electronic Measurement and Instrumentation*, vol. 30, no. 3, 2016.
- [16] L. Qi, T. Jia, and H. Shi, "A novel sliding mode observer for PMSM sensorless vector control," in *Proceedings of the 2011 IEEE International Conference on Mechatronics and Automation, ICMA 2011*, pp. 1646–1650, China, August 2011.
- [17] D. Liang, J. Li, R. Qu, and W. Kong, "Adaptive Second-Order Sliding-Mode Observer for PMSM Sensorless Control Considering VSI Nonlinearity," *IEEE Transactions on Power Electronics*, 2017.
- [18] X. Wang, T. Fu, and X. Wang, "Position sensorless control of BLDC motors based on global fast terminal sliding mode observer," *Journal of Power Electronics*, vol. 15, no. 6, pp. 1559–1566, 2015.
- [19] P. Mercorelli, "Parameters identification in a permanent magnet three-phase synchronous motor of a city-bus for an intelligent drive assistant," *International Journal of Modelling, Identification and Control*, vol. 21, no. 4, pp. 352–361, 2014.
- [20] D. C. Huynh and M. W. Dunnigan, "Advanced particle swarm optimisation algorithms for parameter estimation of a single-phase induction machine," *International Journal of Modelling, Identification and Control*, vol. 15, no. 4, pp. 227–240, 2012.
- [21] M. Jain, M. Singh, A. Chandra, and S. S. Williamson, "Sensorless control of permanent magnet synchronous motor using ANFIS based MRAS," in *Proceedings of the 2011 IEEE International Electric Machines and Drives Conference, IEMDC 2011*, pp. 599–606, Canada, May 2011.
- [22] L. Zhao, J. Huang, H. Liu, B. Li, and W. Kong, "Second-order sliding-mode observer with online parameter identification for sensorless induction motor drives," *IEEE Transactions on Industrial Electronics*, vol. 61, no. 10, pp. 5280–5289, 2014.
- [23] K. Liu, Z. Q. Zhu, and D. A. Stone, "Parameter estimation for condition monitoring of PMSM stator winding and rotor permanent magnets," *IEEE Transactions on Industrial Electronics*, vol. 60, no. 12, pp. 5902–5913, 2013.
- [24] D. Liang, J. Li, and R. Qu, "Sensorless Control of Permanent Magnet Synchronous Machine Based on Second-Order Sliding-Mode Observer With Online Resistance Estimation," *IEEE Transactions on Industry Applications*, vol. 53, no. 4, pp. 3672–3682, 2017.
- [25] A. Levant, "Sliding order and sliding accuracy in sliding mode control," *International Journal of Control*, vol. 58, no. 6, pp. 1247–1263, 1993.
- [26] A. Levant, "Robust exact differentiation via sliding mode technique," *Automatica*, vol. 34, no. 3, pp. 379–384, 1998.
- [27] T. Nagasaka and K. Kobayashi, "Wiener-Hopf analysis of the diffraction by a thin material strip," in *Proceedings of the 2016 URSI International Symposium on Electromagnetic Theory, EMTS 2016*, pp. 557–560, Finland, August 2016.

## Research Article

# A New Direct Speed Estimation and Control of the Induction Machine Benchmark: Design and Experimental Validation

Ali Hmidet <sup>1</sup>, Rachid Dhifaoui <sup>2</sup> and Othman Hasnaoui<sup>3</sup>

<sup>1</sup>Tunis El Manar University, Tunisia

<sup>2</sup>Tunis Carthage University, Tunisia

<sup>3</sup>University of Tunis, Tunisia

Correspondence should be addressed to Ali Hmidet; [hmidetali@yahoo.fr](mailto:hmidetali@yahoo.fr)

Received 24 July 2018; Accepted 9 September 2018; Published 8 October 2018

Guest Editor: Mihai Lungu

Copyright © 2018 Ali Hmidet et al. This is an open access article distributed under the Creative Commons Attribution License, which permits unrestricted use, distribution, and reproduction in any medium, provided the original work is properly cited.

Speed sensorless control schemes have potential benefits for industrial applications because they contribute to reducing process cost and they avoid using fragile sensors as encoders or resolvers in hostile environment. In addition, simplicity, reliability, and fast response of control structures to signal commands are much-needed features. In this paper, a new Speed Sensorless Direct Control (SSDC) technique allowing the achievement of these objectives is proposed. This technique combines Field Oriented Control (FOC) and Direct Torque Control (DTC) properties in the same approach. The estimated speed is reached only according to the measured current and voltage of the stator. DTC is extended to speed sensorless direct control with any notable modification. The proposed scheme is implemented to the induction machine benchmark and evaluated in real time under various possible scenarios of use. Experimental results show that the proposed SSDC has interesting capabilities to conduct induction motor in real time operation with good accuracy.

## 1. Introduction

The variable speed control of electric drives has benefited in recent years from significant methodological and technological advances. In fact, advances in digital signal processors such as DSP and dSPACE kits and the development of power components today make it possible to implement very complex algorithms with a short computation time. Several control algorithms are developed, tested, and industrialized. Field oriented control (FOC) [1–3] and direct torque control (DTC) [4–8] are typical examples.

As is known, the available FOC structures require a speed sensor and the supply voltage is generated by an inverter governed by the Space Vector Pulse Width Modulation (SVPWM) strategy which is switching period generally in the order of 100 to 200 microseconds. By modulation principle, the switching times of the inverter IGBTs are variable in this range and can therefore reach very low values. The waveform of the current is then sufficiently smooth. The torque and speed rising times in the closed loop operating points are

about the rotor time constant [9]. FOC has the disadvantage that requiring the use of a speed sensor or position which imposes an additional cost and increases the complexity of the drive system.

Conventionally, DTC structures are speed sensorless controls. In contrast to the FOC method, the DTC technique eliminates PI controllers, transform matrices, current regulators, and PWM stage. Inverter IGBTs are in fact controlled with constant switching time that lies in general in the range of 25 to 50 microseconds. Torque and stator flux magnitude are regulated by adequately selecting a voltage vector among those available on the inverter [6, 8]. The practical implementation is therefore more economical and simpler and requires a shorter calculation time. The cancellation of a speed sensor is certainly a significant advantage. The speed response of the DTC is slow, unlike the torque response. Furthermore, torque response is very fast. Such a property is in demand in many industrial applications such as electric traction and tools-machine. Important current and torque ripples occur if the selected voltage vector isn't the best one. In practical point

of view, the DTC scheme can fall down if torque and flux hysteresis bands do not adequately take into account values of switching period and inverter dc voltage [10].

FOC and DTC are well studied and compared in various publications [9, 11–13]. Specific features, advantages, and drawbacks are outlined. However, the possibility of connection of FOC and DTC in the same purpose is not sufficiently investigated. In fact, a Like-FOC or Like-DTC or FOC-DTC approach can be of great interest. The key point of this paper deals with this aspect. It consists of combining FOC and DTC functionalities to study an important practical problem dealing with speed estimation and control of induction machines benchmark. It is based on the extension of the good torque regulation in the DTC structure into a speed regulation while benefiting of its advantages. Speed sensing based on encoders or resolvers is expensive on one hand and is vulnerable to hostile environment on the other hand. Closed loop control based on numerical estimation of machine rpm is therefore highly demanded [14–20].

The proposed algorithm for estimating and controlling the speed of the induction machine benchmark is experimentally verified in real time running on Dspace DS1104. Practical results prove that the DTC scheme can be extended to realize a reliable and efficient speed sensorless approach. This approach uses some expressions and properties of FOC. The developed method is here labelled Speed Sensorless Direct Control (SSDC).

The paper is organized as follows. Section 2 presents the theoretical background of induction machine benchmark and some properties emerging from selecting adequate reference frame. Section 3 develops theoretical and practical features of standard DTC technique. Section 4 describes the speed estimation and control approach. The idea is focused on how to use standard Takahashi switching table to control induction machine speed. Section 5 deals with practical results and discussion.

## 2. Basics of Induction Machine Benchmark

The dynamic model of induction machine can be formulated according to d-q-axis components in various reference frames. Let us first consider Concordia's stationary reference frame. The usual following set of equations is used [21]:

$$\bar{e}_s = \frac{d\bar{\varphi}_s}{dt} = \bar{v}_s - R_s \bar{i}_s \quad (1)$$

$$\bar{e}_r = \frac{d\bar{\varphi}_r}{dt} = j\omega \bar{\varphi}_r - R_r \bar{i}_r \quad (2)$$

$$\bar{\varphi}_s = \ell_s \bar{i}_s + m \bar{\varphi}_r \quad (3)$$

where  $\bar{v}_s$  and  $\bar{i}_s$  correspond to stator voltage and current vectors,  $\bar{e}_s$  and  $\bar{e}_r$  are stator and rotor electromotive forces (back emfs), and  $\bar{\varphi}_s$  and  $\bar{\varphi}_r$  are stator and rotor flux vectors. Variable  $\omega$  holds for electrical rotor speed. Parameters  $R_s$ ,  $R_r$ ,  $\ell_s$ , and  $m$  are stator and rotor resistance, leakage inductance, and the ratio between mutual inductance  $M$  and rotor inductance  $L_r$ , respectively. This model is established under the assumption of no eddy currents, no saturation of the

magnetic circuit, and the additional assumption of sinusoidal distribution of the stator and rotor windings.

In normal steady state, stator and rotor electrical variables have sinusoidal wave forms with the same frequency and different magnitudes that depend on the considered operating point. These quantities vary in transient regime according to the adopted control. Various expressions can be used to calculate electromagnetic torque. The most used relation is the following where  $p$  holds for the number of pairs of poles and  $\Im_m(\cdot)$  designates the imaginary component of the treated complex quantity. This relation is common for steady state and transient regimes [3, 6].

$$T_e = -p \Im_m(\bar{\varphi}_s \bar{i}_s^*) = p(\varphi_{ds} i_{qs} - \varphi_{qs} i_{ds}) \quad (4)$$

In what follows, it will be very helpful to express stator and rotor flux vectors as functions of their magnitudes and angles:

$$\begin{aligned} \bar{\varphi}_s &= \Phi_s e^{j\theta_s} \\ \bar{\varphi}_r &= \Phi_r e^{j\theta_r} \end{aligned} \quad (5)$$

Let us now consider a reference frame rotating with an angle  $\theta_p$  (or frequency  $\omega_p$ ) with respect to Concordia's stationary reference frame. The famous Park's d-q axes system is considered. Voltage equations (1) and (2) of Concordia's model become as follows in this new rotating reference frame; the capital letters is used to distinguish between these two systems [22]:

$$\bar{E}_s = j\omega_p \bar{\Phi}_s + \frac{d\bar{\Phi}_s}{dt} = \bar{V}_s - R_s \bar{I}_s \quad (6)$$

$$\bar{E}_r = j\omega_p \bar{\Phi}_r + \frac{d\bar{\Phi}_r}{dt} = j\omega \bar{\Phi}_r - R_r \bar{I}_r \quad (7)$$

Transition from Concordia's variables to Park's ones is realized by the rotation operator  $e^{-j\theta_p}$ . For example, stator current becomes [7, 20, 22]

$$\bar{I}_s = \bar{i}_s e^{-j\theta_p} \quad (8)$$

According to a specific topic, a suitable Park reference frame is selected. In practical point of view, there are two very interesting cases. The first one concerns a rotating reference frame whose d-axis is aligned to stator flux vector  $\bar{\varphi}_s$ . This case leads to some interesting properties used in control strategies considering machine stator control as fundamental target. The second case deals with a rotating reference synchronized with rotor flux vector  $\bar{\varphi}_r$ . The attention is then focused on rotor variables control as flux magnitude and slip frequency control schemes.

In the case of a stator flux reference frame, angle  $\theta_p$  is equal to  $\theta_s$ , which means  $\Phi_{ds} = \Phi_s$  and  $\Phi_{qs} = 0$ . Thus, decomposing (6) into d-q components leads to

$$\frac{d\Phi_s}{dt} = E_{ds} = V_{ds} - R_s I_{ds} \quad (9)$$

$$\frac{d\theta_s}{dt} = \omega_s = \frac{E_{qs}}{\Phi_s} = \frac{V_{qs} - R_s I_{qs}}{\Phi_s} \quad (10)$$

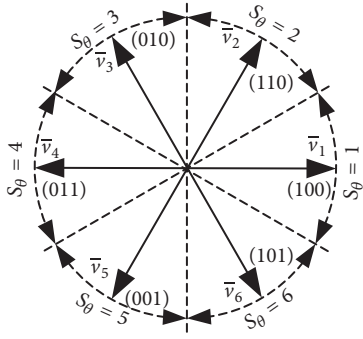


FIGURE 1: Inverter voltage vectors in Concordia's reference frame.

The most important conclusion that can be derived from this model is the fact that stator flux magnitude  $\Phi_s$  is controllable from direct back emf component  $E_{ds}$  while control of stator flux pulsation  $\omega_s$  can be achieved by quadrature back emf component  $E_{qs}$  [23–25]. This implies that stator control is by principle a voltage control.

For a rotor flux reference frame, angle  $\theta_p$  is equal to  $\theta_r$ , which means  $\Phi_{dr} = \Phi_r$  and  $\Phi_{qr} = 0$ . Therefore, decomposing (7) into d and q components leads to the following model, where  $\tau_r$  holds for rotor time constant ( $\tau_r = L_r/R_r$ ):

$$\frac{d\Phi_r}{dt} = \frac{MI_{ds} - \Phi_r}{\tau_r} \quad (11)$$

$$\frac{d(\theta_r - \theta)}{dt} = \omega_{sl} = \omega_r - \omega = \frac{MI_{qs}}{\tau_r \Phi_r} \quad (12)$$

This model implies that rotor flux magnitude  $\Phi_r$  is controllable from direct stator current component  $I_{ds}$  while control of electrical slip frequency  $\omega_{sl}$  can be achieved by controlling quadrature current component  $I_{qs}$ . This is the most important theoretical result of FOC schemes. Rotor-based control is by principle a current control.

### 3. Fundamentals of the DTC Scheme

In variable AC drives, a three-phase voltage source inverter feeds the induction machine. For a lossless-admitted inverter, the output voltage is strictly defined by the dc bus voltage  $V_{dc}$  of the inverter and the logical state of the three highest IGBT's signals ( $c_1, c_2, c_3$ ) of its configuration. There are only eight possible different logical combinations of ( $c_1, c_2, c_3$ ) leading to six active voltage vectors and two zero voltage vectors. It is well known that, for a specified switching combination of ( $c_1, c_2, c_3$ ), the space vector of the inverter output voltage  $\bar{v}_k$  can be expressed as follows where  $k$  an integer is indicating the switching combinations [22, 23]:

$$\bar{v}_k = \sqrt{\frac{2}{3}} V_{dc} e^{j(k-1)(\pi/3)} \quad k = 1, 2, \dots, 6 \quad (13)$$

$$\bar{v}_k = 0 \quad k = 0, 7$$

Figure 1 summarizes this model by indicating on each vector the associated combination of signal commands  $c_1, c_2,$

and  $c_3$ . Also, it is useful to identify active voltage vectors by six centered sector  $S_\theta = 1, \dots, 6$ .

Any proposed control scheme is developed to find out different solutions with two major objectives, accurate and quick control of the motor regime on one hand and reduction of the complexity and the cost of the algorithm on the other hand. Direct torque control (DTC) scheme developed and presented by I. Takahashi [3] is straight forward in these objectives. DTC is in fact characterized by the absence of PI regulators, absence of coordinate transformations, absence of current regulators, and absence of PWM signals generators.

First, let us note that induction machine benchmark achieves the demanded load if adequate stator flux magnitude and frequency are realised. Stator flux vector is therefore a key variable in any emphasised control. It is observed by Takahashi that stator flux control can be achieved in a simple way if the motor is fed by a three phase inverter. According to (1), stator flux vector can be generated by simple integration as follows:

$$\bar{\varphi}_s = \int \bar{e}_s dt \quad (14)$$

Furthermore, if the inverter command is maintained during a time interval  $T_s$ , it is possible to directly calculate stator flux vector variation according to (15) because voltage vector is constant.

$$\bar{\varphi}_s(t_o + T_s) = \bar{\varphi}_s(t_o) + T_s \bar{v}_s \quad (15)$$

According to this relation, selecting a null  $\bar{v}_s$  vector stops the stator flux vector in the d-q plane. Instead, the selection of an active  $\bar{v}_s$  vector moves the stator flux vector along the direction of the applied stator voltage. Furthermore, vector flux deviation is known and is strictly defined by the switching period  $T_s$  and the inverter dc link voltage  $V_{dc}$  as

$$\|\bar{\varphi}_s(t_o + T_s) - \bar{\varphi}_s(t_o)\| = \sqrt{\frac{2}{3}} T_s V_{dc} \quad (16)$$

Consequently, with appropriate sequence of the inverter command, the stator flux vector can be driven along any trajectory with a predefined average speed. The most appropriate flux trajectory for electrical machines control is naturally the circular path in the d-q plane. A very simple way to obtain this trajectory is to use a hysteresis comparator to control the flux vector. In order to maintain the flux within the hysteresis band, the motor should be currently fed by a suitable voltage vector with a constant switching period  $T_s$ . The direct component  $v_{ds}$  acts on the flux magnitude while the tangential component  $v_{qs}$  determines the vector rotation. This is compatible with (9) and (10) that give the following under the assumption of constant current over the switching period:

$$\Delta\Phi_s = \frac{d\Phi_s}{dt} T_s = (V_{ds} - R_s I_{ds}) T_s \quad (17)$$

$$\Delta\theta_s = \frac{d\theta_s}{dt} T_s = \frac{(V_{qs} - R_s I_{qs}) T_s}{\Phi_s} \quad (18)$$

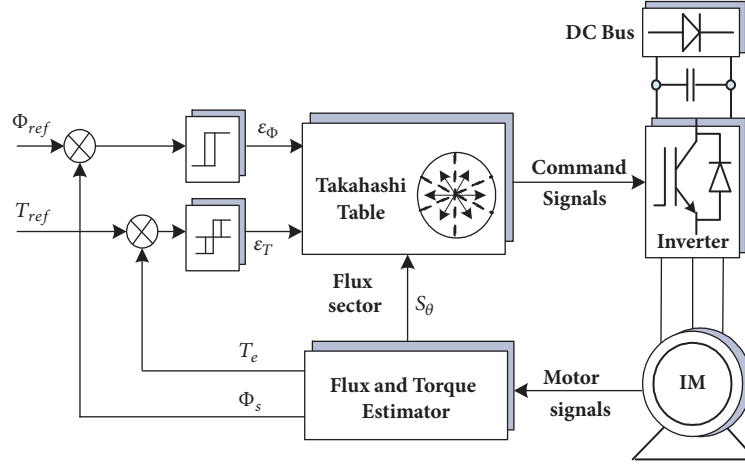


FIGURE 2: General structure of a DTC scheme.

On the other hand, accelerating or decelerating stator flux rotation is naturally linked to electromagnetic torque variation. Therefore, variation of angle  $\theta_s$  can be used to control torque. Theoretically speaking, one can establish the sensitivity coefficient of  $T_e$  with respect to flux magnitude and angle [23–26]. Let us consider (19) to describe electromagnetic torque. This equation is deduced from (3), (4), and (5):

$$T_e = \frac{pm\Phi_s\Phi_r}{\ell_s} \sin(\theta_s - \theta_r) \quad (19)$$

Stator and rotor machine circuits have different time responses. It is well known that stator variables vary more rapidly as compared to rotor ones. Stator quantities define a fast mode while rotor quantities correspond to a slow mode. Therefore, if flux magnitude is first controlled, a negative deviation of  $T_e$  can be achieved by decelerating  $\theta_s$  while a positive deviation is obtained by accelerating  $\theta_s$ . This means that by the same voltage vector  $\bar{v}_s$  one can control simultaneously electromagnetic torque and stator flux magnitude. As done for stator flux magnitude control, a simple hysteresis control can be used to command torque. During this kind of control, torque value remains in the considered hysteresis band if the voltage vector is adequately selected.

Note finally that the effect of a particular voltage vector on torque and flux magnitude depends on the position  $\theta_s$  of  $\bar{\varphi}_s$  in the d-q plane. The choice of hysteresis bands and voltage vector affect the performance of the drive. This problem is largely studied in the related literature and people experience is today summarized by the well-known Takahashi Switching Table principle. Various switching solutions are established to control the torque according to whether the stator flux has to be increased or decreased. These solutions have similar capabilities in terms of torque ripples. In all cases, Figure 2 shows DTC structure.

The widely used DTC algorithm is built with six centered sectors for  $\theta_s$ , one level hysteresis comparator for stator flux

TABLE 1: Flux and torque errors codification.

Flux and torque errors	Hysteresis index
$ \Delta\Phi_s  > \varepsilon_\Phi$	$k_\Phi = 1$
$ \Delta\Phi_s  \leq \varepsilon_\Phi$	$k_\Phi = 2$
$\Delta T_e > \varepsilon_T$	$k_T = 1$
$ \Delta T_e  \leq \varepsilon_T$	$k_T = 2$
$\Delta T_e < -\varepsilon_T$	$k_T = 3$

TABLE 2: A Takahashi switching table.

$k_\Phi$	1	1	1	2	2	2
$k_T$	1	2	3	1	2	3
$S_\theta = 1$	$\bar{v}_2$	$\bar{v}_0$	$\bar{v}_6$	$\bar{v}_3$	$\bar{v}_7$	$\bar{v}_5$
$S_\theta = 2$	$\bar{v}_3$	$\bar{v}_7$	$\bar{v}_1$	$\bar{v}_4$	$\bar{v}_0$	$\bar{v}_6$
$S_\theta = 3$	$\bar{v}_4$	$\bar{v}_0$	$\bar{v}_2$	$\bar{v}_5$	$\bar{v}_7$	$\bar{v}_1$
$S_\theta = 4$	$\bar{v}_5$	$\bar{v}_7$	$\bar{v}_3$	$\bar{v}_6$	$\bar{v}_0$	$\bar{v}_2$
$S_\theta = 5$	$\bar{v}_6$	$\bar{v}_0$	$\bar{v}_4$	$\bar{v}_1$	$\bar{v}_7$	$\bar{v}_3$
$S_\theta = 6$	$\bar{v}_1$	$\bar{v}_7$	$\bar{v}_5$	$\bar{v}_2$	$\bar{v}_0$	$\bar{v}_4$

magnitude control and a two levels hysteresis comparator for torque control. Let  $\Delta T_e$  and  $\Delta\Phi_s$  be the torque and flux errors with respect to their reference values.

$$\begin{aligned} \Delta T_e &= T_{ref} - T_e \\ \Delta\Phi_s &= \Phi_{ref} - \Phi_s \end{aligned} \quad (20)$$

Let also  $\varepsilon_T$  and  $\varepsilon_\Phi$  be the considered values of associated hysteresis bands. Table 1 reports the different possible situations and associates two indexes  $k_T$  and  $k_\Phi$  for codification purpose.

In the sense of this codification, Table 2 defines Takahashi Switching Table where states for the sector location of stator flux vector.

TABLE 3: Flux and speed errors codification for two cases of loads.

Flux and speed errors	Hysteresis index for Load 1	Hysteresis index for load 2
$ \Delta\Phi_s  \leq \varepsilon_\Phi$	$k_\Phi = 1$	$k_\Phi = 1$
$ \Delta\Phi_s  > \varepsilon_\Phi$	$k_\Phi = 2$	$k_\Phi = 2$
$\Delta\omega > \varepsilon_\omega$	$k_\omega = 1$	$k_\omega = 3$
$ \Delta\omega  \leq \varepsilon_\omega$	$k_\omega = 2$	$k_\omega = 2$
$\Delta\omega < -\varepsilon_\omega$	$k_\omega = 3$	$k_\omega = 1$

#### 4. Extension of the DTC Scheme to Direct Speed Estimation and Control

It has seen in the previous section that electromagnetic torque varies in the same sense as stator flux vector angle  $\theta_s$ . Therefore, if the load torque-speed curve of an industrial process has positive slope over the operating area, machine speed should also vary in the same sense of  $\theta_s$ . Processes having linear, parabolic, or in general positive polynomial torque-speed curves correspond to this situation. A typical and didactic example is the case of an induction machine loaded by a dc generator. On the contrary, if the load mechanical torque-speed curve has a negative slope, such as machine tools, the speed should be adjusted is the reverse sense of flux angle  $\theta_s$ . Let these two cases of loads be noted "Load1" and "Load2," respectively.

Therefore, one can use the same DTC algorithm previously defined to control the motor speed with minor modification. This modification should not affect the switching table and should only affect its codification. First, it is necessary to change the input corresponding to electromagnetic torque  $T_e$  by an input associated to machine speed  $\omega$ . Hysteresis band  $\varepsilon_T$  corresponding to  $T_e$  should be consequently changed by an adequate band  $\varepsilon_\omega$ . Then, if the used load is "Load1" there is no additional modification to do. In contrary, if one deals with "Load2," he permutes indexes  $k_T = 1$  and  $k_T = 3$ . Table 1 is then transformed into Table 3 where

$$\Delta\omega = \omega_{ref} - \omega \quad (21)$$

Now, the problem is how to estimate motor electrical rotor speed  $\omega$ . This can be done according to SFOC and RFOC properties. This means that the potentialities of these two control options must be combined with DTC principle. For this purpose, assume that stator flux vector  $\bar{\varphi}_s$  is obtained by integration of stator back emf  $\bar{e}_s$  as indicated by (14) and rotor flux vector  $\bar{\varphi}_r$  is deduce from (3); stator current being measured. Stator flux magnitude  $\Phi_s$  and angle  $\theta_s$  and rotor flux magnitude  $\Phi_r$  and angle  $\theta_r$  are thus available. Also, quadrature component  $E_{qs}$  of  $\bar{e}_s$  with respect to vector  $\bar{\varphi}_s$  and quadrature current component  $I_{qs}$  with respect to vector  $\bar{\varphi}_r$  become available by setting:

$$E_{qs} = \mathfrak{I}_m(\bar{e}_s e^{-j\theta_s}) \quad (22)$$

$$I_{qs} = \mathfrak{I}_m(\bar{i}_s e^{-j\theta_r}) \quad (23)$$

As outlined in Section 2, (10) gives an estimate of instantaneous stator flux pulsation  $\omega_s$ . On the other hand, electrical

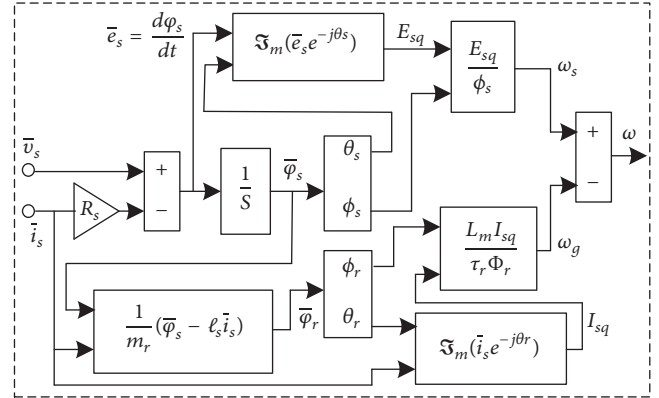


FIGURE 3: Schematic diagram of rotor speed estimation.

rotor-slip pulsation  $\omega_{sl}$  can be derived from (12) that needs rotor flux magnitude  $\Phi_r$  and quadrature current component  $I_{qs}$  with respect to vector  $\bar{\varphi}_r$ . By considering the assumption that in steady state, fluxes vectors  $\bar{\varphi}_s$  and  $\bar{\varphi}_r$  have the same pulsation [27] and one can estimate electrical machine speed  $\omega$  by

$$\omega \approx \frac{E_{qs}}{\Phi_s} - \frac{MI_{qs}}{\tau_r \Phi_r} \quad (24)$$

In the previous equation,  $E_{qs}$  and  $I_{qs}$  are filtered values of  $E_{qs}$  and  $I_{qs}$ , respectively. Note here that there is no need to filter flux magnitudes  $\Phi_s$  and  $\Phi_r$  because they are sufficiently smooth. Furthermore, simple first order transfer functions with constant time about 5 ms are sufficient to have acceptable smooth signal. The hypothesis considering equality of  $\omega_s$  and  $\omega_r$  can be a subject to discuss. However, keeping in mind that speed command is executed with some delay with respect to flux command; this hypothesis will be verified in practical implementation.

It is also important to note that error between actual rotor speed sensed for example by a tachometer or encoder and estimated speed defined by (24) can only be important during the first instant of the motor start-up operation. This has no effect on the final accuracy of the proposed estimation procedure because the estimated speed value is dominated by the first right term of (24). In other words, estimated stator flux pulsation that governs speed is the direct result of dc link inverter voltage and the controlled stator flux magnitude. Figure 3 illustrates the block diagram of the proposed algorithm to estimate motor electrical rotor speed.

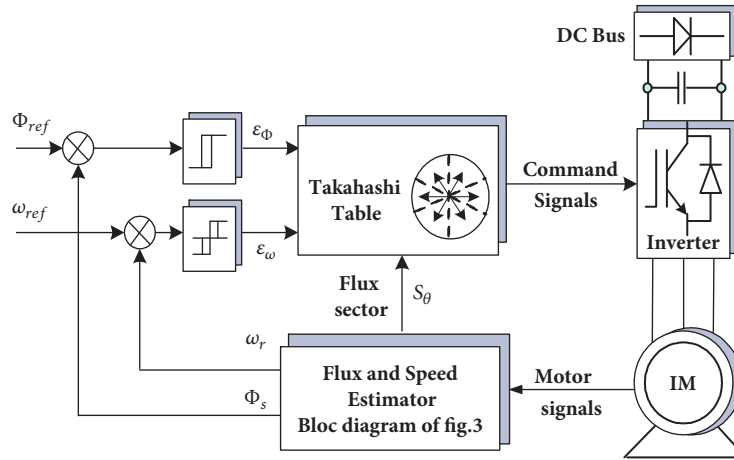


FIGURE 4: General Structure of the proposed SSDC control.



FIGURE 5: Photo of one side of the experimental setup.

As a result of this development, Figure 2 is transformed into Figure 4

We note here that this structure can be used as direct voltage control structure by replacing the input electrical rotor speed  $\omega_r$  by stator electrical speed  $\omega_s$ .

## 5. Real Time Experimental Validation

**5.1. Brief Description of the Benchmark.** The previous developed algorithm is implemented and tested in an experimental environment. Photo of Figure 5 presents actual views of the experimental setup. The benchmark consists of

- (i) a dSpace DS1104 controller board with TMS320F240 slave processor and ADC interface board CP1104. The DS1104 board is installed in Intel(R) Pentium(R) D CPU 3.4 GHz PC for software development and results visualization,
- (ii) a four poles induction motor loaded with a dc generator. Actual rotor speed is sensed from a tachometer coupled to machine shaft. Motor parameters and rated values are given below:

$$\begin{aligned} R_s &= 7.5 \, \Omega, R_r = 6.5 \, \Omega, L_s = L_r = 0.354 \, \text{H}, M = 0.34 \, \text{H}, \\ p &= 2, F = 50 \, \text{Hz}, W_n = 293.22 \, \text{rad/s}, P_n = 1 \, \text{KW}, \\ \cos \varphi_n &= 0.78, 220\text{V}/380 \, \text{V}. \end{aligned}$$

- (iii) a three-phase VSI whose dc bus voltage is generated by a rectifier connected to 400 V 50 Hz AC electrical sources,
- (iv) a four channels 150 MHz digital oscilloscope and two channels 20 MHz analog oscilloscope support the experiment for online recording and visualization,
- (v) current and voltage sensors LEM-based and calibrated so that the analogue obtained signals should remain in the range 0 to  $\pm 10$  V required by dSpace converters.

The benchmark includes many other devices such as standard measurement equipment, analogue signal filters, analogues circuits defining d-q voltage, and currents components.

**5.2. Results and Comments.** To evaluate the performance of the proposed SSDC algorithm, it was implemented in Simulink dSPACE DS1104 environment. The implemented structure is composed by four blocs: voltage and current acquisition, flux and speed estimation, switching table and command signals. A constant switching period  $T_s = 50 \, \mu\text{s}$  is considered. The three-phase VSI is supplied by a dc voltage  $V_{dc} = 500 \, \text{V}$  and motor windings are star connected. Induction motor is loaded by a dc generator giving an open circuit voltage about 150 V at nominal speed. This generator supplies an adjustable resistance. All results are realized in real time closed loop control.

**Case 1 (no load test).** This case verifies the algorithm for a motor start-up scenario under no load condition. Stator flux and electrical rotor speed commands are set to  $\Phi_{ref} = 1 \, \text{Wb}$  and  $\omega_{ref} = 293 \, \text{rad/s}$ , respectively. Associated hysteresis bands are taken equal to 5% of the command values;  $\epsilon_T = 0.05 \, \text{Wb}$  and  $\epsilon_\omega = 14.7 \, \text{rad/s}$ . Stator flux vector pulsation  $\omega_s$  and rotor slip frequency  $\omega_{sl}$  are filtered with first-order transfer functions of 10 ms time constants. Figure 6 compares the estimated motor speed (grey color) to the actual speed (dark color) acquired from a dc tachometer. These signals are given in electrical values. It is here to note that the

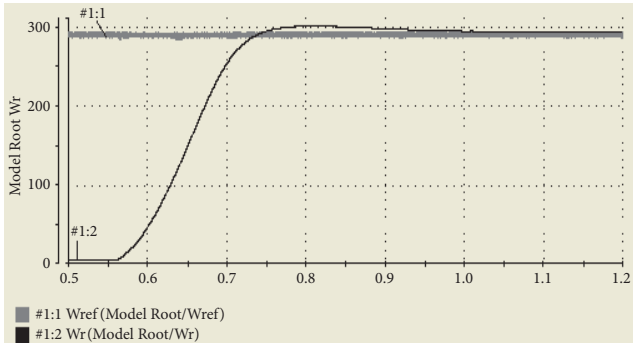


FIGURE 6: Predicted and actual speed (rad/s) versus time (s).

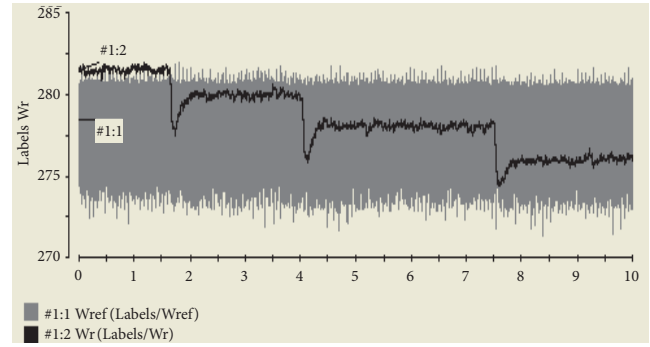


FIGURE 9: Estimated and actual speed during load changing.

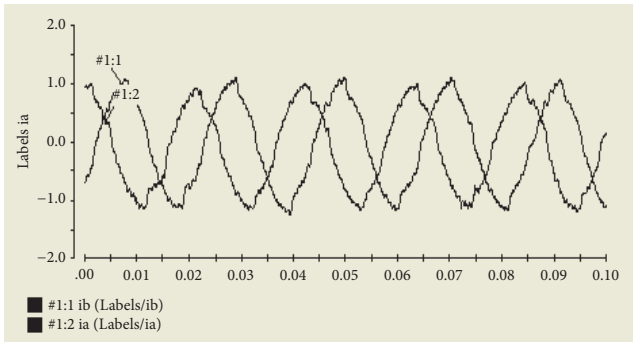


FIGURE 7: Instantaneous waveform of measured stator current.

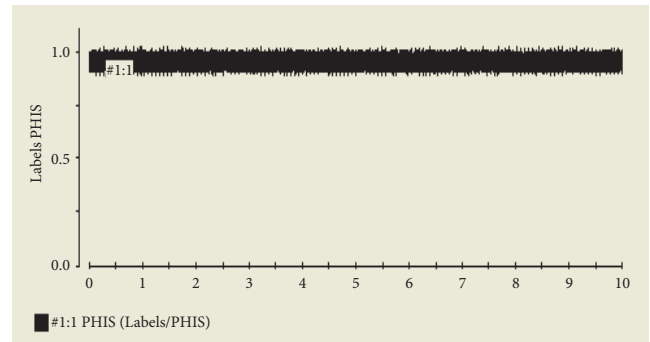


FIGURE 10: Stator flux magnitude during load changing.

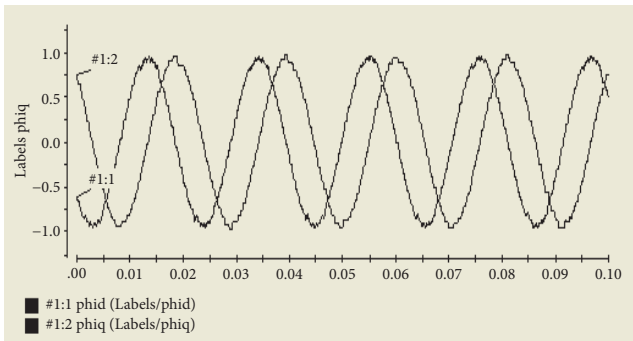


FIGURE 8: Instantaneous waveform of stator flux.

actual speed is only used for the comparison purpose. This figure proves that the control scheme has worked successfully. Estimated speed is very close to the reference value  $\omega_{ref}$ . The ripple is not significant. This question will be discussed in Case 3. The overshoot effect on the actual speed is 2.3% and is rapidly damped.

Figure 7 shows instantaneous waveforms of stator currents a and b in steady state. The observed distortion is related to the fact that the motor is not loaded. Figure 8 gives the temporal waveforms of d-q components of stator flux vector. This confirms that quality of obtained signals is very similar to that of standard DTC technique.

Case 2 (test under load varying). From the no load steady state operating point previously described, three steps of

motor load are executed by closing the dc generator armature circuit on successive three decreasing resistances. The reference values and hysteresis bands are those of Case 1. Figure 9 shows that the estimated speed (grey color) has an average value 277 rad/s. The programmed hysteresis band is therefore well respected. Actual motor speed (dark color) has changed from no load condition to full load condition of about 5 rad/s which corresponds to 1.78% with respect to initial condition and it also remains in the hysteresis band. Stator flux magnitude is well regulated as shown by Figure 10. This result implies that speed sensorless objective is well achieved.

Figures 11, 12, and 13 show stator power, electromagnetic torque, and rotor slip frequency behaviors, respectively. The good stability of signal trajectories in fast and important load changing is observed.

Case 3 (speed tolerance enhancement). During simulation and practical tests, it was discovered that the speed hysteresis band could be reduced to a very high precision level. In fact, the proposed control scheme works very well even if one imposes a severe speed hysteresis band around 1 to 2%. This performance cannot be realized in the standard DTC algorithm with this tolerance for the torque. Ripple range of machine electromagnetic torque is very sensitive to the switching period and dc bus voltage of the VSI. A severe torque hysteresis band exhibits a dramatic full down of the DTC algorithm. The same phenomenon occurs if

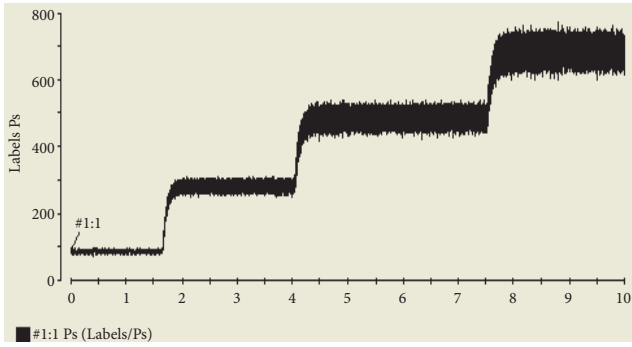


FIGURE 11: Stator power evolution during load changing.

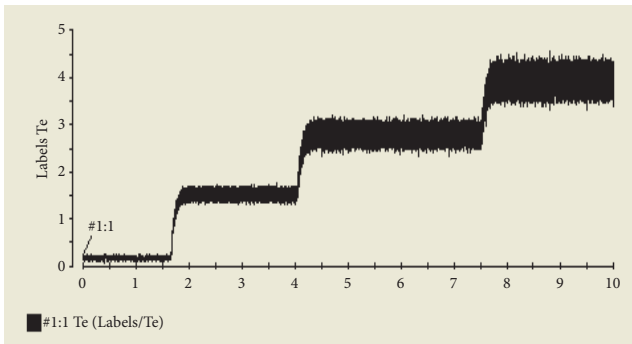


FIGURE 12: Torque evolution during load changing.

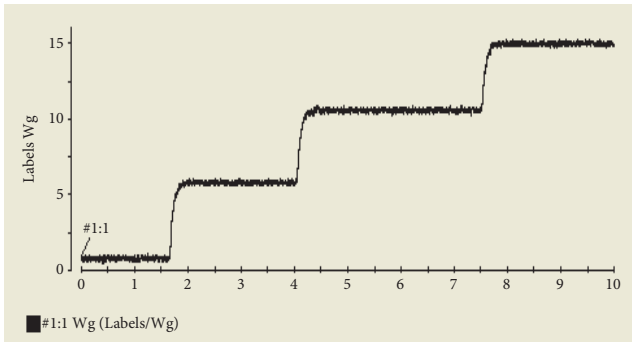


FIGURE 13: Rotor slip pulsation evolution during load changing.

one proceeds to filter the torque signal. For the proposed algorithm, filtering speed estimate is possible.

To illustrate these observations, speed tolerance was reduced to 2% (5.86 rad/sec) while keeping other data of Case 1. Figure 14 corresponds to this case and shows estimated motor speed (grey color) and its actual value (dark color). Estimated value remains between 290 and 282 rad/s which corresponds to an average value closed to 286 rad/s. This means that there is an error of 2.4% with respect to the reference value  $\omega_{ref} = 293 \text{ rad/s}$ . When calculating the actual errors corresponding to the difference between actual speed and command speed, an error of 3.1% was found. Rotor slip pulsation  $\omega_g$  is shown by Figure 15. Its final value in steady

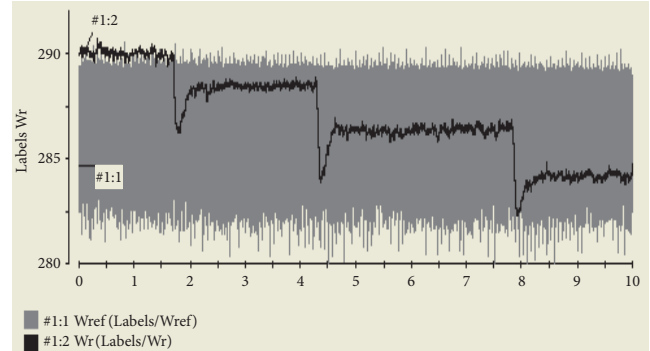


FIGURE 14: Estimated and actual motor speed with 2% hysteresis band.

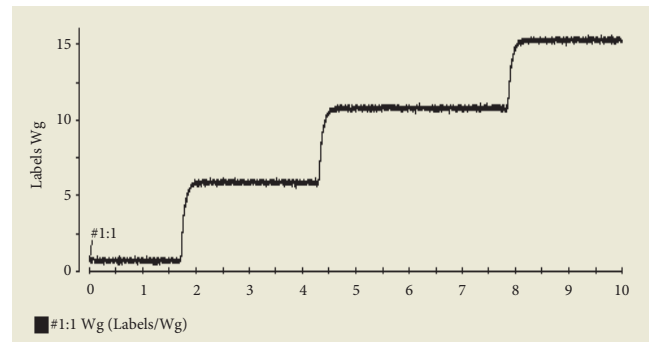


FIGURE 15: Evolution of rotor slip pulsation with 2% hysteresis band.

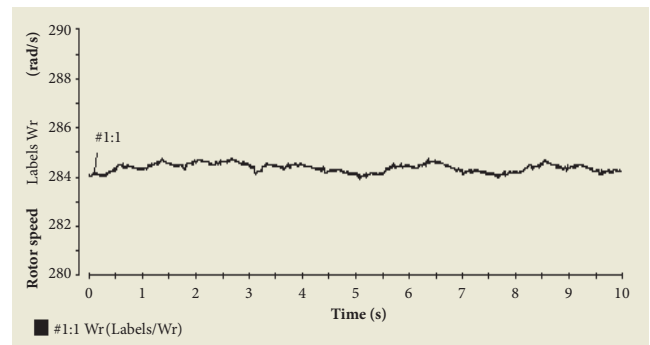


FIGURE 16: Actual electrical machine speed in unregulated scenario.

state with full load is close to 15.5 rad/s. This means that average value of stator pulsation  $\omega_s$  is 301 rad/s.

To confirm the promising accuracy of developed approach, another program that controls stator flux magnitude and frequency by PI regulators under SPWM modulation technique was used also in real time. Reference values of  $\Phi_s$  and  $\omega_s$  are, respectively, set to 1Wb and 301 rad/s. Figure 16 shows that the electrical machine speed is 284 rad/s. That value implies a rotor slip frequency of 17 rad/s which is sufficiently compatible with Figure 13.

Case 4 (direct frequency control). It is obvious that the developed algorithm can be used for direct control of stator

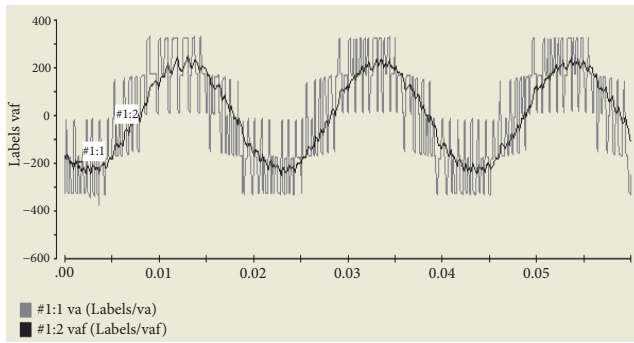


FIGURE 17: Voltage output in DVC case.

electrical frequency. The input  $\omega$  of the Takahashi table is simply replaced by  $\omega_s$ . In this case, the algorithm becomes a direct voltage control (DVC) solution. In fact, imposing stator flux magnitude and frequency defines the voltage to supply the motor. This solution was successfully tested and the demanding regime was obtained as shown by Figure 17 corresponding to a demanded frequency of 50 Hz. This figure superposes the switched voltage waveform and the filtered one.

## 6. Conclusion

A direct speed estimation and control scheme has been developed theoretically and practically validated in this work. The proposed approach combines properties of FOC and DTC techniques. It extends DTC structure to speed sensorless direct control. The idea is focused on how to use standard Takahashi switching table to control induction machine speed. Software implementation needs no major modification of the standard DTC scheme. All necessary developments are presented and commented. Real time practical results obtained by the dSpace DS1104 board have good performances. In fact, the error between estimated and measured actual speed does not exceed 2.4%. The proposed technique can provide interesting benefit for industrial applications because it avoids using fragile speed sensors in hostile environment. Furthermore, the method can work as direct voltage control structure by controlling stator electrical frequency.

Admittedly, control without a speed sensor is nowadays a hot topic, especially in terms of the constraints of adaptation of the parameters; adaptation that does not reduce the dynamic stability of the algorithm. This is our perspective subject.

## Data Availability

The data used to support the findings of this study are included within the article.

## Conflicts of Interest

The authors declare that they have no conflicts of interest.

## References

- [1] F. Wang, Z. Zhang, X. Mei, J. Rodríguez, and R. Kennel, "Advanced Control Strategies of Induction Machine: Field Oriented Control, Direct Torque Control and Model Predictive Control," *Energies*, vol. 11, no. 1, p. 120, 2018.
- [2] Z. Guo, J. Zhang, Z. Sun, and C. Zheng, "Indirect Field Oriented Control of Three-phase Induction Motor Based on Current-source Inverter," *Procedia Engineering*, vol. 174, pp. 588–594, 2017.
- [3] H. Krisztián and K. Márton, "Speed Sensorless Field Oriented Control of Induction Machines Using Unscented Kalman Filter," in *Proceedings of the IEEE International Conference OPTIM & Intl ACEMP*, pp. 25–27, Brasov, Romania, 2017.
- [4] C. Liu and Y. Luo, "Yixiao Luo, Overview of advanced control strategies for electric machines," *Chinese Journal of Electrical Engineering*, vol. 3, no. 2, pp. 53–61, September 2017.
- [5] R. Kaur and G. S. Brar, "Induction motor drives-A literature review," *Control Theory and Technology*, vol. 9, no. 16, pp. 8071–8081, 2016.
- [6] Y. Wang, N. Niimura, and R. D. Lorenz, "Real-time parameter identification and integration on deadbeat-direct torque and flux control (DB-DTFC) without inducing additional torque ripple," in *Proceedings of the 2015 IEEE Energy Conversion Congress and Exposition*, pp. 2184–2191, Montreal, QC, Canada, September 2015.
- [7] R. Kumar, S. Das, and A. K. Chattopadhyay, "Comparative assessment of two different model reference adaptive system schemes for speed-sensorless control of induction motor drives," *IET Electric Power Applications*, vol. 10, no. 2, pp. 141–154, 2016.
- [8] T. Sutikno, N. R. N. Idris, and A. Jidin, "A review of direct torque control of induction motors for sustainable reliability and energy efficient drives," *Renewable & Sustainable Energy Reviews*, vol. 32, pp. 548–558, 2014.
- [9] H. M. Soliman, "Performance characteristics of induction motor with field oriented control compared to direct torque control," *International Journal of Power Electronics and Drive Systems*, vol. 7, no. 4, pp. 1125–1133, 2016.
- [10] C. Reddy, K. K. Prabhakar, A. K. Singh, and P. Kumar, "Flux estimation in DTC for wide speed range," in *Proceedings of the 2016 IEEE Power and Energy Society General Meeting (PESGM)*, pp. 1–5, Boston, MA, USA, July 2016.
- [11] J. W. Finch and D. Giaouris, "Controlled AC electrical drives," *IEEE Transactions on Industrial Electronics*, vol. 55, no. 2, pp. 481–491, 2008.
- [12] D. Casadei, F. Profumo, G. Serra, and A. Tani, "FOC and DTC: two viable schemes for induction motors torque control," *IEEE Transactions on Power Electronics*, vol. 17, no. 5, pp. 779–787, 2002.
- [13] F. Naceri, S. Belkacem, M. Kercha, and T. Benmokrane, "Performance analysis of field-oriented control and direct torque control for sensorless induction motor drives," *Asian journal of Information Technology*, vol. 6, no. 2, pp. 215–221, 2007.
- [14] J. Kim, Y. Lee, J. Lee, and J. Lee, "Improvement of flux estimation using programmable low pass filter with synchronous angular frequency error compensator in sensorless AC induction motor," in *Proceedings of the IEEE Transportation Electrification Conference and Expo, Asia-Pacific (ITEC Asia-Pacific '16)*, pp. 924–928, Busan, South Korea, June 2016.
- [15] R. Zhao, Z. Xin, P. C. Loh, and F. Blaabjerg, "A novel flux estimator based on SOGI with FLL for induction machine

- drives,” in *Proceedings of the IEEE Applied Power Electronics Conference and Exposition (APEC '16)*, pp. 1995–2002, Long Beach, CA, USA, March 2016.
- [16] C. Lascu, I. Boldea, and F. Blaabjerg, “Direct torque control of sensorless induction motor drives: A sliding-mode approach,” *IEEE Transactions on Industry Applications*, vol. 40, no. 2, pp. 582–590, 2004.
- [17] I. Boldea, M. C. Paicu, G.-D. Andreescu, and F. Blaabjerg, ““Active Flux” DTFC-SVM sensorless control of IPMSM,” *IEEE Transactions on Energy Conversion*, vol. 24, no. 2, pp. 314–322, 2009.
- [18] M. Boussak and K. Jarray, “A high-performance sensorless indirect stator flux orientation control of induction motor drive,” *IEEE Transactions on Industrial Electronics*, vol. 53, no. 1, pp. 41–49, 2006.
- [19] R. Zhao, Z. Xin, P. C. Loh, and F. Blaabjerg, “A Novel Flux Estimator Based on Multiple Second-Order Generalized Integrators and Frequency-Locked Loop for Induction Motor Drives,” *IEEE Transactions on Power Electronics*, vol. 32, no. 8, pp. 6286–6296, 2017.
- [20] D. Stojić, M. Milinković, S. Veinović, and I. Klasnić, “Improved stator flux estimator for speed sensorless induction motor drives,” *IEEE Transactions on Power Electronics*, vol. 30, no. 4, pp. 2363–2371, 2015.
- [21] F. Wang et al., “Predictive Field-Oriented Control for Electric Drives,” *Chinese Journal of Electrical Engineering*, vol. 3, no. 1, pp. 73–78, June 2017.
- [22] H. Hiba, H. Ali, and H. Othmen, “DTC-SVM control for three phase induction motors,” in *Proceedings of the 2013 International Conference On Electrical Engineering and Software Applications (ICEESA)*, pp. 1–7, Hammamet, Tunisia, March 2013.
- [23] Y. Oguz and M. Dede, “Speed estimation of vector controlled squirrel cage asynchronous motor with artificial neural networks,” *Energy Conversion and Management*, vol. 52, no. 1, pp. 675–686, 2011.
- [24] F. Zidani and D. Diallo, “Direct torque control of induction motor with fuzzy stator resistance adaptation,” *IEEE Transactions on Energy Conversion*, vol. 21, no. 2, pp. 619–621, 2006.
- [25] Y. Liu, Z. Q. Zhu, and D. Howe, “Instantaneous torque estimation in sensorless direct-torque-controlled brushless DC motors,” *IEEE Transactions on Industry Applications*, vol. 42, no. 5, pp. 1275–1283, 2006.
- [26] O. Ellabban, J. Van Mierlo, and P. Lataire, “A comparative study of different control techniques for an induction motor fed by a Z-source inverter for electric vehicles,” in *Proceedings of the 3rd IEEE International Conference on Power Engineering, Energy and Electrical Drives*, Torremolinos, Spain, May 2011.
- [27] G. Foo, S. Sayeef, and M. F. Rahman, “Low-speed and standstill operation of a sensorless direct torque and flux controlled IPM synchronous motor drive,” *IEEE Transactions on Energy Conversion*, vol. 25, no. 1, pp. 25–33, 2010.

## Research Article

# A Finite-Time Disturbance Observer Based Full-Order Terminal Sliding-Mode Controller for Manned Submersible with Disturbances

Xing Fang  and Fei Liu 

Key Laboratory of Advanced Process Control for Light Industry (Ministry of Education), Institute of Automation, Jiangnan University, Wuxi 214122, China

Correspondence should be addressed to Xing Fang; [xingfang@jiangnan.edu.cn](mailto:xingfang@jiangnan.edu.cn)

Received 15 June 2018; Revised 10 September 2018; Accepted 16 September 2018; Published 30 September 2018

Academic Editor: Luis J. Yebra

Copyright © 2018 Xing Fang and Fei Liu. This is an open access article distributed under the Creative Commons Attribution License, which permits unrestricted use, distribution, and reproduction in any medium, provided the original work is properly cited.

A novel full-order terminal sliding-mode controller (FOTSMC) based on the finite-time disturbance observer (FTDO) is proposed for the “JIAOLONG” manned submersible with lumped disturbances. First, a finite-time disturbance observer (FTDO) is developed to estimate the lumped disturbances including the external disturbances and model uncertainties. Second, a full-order terminal sliding-mode surface is designed for the manned submersible, whose sliding-mode motion behaves as full-order dynamics rather than reduced-order dynamics in conventional sliding-mode control systems. Then, a continuous sliding-mode control law is developed to avoid chattering phenomenon, as well as to drive the system outputs to the desired reference trajectory in finite time. Furthermore, the closed-loop system stability analysis is given by Lyapunov theory. Finally, the simulation results demonstrate the satisfactory tracking performance and excellent disturbance rejection capability of the proposed finite-time disturbance observer based full-order terminal sliding-mode control (FTDO-FOTSMC) method.

## 1. Introduction

Manned submersibles have always been indispensable equipment for navy and marine development. Recently, there are great many manned submersibles that are on active service around the world [1], such as Alvin (USA), Shinkai 6500 (Japan), and so on. China’s manned submersible named “JIAOLONG” is designed for deep-sea exploration [2, 3]. JIAOLONG carried out its 7000 m exploration cruise in June 2012, which implies that JIAOLONG is able to cover 99.8% of the ocean area all over the world.

Manned submersibles always work in complicated ocean environment, including large water pressure in deep sea, time-varying ocean currents, unpredictable external disturbances, unknown obstacles, and so on [4, 5]. Furthermore, manned submersibles are known as strong nonlinear systems with various disturbances and time-varying dynamics [6, 7]. To the best of the authors’ knowledge, there are only few published papers regarding the robust controller design for manned submersibles, especially to attenuate the various

disturbances. Therefore, it is an open challenging research area to investigate the high-performance controller for manned submersibles with disturbances.

In the past decades, some attempts have been made to handle the control problem of manned submersibles. A robust controller based on  $H_\infty$  algorithm is developed for the manned submersible to suppress the external disturbances [8]. However, the control law is designed based on the worst case, which will result in overconservative control performance. Adaptive control techniques have been employed to deal with parameter uncertainties of the manned submersibles [9]. Unfortunately, the adaptive control may fail to handle the parameter uncertainties when the parameter changing speed is beyond its adapting capability. With the unique disturbance attenuation capability, sliding-mode control (SMC) methods have been employed to suppress the external disturbances and model uncertainties of manned submersibles [10–13]. However, the conventional SMC method will bring about chattering phenomenon for

its discontinuous control action [14]. Thus, some attempts have been made to alleviate the chattering phenomenon [15–17]. To sum up, the aforementioned control methods deal with the external disturbances and model uncertainties with the manner of feedback control action indirectly and slowly, rather than the feed-forward control action that is able to compensate the effects of the disturbances and uncertainties directly. Therefore, feedback control methods may fail to reject the severe disturbances and uncertainties of the manned submersible systems.

In recent years, the disturbance-observer-based control (DOBC) methods have been proposed to deal with the disturbances and uncertainties widely [18–20]. The DOBC technique is regarded as a two-degree-of-freedom control method, which consists of a nominal controller and a disturbance rejector [21]. The nominal controller is developed to achieve the requirements on tracking performance specifications and stability of the system. On the other hand, the disturbance rejector will be designed to meet the requirements on disturbance rejection and robustness for the system. That is to say, these two (often conflicting) requirements can be satisfied by developing the nominal feedback controller and disturbance rejector separately [22]. Furthermore, the DOBC methods have been applied to a wide range of engineering systems, such as permanent magnet synchronous motor (PMSM) system [23], unmanned helicopter system [24], power plant system [25], and so on.

Among the large number of DOBC methods, the combination of sliding-mode control technique and disturbance observer has drawn much attention of the scholars, which is called as disturbance-observer based sliding-mode control (DOB-SMC) method. For the reason that the SMC techniques not only have the powerful disturbance-attenuation capability, but also possess the simple design procedure of the controller. In the past few years, a nonlinear disturbance observer based sliding-mode control is employed to attenuate the external disturbances and model uncertainties, which is applied to MAGLEV suspension system [26]. In addition, a new disturbance observer based terminal sliding mode control method is designed for multiple-input multiple-output (MIMO) nonlinear system, which is able to suppress both the disturbances generated by an exogenous system and the disturbances with bounded  $H_2$  norm [27]. The article [28] develops an extended disturbance observer based sliding-mode control to reject both the matched and mismatched disturbances of the unmanned helicopter systems. Recently, an extended state observer based integral sliding-mode control method has been employed to attenuate the disturbances and uncertainties of the underwater robot system [29]. Although the aforementioned DOB-SMC methods are able to attenuate the disturbances effectively, the chattering phenomenon exists in the system all the same because of the discontinuous control actions. Furthermore, all the existing DOB-SMC methods belong to reduced-order sliding-mode control techniques, which means that the sliding-mode motion of the system behaves as desirable reduced-order dynamics rather than desirable full-order dynamics. Recently, a full-order sliding-mode control (FOSMC) algorithm is designed in article [30]. However, the sliding variable of the proposed

FOSMC algorithm is not available directly, which brings about the difficulties for controller implementation. Additionally, this FOSMC method attenuates the disturbances by the means of feedback control technique indirectly. Therefore, the disturbance rejection capability needs to be further improved.

In this paper, a novel finite-time disturbance observer based full-order terminal sliding-mode control (FTDO-FOTSMC) method is developed for the manned submersible subject to external disturbances and model uncertainties. By designing the full-order terminal sliding-mode surface, the ideal sliding-mode motion of the manned submersible system behaves as desirable full-order dynamics. Furthermore, with the estimation of the disturbances by FTDO, the continuous sliding-mode control law is designed to compensate the lumped disturbances of manned submersible and to meet the requirements on tracking performance. Finally, both the rigorous theoretical analysis and simulation results are presented to verify the superiority of the proposed FTDO-FOTSMC method.

The most outstanding novelties of this paper are highlighted as follows. First of all, under the proposed novel FTDO-FOTSMC method, the ideal sliding-mode motion of the system behaves as desirable full-order dynamics rather than reduced-order dynamics. Additionally, the FTDO-FOTSMC method is able not only to reject the external disturbances and model uncertainties, but also to eliminate the chattering phenomenon in conventional sliding-mode control systems. Furthermore, the FTDO-FOTSMC method is applied to the “JIAOLONG” manned submersible system, which achieves satisfactory control performance.

This paper is organized as follows. Section 2 analyzes the manned submersible system. A novel FTDO-FOTSMC method is proposed for the manned submersible system to reject the lumped disturbances in Section 3. The stability analysis and simulation results are presented in Sections 4 and 5, respectively. Finally, some conclusions are drawn in Section 6.

## 2. Manned Submersible Model

This section presents the nonlinear dynamic model of the manned submersible. The manned submersible is considered as a six-degree-of-freedom rigid body model [6]. Furthermore, it is subject to external disturbances and model uncertainties, which is treated as the lumped disturbances.

To develop the model of manned submersible, two reference frames, i.e., the navigation frame  $F_n = \{O_n, i_n, j_n, k_n\}$  and body frame  $F_b = \{O_b, i_b, j_b, k_b\}$ , are defined, which are shown in Figure 1.

The nonlinear model can be presented by the following [7]:

$$\dot{\eta} = J(\eta) v, \quad (1)$$

$$M\dot{v} + C(v)v + D(v)v + G(\eta) = F + d, \quad (2)$$

where  $\eta = [\eta_1^T \ \eta_2^T]^T \in R^6$  denotes the position and Euler angle vector in the navigation frame, and  $v = [v_1^T \ v_2^T]^T \in R^6$

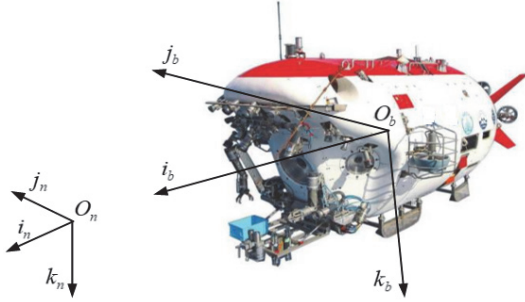


FIGURE 1: Navigation and body frames of manned submersible.

denotes the linear velocity and angular velocity vector in the body frame. Furthermore,  $\eta_1 = [x \ y \ z]^T$ ,  $\eta_2 = [\varphi \ \theta \ \psi]^T$ ,  $v_1 = [u \ v \ w]^T$  and  $v_2 = [p \ q \ r]^T$ . The notations  $J(\eta) \in R^{6 \times 6}$ ,  $M \in R^{6 \times 6}$ ,  $C(v) \in R^{6 \times 6}$ ,  $D(v) \in R^{6 \times 6}$  and  $G(\eta) \in R^6$  represent the rotation matrix, inertia matrix, Coriolis and centrifugal matrix, hydrodynamic damping matrix, and the gravity and buoyancy forces, respectively.  $F \in R^6$  represents the control forces and moments acting on the manned submersible, and  $d \in R^6$  denotes the external disturbances.

In practical engineering applications, it is difficult to acquire the accurate hydrodynamics coefficients of the manned submersible. Therefore, the hydrodynamics coefficients can be divided into two parts: nominal value and bias value.  $M = M_0 + \Delta M$ ,  $C(v) = C_0(v) + \Delta C(v)$ ,  $D(v) = D_0(v) + \Delta D(v)$  and  $G(\eta) = G_0(\eta) + \Delta G(\eta)$ , where  $(\cdot)_0$  denotes the nominal value, and  $\Delta(\cdot)$  denotes the bias value.

On the other hand, the manned submersible equips seven thrusters and one trim adjusting mercury pump, which are the main power sources of the submersible. Thus, the control forces and moments can be described by

$$F = Bu, \quad (3)$$

where  $u \in R^8$  is the true control input vector, and  $B \in R^{6 \times 8}$  is the force allocation matrix.

Considering the factors mentioned above, the dynamics equation (2) of the manned submersible can be rewritten by

$$M_0 \dot{v} + C_0(v)v + D_0(v)v + G_0(\eta) = Bu + d_s, \quad (4)$$

where  $d_s$  presents the lumped disturbances containing the external disturbances and model uncertainties, which can be described by

$$d_s = d - \Delta M \dot{v} - \Delta C(v)v - \Delta D(v)v - \Delta G(\eta). \quad (5)$$

Furthermore, for the convenience of controller design, the complete nonlinear model of the manned submersible can be written by

$$\dot{\eta} = v_a, \quad (6)$$

$$\dot{v}_a = -\overline{C}(\eta, v)v_a - \overline{D}(\eta, v)v_a - \overline{G}(\eta, v) + \overline{M}(\eta, v)Bu + d_l, \quad (7)$$

where  $v_a = J(\eta)v$  is the new state vector,  $d_l = \overline{M}(\eta, v)d_s$  is the new lumped disturbances.  $\overline{C}(\eta, v) = J(\eta)M_0^{-1}C_0(v)J^{-1}(\eta) -$

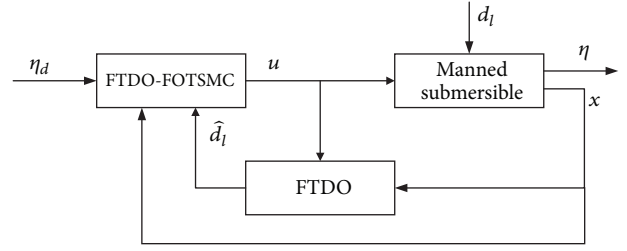


FIGURE 2: The controller structure of manned submersible.

$j(\eta)J^{-1}(\eta)$ ,  $\overline{D}(\eta, v) = J(\eta)M_0^{-1}D_0(v)J^{-1}(\eta)$ ,  $\overline{G}(\eta, v) = J(\eta)M_0^{-1}G(\eta)$  and  $\overline{M}(\eta, v) = J(\eta)M_0^{-1}$ . Additionally, for the sake of convenience in writing, the notations  $\overline{C}$ ,  $\overline{D}$ ,  $\overline{G}$  and  $\overline{M}$  are used to replace  $\overline{C}(\eta, v)$ ,  $\overline{D}(\eta, v)$ ,  $\overline{G}(\eta, v)$ , and  $\overline{M}(\eta, v)$  in this paper.

### 3. Controller Design

In this section, a novel finite-time disturbance observer based full-order terminal sliding mode controller (FTDO-FOTSMC) is designed for the manned submersible system. The controller is able to drive the position and Euler angle of the manned submersible to track the desired reference trajectory of  $\eta_d = [x_d \ y_d \ z_d \ \varphi_d \ \theta_d \ \psi_d]^T$  despite the presence of lumped disturbances  $d_l$ . The composite controller structure of manned submersible is illustrated in Figure 2.

**3.1. Finite-Time Disturbance Observer (FTDO).** A finite-time disturbance observer (FTDO) will be developed to estimate the lumped disturbances  $d_l$  of the manned submersible in finite time.

To design the FTDO conveniently, the dynamics model (7) of manned submersible is rewritten by

$$\dot{v}_a = f(\eta, v_a, u) + d_l, \quad (8)$$

where  $f(\eta, v_a, u) = -\overline{C}(\eta, v)v_a - \overline{D}(\eta, v)v_a - \overline{G}(\eta, v) + \overline{M}(\eta, v)Bu \in R^6$  is the vector function. Additionally, the notation  $f$  is used to replace  $f(\eta, v_a, u)$ .

A first-order FTDO is designed to estimate the lumped disturbances  $d_l$  as follows [31]:

$$\begin{aligned} \dot{\xi}_0(i) &= f(i) + \varepsilon_0(i), \\ \varepsilon_0(i) &= -\lambda_0 L^{1/2} |\xi_0(i) - v_a(i)|^{1/2} \text{sign}(\xi_0(i) - v_a(i)) \\ &\quad + \xi_1(i), \\ \dot{\xi}_1(i) &= \varepsilon_1(i), \\ \varepsilon_1(i) &= -\lambda_1 L \text{sign}(\xi_1(i) - \varepsilon_0(i)), \end{aligned} \quad (9)$$

where  $\xi_0(i)$  and  $\xi_1(i)$  are the estimations of  $v_a(i)$  and disturbance  $d_l(i)$ , respectively,  $i = 1, 2, \dots, 6$ .  $\lambda_0$ ,  $\lambda_1$  and  $L$  are the coefficients of the FTDO to be selected.

Considering the dynamics model (8) and FTDO (9), the error dynamics of the FTDO understood in the Filippov sense can be obtained by

$$\begin{aligned}\dot{e}_0(i) &= -\lambda_0 L^{1/2} |e_0(i)|^{1/2} \text{sign}(e_0(i)) + e_1(i), \\ \dot{e}_1(i) &\in -\lambda_1 L \text{sign}(e_1(i) - \dot{e}_0(i)) + [-L, L],\end{aligned}\quad (10)$$

where the estimation errors are defined by  $e_0 = \xi_0 - v_a$  and  $e_1 = \xi_1 - d_l$ . It follows from [31, 32] that the estimation errors  $e_0(t)$  and  $e_1(t)$  will converge to zero in finite time, which implies that there exists a time constant  $t_f > 0$  such that  $e_0(t) = 0$  and  $e_1(t) = 0$  for  $t > t_f$ . Additionally, it is true that  $\xi_1 = e_0$  for  $t > t_f$ .

**3.2. Finite-Time Disturbance Observer Based Full-Order Terminal Sliding Mode Controller (FTDO-FOTSMC).** Define the tracking errors of the manned submersible as

$$\begin{aligned}e_\eta &= \eta - \eta_d, \\ e_v &= v_a - \dot{\eta}_d,\end{aligned}\quad (11)$$

where  $\eta_d$  and  $\dot{\eta}_d$  are the desired reference trajectory and its derivative, respectively.

The error dynamics of the manned submersible can be obtained by

$$\begin{aligned}\dot{e}_\eta &= e_v, \\ \dot{e}_v &= -\bar{C}v_a - \bar{D}v_a - \bar{G} + \bar{M}Bu + d_l - \dot{\eta}_d.\end{aligned}\quad (12)$$

The full-order terminal sliding surface is designed by

$$\sigma = e_v + \int_0^\tau \left( \Lambda_\eta \frac{e_\eta}{\|e_\eta\|^{1-\alpha_\eta}} + \Lambda_v \frac{e_v}{\|e_v\|^{1-\alpha_v}} \right) d\tau, \quad (13)$$

where  $\Lambda_\eta = \text{diag}\{\lambda_{\eta 1}, \dots, \lambda_{\eta 6}\}$  and  $\Lambda_v = \text{diag}\{\lambda_{v 1}, \dots, \lambda_{v 6}\}$  are the positive definite diagonal matrices, whose elements make  $P_i(s) = s^2 + \lambda_{vi}s + \lambda_{\eta i}$  ( $i = 1, \dots, 6$ ) be Hurwitz polynomials. The parameters  $\alpha_\eta$  and  $\alpha_v$  satisfy the equation of  $\alpha_\eta = \alpha_v \alpha / (2\alpha - \alpha_v)$ , where  $\alpha \in (0, 1)$ .

Taking the time derivative of the full-order terminal sliding surface (13) along the error dynamics (12), we can obtain the sliding-mode dynamics as

$$\begin{aligned}\dot{\sigma} &= \dot{e}_v + \Lambda_\eta \frac{e_\eta}{\|e_\eta\|^{1-\alpha_\eta}} + \Lambda_v \frac{e_v}{\|e_v\|^{1-\alpha_v}} \\ &= -\bar{C}v_a - \bar{D}v_a - \bar{G} + \bar{M}Bu + d_l - \dot{\eta}_d + \Lambda_\eta \frac{e_\eta}{\|e_\eta\|^{1-\alpha_\eta}} \\ &\quad + \Lambda_v \frac{e_v}{\|e_v\|^{1-\alpha_v}}.\end{aligned}\quad (14)$$

The continuous sliding-mode control law can be designed as

$$\begin{aligned}u &= (\bar{M}B)^\dagger (u_{equ} + u_{smc}), \\ u_{equ} &= \bar{C}v_a + \bar{D}v_a + \bar{G} + \dot{\eta}_d - \Lambda_\eta \frac{e_\eta}{\|e_\eta\|^{1-\alpha_\eta}}\end{aligned}$$

$$- \Lambda_v \frac{e_v}{\|e_v\|^{1-\alpha_v}} - \xi_1,$$

$$u_{smc} = -k_1 \sigma - k_2 \frac{\sigma}{\|\sigma\|^{1-\beta}}, \quad (15)$$

where  $(\bar{M}B)^\dagger = (\bar{M}B)^T [(\bar{M}B)(\bar{M}B)^T]^{-1}$  represents the pseudo-inverse.  $k_1 > 0$ ,  $k_2 > 0$  and  $0 < \beta < 1$  are the controller parameters to be selected.

## 4. Stability Analysis

The stability analysis of the closed-loop manned submersible system is given in this section.

**Theorem 1.** *For the manned submersible system (12) with the full-order terminal sliding surface (13) under the continuous sliding-mode control law (15), the tracking error  $e_\eta$  of the manned submersible will converge to the origin in finite time despite the presence of lumped disturbances.*

*Proof.* In the first step, we will show that the bounded estimation errors  $e_1$  will not make the sliding variable  $\sigma$  go to infinity in finite time.

Substituting the sliding-mode control law (15) into the sliding-mode dynamics (14), we can obtain the closed-loop sliding-mode dynamics as follows:

$$\dot{\sigma} = -k_1 \sigma - k_2 \frac{\sigma}{\|\sigma\|^{1-\beta}} + e_1, \quad (16)$$

where  $e_1 = \xi_1 - d_l$  is estimation error of the FTDO. Furthermore, according to the Section 3.1, we can obtain that the estimation error  $e_1$  will converge to zero in finite time  $t_f > 0$ .

Define a finite-time bounded (FTB) function [33] for (16) as

$$V_1(\sigma) = \frac{1}{2} \sigma^T \sigma. \quad (17)$$

Taking the time derivative of the FTB function (17) along the dynamics (16), we can obtain the following:

$$\begin{aligned}\dot{V}_1(\sigma) &= \sigma^T \dot{\sigma} \\ &= \sigma^T \left( -k_1 \sigma - k_2 \frac{\sigma}{\|\sigma\|^{1-\beta}} + e_1 \right) \\ &= -k_1 \|\sigma\|^2 - k_2 \|\sigma\|^{1+\beta} + \sigma^T e_1 \\ &\leq \sigma^T e_1 \\ &\leq \frac{1}{2} (\|\sigma\|^2 + \|e_1\|^2) \\ &\leq K_{v1} V_1 + L_{v1},\end{aligned}\quad (18)$$

where  $K_{v1} = 1$  and  $L_{v1} = (1/2)\|e_1\|^2$ .

Therefore, it can be acquired from (18) that  $V_1(\sigma)$  and so  $\sigma$  will not escape to infinity in any finite time.

In the second step, we will show that the bounded sliding variable  $\sigma$  will not drive  $e_\eta$  and  $e_v$  to infinity in finite time.

According to the manned submersible system (12) and the full-order terminal sliding surface (13), we can obtain the error dynamics as follows:

$$\begin{aligned} \dot{e}_\eta &= e_v, \\ \dot{e}_v &= -\Lambda_\eta \frac{e_\eta}{\|e_\eta\|^{1-\alpha_\eta}} - \Lambda_v \frac{e_v}{\|e_v\|^{1-\alpha_v}} + \dot{\sigma}. \end{aligned} \quad (19)$$

Define a finite-time bounded (FTB) function for (19) as

$$V_2(e_\eta, e_v) = \frac{1}{2}e_\eta^T e_\eta + \frac{1}{2}e_v^T e_v. \quad (20)$$

Taking the time derivative of the FTB function (20) along the dynamics (19), and using the inequality  $\|x\|^\rho < 1 + \|x\|$  for  $\rho \in (0, 1)$ , we can obtain the following:

$$\begin{aligned} \dot{V}_2(e_\eta, e_v) &= \frac{1}{2}e_\eta^T \dot{e}_\eta + \frac{1}{2}e_v^T \dot{e}_v = e_\eta^T \dot{e}_\eta + e_v^T \dot{e}_v = e_\eta^T e_v \\ &+ e_v^T \left( -\Lambda_\eta \frac{e_\eta}{\|e_\eta\|^{1-\alpha_\eta}} - \Lambda_v \frac{e_v}{\|e_v\|^{1-\alpha_v}} + \dot{\sigma} \right) \\ &\leq \|e_\eta\| \|e_v\| + \|e_v\| (\gamma_\eta \|e_\eta\|^{\alpha_\eta} + \gamma_v \|e_v\|^{\alpha_v} + k_1 \|\sigma\| \\ &\quad + k_2 \|\sigma\|^\beta + \|e_1\|) \\ &\leq \|e_\eta\| \|e_v\| + \|e_v\| (\gamma_\eta (1 + \|e_\eta\|) + \gamma_v (1 + \|e_v\|) \\ &\quad + k_1 \|\sigma\| + k_2 (1 + \|\sigma\|) + \|e_1\|) \\ &\leq \frac{\|e_\eta\|^2 + \|e_v\|^2}{2} + \gamma_\eta \left( \frac{\|e_v\|^2 + 1}{2} + \frac{\|e_v\|^2 + \|e_\eta\|^2}{2} \right) \\ &\quad + \gamma_v \left( \frac{\|e_v\|^2 + 1}{2} + \|e_v\|^2 \right) \\ &\quad + k_1 \frac{\|e_v\|^2 + \|\sigma\|^2}{2} + k_2 \left( \frac{\|e_v\|^2 + 1}{2} + \frac{\|e_v\|^2 + \|\sigma\|^2}{2} \right) \\ &\quad + \frac{\|e_v\|^2 + \|e_1\|^2}{2} \\ &\leq \left( \frac{1}{2} + \frac{\gamma_\eta}{2} \right) \|e_\eta\|^2 + \left( 1 + \gamma_\eta + \frac{3\gamma_v}{2} + \frac{k_1}{2} + k_2 \right) \|e_v\|^2 \\ &\quad + \frac{\gamma_\eta}{2} + \frac{\gamma_v}{2} + \frac{k_1}{2} \|\sigma\|^2 + \frac{k_2}{2} (1 + \|\sigma\|^2) + \frac{1}{2} \|e_1\|^2 \\ &\leq K_{v2} V_2 + L_{v2}, \end{aligned} \quad (21)$$

where  $K_{v2} = 2 + 2\gamma_\eta + 3\gamma_v + k_1 + 2k_2$  and  $L_{v2} = \gamma_\eta/2 + \gamma_v/2 + (k_1/2)\|\sigma\|^2 + (k_2/2)(1 + \|\sigma\|^2) + (1/2)\|e_1\|^2$ .  $\gamma_\eta$  and  $\gamma_v$  denote the maximum eigenvalue of the matrices  $\Lambda_\eta$  and  $\Lambda_v$ , respectively.

Therefore, we can obtain that  $V_2(e_\eta, e_v)$  and so  $e_\eta, e_v$  will not escape to infinity in any finite time.

In the third step, we will show that the sliding variable  $\sigma$  will converge to the desired sliding surface  $\sigma = 0$  in finite time.

Since the estimation error  $e_1$  of FTDO will converge to zero in finite time, the sliding-mode dynamics (16) will reduce to

$$\dot{\sigma} = -k_1 \sigma - k_2 \frac{\sigma}{\|\sigma\|^{1-\beta}}. \quad (22)$$

It follows from [34] that the sliding variable  $\sigma$  is able to converge to the desired sliding surface  $\sigma = 0$  in finite time.

In the fourth step, we will show that the tracking error  $e_\eta$  of the manned submersible will converge to the origin in finite time.

Once the sliding surface  $\sigma = 0$  is achieved in finite time, the system dynamics (19) will reduce to

$$\begin{aligned} \dot{e}_\eta &= e_v, \\ \dot{e}_v &= -\Lambda_\eta \frac{e_\eta}{\|e_\eta\|^{1-\alpha_\eta}} - \Lambda_v \frac{e_v}{\|e_v\|^{1-\alpha_v}}. \end{aligned} \quad (23)$$

It can be obtained from [34] that system (23) is finite-time stable, which means that the tracking error  $e_\eta$  will converge to zero in finite time.

In summary, the position and Euler angle of the manned submersible is able to track the desired trajectory in finite time despite the presence of lumped disturbances.  $\square$

## 5. Simulation Results

This section presents some numerical simulation results to demonstrate the effectiveness of the proposed finite-time disturbance observer based full-order terminal sliding-mode controller (FTDO-FOTSMC) of the manned submersible. Additionally, in order to verify the superiority of the proposed control method, both the conventional full-order terminal sliding-mode control (FOTSMC) method [30] and nonlinear disturbance observer based sliding-mode control (NDO-SMC) method [26] are employed as comparative methods.

The parameters of the controllers are given as follows. The coefficients of the FTDO are  $\lambda_0 = 3$ ,  $\lambda_1 = 3$  and  $L = 12$ . The coefficients of the full-order terminal sliding surface are  $\Lambda_\eta = \text{diag}(6, \dots, 6)$ ,  $\Lambda_v = \text{diag}(9, \dots, 9)$ ,  $\alpha_\eta = 2/3$  and  $\alpha_v = 4/5$ . The control gains are  $k_1 = 1$ ,  $k_2 = 0.5$  and  $\beta = 0.5$ .

The lumped disturbances applied to the manned submersible system are given by  $d_t = \bar{M}(\eta, v)d_s = \bar{M}(\eta, v)(d_\Delta + d)$ , where  $d_\Delta$  represents the model uncertainties  $d_\Delta = -\Delta M\dot{v} - \Delta C(v)v - \Delta D(v)v - \Delta G(\eta)$  and  $d$  represents the external disturbances  $d = \sum_{i=1}^N [A_{i1} \cos(\omega_i t + \alpha_i) + A_{i2} \sin(\omega_i t + \alpha_i)]$  [35].

All the initial values of the state variables of the manned submersible are set to be zero, except for the position  $z_0 = -4\text{m}$ .

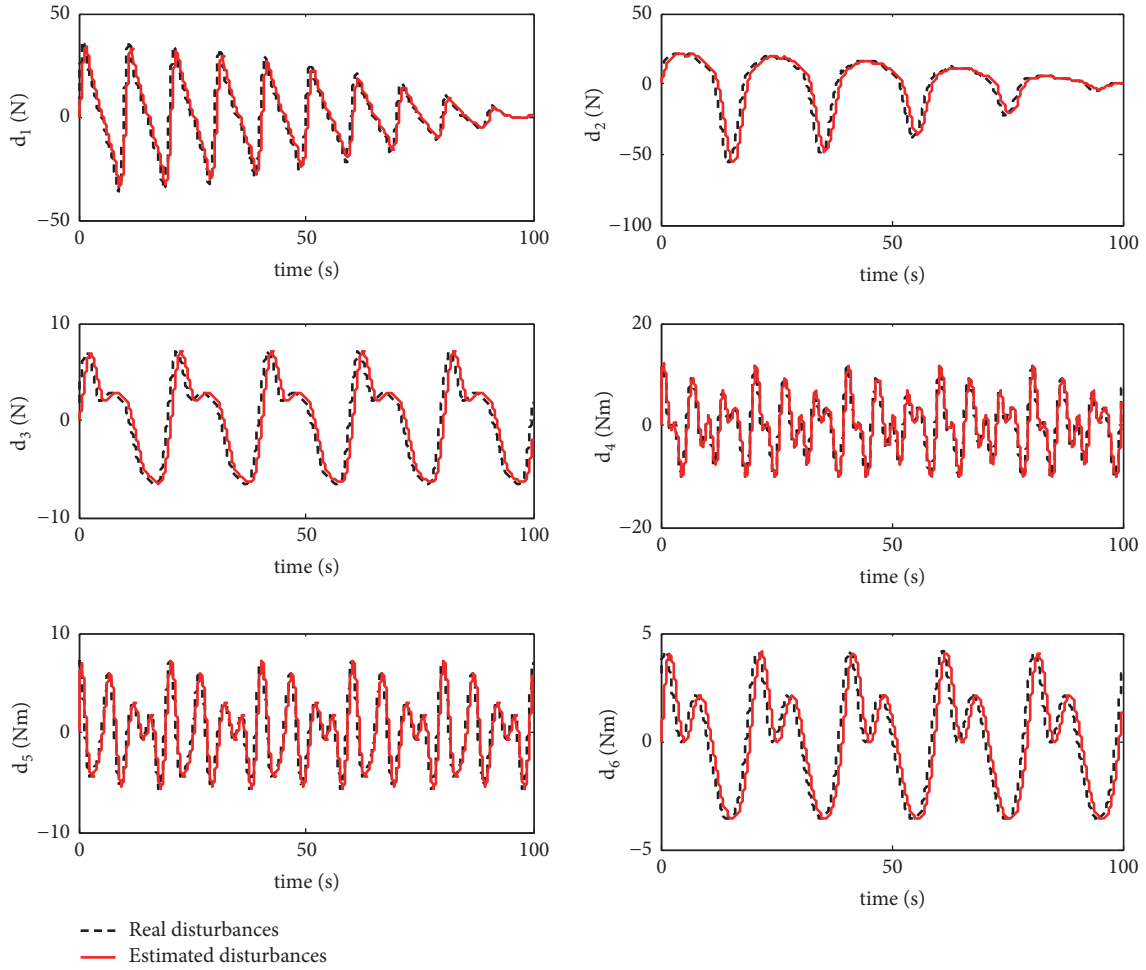


FIGURE 3: Disturbances estimation.

The desired reference trajectory is given by

$$\begin{aligned}
 x_r &= \begin{cases} 0 & t \leq 25s, \\ t - 25 & 25 < t \leq 50s, \\ 25 & 50 < t \leq 75s, \\ -t + 100 & t > 75s, \end{cases} \\
 y_r &= \begin{cases} t & t \leq 25s, \\ 25 & 25 < t \leq 50s, \\ -t + 75 & 50 < t \leq 75s, \\ 0 & t > 75s, \end{cases} \quad (24) \\
 z_r &= -4 - 0.01t \quad t > 0s, \\
 \varphi_r &= 0.1 \sin(0.3t) \quad t > 0s, \\
 \theta_r &= -0.05 \sin(0.3t) \quad t > 0s, \\
 \psi_r &= 0.005\pi t \quad t > 0s.
 \end{aligned}$$

The manned submersible is required to track a square reference trajectory in the X-Y plane. Meanwhile, it descends from the depth of 4 m to 5 m in the vertical direction. Additionally, the Euler angles of the manned submersible should track a time-varying trajectory. This comprehensive reference trajectory mainly examines the forward and sideslip control performances, as well as to verify the existence of the cross-couplings among pitch, roll and yaw axes.

The simulation results are shown in Figures 3–8. Figure 3 depicts the estimations of the lumped disturbances by FTDO. It can be observed that the FTDO is able to estimate the disturbances accurately and timely, which is the basis of compensating the lumped disturbances. Figures 4 and 5 illustrate the response curves of position and Euler angles, respectively. We can see that the decent tracking performances can be obtained in all six channels under the proposed FTDO-FOTSMC method. The position and Euler angles of the manned submersible under the conventional FOTSMC are almost able to track the reference trajectory. However, it suffers from fluctuations to some degree. Additionally, the position and Euler angles of the manned submersible under the NDO-SMC are able to track the reference trajectory. Its tracking accuracy is better than FOTSMC method, but worse

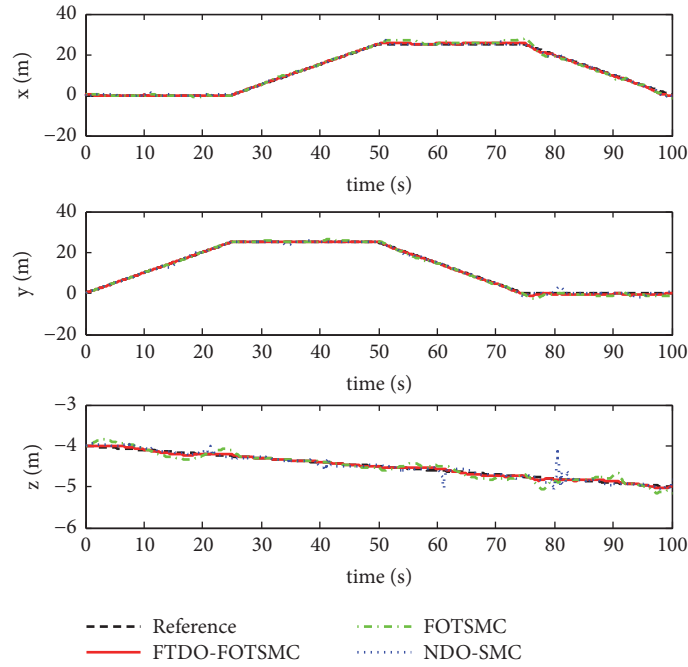


FIGURE 4: Response curves of position.

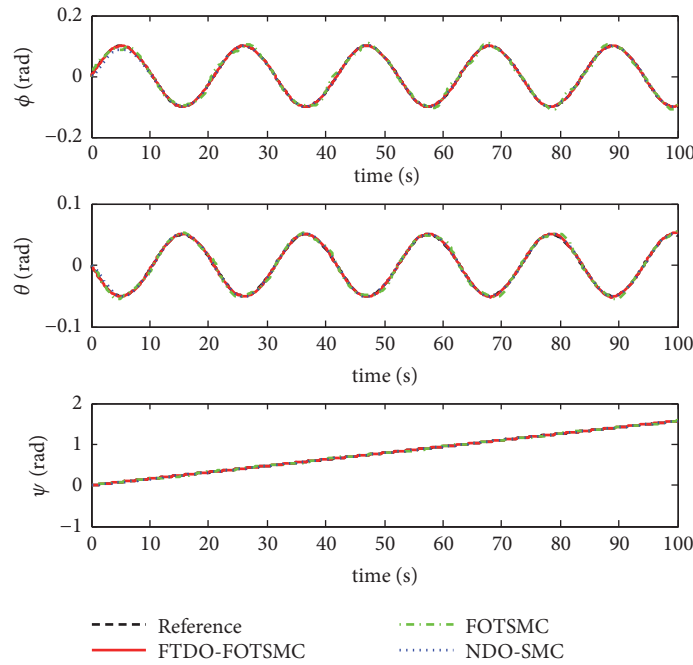


FIGURE 5: Response curves of Euler angles.

than FTDO-FOTSMC method. Moreover, to stand out the superiority of the proposed FTDO-FOTSMC method, the response curves of tracking errors under three control methods are given in Figure 6. The tracking errors of the manned submersible under the proposed FTDO-FOTSMC method are smaller than the conventional FOTSMC method and

NDO-SMC method, which implies that the proposed FTDO-FOTSMC method outperforms the conventional FOTSMC method and NDO-SMC method for its much more accurate tracking performance and milder transient process. Furthermore, the tracking performance of the manned submersible in X-Y plane is depicted in Figure 7. It can be acquired that the

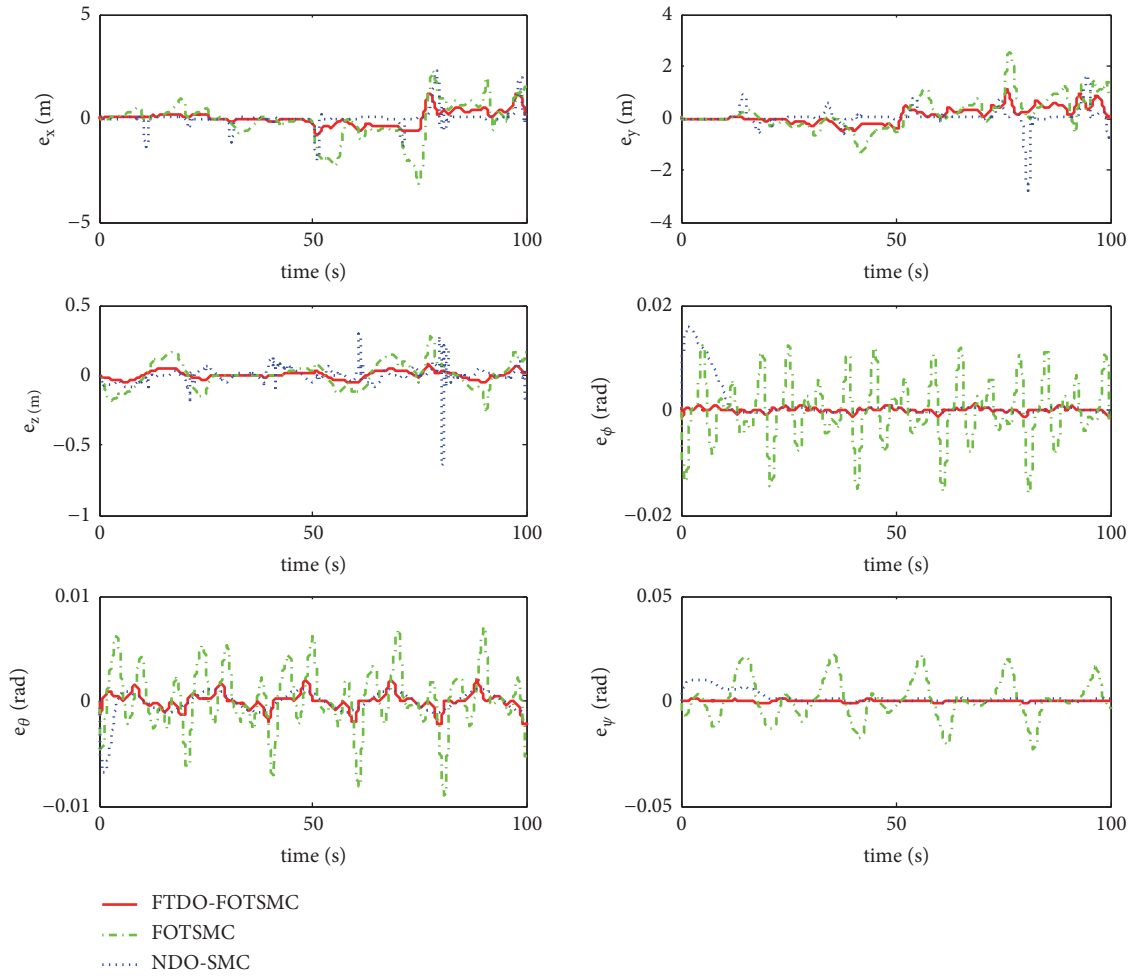


FIGURE 6: Response curves of tracking errors.

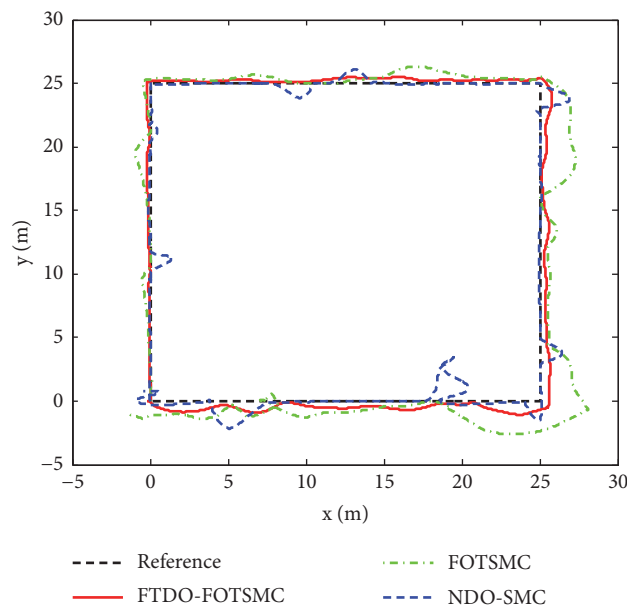


FIGURE 7: Response curves of position in X-Y plane.

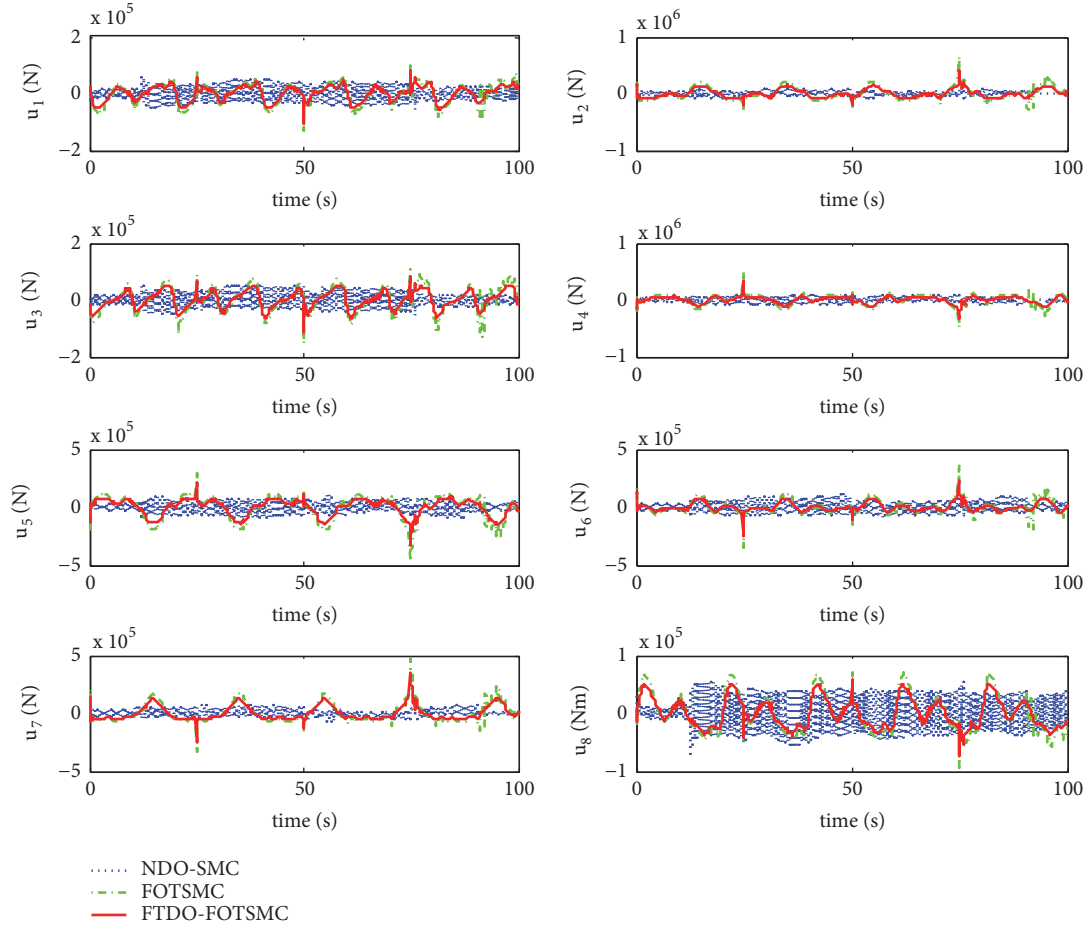


FIGURE 8: Response curves of control inputs.

TABLE 1: The root-mean-square (RMS) of tracking errors.

	$(e_x)_{RMS}$	$(e_y)_{RMS}$	$(e_z)_{RMS}$	$(e_\varphi)_{RMS}$	$(e_\theta)_{RMS}$	$(e_\psi)_{RMS}$
FTDO-FOTSMC	0.3591m	0.3289m	0.0277m	0.0005rad	0.0008rad	0.0004rad
FOTSMC	0.9082m	0.6322m	0.0920m	0.0061rad	0.0030rad	0.0097rad
NDO-SMC	0.4170m	0.4479m	0.0612m	0.0036rad	0.0012rad	0.0033rad

manned submersible is able to perform the square trajectory precisely under the proposed FTDO-FOTSMC method. On the other hand, both the conventional FOTSMC method and NDO-SMC method drive the manned submersible to track the square trajectory with relatively large errors. Finally, the response curves of control inputs are shown in Figure 8. With the continuous control law of the proposed FTDO-FOTSMC method and FOTSMC method, the chattering phenomenon can be alleviated greatly or even eliminated completely. However, the NDO-SMC method is subject to chattering phenomenon to a certain degree for its discontinuous control action.

To further demonstrate the superiority of the proposed FTDO-FOTSMC method, the tracking performance is compared quantitatively. The root-mean-square (RMS) that is a common criterion to measure the tracking performance

is given in Table 1. As reported in Table 1, the proposed FTDO-FOTSMC method attains the smaller RMS values than the conventional FOTSMC method and NDO-SMC method in all six channels, which reveals that the proposed FTDO-FOTSMC method is able to deal with the external disturbances and model uncertainties, as well as to achieve accurate tracking performance.

## 6. Conclusions

A novel finite-time disturbance observer based full-order terminal sliding mode control (FTDO-FOTSMC) method is proposed for the manned submersible with external disturbance and model uncertainties. With the proposed control method, the ideal sliding-mode motion of the manned

submersible system behaves as desirable full-order dynamics. Furthermore, the outputs of the manned submersible system are able to converge to the desired reference trajectory in finite time. Finally, both the stability analysis and simulation results demonstrate the effectiveness of the proposed FTDO-FOTSMC method for the manned submersible system. The future work will focus on the experimental tests on the manned submersible system. Additionally, the applications of the FTDO-FOTSMC method on unmanned underwater vehicles is another important work in future.

## Data Availability

The data used to support the findings of this study are included within the article.

## Conflicts of Interest

The authors declare that they have no conflicts of interest.

## Acknowledgments

This work is supported by the National Natural Science Foundation of China under grants 61803182, 61703118, and the Natural Science Foundation of Jiangsu Province under grants BK20180593, BK20180592.

## References

- [1] W. Kohnen, "2007 MTS overview of manned underwater vehicle activity," *Marine Technology Society Journal*, vol. 42, no. 1, pp. 26–37, 2008.
- [2] F. Liu, W. Cui, and X. Li, "China's first deep manned submersible, JIAOLONG," *Science China Earth Sciences*, vol. 53, no. 10, pp. 1407–1410, 2010.
- [3] D. Zhu, Q. Liu, and Z. Hu, "Fault-tolerant control algorithm of the manned submarine with multi-thruster based on quantum-behaved particle swarm optimisation," *International Journal of Control*, vol. 84, no. 11, pp. 1817–1829, 2011.
- [4] E. Zakeri, S. Farahat, S. A. Moezi, and A. Zare, "Path planning for unmanned underwater vehicle in 3D space with obstacles using spline-imperialist competitive algorithm and optimal interval type-2 fuzzy logic controller," *Latin American Journal of Solids and Structures*, vol. 13, no. 6, pp. 1054–1085, 2016.
- [5] E. Zakeri, S. Farahat, S. A. Moezi, and M. Zare, "Optimal robust control of an unmanned underwater vehicle independent of hydrodynamic forces using firefly optimization algorithm," in *Proceedings of the 24th Annual International Conference on Mechanical Engineering*, pp. 1–6, 2016.
- [6] T. I. Fossen, *Guidance and control of ocean vehicles*, Wiley, New York, NY, USA, 1994.
- [7] J. Y. Xie, W. B. Xue, H. Zhang, P. F. Xu, and W. C. Cui, "Dynamic modeling and investigation of maneuver characteristics of a deep-sea manned submarine vehicle," *China Ocean Engineering*, vol. 23, no. 3, pp. 505–516, 2009.
- [8] L. Moreira and C. Guedes Soares, "H2 and Hinfin; designs for diving and course control of an autonomous underwater vehicle in presence of waves," *IEEE Journal of Oceanic Engineering*, vol. 33, no. 2, pp. 69–88, 2008.
- [9] H. Wang, K. Liu, and S. Li, "Command filter based globally stable adaptive neural control for cooperative path following of multiple underactuated autonomous underwater vehicles with partial knowledge of the reference speed," *Neurocomputing*, vol. 27, no. 5, pp. 1478–1489, 2018.
- [10] B. Sun, D. Zhu, and S. X. Yang, "A bioinspired filtered backstepping tracking control of 7000-m manned submarine vehicle," *IEEE Transactions on Industrial Electronics*, vol. 61, no. 7, pp. 3682–3693, 2014.
- [11] R. Yu, Q. Zhu, G. Xia, and Z. Liu, "Sliding mode tracking control of an underactuated surface vessel," *IET Control Theory & Applications*, vol. 6, no. 3, pp. 461–466, 2012.
- [12] E. Zakeri, S. Farahat, S. A. Moezi, and A. Zare, "Robust sliding mode control of a mini unmanned underwater vehicle equipped with a new arrangement of water jet propulsions: Simulation and experimental study," *Applied Ocean Research*, vol. 59, pp. 521–542, 2016.
- [13] M. T. Alrifai and M. Zribi, "Sliding Mode Control of Chaos in a Single Machine Connected to an Infinite Bus Power System," *Mathematical Problems in Engineering*, vol. 2018, Article ID 2703684, 13 pages, 2018.
- [14] A. Šabanovic, "Variable structure systems with sliding modes in motion control—a survey," *IEEE Transactions on Industrial Informatics*, vol. 7, no. 2, pp. 212–223, 2011.
- [15] E. Zakeri, S. A. Moezi, and M. Eghtesad, "Tracking control of ball on sphere system using tuned fuzzy sliding mode controller based on artificial bee colony algorithm," *International Journal of Fuzzy Systems*, vol. 20, no. 1, pp. 295–308, 2018.
- [16] A. Levant, "Principles of 2-sliding mode design," *Automatica*, vol. 43, no. 4, pp. 576–586, 2007.
- [17] V. I. Utkin, *Sliding Modes in Control Optimization*, Springer, Berlin, Germany, 1992.
- [18] S. H. Li, J. Yang, W. H. Chen, and X. Chen, *Disturbance observer based control: methods and applications*, USA, Prentice-Hall, 2014.
- [19] J. Yang, J. Su, S. Li, and X. Yu, "High-order mismatched disturbance compensation for motion control systems via a continuous dynamic sliding-mode approach," *IEEE Transactions on Industrial Informatics*, vol. 10, no. 1, pp. 604–614, 2014.
- [20] B. Xu and F. C. Sun, "Composite intelligent learning control of strict-feedback systems with disturbance," *IEEE Transactions on Cybernetics*, vol. 48, no. 2, pp. 730–741, 2018.
- [21] Z. Gao, "On the centrality of disturbance rejection in automatic control," *ISA Transactions*, vol. 53, no. 4, pp. 850–857, 2014.
- [22] W. H. Chen, J. Yang, L. Guo, and S. H. Li, "Disturbance-observer-based control and related methods-an overview," *IEEE Transactions on Industrial Electronics*, vol. 63, no. 2, pp. 1083–1095, 2016.
- [23] J. Yang, W.-H. Chen, S. Li, L. Guo, and Y. Yan, "Disturbance/Uncertainty Estimation and Attenuation Techniques in PMSM Drives - A Survey," *IEEE Transactions on Industrial Electronics*, vol. 64, no. 4, pp. 3273–3285, 2017.
- [24] X. Fang, A. Wu, Y. Shang, and C. Du, "Multivariable Super Twisting Based Robust Trajectory Tracking Control for Small Unmanned Helicopter," *Mathematical Problems in Engineering*, vol. 2015, Article ID 620357, 13 pages, 2015.
- [25] L. Sun, Q. Hua, D. Li, L. Pan, Y. Xue, and K. Y. Lee, "Direct energy balance based active disturbance rejection control for coal-fired power plant," *ISA Transactions*, vol. 70, pp. 486–493, 2017.

- [26] J. Yang, S. Li, and X. Yu, "Sliding-mode control for systems with mismatched uncertainties via a disturbance observer," *IEEE Transactions on Industrial Electronics*, vol. 60, no. 1, pp. 160–169, 2013.
- [27] X. Wei and L. Guo, "Composite disturbance-observer-based control and terminal sliding mode control for non-linear systems with disturbances," *International Journal of Control*, vol. 82, no. 6, pp. 1082–1098, 2009.
- [28] X. Fang, A. Wu, Y. Shang, and N. Dong, "A novel sliding mode controller for small-scale unmanned helicopters with mismatched disturbance," *Nonlinear Dynamics*, vol. 83, no. 1-2, pp. 1053–1068, 2016.
- [29] R. Cui, L. Chen, C. Yang, and M. Chen, "Extended State Observer-Based Integral Sliding Mode Control for an Underwater Robot With Unknown Disturbances and Uncertain Non-linearities," *IEEE Transactions on Industrial Electronics*, vol. 64, no. 8, pp. 6785–6795, 2017.
- [30] Y. Feng, F. Han, and X. Yu, "Chattering free full-order sliding-mode control," *Automatica*, vol. 50, no. 4, pp. 1310–1314, 2014.
- [31] A. Levant, "Higher-order sliding modes, differentiation and output-feedback control," *International Journal of Control*, vol. 76, no. 9-10, pp. 924–941, 2003.
- [32] Y. B. Shtessel, I. A. Shkolnikov, and A. Levant, "Smooth second-order sliding modes: missile guidance application," *Automatica*, vol. 43, no. 8, pp. 1470–1476, 2007.
- [33] S. Li and Y. Tian, "Finite-time stability of cascaded time-varying systems," *International Journal of Control*, vol. 80, no. 4, pp. 646–657, 2007.
- [34] S. P. Bhat and D. S. Bernstein, "Geometric homogeneity with applications to finite-time stability," *Mathematics of Control, Signals, and Systems*, vol. 17, no. 2, pp. 101–127, 2005.
- [35] Z. Liu, "Ship Adaptive Course Keeping Control with Nonlinear Disturbance Observer," *IEEE Access*, vol. 5, pp. 17567–17575, 2017.

## Research Article

# Attitude Controller Design with State Constraints for Kinetic Kill Vehicle Based on Barrier Lyapunov Function

Tao Zhang , Jiong Li, Huaji Wang , ChuHan Xiao, and Wanqi Li

*Air and Missile Defense College, Air Force Engineering University, Xi'an, Shaanxi 710051, China*

Correspondence should be addressed to Tao Zhang; zhangtaov2016@163.com

Received 14 April 2018; Revised 22 July 2018; Accepted 9 August 2018; Published 5 September 2018

Academic Editor: Mihai Lungu

Copyright © 2018 Tao Zhang et al. This is an open access article distributed under the Creative Commons Attribution License, which permits unrestricted use, distribution, and reproduction in any medium, provided the original work is properly cited.

An adaptive attitude controller is designed based on Barrier Lyapunov Function (BLF) to meet the state constraints caused by side window detection. Firstly, the attitude controller is designed based on the BLF, but the stabilization function is complex and its time derivative will cause “differential explosion”. Therefore, Finite-time-convergent Differentiator (FD) is used to estimate the first derivative of the stabilization function. If the tracking error is outside the BLF's convergence domain, BLF controller cannot guarantee the error global convergence. Sliding mode controller (SMC) is used to make the system's error converge to set domain, and then the BLF controller could be used to ensure that the output constraint is not violated. Uncertainties and unknown time-varying disturbances usually make the control precision worse and Nonlinear Disturbance Observer (NDO) is designed for estimation and compensation uncertainties and disturbances. The pseudo rate modulator (PSR) is used to shape the continuous control command to pulse or on-off signals to meet the requirements of the thruster. Numerical simulations show that the proposed method can achieve state constraints, pseudo-linear operation, and high accuracy.

## 1. Introduction

With the development of small-size propulsion systems, accurate sensors, and precision guidance systems, the kinetic kill vehicle (KKV) is now becoming both technically and economically feasible [1–3]. In order to satisfy the requirements of intercepting hypersonic targets in near space, KKV is generally flying at a high speed and equipped with infrared imaging seeker. However, when KKV is flying in near space with high speed, strong aerodynamic heating will seriously affect the seeker detection accuracy. To solve this problem, the seeker is usually mounted on the KKV's lateral side to avoid heat-intensive areas in front of the body. The installation and detection method of configuring the seeker on the lateral side of the missile is defined as side window detection [4, 5].

Side window detection will inevitably affect the field of view of seeker and in order to ensure that the target is always located in the field of view, the elevation angle  $q_\varepsilon^b$  and the azimuth angle  $q_\beta^b$  in body-LOS coordinate should be maintained in  $[q_{\varepsilon \min}^b, q_{\varepsilon \max}^b]$  and  $[q_{\beta \min}^b, q_{\beta \max}^b]$ , and the system overshoot is within this range [6]. In the terminal

guidance, the control system is a fast variable relative to the guidance system, so we mainly rely on the control system to ensure that the target is always in the field of view of the seeker. It is necessary to constrain the steady-state performance and dynamic performance of the attitude control system to the set domain. The above problem can be attributed to the stabilization of the nonlinear system with output constraints.

The current methods of controller design, such as sliding mode control [7–9], backstepping control [10, 11], and dynamic surface control [12, 13], are usually unable to design the dynamic performance of the controller. Control design for the constrained nonlinear system is commonly carried out using a two-step approach. After a closed-loop system design has been determined, often without explicitly considering state constraints, the dynamic behavior is investigated most often by simulation studies. Control design is usually based on mathematical models, which are subject to uncertainties and unknown time-varying disturbances. Therefore, any control design approach should systematically account for both state constraints and uncertainty.

Constraint-handling methods based on set invariance [14], model predictive control [15], override control [16, 17], and reference governors [18] are well established. However, these methods are essentially based on numerical calculations, and the calculations are more complicated.

More recently, the use of BLF has been proposed to realize the output and state constraints for strict feedback and output feedback nonlinear system. Ngo [19] constructs an arctangent and logarithmic barrier function as the control Lyapunov function for the Brunovsky standard system and realizes state constraints. The work in [20] presented control designs for strict feedback nonlinear systems with a constant output constraint and [21, 22] further extend the results to strict feedback nonlinear systems with time-varying output constraint. Tee [23] rigorously proved that the backstepping controller designed with symmetric BLF or asymmetric BLF can ensure the system output is bounded for a strict feedback nonlinear system. But this method requires the system to be in a small convergence domain and the output to be continuously differentiable, and this is usually not satisfied in the actual system. Tee [24] then proposed an improved method. If the initial state of the system is outside the convergence domain, it is necessary to reselect the BLF to make the system converge to the set domain. This method can guarantee the system converges to the set domain, but the initial state is difficult to obtain and system cannot realize the adaptive control. In addition, BLF-based control has been applied to practical systems, such as electrostatic oscillators [25], flexible crane system [26], and diesel engines [27].

Many controllers designed with nonlinear control theory are continuous and they cannot be directly applied to the attitude control system of KKV. To solve this problem, many pulse modulators have been proposed to convert continuous control variables into a pulse or on-off signals, such as pulse width modulation (PWM), pulse frequency modulation (PFM), and pulse width pulse frequency modulation (PWPF) [2, 28–30]. PWPF modulation method is widely used in aircraft attitude control systems with its good control performance. Reference [2] uses the PWPF modulator to shape the continuous control command to pulse or on-off signals to meet the requirements of the reaction thrusters and the methods to select the appropriate parameters are presented in detail. Reference [28] discusses the performance of PWPF modulators in terms of approximate linear space, fuel consumption, and thruster operating frequency for the attitude control. In [29], the variable dead-zone PWPF modulator was designed, and the stability was proved by using the description function method. The simulation results show the superiority of the algorithm in fuel consumption and control accuracy. Reference [30] proposes a nonlinear objective optimization function for the limitations of PWPF modulator parameters setting. The genetic algorithm is used to optimize the parameters of the PWPF regulator which considers the performance requirements of guidance systems such as linear work area requirements, miss distance, and fuel consumption of PWPF regulators. PWPF can output pulse instructions of different width and the static characteristics are not related to the parameters of the aircraft, but the PWPF

modulator has the problem of phase lag which could cause instability of the system.

Motivated by the above discussions, to meet the state constraints caused by side window detection, an attempt is made to exploit Barrier Lyapunov Function to design the attitude controller. To break through the limitation that the initial error has to be in a small domain and the tracking error cannot guarantee global convergence, sliding mode control is used to make the tracking error converge to the set domain if the initial error is not in the set domain. What is more, BLF-based control relies on the accurate model and requires the output continuously differentiable, NDO is designed for estimation and compensation these uncertainties and disturbances, and FD is designed to estimate derivative. The special contributions of this paper are summarized as follows:

- (1) This paper investigate a BLF for KKV to meet the state constraints and achieve satisfactory dynamic performance and stationary performance compared with the existing work [2, 11].
- (2) To overcome the shortcoming which requires that the initial error has to be in a small domain, existing in the work [19, 23, 24], sliding mode control is used to make the tracking error converge to the set domain if the initial error is not in the set domain.
- (3) The PSR modulator is used to transform the continuous control law into the pulse control law. The constant thrust control is realized and the phase lag problem of the PWPF modulator is overcome compared with the existing work [2, 28, 30].

## 2. Problem Formulation and Preliminaries

*2.1. The Mathematical Model of KKV.* KKV is small enough to ignore the elastic vibration and study as a rigid body. The nonlinear equations of dynamic and kinematic are formulated as [11]

$$\begin{aligned}
 J_x \dot{\omega}_x + (J_z - J_y) \omega_y \omega_z &= M_x + d_x \\
 J_y \dot{\omega}_y + (J_x - J_z) \omega_z \omega_x &= M_y + d_y \\
 J_z \dot{\omega}_z + (J_y - J_x) \omega_x \omega_y &= M_z + d_z \\
 \dot{\gamma} &= \omega_x - \tan \vartheta (\omega_y \cos \gamma - \omega_z \sin \gamma) \\
 \dot{\psi} &= \frac{(\omega_y \cos \gamma - \omega_z \sin \gamma)}{\cos \vartheta} \\
 \dot{\vartheta} &= \omega_y \sin \gamma + \omega_z \cos \gamma
 \end{aligned} \tag{1}$$

where the rigid body states  $\omega_x$ ,  $\omega_y$ , and  $\omega_z$  represent roll angle velocity, yaw angle velocity, and pitch angle velocity, respectively.  $J_x$ ,  $J_y$ , and  $J_z$  are the moment of inertia of each axis.  $M_x$ ,  $M_y$ , and  $M_z$  are the control torque on the axes which are provided by the thrusters.  $d_x$ ,  $d_y$ , and  $d_z$  are the total uncertainties of each channel.

KKV has no rudder and no wing, and attitude adjustment of the KKV is realized only by the attitude control system

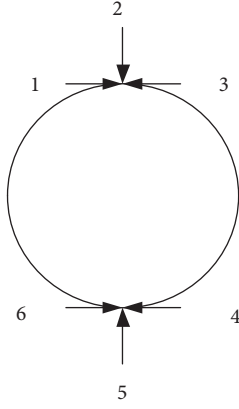


FIGURE 1: Attitude control thruster layout.

installed at the rear of the body. KKV attitude is adjusted through 6 thrusters which are shown in Figure 1, with (2#+5#) thrusters controlling the pitch channel, (1#+6#) and (3#+4#) thrusters controlling the yaw channel, and (1#+4#) and (3#+6#) thrusters controlling the roll channel. The attitude control thrusters belong to the direct lateral jet propeller and it can only output the constant thrust.

The thrusts generated by the attitude control thrusters along each axis in the body coordinate are as follows:

$$\begin{aligned} F_{zx_1} &= 0 \\ F_{zy_1} &= F_{z5} - F_{z2} \\ F_{zz_1} &= F_{z1} + F_{z4} - F_{z3} - F_{z6} \end{aligned} \quad (2)$$

Then, we can obtain the control torque

$$\begin{aligned} M_{zx_1} &= (F_{z1} + F_{z4} - F_{z3} - F_{z6}) \cdot r \\ M_{zy_1} &= (F_{z1} + F_{z6} - F_{z3} - F_{z4}) \cdot l \\ M_{zz_1} &= (F_{z2} - F_{z5}) \cdot l \end{aligned} \quad (3)$$

where  $F_{zi}$  ( $i = 1, \dots, 6$ ) is the thrust in a different direction;  $r$  is the radius of the body;  $l$  is the distance from the location of the thruster to the center of mass.

In the actual working process, in order to ensure the stability of the work and reduce the impact of thruster work on the system, the attitude control thruster usually works in pairs. Considering that the performance of the thruster is basically similar, (3) can be simplified to the following form:

$$\begin{aligned} M_{zx_1} &= 2F_z \cdot r \delta_{Fx} \\ M_{zy_1} &= 2F_z \cdot l \delta_{Fy} \\ M_{zz_1} &= F_z \cdot l \delta_{Fz} \end{aligned} \quad (4)$$

where  $F_z$  is the thrust of a single attitude control thruster and  $\delta_{Fx}$ ,  $\delta_{Fy}$ , and  $\delta_{Fz}$  determine whether to turn on.

When the attitude control thruster is turned on, the lateral jet flow interferes with the external flow field, forming a complicated flow field with a complicated structure. Jet

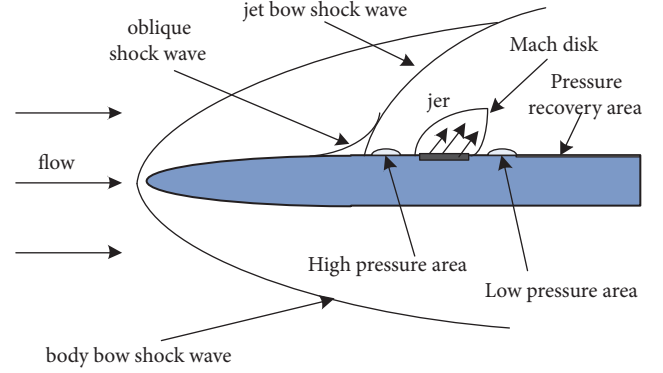


FIGURE 2: Jet Interaction Effects diagram.

flow produces a strong boundary layer separation, which causes oblique shock wave, split shock wave, bow shock wave, reattach shock wave, splitting nest, and secondary splitting nest in the flow field, and the expansion wave appears on both sides of the jet. There may be complex physical phenomena such as internal shock waves and Mach disk in the jet stream area. This phenomenon is called lateral jet flow disturbance effect. Typical lateral jet flow and external flow field interference phenomena are shown in Figure 2.

The disturbing flow field is very complex and has the characteristics of distributed parameters. Yet there is no accurate mathematical model to describe it. Almost all the references adopt thrust amplification factor  $K_T$  and torque amplification factor  $K_M$  to describe the forces and moments generated on the aircraft due to the side spray and the incoming flow interfere with each other. Its definition is as follows:

$$\begin{aligned} K_T &= \frac{(T_c + T_d)}{T_c} \\ K_M &= \frac{(M_c + M_d)}{M_c} \end{aligned} \quad (5)$$

Among them,  $T_d$  is the interference force caused by the jet,  $T_c$  is the static thrust on the ground,  $M_d$  is the disturbance torque caused by the jet, and  $M_c$  is the static moment of the thruster on the ground. The direct control force and torque are

$$T = (T_c + T_d) = K_T T_c \quad (6)$$

$$M_T = (M_c + M_d) = K_M M_c$$

Therefore, considering the jet flow disturbance, the actual torque can be expressed as

$$\begin{aligned} M_{jx} &= M_{zx} \\ M_{jy} &= K_{My} M_{zy} + \Delta M_{jy} \\ M_{jz} &= K_{Mz} M_{zz} + \Delta M_{jz} \end{aligned} \quad (7)$$

where  $M_{jx}$ ,  $M_{jy}$ , and  $M_{jz}$ , respectively, represent the components of each axis in the KKV body coordinate system under

consideration of the jet flow disturbances.  $\Delta M_{jy}$  and  $\Delta M_{jz}$  are the disturbance moments in the  $Oy_1$  axis and  $Oz_1$  axis.

Define  $\mathbf{X}_1 = [\vartheta \ \psi \ \gamma]^T$ ,  $\mathbf{X}_2 = [\omega_x \ \omega_y \ \omega_z]^T$  and  $\mathbf{u} = [\delta_{Fx} \ \delta_{Fy} \ \delta_{Fz}]$ , then (1) can be rewritten in a more compact form as

$$\begin{aligned} \dot{\mathbf{X}}_1 &= \mathbf{G}\mathbf{X}_2 \\ \mathbf{J}\dot{\mathbf{X}}_2 &= \mathbf{F} + \mathbf{L}\mathbf{u} + \mathbf{D}(t) \end{aligned} \quad (8)$$

where

$$\begin{aligned} \mathbf{G} &= \begin{bmatrix} 0 & \sin \gamma & \cos \gamma \\ 0 & \frac{\cos \gamma}{\cos \vartheta} & -\frac{\sin \gamma}{\cos \vartheta} \\ 1 & -\tan \vartheta \cos \gamma & \tan \vartheta \sin \gamma \end{bmatrix} \\ \mathbf{J} &= \begin{bmatrix} J_x & 0 & 0 \\ 0 & J_y & 0 \\ 0 & 0 & J_z \end{bmatrix}, \\ \mathbf{F} &= \begin{bmatrix} (J_z - J_y)\omega_y\omega_z \\ (J_x - J_z)\omega_z\omega_x \\ (J_y - J_x)\omega_x\omega_y \end{bmatrix} \\ \mathbf{L} &= \begin{bmatrix} 2F_z \cdot r & 0 & 0 \\ 0 & 2K_{My}F_z \cdot l & 0 \\ 0 & 0 & K_{Mz}F_z \cdot l \end{bmatrix}, \\ \mathbf{D}(t) &= \begin{bmatrix} d_x \\ d_y + \Delta M_{jy} \\ d_z + \Delta M_{jz} \end{bmatrix} \end{aligned} \quad (9)$$

When the KKV adjusts the attitude or orbit, thruster consumes fuel which leads to the change of the moment of inertia and the drift of the center of mass. It is described as follows:

$$\begin{aligned} \mathbf{J} &= \mathbf{J}_0 + \Delta\mathbf{J} \\ \mathbf{F} &= \mathbf{F}_0 + \Delta\mathbf{F} \\ \mathbf{L} &= \mathbf{L}_0 + \Delta\mathbf{L} \end{aligned} \quad (10)$$

where  $\mathbf{J}_0$ ,  $\mathbf{F}_0$ , and  $\mathbf{L}_0$  are the initial value of  $\mathbf{J}$ ,  $\mathbf{F}$ , and  $\mathbf{L}$  and  $\Delta\mathbf{J}$ ,  $\Delta\mathbf{F}$ , and  $\Delta\mathbf{L}$  are the variation of parameters which satisfy the following assumption.

*Assumption 1.* The disturbance moment satisfies the bounded condition and there is a bounded function  $\xi(t)$  to let  $\|\mathbf{D}(t)\| \leq \xi(t)$ .

*Assumption 2.* The distance uncertainty of the attitude control torque satisfies the  $\Delta l_i \leq l_{\theta i}$ , where  $l_{\theta i}$  ( $i = r, l$ ) are the arithmetic number.

*Assumption 3.*  $\mathbf{J}_0^{-1}$  exists and there are the uncertain constants  $\mu_1$ ,  $\mu_2$ , and  $\mu_3$  to satisfy

$$\begin{aligned} \|\mathbf{J}_0\| &\leq \mu_1 < \infty, \\ \|\mathbf{J}^{-1}\| &\leq \mu_2 < \infty, \\ \|\Delta\mathbf{J}\| &\leq \mu_3 < \infty. \end{aligned} \quad (11)$$

Substituting (10) into (8)

$$(\mathbf{J}_0 + \Delta\mathbf{J})\dot{\mathbf{X}}_2 = (\mathbf{F}_0 + \Delta\mathbf{F}) + (\mathbf{L}_0 + \Delta\mathbf{L})\mathbf{u} + \mathbf{D}(t) \quad (12)$$

Then the problem has the following state-space representation:

$$\begin{aligned} \dot{\mathbf{X}}_1 &= \mathbf{G}\mathbf{X}_2 \\ \dot{\mathbf{X}}_2 &= \mathbf{J}_0^{-1}\mathbf{F}_0 + \mathbf{J}_0^{-1}\mathbf{L}_0\mathbf{u} + \mathbf{H}(t) \end{aligned} \quad (13)$$

where

$$\begin{aligned} \mathbf{H}(t) &= \mathbf{J}_0^{-1}(\Delta\mathbf{F} + \Delta\mathbf{L}\mathbf{u} + \mathbf{D}(t)) \\ &+ \Delta\tilde{\mathbf{J}}[\mathbf{F}_0 + \Delta\mathbf{F} + \mathbf{L}_0\mathbf{u} + \Delta\mathbf{L}\mathbf{u} + \mathbf{D}(t)] \end{aligned} \quad (14)$$

From (13), we can know that the mathematical model of KKV attitude system is strict feedback form which includes state constraints and uncertainty.

*2.2. Finite-Time-Convergent Differentiator.* Without loss of generality, we consider the following uncertain dynamic system:

$$\begin{aligned} \dot{x}_1 &= x_2 \\ \dot{x}_2 &= x_3 \\ &\vdots \\ \dot{x}_{n-1} &= x_n \\ \dot{x}_n &= f(x_1, x_2, \dots, x_n) \end{aligned} \quad (15)$$

where  $x_1, x_2, \dots, x_n \in \mathbf{R}$  are the state variables,  $f_A(\bullet)$  is a continuous function, and  $f(0, \dots, 0) = 0$ .

**Lemma 4** (see [31]). For system (16)

$$\begin{aligned} \dot{z}_1 &= z_2 \\ \dot{z}_2 &= F(z_1(t), z_2(t)) \end{aligned} \quad (16)$$

where  $z_1 \in \mathbf{R}$ ,  $z_2 \in \mathbf{R}$ , if system (16) satisfies  $z_1(t) \rightarrow 0$ ,  $z_2(t) \rightarrow 0(t \rightarrow \infty)$ . For any an arbitrary bounded function  $v(t)$  and a constant  $T > 0$ , the solution of the system

$$\begin{aligned} \dot{x}_1 &= x_2 \\ \dot{x}_2 &= R^2 F\left(x_1(t) - v(t), \frac{x_2}{R}\right) \end{aligned} \quad (17)$$

satisfies

$$\lim_{R \rightarrow \infty} \int_0^T |x_1 - v(t)| dt = 0 \quad (18)$$

*Remark 5.*  $x_1(t)$  averagely converges to the input signal  $v(t)$  and  $x_2(t)$  converges to the generalized derivative of  $v(t)$ . In (17),  $R > 0$  is a design parameter.

According to Lemma 4, a simple FD is presented as follows:

$$\begin{aligned}\dot{\varsigma}_1 &= \varsigma_2 \\ \dot{\varsigma}_2 &= \varsigma_3 \\ &\vdots \\ \dot{\varsigma}_{n-1} &= \varsigma_n\end{aligned}\quad (19)$$

$$\begin{aligned}\dot{\varsigma}_n &= R^n \left[ -a_1 \tanh(\varsigma_1 - v(t)) - a_2 \tanh\left(\frac{\varsigma_2}{R}\right) - \right. \\ &\quad \left. \cdots - a_n \tanh\left(\frac{\varsigma_n}{R^{n-1}}\right) \right]\end{aligned}$$

where  $R, a_i$  ( $i = 1, 2, \dots, n$ )  $\in \mathbf{R}^+$  is design parameter and there are  $\phi > 0$  and  $i\phi > n$  which satisfies

$$\varsigma_i - v^{(i-1)}(t) = O\left(\left(\frac{1}{R}\right)^{i\phi-i+1}\right), \quad i = 1, 2, \dots, n \quad (20)$$

where  $O((1/R)^{i\phi-i+1})$  is the  $(1/R)^{i\phi-i+1}$  order error of  $v^{(i-1)}(t)$ ,  $\phi = (1 - \vartheta)/\vartheta$ ,  $\vartheta \in (0, \min\{t/(t+n), 1/2\})$ ,  $n \geq 2$ .

**2.3. Nonlinear Disturbance Observers.** In this section, a new NDO is designed based on FD. Without loss of generality, we consider the following uncertain dynamic system:

$$\dot{v} = F(v) + G(v)u + d \quad (21)$$

where  $v \in \mathbb{R}$  and  $u \in \mathbb{R}$  are the state and control input respectively.  $F(v)$  and  $G(v) \neq 0$  are the continuous function.  $d \in \mathbb{R}$  denotes the disturbance.

**Theorem 6.** *The following new NDO is designed for the uncertain system (21):*

$$\begin{aligned}\hat{v} &= F(v) + G(v)u + \hat{d} \\ \dot{\hat{d}} &= R^2 \left[ -a_1 \tanh(\hat{v} - v) - a_2 \tanh\left(\frac{\hat{d}}{R}\right) \right]\end{aligned}\quad (22)$$

where  $v$  is the estimated value of  $\hat{v}$  and  $d$  is the estimated value of  $\hat{d}$ ; if  $R \rightarrow +\infty$ , then

$$\begin{aligned}\hat{v} - v &= O\left(\left(\frac{1}{R}\right)^\phi\right) \\ \hat{d} - d &= O\left(\left(\frac{1}{R}\right)^{\phi-1}\right)\end{aligned}\quad (23)$$

*Proof.* There are two main steps in the proof.

Step 1

If  $\hat{v} - v = 0$ , then compared to the first equation of (22) and (23), we can obtain that  $\hat{d} - d = 0$ . Theorem 6 holds obviously.

Step 2

If  $\hat{v} - v \neq 0$ , when  $R \rightarrow +\infty$ ,  $\tanh(\hat{d}/R) \rightarrow 0$ , we can obtain

$$-a_1 \tanh(\hat{v} - v) - a_2 \tanh\left(\frac{\hat{d}}{R}\right) \neq 0 \quad (24)$$

Then

$$\left| \dot{\hat{d}} \right| = R^2 \left| -a_1 \tanh(\hat{v} - v) - a_2 \tanh\left(\frac{\hat{d}}{R}\right) \right| \rightarrow +\infty \quad (25)$$

Compared to  $v$  and  $F(v) + G(v)u$ ,  $\hat{d}$  is fast variable. According to [31], we obtain

$$\begin{aligned}\lim_{R \rightarrow +\infty} \frac{d[F(v) + G(v)u + \hat{d}]}{dt} &= \dot{\hat{d}} \\ \lim_{R \rightarrow +\infty} \frac{F(v) + G(v)u + \hat{d}}{R} &= \frac{\hat{d}}{R}\end{aligned}\quad (26)$$

If  $n=2$ , then (19) is

$$\begin{aligned}\dot{\varsigma}_1 &= \varsigma_2 \\ \dot{\varsigma}_2 &= R^2 \left[ -a_1 \tanh(\varsigma_1 - v(t)) - a_2 \tanh\left(\frac{\varsigma_2}{R}\right) \right]\end{aligned}\quad (27)$$

Substituting  $F(v) + G(v)u + \hat{d}$  into (27) and combining with (26), Theorem 6 holds obviously.  $\square$

### 3. Attitude Controller Design and Realization

Throughout this paper, we denote by  $\mathbb{R}_+$  the set of non-negative real numbers,  $\|\bullet\|$  the Euclidean vector norm in  $\mathbb{R}^m$ , and  $\lambda_{\max}(\bullet)$  and  $\lambda_{\min}(\bullet)$  the maximum and minimum eigenvalues of  $\bullet$ , respectively. For illustration purpose, we consider a class of second-order strict feedback systems and outline the control design based on a BLF to ensure that the output constraint is not violated. Consider the system

$$\begin{aligned}\dot{x}_1 &= f_1(x_1) + g_1(x_1)x_2 + d_1 \\ \dot{x}_2 &= f_2(x_1, x_2) + g_2(x_1, x_2)u + d_2 \\ y &= x_1\end{aligned}\quad (28)$$

where  $f_1(x_1)$ ,  $f_2(x_1, x_2)$ ,  $g_1(x_1)$ , and  $g_2(x_1, x_2)$  are smooth functions,  $u \in \mathbb{R}$  is the control input, and  $x_1, x_2 \in \mathbb{R}$  are the states, with  $y$  required to satisfy  $|y| < k_{c1}$ ,  $\forall t \geq 0$ , with  $k_{c1}$  being a positive constant.

*Assumption 7.* The function  $g_i(x_i)$ ,  $i = 1, 2, \dots, n$ , is known, and there exists a positive constant  $g_0$  such that  $0 < g_0 \leq |g_i(x_i)|$  for  $|x_i| < k_{c1}$ . Without loss of generality, we further assume that  $g_i(x_i)$  are all positive for  $|x_i| < k_{c1}$ .

**Lemma 8.** *For any positive constants  $k_{a1}$  and  $k_{b1}$ , let  $\mathbb{Z}_1 := \{z_1 \in \mathbb{R} : -k_{a1} < z_1 < k_{b1}\} \subset \mathbb{R}$  and  $\mathbb{N} := \mathbb{R}^l \times \mathbb{Z}_1 \subset \mathbb{R}^{l+1}$  be open sets. Consider the system*

$$\dot{\eta} = h(t, \eta) \quad (29)$$

where  $\eta := [w, z_1]^T \in \mathbb{N}$  and  $h : \mathbb{R}_+ \times \mathbb{N} \rightarrow \mathbb{R}^{l+1}$  is piecewise continuous in  $t$  and locally Lipschitz in  $z$ , uniform in  $t$ , on  $\mathbb{R}_+ \times \mathbb{N}$ . Suppose that there exist functions  $U : \mathbb{R}^l \rightarrow \mathbb{R}_+$  and  $V_1 : \mathbb{Z}_1 \rightarrow \mathbb{R}_+$ , continuously differentiable and positive definite in their respective domains, such that

$$V_1(z_1) \rightarrow \infty \quad \text{as } z_1 \rightarrow -k_{a_1} \text{ or } z_1 \rightarrow k_{b_1} \quad (30)$$

$$\gamma_1(\|w\|) \leq U(w) \leq \gamma_2(\|w\|) \quad (31)$$

where  $\gamma_1$  and  $\gamma_2$  are class  $K_\infty$  functions. Let  $V(\eta) := V_1(z_1) + U(w)$ , and  $z_1(0)$  belong to the set  $z_1 \in (-k_{a_1}, k_{b_1})$ . If the inequality holds

$$\dot{V} = \frac{\partial V}{\partial \eta} h \leq 0 \quad (32)$$

then  $z_1(t)$  remains in the open set  $z_1 \in (-k_{a_1}, k_{b_1}) \forall t \in [0, \infty)$ .

*Remark 9.* In Lemma 8, we split the state space into  $z_1$  and  $w$ , where  $z_1$  is the state to be constrained and  $w$  is the free states. The constrained state  $z_1$  requires the barrier function  $V_1$  to prevent it from reaching the limits  $-k_{a_1}$  and  $k_{b_1}$ , while the free states may involve quadratic functions.

For system (28), we employ backstepping design as follows.

*Step 1.* Let  $z_1 = y_1 - y_d$ ,  $z_2 = x_2 - \alpha_1$ , where  $y_d$  is the desired value, and  $\alpha_1$  is a stabilizing function to be designed. Choose the following symmetric BLF candidate:

$$V_1 = \frac{1}{2} \log \frac{k_{b_1}^2}{k_{b_1}^2 - z_1^2} \quad (33)$$

where  $\log(\bullet)$  denotes the natural logarithm of  $\bullet$  and  $k_{b_1} = k_{c_1} - y_d$  denotes the constraint on  $z_1$ . We require  $|z_1| < k_{b_1}$ . It can be shown that  $V_1$  is positive definite and thus a valid Lyapunov function candidate. The derivative of  $V_1$  is given by

$$\dot{V}_1 = \frac{z_1 \dot{z}_1}{k_{b_1}^2 - z_1^2} = \frac{z_1 (f_1 + g_1(z_2 + \alpha_1) + d_1 - \dot{y}_d)}{k_{b_1}^2 - z_1^2} \quad (34)$$

Design the stabilizing function  $\alpha_1$  as

$$\alpha_1 = \frac{1}{g} \left( -f_1 - (k_{b_1}^2 - z_1^2) k_1 z_1 - d_1 + \dot{y}_d \right) \quad (35)$$

where  $k_1 > 0$  is a constant. Substituting (35) into (34) yields

$$\dot{V}_1 = -k_1 z_1^2 + \frac{g_1 z_1 z_2}{k_{b_1}^2 - z_1^2} \quad (36)$$

where the coupling term  $g_1 z_1 z_2 / (k_{b_1}^2 - z_1^2)$  is cancelled in the subsequent step.

*Step 2.* Since  $x_2$  does not need to be constrained, we choose a Lyapunov function candidate by augmenting  $V_1$  with a quadratic function:

$$V_2 = V_1 + \frac{1}{2} z_2^2 \quad (37)$$

The time derivative of  $V_2$  is given by

$$\dot{V}_2 = -k_1 z_1^2 + \frac{g_1 z_1 z_2}{k_{b_1}^2 - z_1^2} + z_2 (f_2 + g_2 u + d_2 - \dot{\alpha}_1) \quad (38)$$

The control law is designed as

$$u_{BLF} = \frac{1}{g_2} \left( -f_2 + d_2 + \dot{\alpha}_1 - k_2 z_2 - \frac{g_1 z_1}{k_{b_1}^2 - z_1^2} \right) \quad (39)$$

where  $k_2 > 0$  is constant and the last term on the right-hand side is to cancel the residual coupling term  $g_1 z_1 z_2 / (k_{b_1}^2 - z_1^2)$  from the first step. Substituting (39) into (38) yields  $\dot{V}_2 = -\sum_{i=1}^2 k_i z_i^2$ . From (39), there is a concern of  $u(t)$  becoming unbounded whenever  $|z_1(t)| = k_{b_1}$ . However, we have established that, in the closed loop, the error signal  $|z_1(t)|$  never reaches  $k_{b_1} \forall t \geq 0$ . As a result, the control  $u(t)$  will not become unbounded because of the presence of terms comprising  $(k_{b_1}^2 - z_1^2(t))$  in the denominator.

According to Lemma 8, we have  $|z_1(t)| < k_{b_1} \forall t > 0$  and the output constraint will never be violated. Provide that the initial conditions satisfy

$$|z_1(0)| < k_{b_1} \quad (40)$$

However, we cannot always guarantee  $|z_1(t)| < k_{b_1} \forall t > 0$  if the initial conditions  $|z_1(0)| > k_{b_1}$ . Next, SMC is used to make the initial error sliding to the set domain if the initial error is not in the set domain.

Firstly, transform system (28) as follows:

$$\dot{x} = f(x) + g(x)u \quad (41)$$

where  $f(x) = [f_1(x_1) + g_1(x_1)x_2, \dots, f_{n-1}(x_{n-1}) + g_{n-1}(x_{n-1})x_n, f_n(x_n)]^T$ ,  $g(x) = [0, 0, \dots, g_n(x_n)]^T$ .

Then, the sliding mode surface is selected as follows:

$$s(x) = cx = c_1 x_1 + c_2 x_2 + \dots + c_n x_n \quad (42)$$

The derivative of  $s(x)$  is given by

$$\dot{s}(x) = c(f(x) + g(x)u_{SMC}) = -\varepsilon \text{sign}(s) - ks \quad (43)$$

If  $cg(x)$  is reversible, we can obtain the control law

$$u_{SMC} = (cg(x))^{-1} (-cf(x) - \varepsilon \text{sign}(s) - ks) \quad (44)$$

Choose the following Lyapunov function candidate:

$$V_0 = \frac{1}{2} s^2 \quad (45)$$

Differentiating  $V_0$  and combining (42)–(44), we can obtain

$$\dot{V}_0 = s\dot{s} = -\varepsilon |s| - ks^2 \leq 0 \quad (46)$$

The system gradually converges to the desired point.

Combining the SMC and BLF backstepping control, the global convergence output constraint robust control law is designed as follows:

$$\mathbf{u} = p\mathbf{u}_{BLF} + (1 - p)\mathbf{u}_{SMC} \quad (47)$$

where

$$p = \begin{cases} 1, & |z_1| < k_{b_1} \\ 0, & |z_1| \geq k_{b_1} \end{cases} \quad (48)$$

Controller combining the SMC and BLF backstepping control can guarantee the error global convergence.

From KKV's mathematical model, we can see that system (13) satisfies the strict feedback form. Next, the method combining the sliding mode control and BLF backstepping control will be applied to design KKV controller with state constraints.

Define

$$\begin{aligned} \mathbf{Z}_1 &= \mathbf{X}_1 - \mathbf{X}_d \\ \mathbf{Z}_2 &= \mathbf{X}_2 - \boldsymbol{\beta}_1 \end{aligned} \quad (49)$$

where  $\mathbf{Z}_1 \in (-\mathbf{K}_{b_1}, \mathbf{K}_{b_1})$ ,  $\mathbf{K}_{b_1} = [\vartheta_{b_1}, \varphi_{b_1}, \gamma_{b_1}] = [1^\circ, 1^\circ, 1^\circ]^T$ . Therefore, the domain of  $\mathbf{Z}_1$  is  $([-1^\circ, 1^\circ], [-1^\circ, 1^\circ], [-1^\circ, 1^\circ])^T$ . Then we can get the stabilizing function  $\boldsymbol{\beta}_1$ :

$$\boldsymbol{\beta}_1 = \frac{1}{\mathbf{G}_0} \left( -(\mathbf{K}_{b_1}^2 - \mathbf{Z}_1^2) \mathbf{K}_1 \mathbf{Z}_1 + \dot{\mathbf{X}}_{1ref} \right) \quad (50)$$

The BLF controller is designed as

$$\begin{aligned} \mathbf{u}_{BLF} &= \frac{1}{\mathbf{J}_0^{-1} \mathbf{L}_0} \left( -\mathbf{J}_0^{-1} \mathbf{F}_0 - \mathbf{H}(t) + \dot{\boldsymbol{\beta}}_1 - \mathbf{K}_2 \mathbf{Z}_2 - \frac{\mathbf{G} \mathbf{Z}_1}{\mathbf{K}_{b_1}^2 - \mathbf{Z}_1^2} \right) \end{aligned} \quad (51)$$

From (50)-(51), we can know that the stabilizing function  $\boldsymbol{\beta}_1$  is complex and the first derivative of  $\boldsymbol{\beta}_1$  will bring about "differential explosion" and affect the efficiency of computer solution. The FD is used to solve this problem. The unknown total disturbance appears in the actual control; [32] points out that the maximum disturbance torque can reach 50 percent of the control torque. Under the condition of such a large disturbance moment, it is difficult to solve this problem only by the robustness of the system. If we do not carry out active control, it will reduce the precision of attitude control and even cause the instability of the system. Therefore, NDO is used to estimate and compensate the unknown disturbance.

Therefore, the first differential value of stabilizing function can be obtained as follows:

$$\begin{aligned} \dot{\boldsymbol{\zeta}}_1 &= \boldsymbol{\zeta}_2 \\ \dot{\boldsymbol{\zeta}}_2 &= \mathbf{R}_1^2 \left[ -\mathbf{A}_1 \tanh(\boldsymbol{\zeta}_1 - \boldsymbol{\beta}_1) - \mathbf{A}_2 \tanh\left(\frac{\boldsymbol{\zeta}_2}{\mathbf{R}}\right) \right] \end{aligned} \quad (52)$$

where  $\mathbf{A}_1 = \text{diag}(a_{11}, a_{12}, a_{13})$ ,  $a_{1i} > 0$ ,  $i = 1, 2, 3$ ,  $\mathbf{A}_2 = \text{diag}(a_{21}, a_{22}, a_{23})$ ,  $a_{2i} > 0$ ,  $i = 1, 2, 3$ ,  $\mathbf{R}_1$  are the design parameters and  $\boldsymbol{\zeta}_2$  is the estimated value of  $\dot{\boldsymbol{\beta}}$ .

For system (13), the following NDO is designed:

$$\begin{aligned} \dot{\hat{\mathbf{X}}}_2 &= \mathbf{F}(v) + \mathbf{G}(v) \mathbf{u} + \hat{\mathbf{H}}(t) \\ \dot{\hat{\mathbf{H}}}(t) &= \mathbf{R}_2^2 \left[ -\mathbf{A}_3 \tanh(\hat{\mathbf{X}}_2 - \mathbf{X}_2) - \mathbf{A}_4 \tanh\left(\frac{\hat{\mathbf{d}}}{\mathbf{R}}\right) \right] \end{aligned} \quad (53)$$

where  $\mathbf{A}_3 = \text{diag}(a_{31}, a_{32}, a_{33})$ ,  $a_{3i} > 0$ ,  $i = 1, 2, 3$ ,  $\mathbf{A}_4 = \text{diag}(a_{41}, a_{42}, a_{43})$ ,  $a_{4i} > 0$ ,  $i = 1, 2, 3$ ,  $\mathbf{R}_2$  are design parameters.

Transform system (13) to a simple form as follows:

$$\dot{\mathbf{x}} = \mathbf{f}(\mathbf{x}) + \mathbf{g}(\mathbf{x}) \mathbf{u} \quad (54)$$

where  $\mathbf{f}(\mathbf{x}) = [\mathbf{G} \mathbf{X}_2, \mathbf{J}_0^{-1} \mathbf{F}_0]$ ,  $\mathbf{g}(\mathbf{x}) = [0, \mathbf{J}_0^{-1} \mathbf{L}_0]$ .

Choose the following sliding mode surface:

$$s(\mathbf{x}) = c\mathbf{x} = c_1 x_1 + c_2 x_2 \quad (55)$$

Then, we can obtain SMC as

$$\mathbf{u}_{SMC} = (c\mathbf{g}(\mathbf{x}))^{-1} (-c\mathbf{f}(\mathbf{x}) - \varepsilon \text{sign}(s) - Ks) \quad (56)$$

Combining the SMC and BLF backstepping controller, the global convergence output constraint robust controller is designed as follows:

$$\mathbf{u} = p\mathbf{u}_{BLF} + (1 - p)\mathbf{u}_{SMC} \quad (57)$$

where

$$\mathbf{p} = \begin{cases} \text{diag}(1, 1, 1), & |x_1| \leq k_{b_1} \\ \text{diag}(0, 0, 0), & |x_1| > k_{b_1} \end{cases} \quad (58)$$

**Theorem 10.** Consider the closed-loop system consisting of plant (13) with control laws (57), FD (52), and NDO (53). The all the signals involved are uniformly ultimately bounded.

*Proof.* Proof can be divided into two steps.

Step 1

When  $|\mathbf{Z}_1| > \mathbf{K}_{b_1}$ , mainly for SMC at work. From (46), we can know the system is stable.

Step 2

When  $|\mathbf{Z}_1| \leq \mathbf{K}_{b_1}$ , mainly for BLF backstepping controller at work.

Define the estimation errors of NDO and FD is

$$\begin{aligned} \tilde{\mathbf{H}} &= \hat{\mathbf{H}}(t) - \mathbf{H}(t) \\ \tilde{\boldsymbol{\beta}} &= \hat{\boldsymbol{\beta}} - \boldsymbol{\beta} \end{aligned} \quad (59)$$

Choose the following Lyapunov function candidate:

$$\mathbf{W}_0 = \frac{1}{2} \log \frac{\mathbf{K}_{b_1}^2}{\mathbf{K}_{b_1}^2 + \mathbf{Z}_1^2} + \frac{1}{2} \mathbf{Z}_2^2 \quad (60)$$

Differentiating  $\mathbf{W}_0$  and combining (59)-(60), we can obtain

$$\dot{\mathbf{W}}_0 = -\mathbf{K}_1 \mathbf{Z}_1^2 - \mathbf{K}_2 \mathbf{Z}_2^2 - \mathbf{Z}_2 \tilde{\mathbf{H}} - \mathbf{Z}_2 \tilde{\boldsymbol{\beta}}_1 \quad (61)$$

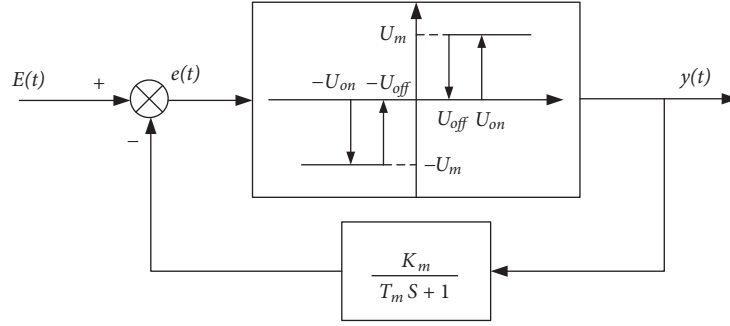


FIGURE 3: PSR modulator diagram.

Note that

$$\begin{aligned} Z_2 \tilde{H} &\leq \frac{Z_2^2}{2} + \frac{\tilde{H}^2}{2} \\ Z_2 \hat{\beta}_1 &\leq \frac{Z_2^2}{2} + \frac{\hat{\beta}_1^2}{2} \end{aligned} \quad (62)$$

Substituting (61) into (62), the following inequality holds:

$$\dot{W}_0 \leq -\left(K_1 + \frac{1}{2}\right) Z_1^2 - \left(K_2 + \frac{1}{2}\right) Z_2^2 - \frac{\tilde{H}^2}{2} - \frac{\hat{\beta}_1^2}{2} \quad (63)$$

Therefore these tracking errors  $Z_1$  and  $Z_2$  are semiglobally uniformly bounded. By choosing the appropriate design parameters  $K_i$  ( $i = 1, 2$ ), these errors can be sufficiently small. This completes the proof.  $\square$

From (57), we can know that the control command is continuous type and cannot meet the pulse thruster requirement. Next, PSR modulator will be introduced to shape the continuous control command to pulse or on-off signals. The structure of the PSR modulator is similar to the PWPF modulator except that the position of the first-order inertial link is different. The PWPF first-order inertial link is located on the forward channel while the PSR modulator is located on the feedback channel. The schematic of the PSR modulator is shown in Figure 3.

When Schmitt trigger input  $E(t)$  is greater than the start threshold, a fixed value of 1 is output. Modulator input  $E(t)$  is exponentially decayed to subtract new  $e(t)$ . The output of the modulator is always 1 before  $e(t)$  decrease to the shutdown threshold. The output of the modulator is 0 when the trigger input is less than the start-up threshold or after  $e(t)$  decrease in the shutdown threshold. Similarly, when the input is negative, the modulator outputs 0 or -1 (negative sign means the modulator is reversed).

When the Schmitt trigger is on

$$e(t) = K_m (E - u_m) \left(1 - e^{-t_1/T_m}\right) + u_{on} e^{-t_1/T_m} \quad (64)$$

$$0 \leq t_1 \leq T_{on}$$

When the Schmitt trigger is off

$$e(t) = K_m (E - u_m) \left(1 - e^{-t_2/T_m}\right) + u_{off} e^{-t_2/T_m} \quad (65)$$

$$0 \leq t_2 \leq T_{off}$$

Then we can get the output pulse width

$$T_{on} = -T_m \ln \left[1 - \frac{h}{K_m u_m - (E - u_{on})}\right] \quad (66)$$

Schmitt trigger off time in one cycle is

$$T_{off} = -T_m \ln \left[1 - \frac{h}{K_m u_m - (E - u_{on})}\right] \quad (67)$$

Switching frequency is

$$f = \frac{1}{T_{on} + T_{off}} \quad (68)$$

Minimum pulse width is

$$\Delta \approx \frac{h T_m}{K_m} \quad (69)$$

The PSR pulse modulator not only has the same advantages which are similar to PWPF, with its static characteristics are also independent of the parameters of the aircraft, the output pulse is related to the error amplitude and error speed. It also provides phase advance performance compared to the PWPF.

#### 4. Simulation Results

In this section, four kinds of simulation are established to verify the performance of the proposed method under the condition of strong disturbance. The control strategy for KKV with side window detection is to adjust the pitch angle and yaw angle accurately and keep the rolling angle stability to ensure the detecting field of view. The initial parameters and disturbance are listed in Table 1, the simulation parameters perturbation are listed in Table 2, and the simulation parameters of FD and NDO are listed in Table 3.

TABLE 1: Simulation initial parameters.

parameter	parameter perturbation
$J_{x0}$	0.4
$J_{y0}$	0.4
$J_{z0}$	0.4
$l$	0.5
$r$	0.16
$d_x$	$3^\circ \sin((\pi/2)t)$
$d_y$	$3^\circ \sin((\pi/2)t)$
$d_z$	$3^\circ \sin((\pi/2)t)$

TABLE 2: Simulation parameters perturbation.

parameter	parameter perturbation
$\Delta J_x$	$J_{x0} \times 20\% \sin(t)$
$\Delta J_y$	$J_{x0} \times 30\% \sin(t)$
$\Delta J_z$	$J_{z0} \times 10\% \sin(t)$
$\Delta l$	$l \times 20\% \sin(t)$
$\Delta r$	$r \times 20\% \sin(t)$

TABLE 3: Simulation parameters of FD and NDO.

parameter	parameter perturbation
$\mathbf{R}_1$	[20, 20, 20]
$\mathbf{A}_1$	[5, 5, 5]
$\mathbf{A}_2$	[5, 5, 5]
$\mathbf{R}_2$	[8, 8, 8]
$\mathbf{A}_3$	[10, 10, 10]
$\mathbf{A}_4$	[3, 3, 3]

*Case 1.* Verify the performance of the controller based on BLF. Suppose the initial values of the attitude angles are  $[\theta_0 \ \psi_0 \ \gamma_0]^T = [0^\circ \ 0^\circ \ 0^\circ]$  and  $\mathbf{X}_{1d} = [\theta_r \ \psi_r \ \gamma_r]^T = [10^\circ \sin(5t) \ 10^\circ \sin(5t) \ 0^\circ]$ . We can know that  $Z_1$  satisfies  $|Z_1| < K_{b_1}$ . Simulation results are shown in Figures 4–9.

The attitude adjustment is divided into two stages, attitude adjustment stage and attitude keeping. From Figure 4, we can intuitively see that attitude controller based on BLF can make the attitude angles track desired attitude angles fast and accurately. During the attitude adjustment stage, the controller can constrain the attitude angle to the initial setting domain even though there are large interference errors in the three channels. In the attitude keeping stage, we can see that the tracking error of the pitch angle can stay within  $\pm 0.2^\circ$  in most of the time and does not exceed  $\pm 0.4^\circ$ , the yaw angle tracking error does not exceed  $\pm 0.5^\circ$ , and the error of the roll angle does not exceed  $\pm 0.2^\circ$ . But, tracking accuracy of the yaw channel is the lowest and it is because the interference torque of is the largest. It can be seen from the simulation results that controller based on BLF can guarantee the tracking error in setting domain  $(-K_{b_1}, K_{b_1})$  in the whole process and the attitude controller satisfies the requirement of fastness and accuracy.

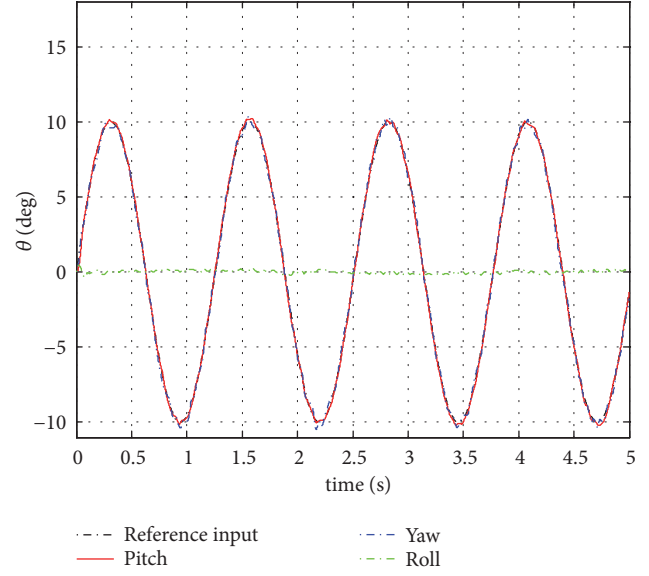


FIGURE 4: Attitude angle tracking curve.

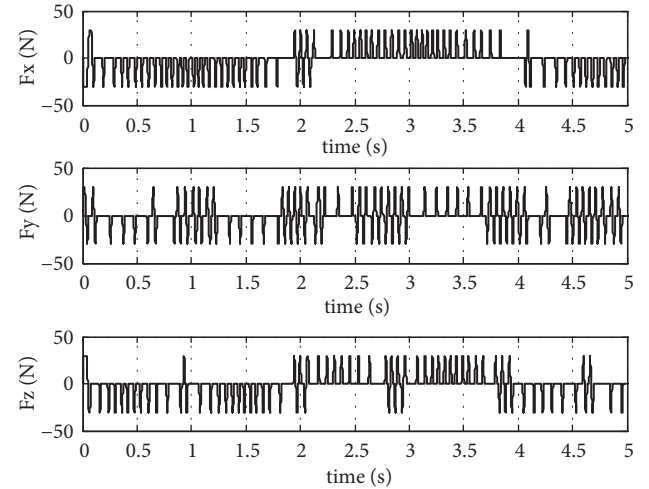


FIGURE 5: Thrust force curve.

As is shown in Figure 5, the thruster has a saturated working area and a large pulse in the initial stage of attitude control. When the thruster enters the duty cycle linear work area, the width of the thrust pulse also gradually decreases, which reflects the PSR modulator to adjust the width and frequency on the thrust. The simulation results show that the thruster starting frequency is low, KKV variable thrust attitude control accuracy and controller has a good performance. As showed in Figure 6, NDO has high approximation accuracy to unknown uncertainties and unknown time-varying disturbances and its estimation error is small. Accurate error estimation and compensation greatly improve the accuracy of attitude control.

*Case 2.* Verify the performance of the controller under strong interference conditions without estimation and compensation of uncertainties and disturbances. Initial values of the

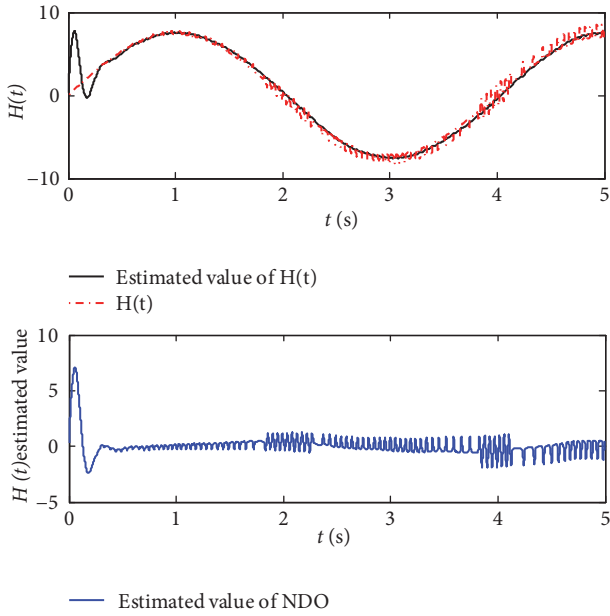


FIGURE 6: Estimated value and error of NDO.

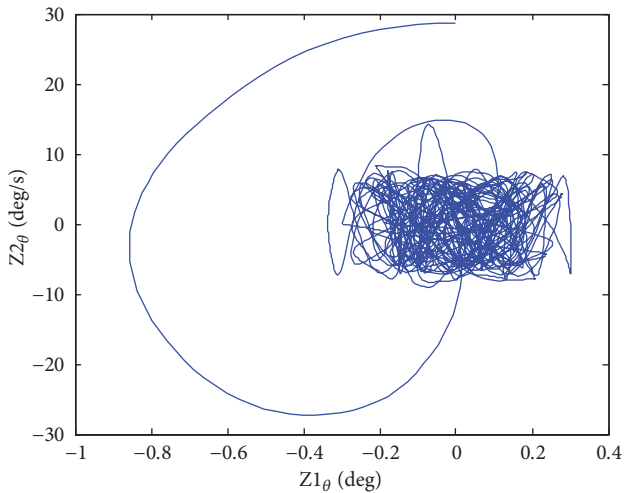


FIGURE 7: Pitch angle tracking error.

attitude angles and simulation settings are the same as Case 1. Simulation results are shown in Figures 10–13.

From Figures 11–13, we can know that the accuracy of controller obviously gets worse without estimation and compensation of uncertainties and disturbances. Pitch angle tracking error stays within  $\pm 0.5^\circ$ , yaw angle tracking error stays within  $\pm 0.6^\circ$ , and roll angle tracking error stays within  $\pm 0.4^\circ$ . From Figure 10, we can know that the frequency of thruster switch is obviously increased, and it will cause more energy consumption. However, controller based on BLF can still guarantee the tracking error in setting domain  $(-K_{b_1}, K_{b_1})$  in the whole process.

Case 3. Verify the performance of controller combining BLF with SMC and compared with the SMC. Suppose the initial values of the attitude angles are

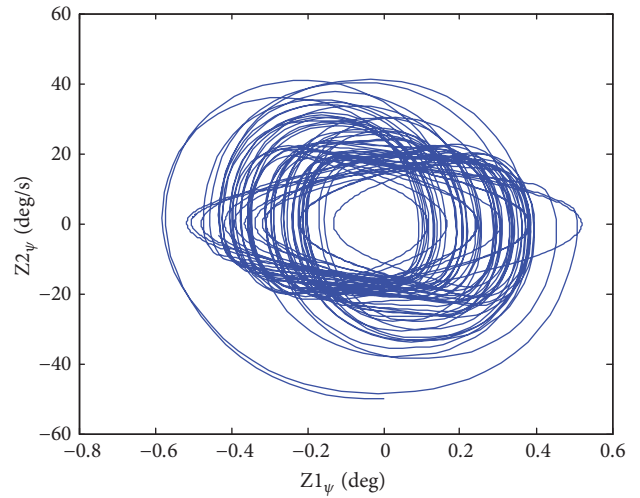


FIGURE 8: Yaw angle tracking error.

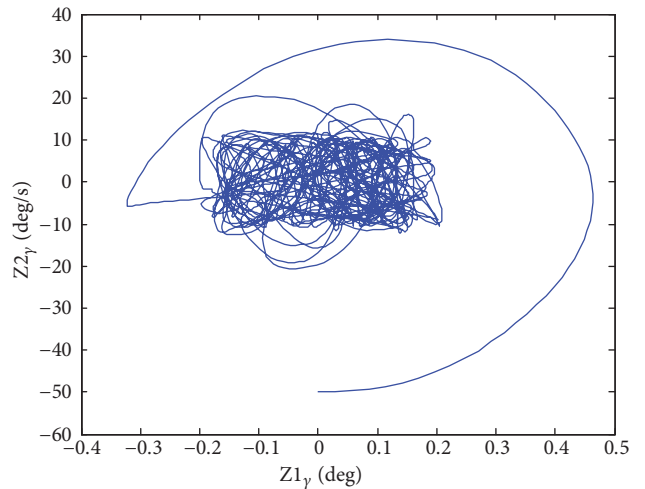


FIGURE 9: Roll angle tracking error.

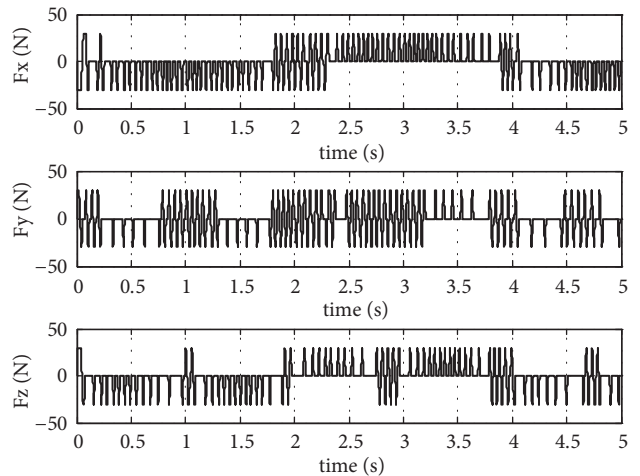


FIGURE 10: Thrust force curve.

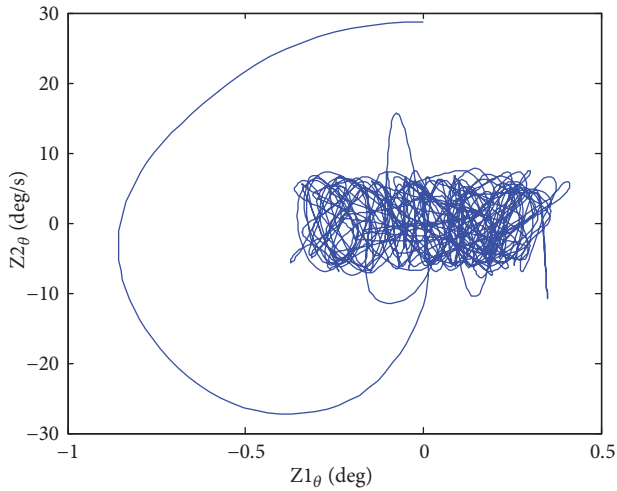


FIGURE 11: Pitch angle tracking error.

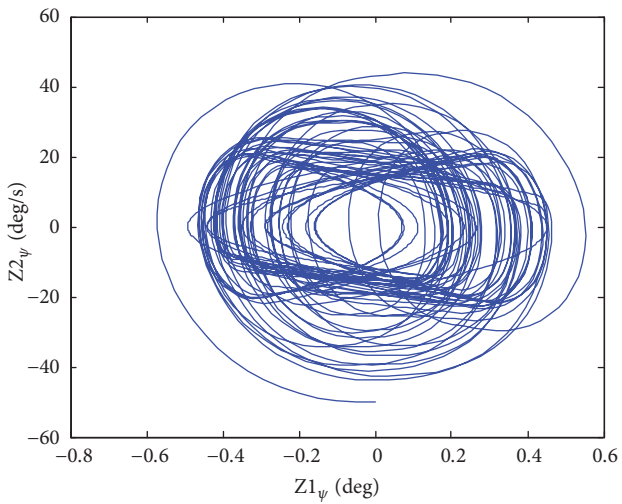


FIGURE 12: Yaw angle tracking error.

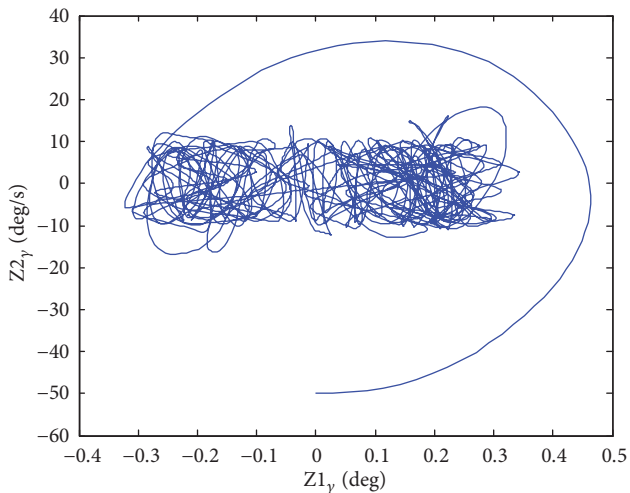


FIGURE 13: Roll angle tracking error.

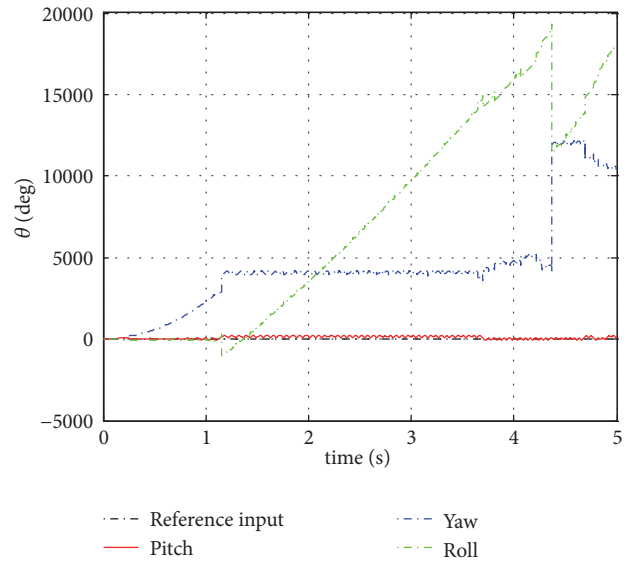


FIGURE 14: Attitude angle tracking curve with BLF controller.

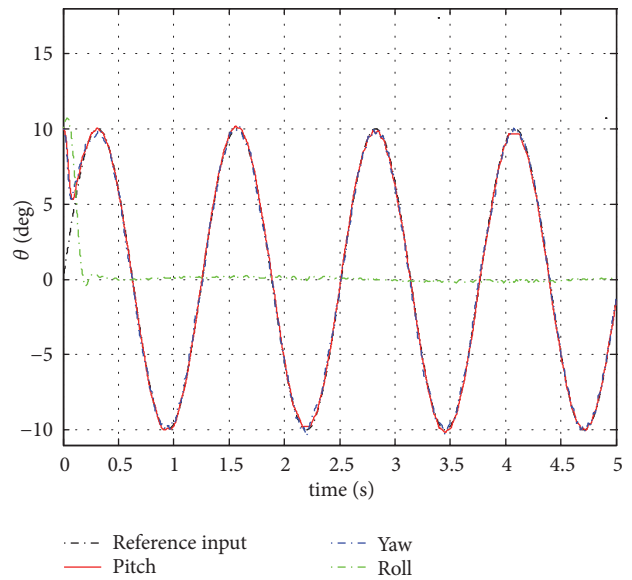


FIGURE 15: Attitude angle tracking curve combining BLF with SMC.

$[\vartheta_0 \ \psi_0 \ \gamma_0]^T = [10^\circ \ 10^\circ \ 10^\circ]$  and  $X_{1d} = [\vartheta_r \ \psi_r \ \gamma_r]^T = [10^\circ \sin(5t) \ 10^\circ \sin(5t) \ 0^\circ]$ . We can know that  $Z_1$  does not satisfy  $|Z_1| < K_{b_1}$ . Simulation results are shown in Figures 14–23.

From Figure 14, we can know that when the initial error  $Z_1$  does not satisfy  $|Z_1| \leq K_{b_1}$ , the BLF controller cannot guarantee the error global convergence. From Figures 17–19 we can know that the controller combining the SMC and BLF can guarantee the error global convergence. This is because when  $|Z_1| > K_{b_1}$ , mainly SMC is at work and it will make  $Z_1$  converge to  $(-K_{b_1}, K_{b_1})$ , and then BLF controller is at work, and it will ensure the output constraint is not violated. From Figures 20–23, we can see that the SMC controller can guarantee a good steady performance, but

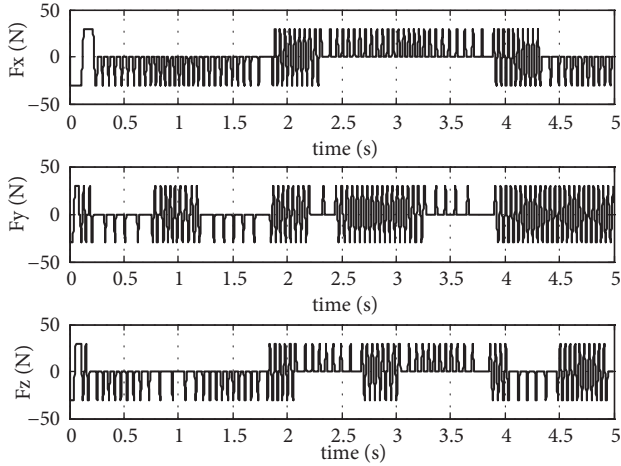


FIGURE 16: Thrust force curve.

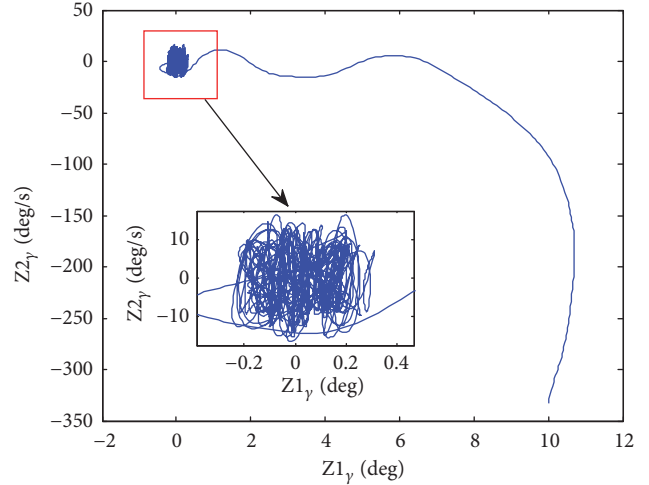


FIGURE 19: Roll angle tracking error.

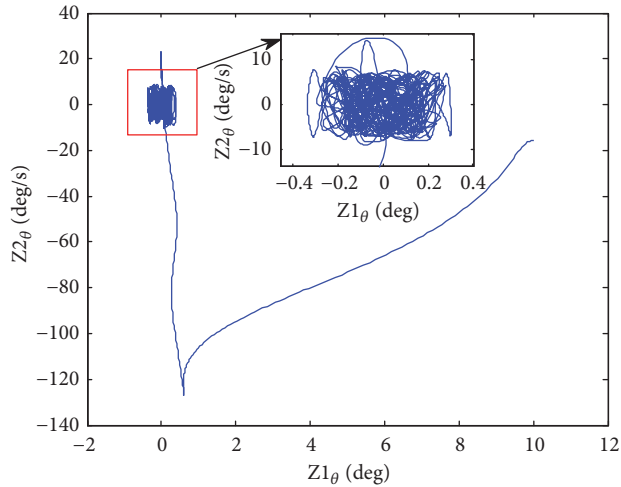


FIGURE 17: Pitch angle tracking error.

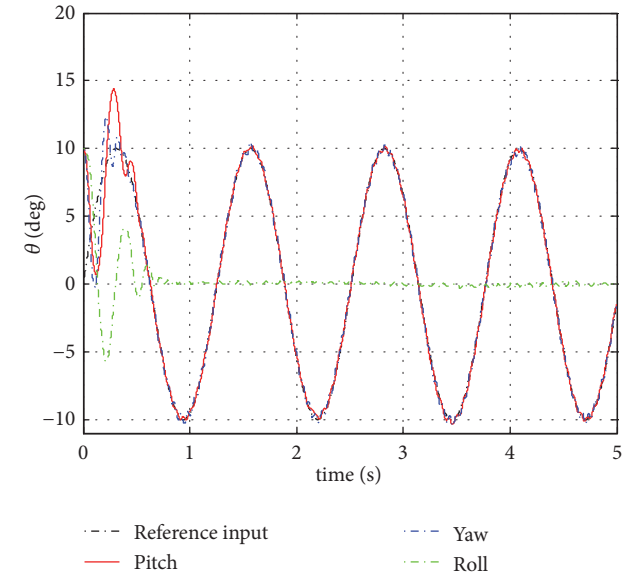


FIGURE 20: Attitude angle tracking curve with SMC controller.

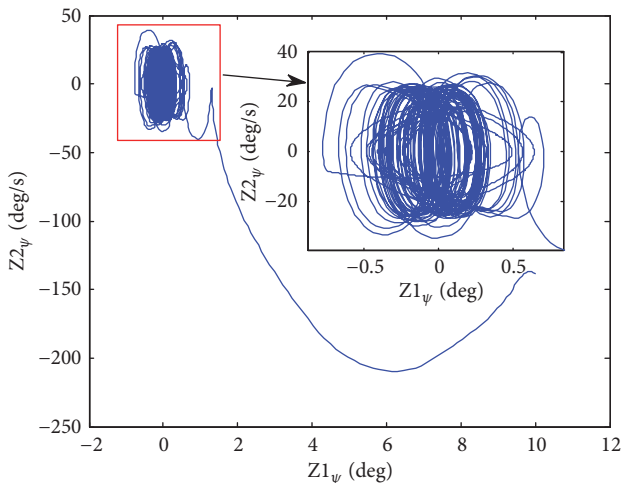


FIGURE 18: Yaw angle tracking error.

its dynamic performance cannot be guaranteed. But the controller combining BLF with SMC has a good dynamic and steady performance.

*Case 4.* Verify the performance of PSR modulator. Compare the PSR modulator with the PWWF modulator. The range of optimal parameters for the PWWF and PSR is shown in Table II in [30]. The simulation parameters are selected as showed in Table 4, and the typical step signal is used as the reference signal. The PWWF and PSR modulator modulation curves are shown in Figure 24.

From Figure 24, we can know that the difference between the PSR modulator and the PWWF modulator is in the initial stage. The PSR modulator is turned on in the initial stage until the error is reduced to the shutdown threshold. However, the PWWF modulator is turned off in the initial stage until

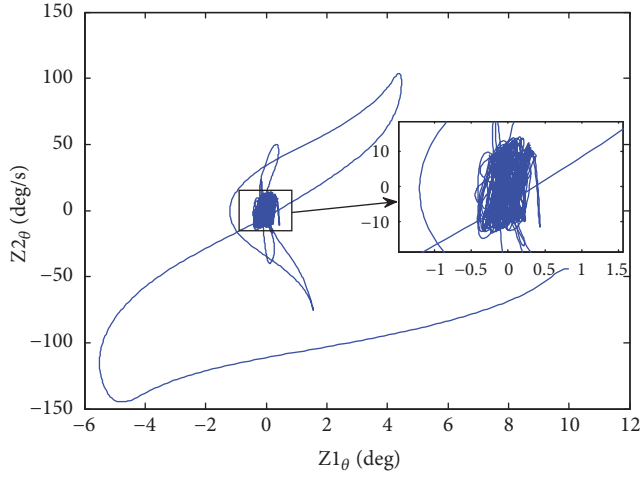


FIGURE 21: Pitch angle tracking error with SMC controller.

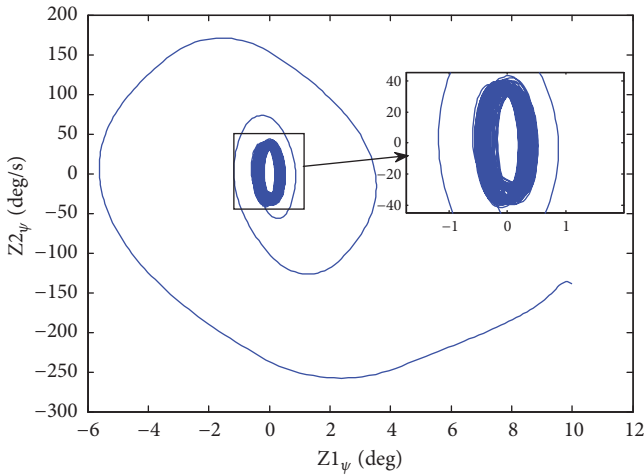


FIGURE 22: Yaw angle tracking error with SMC controller.

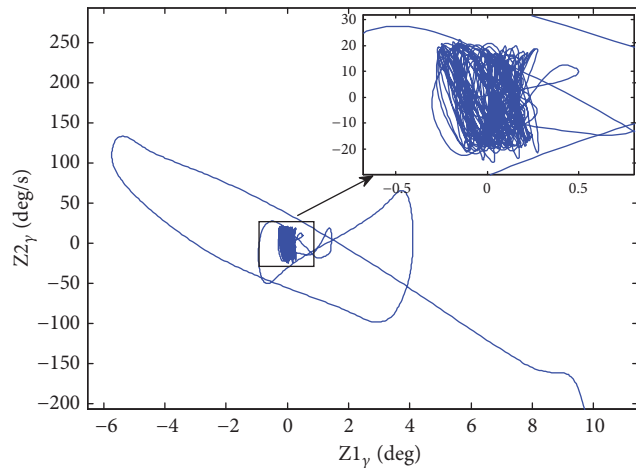


FIGURE 23: Roll angle tracking error with SMC controller.

TABLE 4: Modulator initial parameters.

PWPF	PSR
$K_m = 4$	$K_m = 2$
$T_m = 0.5$	$T_m = 0.3$
$U_{on} = 0.5$	$U_{on} = 0.45$
$U_{off} = 0.12$	$U_{off} = 0.3$

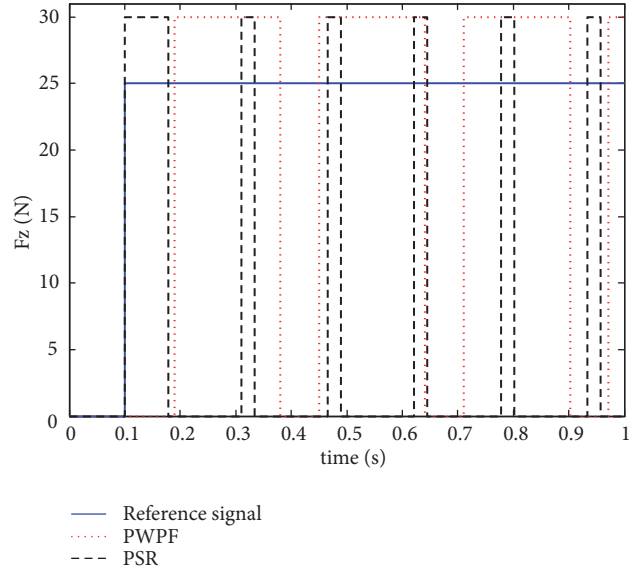


FIGURE 24: Modulators of PSR and PWPF response curves.

the error reaches the start-up threshold. This characteristic causes phase delay for PWPF modulator compared to the PSR modulator and may cause control system instability. At the same time, we clearly see from Figure 20 that the start-up time of the PWPF modulator is significantly longer than the PSR, which will lead to wasting fuel. Therefore, PSR modulator has obvious advantages compared with PWPF modulator.

### 5. Conclusion

In this paper, KKV attitude controller has been designed combining BLF with SMC to meet the state constraints caused by side window detection, and FD and NDO have been used to solve the problem of “differential explosion” and uncertainties estimation and compensation. Numerical simulations show that the designed controller can achieve attitude angles constraint and guarantee the error global convergence with fast convergence speed, high convergence accuracy and good robustness. NDO can achieve fast, smooth and accurate estimation of uncertainties, and unknown time-varying disturbances. PSR modulator can shape the continuous control command to pulse or on-off signals to meet the requirements of the thruster and achieve pseudo-linear operation. Meanwhile, it solved the PWPF modulator phase delay problem.

## Data Availability

The data used to support the findings of this study are available from this paper.

## Conflicts of Interest

The authors declare that they have no conflicts of interest.

## Acknowledgments

This work was supported by the National Nature Science Foundation of China (nos. 61773398 and 61703421)

## References

- [1] Y. Yu, M. Hou, S. Zhang, and C. Yin, "A new adaptive proportional navigation based on side window detection," *Journal of Northwestern Polytechnical University*, vol. 34, no. 2, pp. 287–293, 2016.
- [2] X. Xu and Y. Cai, "Pulse-width pulse-frequency based optimal controller design for kinetic kill vehicle attitude tracking control," *Applied Mathematics*, vol. 2, no. 25, pp. 565–574, 2011.
- [3] J. Huang, H. Zhang, G. Li, and G. Tang, "Terminal guidance and control for kinetic kill vehicle adopting side window detection," in *Proceedings of the 7th IEEE Chinese Guidance, Navigation and Control Conference, CGNCC 2016*, pp. 363–368, Nanjing, China, August 2016.
- [4] B. Q. Yang, T. Y. Zheng, S. L. Zhang et al., "Analysis and modeling of terminal guidance system for a flight vehicle with side-window detection," in *Proceedings of the Chinese Control Conference*, pp. 1051–1054, Nanjing, China, 2014.
- [5] Y. Wang, J. Zhou, B. Zhao, and Y.-H. You, "Orbit control scheme of the terminal course of side window detection kinetic kill vehicle," *Journal of Solid Rocket Technology*, vol. 39, no. 4, pp. 588–593, 2016.
- [6] T. Y. Zheng, Y. Yao, F. H. He et al., "Integrated guidance and control design of flight vehicle with side-window detection," *Chinese Journal of Aeronautics*, vol. 2, no. 3, p. 16, 2018.
- [7] X. Wang, J. Guo, S. Tang, Q. Xu, Y. Ma, and Y. Zhang, "Robust nonsingular Terminal sliding mode backstepping control for air-breathing hypersonic vehicles," *Acta Aeronautica et Astronautica Sinica*, vol. 38, no. 3, pp. 3202871–32028713, 2017.
- [8] M. Yue, L. J. Wang, and T. Ma, "Neural network based terminal sliding mode control for WMRs affected by an augmented ground friction with slippage effect," *IEEE/CAA Journal of Automatica Sinica*, vol. 4, no. 3, pp. 498–506, 2017.
- [9] D. Ye, Y. Tu, and Z. Sun, "Sliding mode control for nonparallel-ground-track imaging using Chebyshev neural network," *Acta Aeronautica et Astronautica Sinica*, vol. 36, no. 9, pp. 3092–3104, 2015.
- [10] Z. Zhu, Y. Xia, and M. Fu, "Attitude stabilization of rigid spacecraft with finite-time convergence," *International Journal of Robust and Nonlinear Control*, vol. 21, no. 6, pp. 686–702, 2011.
- [11] X. Yang, X.-X. Yao, J. Zhang, and Y.-X. Liu, "Attitude tracking of KKV based on adaptive backstepping sliding mode control," *Journal of Solid Rocket Technology*, vol. 39, no. 5, pp. 715–722, 2016.
- [12] T. Zhang, X. Shi, and Q. SHen, "Adaptive neural network dynamic surface control with unmodeled dynamics," *Control Theory & Application*, vol. 30, no. 4, pp. 475–482, 2013.
- [13] M. Ran, Q. Wang, D. Hou, and C. Dong, "Backstepping design of missile guidance and control based on adaptive fuzzy sliding mode control," *Chinese Journal of Aeronautics*, vol. 27, no. 3, pp. 634–642, 2014.
- [14] J. M. Bravo, D. Limon, T. Alamo, and E. F. Camacho, "On the computation of invariant sets for constrained nonlinear systems: an interval arithmetic approach," *Automatica*, vol. 41, no. 9, pp. 1583–1589, 2005.
- [15] D. Limon, I. Alvarado, T. Alamo, and E. F. Camacho, "MPC for tracking piecewise constant references for constrained linear systems," *Automatica*, vol. 44, no. 9, pp. 2382–2387, 2008.
- [16] T. Hatanaka and K. Takaba, "Computations of probabilistic output admissible set for uncertain constrained systems," *Systems Control and Information*, vol. 51, no. 11, pp. 499–512, 2007.
- [17] G. Herrmann, M. C. Turner, and I. Postlethwaite, "A robust override scheme enforcing strict output constraints for a class of strictly proper systems," *Automatica*, vol. 44, no. 3, pp. 753–760, 2008.
- [18] K. Kogiso and K. Hirata, "Reference governor for constrained systems with time-varying references," *Robotics and Autonomous Systems*, vol. 57, no. 3, pp. 289–295, 2009.
- [19] K. B. Ngo, R. Mahony, and Z. Jiang, "Integrator backstepping using barrier functions for systems with multiple state constraints," in *Proceedings of the 44th IEEE Conference on Decision and Control, and the European Control Conference (CDC-ECC '05)*, pp. 8306–8312, Seville, Spain, December 2005.
- [20] Y. Qiu, X. Liang, Z. Dai, J. Cao, and Y. Chen, "Backstepping dynamic surface control for a class of non-linear systems with time-varying output constraints," *IET Control Theory & Applications*, vol. 9, no. 15, pp. 2312–2319, 2015.
- [21] B. Niu and J. Zhao, "Tracking control for output-constrained nonlinear switched systems with a barrier Lyapunov function," *International Journal of Systems Science*, vol. 44, no. 5, pp. 978–985, 2013.
- [22] Y.-J. Liu and S. Tong, "Barrier Lyapunov functions-based adaptive control for a class of nonlinear pure-feedback systems with full state constraints," *Automatica*, vol. 64, pp. 70–75, 2016.
- [23] K. P. Tee, S. S. Ge, and E. H. Tay, "Barrier Lyapunov functions for the control of output-constrained nonlinear systems," *Automatica*, vol. 45, no. 4, pp. 918–927, 2009.
- [24] K. P. Tee, B. Ren, and S. S. Ge, "Control of nonlinear systems with time-varying output constraints," *Automatica*, vol. 47, no. 11, pp. 2511–2516, 2011.
- [25] W. Sun, J. Lan, and J. T. W. Yeow, "Constraint adaptive output regulation of output feedback systems with application to electrostatic torsional micromirror," *International Journal of Robust and Nonlinear Control*, vol. 25, no. 4, pp. 504–520, 2015.
- [26] W. He, S. Zhang, and S. S. Ge, "Adaptive control of a flexible crane system with the boundary output constraint," *IEEE Transactions on Industrial Electronics*, vol. 61, no. 8, pp. 4126–4133, 2014.
- [27] F. Yan and J. Wang, "Fuel-assisted in-cylinder oxygen fraction transient trajectory shaping control for diesel engine combustion mode switching," in *Proceedings of the 2011 American Control Conference, ACC 2011*, pp. 1573–1578, San Francisco, Calif, USA, July 2011.
- [28] D. Meijun, D. Zhou, and C. Dalian, "Research of terminal guidance law and PWPF modulator for near space interceptor based on finite time theory," *Acta Aeronautica et Astronautica Sinica*, vol. 38, no. 25, pp. 341481–341483, 2017.

- [29] Q. Wang, B.-Q. Yang, and K.-M. Ma, "PWPF optimizing design and its application research to terminal guidance of Kinetic killing vehicle," *Yuhang Xuebao/Journal of Astronautics*, vol. 26, no. 5, pp. 576–580, 2005.
- [30] M. Navabi and H. Rangraz, "Comparing optimum operation of Pulse Width-Pulse Frequency and Pseudo-Rate modulators in spacecraft attitude control subsystem employing thruster," in *Proceedings of the 6th International Conference on Recent Advances in Space Technologies, RAST 2013*, pp. 625–630, Istanbul, Turkey, June 2013.
- [31] Y. Tang, Y. Wu, M. Wu, X. Hu, and L. Shen, "Nonlinear tracking-differentiator for velocity determination using carrier phase measurements," *IEEE Journal of Selected Topics in Signal Processing*, vol. 3, no. 4, pp. 716–725, 2009.
- [32] B. Q. Yang, *Research on guidance and control law for exo-atmospheric KKV based on predictive control [Ph. D. thesis]*, Harbin Institute of Technology, Harbin, China, 2009.

## Research Article

# Unknown Inputs Nonlinear Observer for an Activated Sludge Process

Feten Smida , Taoufik Ladhari , Salim Hadj Saïd, and Faouzi M'sahli

*Department of Electrical Engineering, ENIM, Road Ibn Eljazzar, 5019 Monastir, Tunisia*

Correspondence should be addressed to Feten Smida; [smida.feten@gmail.com](mailto:smida.feten@gmail.com)

Received 6 March 2018; Revised 15 May 2018; Accepted 5 August 2018; Published 16 August 2018

Academic Editor: Olfa Boubaker

Copyright © 2018 Feten Smida et al. This is an open access article distributed under the Creative Commons Attribution License, which permits unrestricted use, distribution, and reproduction in any medium, provided the original work is properly cited.

This paper deals with the jointly estimation problem of unknown inputs and nonmeasured states of one altering aerated activated sludge process (ASP). In order to provide accurate and economic concentration measures during aerobic and anoxic phases, a cascade high gain observer (HGO) approach is developed. Only two concentrations are available; the other process's states are assumed unavailable. The observer converges asymptotically and it leads to a good estimation of the unavailable states which are the ammonia and substrate concentration, as well as a quite reconstruction of the unknown inputs, which are the influent ammonia and the influent substrate concentrations. To highlight the efficiency of the proposed HGO with this MIMO system's dynamics, simulation results are validated with experimental data.

## 1. Introduction

The environmental conservation and the biological treatment of waste water are required to preserve the ecosystems. Therefore, modeling an activated sludge (AS) Waste Water Treatment Process (WWTP) has been one important area of research for three decades. This AS wastewater treatment process is physically, chemically, and biologically very complex. Furthermore the AS is nonlinear and unsteady system; this is caused by the flow rate variations in a waste water and its composition, joined to reactions varying in time within mingled microorganisms. In order to model the biological plant of the activated sludge process, a lot of models have been suggested: Activated Sludge Process Model N1 (ASM(1)) in [1], the ASM(2) in [2], ASM(2d) in [3], and ASM(3) in [4]. Due to the complexity of these models, various types of an activated sludge-plant reduced model have been put forward in the literature [5–10]. In [11] the authors presented one new model to alternate activated sludge models. In fact the mean continuous model would capture the switching dynamics governing behavior (i.e., aerobic-anaerobic phases), without any consideration of any switching behavior. Recently, [12] proposed a generalized state-identification classification modeling. As a matter of

fact, image processing and analysis have been utilized on the basis of linear regression modeling.

More generally, waste water treatment processes have a few measurement and control equipment. Under these circumstances various models are utilized in controller design. Among control methods applied to the bioprocess we quote robust multimodel control using the Quantitative Feedback Theory (QFT) techniques in [13], adaptive control in [14, 15], and model predictive control (MPC) in [16, 17] and recently networked control in [18]. Nonetheless, the state variables of the ASM are not all available which present some difficulties in the eventual implementation.

In practice, for activated sludge process control and/or supervision, there are some nonlinear measured inputs, states, or concentrations (substrate concentration). Alternatively, these latter can also be hardly measured (ammonia and nitrate concentration): indeed the main difficulty towards the establishment of control strategies originates in general from the absence online, cheap, and reliable instrumentation. Even the existing sensors can be in many cases noisy and may require high maintenance and implementation cost. In the objective of solving such a problem, various observation methods are proposed. Among the observation method already studied we quote the following: [19] proposed for

the nonlinear ASP model an extended Kalman filter, which works within the alternating aerobic-anoxic phase. The filter has been utilized for estimating states and nonstationary disturbances; [20] provided a brief summary of some results concerning state and parameter estimation approaches in relation to the chemical and biochemical processes. In [21] the authors resorted to a linear matrix inequality (LMI) to determine the values of the gain matrix of the asymptotic and classic observer, those are applied to a linearized bioprocess model. In the same framework a nonlinear observer which actually utilized both LMI and Lyapunov function was studied in [22]. In [11], the authors applied one classical Luenberger observer which was dedicated to continuous nonlinear models after linearization and it allows the estimation of nitrate and ammonia concentrations. Furthermore, to better developing the control strategies in presence of unknown inputs, several researches are devoted to such observation.

Studying dynamical systems when having UIs has highly given an incentive for research activities in state estimation, fault reconstruction, and control theory. By means of one Unknown Input Observer (UIO), simultaneously estimating the system state and the UIs is achievable. In [23], the authors extended the MIMO systems triangular class. In actual fact, these systems involved nonlinear inputs. In addition, they proposed one full order high gain observer in order to conjointly estimate nonmeasured state and UIs. The authors in [24] gave an essential and sufficient condition for UIO existence. In [25], the authors worked out UIO for one nonlinear system's canonical observable form in presence of uncertainties in LMI terms. The author in [26] designed a nonlinear differential algebraic systems' observation scheme with UI. The authors in [27] extended a standard high gain observer (HGO) with the aid of a sliding-mode-based term. This latter would follow the UI vector. Extending the work of [28, 29] designed a set of cascade high gain observers for many nonlinear MIMO systems. Each observer would provide the estimation of just an UI-vector component, with the exception of the last one which would really give an adjustment of full state variables. Given its utility, UIO has received big attention and has been applied to ASP, as in [30] where the authors suggested estimated states and the UIs as regards a minimized ASP nonlinear model through the use of the Extended Kalman Filter (EKF). Reference [31] treated the problems of Waste Water Treatment Plants (WWTP) sensor fault detection with the basic UIO (HGO). In fact, faults are just considered as unknown inputs. In a recent work, [32], an UIO is used to estimate jointly the states and an UI of the bioprocess linearized model.

The purpose of this paper is to estimate UIs and unavailable states of ASP. This contribution deals with the use of high gain UIO, which is relatively simple to design, can provide global or semiglobal stability results for a large class of nonlinear systems, robust to modeling uncertainty and external disturbances, and has a single adjustment parameter. The concentrations of ammonia and substrate in the inputs ( $S_{sin}$  and  $S_{NH_4in}$ ) are very influential in the solution of the system model [33]. So the continuous varying inputs may seriously affect the system control; such problem can be solved by the use of an unknown inputs observer.

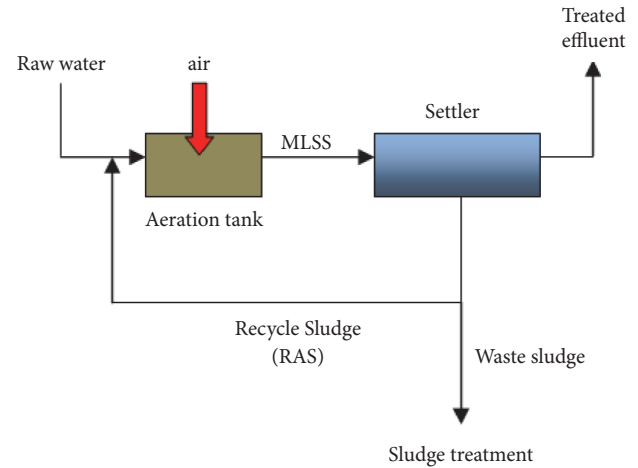


FIGURE 1: ASP diagram.

The paper is planned as follows. Initially we introduce a nonlinear ASP model. This model belongs to one specific nonlinear system class for which the development of a corresponding UIO is then detailed in section three; some preliminaries on the nonlinear systems class and state transformations are given in this section. Thereafter, in section four, and to facilitate applying the observation algorithm, we have proposed an appropriate repartition of ASP states. Simulation results are presented in the aim of highlighting the effectiveness of the proposed observer in curing one systematic routine so as to reconstruct jointly UIs and state variables for the ASP. A final conclusion ends the paper.

## 2. Process Description

There is a various model of ASP design. Precisely an ASP is composed of three principal components. The first component is an aeration tank. The latter will serve as a bioreactor. The second component is a settling tank (final clarifier). It was used to separate AS solids and treated waste water. The third one is a Return Activated Sludge (RAS) which is a tool for transferring settled AS from the clarifier into the aeration tank influent, (Figure 1). Added to that, the atmospheric air, or pure oxygen, will be put into a combination of primary treated sewage (waste water) which will be mixed with organisms in the purpose of developing a biological floc. In general, such a mixture is named as Mixed Liquor. Frequently, the concentration of the dry solids of mixed liquor suspended solid ranges between 3 and 6 g/L. Thereby, we control any removal efficiency by means of multiple operative conditions, for example, the aeration tank hydraulic residence time. To make it clear, the latter is determined by the division of the volume of the aeration tank over the flow rate. It is worth mentioning other factors like influent load (BOD5: Biological Oxygen Demand within 5 days, COD: Chemical Oxygen Demand, Nitrogen, etc.). The last factor is related to the AS solids which are existing in the aeration tank. We can mention here two other factors: oxygen supply and temperature. Mixed liquor will be evacuated, at the aeration

tank discharge, into settling tanks. In addition to that the supernatant (treated waste water) ought to or should run off in the purpose of being discharged to a natural water. It can as well undergo further treatment before discharge. Because of biological growth, excess sludge has an eventual accumulation beyond the desired mixed liquor suspended solid concentration in the aeration tank. We remove such a solid amount from the treatment process in the target of keeping the biomass ratio to supplied food in balance. This solid amount, which is called the waste activated sludge, should be kept aside in storage tanks and should be further treated by digestion. This can be done prior to disposal under anaerobic or aerobic conditions.

**2.1. Materiel and Method.** The process considered in this work is the pilot ASWWTP unit in the Engineering Laboratory of Environmental Processes (ELEP) of the National Institution of Applied Sciences (NIAS) in Toulouse, France. It comprises a unique aeration tank with a volume  $V_a = 0.03m^3$  equipped with an aeration surface that provides the necessary oxygen in the reactor in the goal of creating nitrification and denitrification conditions. It is obvious that the settler is a tank in which, in general, biomass is recirculated within the tank. In [34] mass balance was applied for each soluble (substrate) or particulate component (biomass). This led to an eleven state model that was subsequently reduced to four state variables. The earlier nonlinear models like ASM(1) were unattractive because of the high complex scheme systems. As a consequence, our focus is on reduced order models, which are on the bases of some biochemical considerations, giving the description of the nonlinear process behavior [33]. As a result, we distinguish aerobic and anoxic phases through the use of state variables associated with four substrate concentrations. As a matter of fact, aerobic phase is the aeration period. In the latter the air is injected within the reactor in big quantities in the objective of converting the pollution as ammonium nitrate. After that, in order to transform nitrate in nitrogen, in the anoxic phase, the aeration is stopped and also an optional extraneous carbon source is added inside the mixer. The operation of altering phases can be caused by the  $k_{la}$  oxygen transfer coefficient value which conspicuously varies from 0 (concerning the anoxic phase) to higher values (in what concerns the aerobic phase) (Figure 2).

**2.2. System Model.** The downsized system model is made up of four state variables which have just one alternating phase operation (alternating aeration). The latter is caused by the  $k_{la}$  oxygen transfer coefficient value changing from 0 to higher values. Tables 1 and 3 provide the process model's variable and parameters, while Table 2 gives the state variables. The process nonlinear model differential equations are expressed in the following [19]:

$$\begin{aligned}\dot{X}_{O_2} &= -(D_s + D_c) X_{O_2} + K_{La} (S_{O_2sat} - X_{O_2}) \\ &\quad - \frac{1 - Y_H}{Y_H} \beta_1 - 4,57\beta_3 \\ \dot{X}_{NO_3} &= -(D_s + D_c) X_{NO_3} - \frac{1 - Y_H}{2,86Y_H} \beta_2 + \beta_3\end{aligned}$$

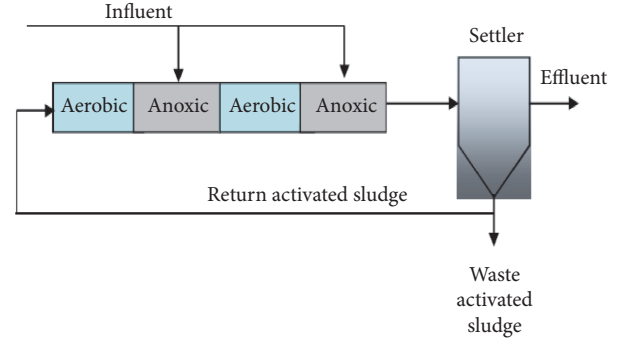


FIGURE 2: Combine aerobic and anoxic conditions to achieve nitrification and denitrification.

TABLE 1: Nonlinear-model parameters.

Parameter	Description	Value
$Y_H \text{ g}\cdot\text{g}^{-1}$	Performance coefficient of heterotrophic biomass	0.67
$i_{NBM} \text{ g}\cdot\text{g}^{-1}$	Nitrogen mass in heterotrophic and autotrophic biomass concentrations	0.080
$\eta_{NO_3h}$	Hydrolysis in anoxic phase correction factor	0.8
$K_{NH_4AUT} \text{ gN}\cdot\text{m}^{-3}$	Average saturation coefficient of ammonia for autotrophic biomass	0.25
$K_{NO_3} \text{ gN}\cdot\text{m}^{-3}$	Average saturation coefficient of nitrate	0.5
$K_{O_2H} \text{ gO}_2\cdot\text{m}^{-3}$	Average saturation coefficient of oxygen for heterotrophic biomass	0.2
$K_{O_2AUT} \text{ gO}_2\cdot\text{m}^{-3}$	Average saturation coefficient of oxygen for autotrophic biomass	0.4
$\alpha_1 \text{ day}^{-1}$	Growth rate of heterotrophic biomass	46.91
$\alpha_2 \text{ g}\cdot\text{m}^{-3}\text{day}^{-1}$	Autotrophic speed of nitrate production	276.73
$\alpha_3 \text{ g}\cdot\text{m}^{-3}\text{day}^{-1}$	Hydrolysis speed of slowly biodegradable substrate by the heterotrophic	87.54
$\alpha_4 \text{ g}\cdot\text{m}^{-3}\text{day}^{-1}$	Ammonification of soluble organic nitrogen	1546.8
$S_{O_2sat} \text{ g}\cdot\text{m}^{-3}$	Concentration of dissolved oxygen saturation	9.0

$$\begin{aligned}\dot{X}_{NH_4} &= D_s X_{NH_{4in}} - (D_s + D_c) X_{NH_4} - i_{NBM} (\beta_1 + \beta_2) \\ &\quad - \beta_3 + \beta_4 \\ \dot{X}_S &= D_s X_{S_{in}} + D_s S_{S_c} - (D_s + D_c) X_S \\ &\quad - \frac{1}{Y_H} (\beta_1 + \beta_2) + \beta_5\end{aligned}\tag{1}$$

TABLE 2: State variables.

Notation	Description
$X_s$	Concentration of biodegradable substrate
$X_{NO_3}$	Concentration of nitrogen as nitrate and nitrite
$X_{NH_4}$	Concentration of nitrogen as ammonia
$X_{O_2}$	Concentration of oxygen
$X_{NH_{4in}}$	Concentration of ammonia input
$X_{sin}$	Concentration of substrate input

TABLE 3: Input variables.

Parameter	Description	Value
$D_s$	Input dilution rate	$2.58 \text{ day}^{-1}$
$D_c$	Dilution rate of external carbon source	$0.016 \text{ day}^{-1}$
$S_{sc}$	External carbon source's concentration	$16000 \text{ g.m}^{-3}$
$k_{La}$	Oxygen transfer coefficient	$215 \text{ or } 0 \text{ day}^{-1}$

with

$$\begin{aligned}
\beta_1 &= \alpha_1 X_s \frac{X_{O_2}}{X_{O_2} + K_{O_2H}} \\
\beta_2 &= \alpha_1 X_s \frac{X_{NO_3}}{X_{NO_3} + K_{NO_3}} \frac{K_{O_2H}}{X_{O_2} + K_{O_2H}} \\
\beta_3 &= \alpha_2 \frac{X_{O_2}}{X_{O_2} + K_{O_{2aut}}} \frac{X_{NH_4}}{X_{NH_4} + K_{NH_{4aut}}} \\
\beta_4 &= \alpha_3 \\
\beta_5 &= \alpha_4 \frac{X_{O_2}}{X_{O_2} + K_{O_{2aut}}} \\
&\quad + \eta_{NO_3h} \frac{X_{NO_3}}{X_{NO_3} + K_{NO_3}} \frac{K_{O_2H}}{X_{O_2} + K_{O_2H}}
\end{aligned} \tag{2}$$

$X_{O_2}$ ,  $X_{NO_3}$ ,  $X_{NH_4}$ , and  $X_s$  are the concentrations of the dissolved oxygen, the nitrate, the ammonia, and the readily biodegradable substrate, respectively.

$X_{S_{in}}$  is the concentration of substrate soluble in water and  $X_{NH_{4in}}$  is the concentration of the ammoniacal nitrogen entering the reactor.  $X_{S_{in}}$  and  $X_{NH_{4in}}$  are considered the IUs of the system.  $S_{sc}$  is an oxygenous carbon source.  $D_s$  and  $D_c$  are the dilution rates determined as

$$\begin{aligned}
D_s &= \frac{Q_s}{V_a}, \\
D_c &= \frac{Q_c}{V_a}
\end{aligned} \tag{3}$$

where  $Q_s$  is the input flow. In addition to that,  $Q_c$  is an external carbon source flow.

$\beta_i$  (for  $i=1..5$ ) is a simpler form of the process kinetics  $\rho_i$ . It is directly linked to the standard mode ASM(1). Moreover,  $\alpha_i$  is a specific parameter of the downsized nonlinear model.

### 3. Studied Nonlinear Class and Design of Unknown Input Observer

It is worth considering the nonlinear multioutput systems. These latter can be as follows:

$$\begin{aligned}
\dot{x} &= f(u, x) + g(u, x, v) + \tilde{\varepsilon}(t) \\
y &= x^1
\end{aligned} \tag{4}$$

With  $x = [x^1 \ x^2 \ \dots \ x^q]^T \in \mathbb{R}^n$  where  $x^k \in \mathbb{R}^{n_k}$  for  $k = 1, 2, \dots, q$  and  $n_1 \geq n_2 \geq \dots, n_q$ ,  $\sum_{k=1}^q n_k = n$ .  $\tilde{\varepsilon}(t) = [0^T, \dots, 0^T, \varepsilon^q]^T$  is an unknown function. The unknown input  $v = v^1 \in \mathbb{R}^m$ , the known input  $u \subset U$  a compact set of  $\mathbb{R}^u$ , and the output  $y \in \mathbb{R}^{n_1}$ ,  $f(u, x) \in \mathbb{R}^n$  with  $f^k(u, x) \in \mathbb{R}^{n_k}$ .  $\lambda_1$  has been related to the unknown inputs. One notates  $1 \leq \lambda_1 \leq q$  such as

$$\forall i < \lambda_1 : \frac{\partial g^i}{\partial v^1}(u, x, v) \equiv 0, \tag{5}$$

$$\frac{\partial g^{\lambda_1}}{\partial v^1}(u, x, v) \neq 0$$

System (1) is presented in its detailed form by the following equations:

$$\begin{aligned}
\dot{x}^1 &= f^1(u, x^1, x^2) + g^1(u, x^1) \\
&\quad \vdots \\
\dot{x}^{\lambda_1-1} &= f^{\lambda_1-1}(u, x^1, \dots, x^{\lambda_1}) + g^{\lambda_1-1}(u, x^1, \dots, x^{\lambda_1-1}) \\
\dot{x}^{\lambda_1} &= f^{\lambda_1}(u, x^1, \dots, x^{\lambda_1+1}) + g^{\lambda_1}(u, x^1, \dots, x^{\lambda_1}, v^1) \\
&\quad \vdots \\
\dot{x}^{q-1} &= f^{q-1}(u, x^1, \dots, x^q) + g^{q-1}(u, x^1, \dots, x^{q-1}, v^1) \\
\dot{x}^q &= f^q(u, x^1, \dots, x^q) + g^q(u, x^1, x^2, \dots, x^q, v^1) + \varepsilon^q \\
y &= x^1
\end{aligned} \tag{6}$$

Note that this nonlinear system class is more general than those studied in [23, 28, 35].

Let

$$\phi^k(u, x, v^1) = f^k(u, x) + g^k(u, x, v) + \tilde{\varepsilon}(t) \tag{7}$$

Our aim is to synthesize an observer to estimate at the same time the nonmeasured states and the vector of unknown inputs. In the target of dealing with the HGO synthesis, we make what follows:

(A.1) For  $1 \leq k \leq q - 1$  the function  $x^{k+1} \mapsto f^k(u, x^1, \dots, x^k, x^{k+1})$  from  $\mathbb{R}^{n_{k+1}} \mapsto \mathbb{R}^{n_k}$  is injective for all  $(u, x^1, \dots, x^k, x^{k+1})$ . Then, there exist  $\alpha_1, \beta_1 > 0$  such that  $\forall k \in \{1, \dots, q-1\}, \forall x \in \mathbb{R}^n, \forall u \in U$

$$0 < \alpha_1^2 I_{n_{k+1}} \leq \left( \frac{\partial f^k}{\partial x^{k+1}}(u, x) \right)^T \frac{\partial f^k}{\partial x^{k+1}}(u, x) \leq \beta_1^2 I_{n_{k+1}} \tag{8}$$

where  $I_{n_{k+1}}$  is a matrix identity, whose dimension is  $(n_{k+1}) \times (n_{k+1})$ .

Assumption (A1) is essential for guaranteeing the diffeomorphism existence which could make an initial system in the canonical form of observability.

(A.2) The function  $(x^{\lambda_1+1}, v^1) \mapsto \varphi^{\lambda_1}(u, x^1, \dots, x^{\lambda_1}, x^{\lambda_1+1}, v^1)$  from  $\mathbb{R}^{n_{\lambda_1+1}+m} \rightarrow \mathbb{R}^{n_{\lambda_1}}$  is injective for all  $(u, x^1, \dots, x^{\lambda_1}, v^1)$ ; we consider

$$F^{\lambda_1}(x, u, v^1) = \left( \frac{\partial \varphi^{\lambda_1}}{\partial x^{\beta_1+1}}(u, x, v^1) \quad \frac{\partial \varphi^{\lambda_1}}{\partial v^1}(u, x, v^1) \right) \quad (9)$$

Such assumption is a rank condition, which has to be opted for to estimate UIs.

Consequently, the next inequality is needed to design UIO:

$$n_{\lambda_1+1} + m \leq n_{\lambda_1} \quad (10)$$

In particular, we need to have

$$m \leq p - 1 \quad (11)$$

**3.1. State Transformation.** Now, a set of coordinate transformations should be introduced so as to canonically form system (4) corresponding to the HGO synthesis. Just as it should be, an augmented system is made up of 2 blocks such that their outputs have the same values as those of the original system (4).  $x^1, \dots, x^{\lambda_1+1}$  and  $v^1$  are related first-block variables. On the other hand, variables linked to the last one should be able to be simple copies of the full system states.

As a consequence, we interpret the studied immersion like an injective map  $\psi$  which is defined as follows:

$$\begin{aligned} \psi : \mathbb{R}^{n+m} &\longrightarrow \mathbb{R}^{n_1+\dots+n_{\lambda_1+1}+m+n} \text{ and} \\ \begin{pmatrix} x \\ v^1 \end{pmatrix} &\mapsto \mu = \psi(x, v) = \begin{pmatrix} \mu^1 \\ \mu^2 \end{pmatrix}, \text{ with:} \\ \mu^1 &= \begin{pmatrix} \mu_1^1 \\ \mu_2^1 \\ \vdots \\ \mu_{\lambda_1+1}^1 \end{pmatrix} \in \mathbb{R}^{n_1+\dots+n_{\lambda_1+1}+m}, \\ \mu^2 &= \begin{pmatrix} \mu_1^2 \\ \mu_2^2 \\ \vdots \\ \mu_q^2 \end{pmatrix} \in \mathbb{R}^n, \end{aligned} \quad (12)$$

$$\psi(x, v) : \begin{cases} \mu_k^1 = x^k, & k = 1, \dots, \lambda_1 \\ \mu_{\lambda_1+1}^1 = \begin{pmatrix} \mu_{\lambda_1+1,1}^1 \\ \mu_{\lambda_1+1,2}^1 \end{pmatrix} = \begin{pmatrix} x^{\lambda_1+1} \\ v^1 \end{pmatrix} \\ \mu_k^2 = x^k, & k = 1, \dots, q \end{cases} \quad (13)$$

Thus, the two subsystems in the  $\mu$  coordinates are given in the following:

$$\begin{aligned} \dot{\mu}_1^1 &= f^1(u, \mu_1^1, \mu_2^1) + g^1(u, \mu_1^1) \\ &\vdots \\ \dot{\mu}_{\lambda_1}^1 &= f^{\lambda_1}(u, \mu_1^1, \mu_2^1, \dots, \mu_{\lambda_1+1,1}^1) + g(u, \mu_1^1, \mu_2^1, \dots, \mu_{\lambda_1}^1, \mu_{\lambda_1+1,2}^1) \\ \dot{\mu}_{\lambda_1+1}^1 &= \begin{pmatrix} f^{\lambda_1+1}(u, \mu_1^1, \mu_2^1, \dots, \mu_{\lambda_1+1,1}^1, \mu_{\lambda_1+2}^1) + g(u, \mu_1^1, \mu_2^1, \dots, \mu_{\lambda_1+1,1}^1, \mu_{\lambda_1+1,2}^1) \\ \varepsilon^1(t) \end{pmatrix} \end{aligned} \quad (14)$$

$$\begin{aligned} y_1 &= \mu_1^1 \\ \dot{\mu}_1^2 &= f^1(u, \mu_1^2, \mu_2^2) + g^1(u, \mu_1^2) \\ &\vdots \\ \dot{\mu}_{q-1}^2 &= f^{q-1}(u, \mu_{1;q}^2) + g^{q-1}(u, \mu_{1;q-1}^2, \mu_{\lambda_1+2}^2) \\ \dot{\mu}_q^2 &= f^q(u, \mu_{1;q}^2) + g^{q-1}(u, \mu_{1;q}^2, \mu_{\lambda_1+2}^2) + \varepsilon^q \\ y_2 &= \mu_1^2 \end{aligned} \quad (15)$$

with  $\varepsilon^1(t)$  is an unknown bounded function.

In order to obtain the canonical form, a second injective map  $\phi$  is introduced as follows:  $\Phi : \mathbb{R}^{n_1 + \dots + n_{\lambda_1+1} + m + n} \rightarrow \mathbb{R}^{p(\lambda_1+1)pq}$ ,

$$\begin{pmatrix} \mu^1 \\ \mu^2 \end{pmatrix} \mapsto \zeta = \Phi(u, \mu) = \begin{pmatrix} \zeta^1 = \Phi_1(u, \mu) \\ \zeta^2 = \Phi_2(u, \mu) \end{pmatrix} \quad (16)$$

with

$$\zeta^1 = \begin{pmatrix} \zeta_1^1 \\ \zeta_2^1 \\ \vdots \\ \zeta_{\lambda_1+1}^1 \end{pmatrix} \in \mathbb{R}^{(\lambda_1+1)p}, \quad (17)$$

$$\zeta^2 = \begin{pmatrix} \zeta_1^2 \\ \zeta_2^2 \\ \vdots \\ \zeta_q^2 \end{pmatrix} \in \mathbb{R}^{qp}$$

$\zeta_j^1$  and  $\zeta_j^2$  are defined such as

$$\begin{aligned} \zeta_1^1 &= \Phi_{1,1}(u, \mu_1^1) = \mu_1^1 \\ \zeta_2^1 &= \Phi_{1,2}(u, \mu_1^1, \mu_2^1) = f^1(u, \mu_1^1, \mu_2^1) \\ \zeta_3^1 &= \Phi_{1,3}(u, \mu_1^1, \mu_2^1, \mu_3^1) = \frac{\partial f^1}{\partial \mu_2^1}(u, \mu_1^1, \mu_2^1) f^1(u, \mu_{1:3}^1) \\ &\vdots \\ \zeta_{\lambda_1}^1 &= \Phi_{1,\lambda_1}(u, \mu_{1:\lambda_1}^1) = \left( \prod_{k=1}^{\lambda_1-2} \frac{\partial f^k}{\partial \mu_{k+1}^1}(u, \mu_{1:k+1}^1) \right) \\ &\quad \cdot f^{\lambda_1-1}(u, \mu_{1:\lambda_1}^1) \\ \zeta_{\lambda_1+1}^1 &= \Phi_{1,\lambda_1+1}(u, \mu_{1:\lambda_1+1}^1) \\ &= \left( \prod_{k=1}^{\lambda_1-1} \frac{\partial f^k}{\partial \mu_{k+1}^1}(u, \mu_{1:k+1}^1) \right) \\ &\quad \cdot (f^{\lambda_1}(u, \mu_{1:\lambda_1}^1, \mu_{\lambda_1+1}^1) + g^{\lambda_1}(u, \mu_{1:\lambda_1}^1, \mu_{\lambda_1+1,2}^1)) \\ \zeta_1^2 &= \Phi_{2,1}(u, \mu_1^2) = \mu_1^2 \\ \zeta_2^2 &= \Phi_{2,2}(u, \mu_1^2, \mu_2^2) = f^1(u, \mu_1^2, \mu_2^2) \\ \zeta_3^2 &= \Phi_{2,3}(u, \mu_1^2, \mu_2^2, \mu_3^2) = \frac{\partial f^1}{\partial \mu_2^2}(u, \mu_1^2, \mu_2^2) \\ &\quad \cdot f^1(u, \mu_1^2, \mu_2^2, \mu_3^2) \\ &\vdots \end{aligned} \quad (18)$$

$$\begin{aligned} \zeta_{\lambda_1}^2 &= \Phi_{2,\lambda_1}(u, \mu_{1:\lambda_1}^2) = \left( \prod_{k=1}^{\lambda_1-2} \frac{\partial f^k}{\partial \mu_{k+1}^2}(u, \mu_{1:k+1}^2) \right) \\ &\quad \cdot f^{\lambda_1-1}(u, \mu_{1:\lambda_1}^2) \\ \zeta_{\lambda_1+1}^2 &= \Phi_{2,\lambda_1+1}(u, \mu_{1:\lambda_1+1}^2) \\ &= \left( \prod_{k=1}^{\lambda_1-1} \frac{\partial f^k}{\partial \mu_{k+1}^2}(u, \mu_{1:k+1}^2) \right) f^{\lambda_1}(u, \mu_{1:\lambda_1+1}^2) \\ &\quad \vdots \\ \zeta_q^2 &= \Phi_{2,q}(u, \mu_{1:q}^2) = \left( \prod_{k=1}^{q-2} \frac{\partial f^k}{\partial \mu_{k+1}^2}(u, \mu_{1:k+1}^2) \right) \\ &\quad \cdot f^{q-1}(u, \mu_{1:q}^2) \end{aligned} \quad (19)$$

Using the adopted notation, system (12) can be written in the new coordinates  $\zeta$  as follows:

$$\begin{aligned} \dot{\zeta}_1^1 &= \zeta_2^1 \\ \dot{\zeta}_2^1 &= \zeta_3^1 + \psi_2^1(u, \dot{u}, \zeta_1^1, \zeta_2^1) \\ &\vdots \\ \dot{\zeta}_{\lambda_1}^1 &= \zeta_{\lambda_1+1}^1 + \psi_{\lambda_1}^1(u, \dot{u}, \zeta_1^1, \dots, \zeta_{\lambda_1}^1) \\ \dot{\zeta}_{\beta_1+1}^1 &= \psi_{\beta_1+1}^1(u, \dot{u}, \zeta) \\ &\quad + \left( \prod_{j=1}^{\lambda_1-1} \frac{\partial f^j}{\partial \mu_{j+1}^1}(u, \zeta^j) \right) \frac{\partial g^{\lambda_1}}{\partial v^1}(u, \zeta^1) \varepsilon(t) \\ \gamma_1 &= \zeta_1^1 \\ \dot{\zeta}_1^2 &= \zeta_2^2 \\ \dot{\zeta}_2^2 &= \zeta_3^2 + \psi_2^2(u, \dot{u}, \zeta_1^2, \zeta_2^2) \\ &\vdots \\ \dot{\zeta}_{\lambda_1}^2 &= \zeta_{\lambda_1+1}^2 + \psi_{\lambda_1}^2(u, \dot{u}, \zeta_1^2, \dots, \zeta_{\lambda_1}^2, \zeta^1) \\ \dot{\zeta}_{\lambda_1+1}^2 &= \zeta_{\lambda_1+2}^2 + \psi_{\lambda_1+1}^2(u, \dot{u}, \zeta_1^2, \dots, \zeta_{\lambda_1}^2, \zeta_{\lambda_1+1}^2, \zeta^1) \\ &\vdots \\ \dot{\zeta}_{q-1}^2 &= \zeta_q^2 + \psi_{q-1}^2(u, \dot{u}, \zeta_1^2, \dots, \zeta_{q-1}^2, \zeta^1) \\ \dot{\zeta}_q^2 &= \psi_q^2(u, \dot{u}, \zeta) \varepsilon^q \\ \gamma_2 &= \zeta_1^2 \end{aligned} \quad (20)$$

with

$$\begin{aligned}
 \psi_{\lambda_1+1}^1(u, \dot{u}, \zeta) &= \frac{\partial \Phi_{1, \lambda_1+1}}{\partial u} (u, \mu_1^1, \dots, \mu_{\lambda_1}^1, \mu_{\lambda_1+2}^1) \dot{u} \\
 &+ \sum_{j=1}^{\lambda_1} \left( \frac{\partial \Phi_{1, \lambda_1+1}}{\partial \mu_j^1} (u, \mu_1^1, \dots, \mu_{\lambda_1+2}^1) (f^k(u, \mu_1^1, \dots, \mu_{j+1}^1) + g^k(u, \mu_1^1, \dots, \mu_j^1)) \right) \\
 &+ \frac{\partial \Phi_{1, \lambda_1+1}}{\partial \mu_{\lambda_1+1}^1} (u, \mu_1^1, \dots, \mu_{\lambda_1+2}^1) (f^{\lambda_1+1}(u, \mu_1^1, \dots, \mu_{\lambda_1+1}^1, \mu_{\lambda_1+2}^1) + g^{\lambda_1+1}(u, \mu_1^1, \dots, \mu_{\lambda_1+2}^1))
 \end{aligned} \quad (22)$$

and

$$\begin{aligned}
 \psi_k^2(u, \dot{u}, \zeta_1^2, \dots, \zeta_k^2) &= \frac{\partial \Phi_{2, k}}{\partial u} (u, \mu_1^2, \dots, \mu_k^2) \dot{u} + \left( \prod_{j=1}^{k-1} \frac{\partial f^j}{\partial \mu_{j+1}^2} (u, \mu_1^2, \dots, \mu_{j+1}^2) \right) g^k(u, \mu_1^2, \dots, \mu_k^2) \\
 &+ \sum_{j=1}^{k-1} \left( \frac{\partial \Phi_{2, k}}{\partial \mu_j^2} (u, \mu_1^2, \dots, \mu_k^2) (f^j(u, \mu_1^2, \dots, \mu_{j+1}^2) + g^j(u, \mu_1^2, \dots, \mu_j^2)) \right)
 \end{aligned} \quad (23)$$

**3.2. Observer Design.** Our purpose is to synthesize an observer to estimate at the same time the vector of UIs as well as the nonmeasured state without the assumption of whatever model for UIs. According to Farza et al. (2004), a coordinate transformation is necessary for synthesizing such an observer. This may make one appropriate system form to synthesize the observer. Hence we should write systems (20)-(21) as follows:

$$\dot{\zeta}^1 = A_1 \zeta^1 + \psi^1(\dot{u}, u, \zeta) + \bar{\varepsilon}^1 \quad (24)$$

$$y_1 = \zeta_1^1$$

$$\dot{\zeta}^2 = A_2 \zeta^2 + \psi^2(\dot{u}, u, \zeta) + \bar{\varepsilon}^2 \quad (25)$$

$$y_2 = \zeta_1^2$$

$$A_1 = \begin{pmatrix} 0 & I_{(\lambda_1+1)p} \\ 0 & 0 \end{pmatrix}, \quad (26)$$

$$A_2 = \begin{pmatrix} 0 & I_{qp} \\ 0 & 0 \end{pmatrix}$$

with

$$\bar{\varepsilon}^1 = [0_{\lambda_1 n_1}^T, \dots, \varepsilon^1]^T \quad (27)$$

with

$$\varepsilon^1 = \left( \prod_{j=1}^{\lambda_1-1} \frac{\partial f^j}{\partial \mu_{j+1}^1} (u, \zeta^1) \right) \frac{\partial g^{\lambda_1}}{\partial v^1} (u, \zeta^1) \varepsilon \quad (28)$$

and

$$\bar{\varepsilon}^2 = \psi_q^2(u, \dot{u}, \zeta) \varepsilon^q \quad (29)$$

By referring to the framework given in [28], we opt for HGO synthesized for nonlinear MIMO systems, which are canonically nontriangular. The observer of systems (24)-(25) is designed as follows:

$$\dot{\hat{\zeta}}^1 = A_1 \hat{\zeta}^1 + \psi^1(\cdot) - \theta^{\delta_1} \Delta_1^{-1}(\theta) S_1^{-1} C_1^T (\hat{\zeta}_1^1 - \zeta_1^1) \quad (30)$$

$$\dot{\hat{\zeta}}^2 = A_2 \hat{\zeta}^2 + \psi^2(\cdot) - \theta^{\delta_2} \Delta_2^{-1}(\theta) S_2^{-1} C_2^T (\hat{\zeta}_2^2 - \zeta_2^2)$$

with

$$S_1^{-1} C_1^T = \begin{bmatrix} C_{\lambda_1+1}^1 I_p \\ C_{\lambda_1+1}^2 I_p \\ \vdots \\ C_{\lambda_1+1}^{\lambda_1+1} I_p \end{bmatrix},$$

$$S_2^{-1} C_2^T = \begin{bmatrix} C_q^1 I_p \\ C_q^2 I_p \\ \vdots \\ C_q^q I_p \end{bmatrix} \quad (31)$$

$$\Delta_1(\theta) = \text{diag} \left( I_p, \frac{1}{\theta^{\delta_1}} I_p, \dots, \frac{1}{\theta^{\lambda_1 \delta_1}} I_p \right)$$

$$\Delta_2(\theta) = \text{diag} \left( I_p, \frac{1}{\theta} I_p, \dots, \frac{1}{\theta^{q-1}} I_p \right)$$

$\theta > 0$  is a real number that represent just one observer design parameter.  $\delta_1 = 2q - 3$ ;  $\delta_2 = 1$ .

Converging the estimation error dynamic was demonstrated in detail in [28].

This observer can also be given in the  $\mu$  coordinates as

$$\begin{aligned}\dot{\hat{\mu}}^1 &= f_1(u, \hat{\mu}) + g_1(u, \hat{\mu}) \\ &\quad - (\Lambda_1(u, \hat{\mu}))^+ \theta^{\delta_1} \Delta_1^{-1}(\theta) S_1^{-1} C_1^T (\hat{\mu}_1^1 - \mu_1^1) \\ \dot{\hat{\mu}}^2 &= f_2(u, \hat{\mu}) + g_2(u, \hat{\mu}) \\ &\quad - (\Lambda_2(u, \hat{\mu}))^+ \theta^{\delta_2} \Delta_2^{-1}(\theta) S_2^{-1} C_2^T (\hat{\mu}_2^2 - \mu_2^2)\end{aligned}\quad (32)$$

Now, we suppose

$$\begin{aligned}\hat{x}^k &= \hat{\mu}_k^2 \quad \text{for } k = 1, \dots, q \\ \hat{\eta}^k &= \hat{\mu}_k^1 \quad \text{for } k = 1, \dots, \lambda_1 \\ \hat{\eta}^{\lambda_1+1} &= \hat{\mu}_{\lambda_1+1}^1 \\ \hat{v}^1 &= \hat{\mu}_{\lambda_1+1,2}^1\end{aligned}\quad (33)$$

Utilizing this notation, we can express the observer as follows:

$$\begin{aligned}\dot{\hat{\eta}}^1 &= f^1(u, \hat{\eta}_1^1, \hat{\eta}_2^1) + g^1(u, \hat{\eta}_1^1) - C_{\lambda_1+1}^1 \theta^{\delta_1} (\hat{\eta}^1 - x^1) \\ &\quad \vdots \\ \dot{\hat{\eta}}^{\lambda_1-1} &= f^{\lambda_1-1}(u, \hat{\eta}^1, \dots, \hat{\eta}^{\lambda_1}) + g^{\lambda_1-1}(u, \hat{\eta}^1, \dots, \hat{\eta}^{\lambda_1-1}) - C_{\lambda_1+1}^{\lambda_1-1} \theta^{(\lambda_1-1)\delta_1} \Lambda_{1,\lambda_1-1}^+ (u, \hat{\eta}) (\hat{\eta}^1 - x^1) \\ \dot{\hat{\eta}}^{\lambda_1} &= f^{\lambda_1}(u, \hat{\eta}^1, \dots, \hat{\eta}^{\lambda_1+1}) + g^{\lambda_1}(u, \hat{\eta}^1, \dots, \hat{\eta}^{\lambda_1}, \hat{v}^1) - C_{\lambda_1+1}^{\lambda_1} \theta^{\lambda_1 \delta_1} \Lambda_{1,\lambda_1}^+ (u, \hat{\eta}) (\hat{\eta}^1 - x^1) \\ \left( \begin{array}{c} \dot{\hat{\eta}}^{\lambda_1+1} \\ \dot{\hat{v}}^1 \end{array} \right) &= \left( \begin{array}{c} f^{\lambda_1+1}(u, \hat{\eta}^1, \hat{\eta}^2, \dots, \hat{\eta}^{\lambda_1+1}, x^{\lambda_1+2}) + g^{\lambda_1+1}(u, \hat{\eta}^1, \hat{\eta}^2, \dots, \hat{\eta}^{\lambda_1+1}, \hat{v}^1) \\ 0 \end{array} \right) \\ &\quad - C_{\lambda_1+1}^{\lambda_1+1} \theta^{(\lambda_1+1)\delta_1} \Lambda_{1,\lambda_1+1}^+ (u, \hat{\eta}^i, \hat{v}^1) (\hat{\eta}^1 - x^1) \\ \dot{\hat{x}}^1 &= f^1(u, x^1, \hat{x}^2) + g^1(u, x^1) - C_q^1 \theta (\hat{x}^1 - x^1) \\ &\quad \vdots \\ \dot{\hat{x}}^{\lambda_1-1} &= f^{\lambda_1-1}(u, x^1, \dots, \hat{x}^{\lambda_1}) + g^{\lambda_1-1}(u, x^1, \dots, \hat{x}^{\lambda_1-1}) - C_q^{\lambda_1-1} \theta^{(\lambda_1-1)} \Lambda_{2,\lambda_1-1}^+ (u, \hat{x}) (\hat{x}^1 - x^1) \\ \dot{\hat{x}}^{\lambda_1} &= f^{\lambda_1}(u, x^1, \dots, \hat{x}^{\lambda_1+1}) + g^{\lambda_1}(u, x^1, \dots, \hat{x}^{\lambda_1}, \hat{v}^1) - C_q^{\lambda_1} \theta^{\lambda_1} \Lambda_{2,\lambda_1}^+ (u, \hat{x}) (\hat{x}^1 - x^1) \\ &\quad \vdots \\ \dot{\hat{x}}^{q-1} &= f^{q-1}(u, x^1, \dots, \hat{x}^q) + g^{q-1}(u, x^1, \dots, \hat{x}^{q-1}, \hat{v}^1) - C_q^{q-1} \theta^{(q-1)} \Lambda_{2,q-1}^+ (u, \hat{x}) (\hat{x}^1 - x^1) \\ \dot{\hat{x}}^q &= f^q(u, x^1, \dots, \hat{x}^q) + g^q(u, x^1, \dots, \hat{x}^q, \hat{v}^1) - C_q^q \theta^q \Lambda_{2,q}^+ (u, \hat{x}) (\hat{x}^1 - x^1)\end{aligned}\quad (34)$$

$$\begin{aligned}\dot{\hat{x}}^1 &= f^1(u, x^1, \hat{x}^2) + g^1(u, x^1) - C_q^1 \theta (\hat{x}^1 - x^1) \\ &\quad \vdots \\ \dot{\hat{x}}^{\lambda_1-1} &= f^{\lambda_1-1}(u, x^1, \dots, \hat{x}^{\lambda_1}) + g^{\lambda_1-1}(u, x^1, \dots, \hat{x}^{\lambda_1-1}) - C_q^{\lambda_1-1} \theta^{(\lambda_1-1)} \Lambda_{2,\lambda_1-1}^+ (u, \hat{x}) (\hat{x}^1 - x^1) \\ \dot{\hat{x}}^{\lambda_1} &= f^{\lambda_1}(u, x^1, \dots, \hat{x}^{\lambda_1+1}) + g^{\lambda_1}(u, x^1, \dots, \hat{x}^{\lambda_1}, \hat{v}^1) - C_q^{\lambda_1} \theta^{\lambda_1} \Lambda_{2,\lambda_1}^+ (u, \hat{x}) (\hat{x}^1 - x^1) \\ &\quad \vdots \\ \dot{\hat{x}}^{q-1} &= f^{q-1}(u, x^1, \dots, \hat{x}^q) + g^{q-1}(u, x^1, \dots, \hat{x}^{q-1}, \hat{v}^1) - C_q^{q-1} \theta^{(q-1)} \Lambda_{2,q-1}^+ (u, \hat{x}) (\hat{x}^1 - x^1) \\ \dot{\hat{x}}^q &= f^q(u, x^1, \dots, \hat{x}^q) + g^q(u, x^1, \dots, \hat{x}^q, \hat{v}^1) - C_q^q \theta^q \Lambda_{2,q}^+ (u, \hat{x}) (\hat{x}^1 - x^1)\end{aligned}\quad (35)$$

with

$$F^{\lambda_1}(u, x, v) = \left( \frac{\partial f^{\lambda_1}}{\partial x^{\lambda_1+1}}(u, x) \frac{\partial g^{\lambda_1}}{\partial v^1}(u, x, v) \right)$$

$$\Lambda_1(u, x, v) = \text{diag} \left( I_p, \frac{\partial f^1}{\partial x^2}(u, x), \dots, \right)$$

$$\prod_{k=1}^{\lambda_1-1} \frac{\partial f^k}{\partial x^{k+1}}(u, x), \prod_{k=1}^{\lambda_1-1} \frac{\partial f^k}{\partial x^{k+1}}(u, x) F^{\lambda_1}(u, x, v)$$

$$\Lambda_2(u, x, v) = \text{diag} \left( I_p, \frac{\partial f^1}{\partial x^2}(u, x), \dots, \right)$$

$$\prod_{k=1}^{q-1} \frac{\partial f^k}{\partial x^{k+1}}(u, x)$$

(36)

## 4. Application of UIO to ASP

**4.1. Observer Synthesis.** The bioprocess belongs to the non-linear class of system (6) with  $p = 2$ ,  $\lambda_1 = r = q = 2$ .  $X_{S_m}$  and  $X_{NH_4}$  are the UIs. The measured states are  $X_{O_2}$  and  $X_{NO_3}$ . The UIO diagram is given by Figure 3, in fact, our objective is to reconstruct the nonmeasured states  $X_s$  and  $X_{NH_4}$  and the UIs. We suppose that the states vector  $x = \begin{pmatrix} x_1 \\ x_2 \end{pmatrix} \in \mathbb{R}^2$ , the

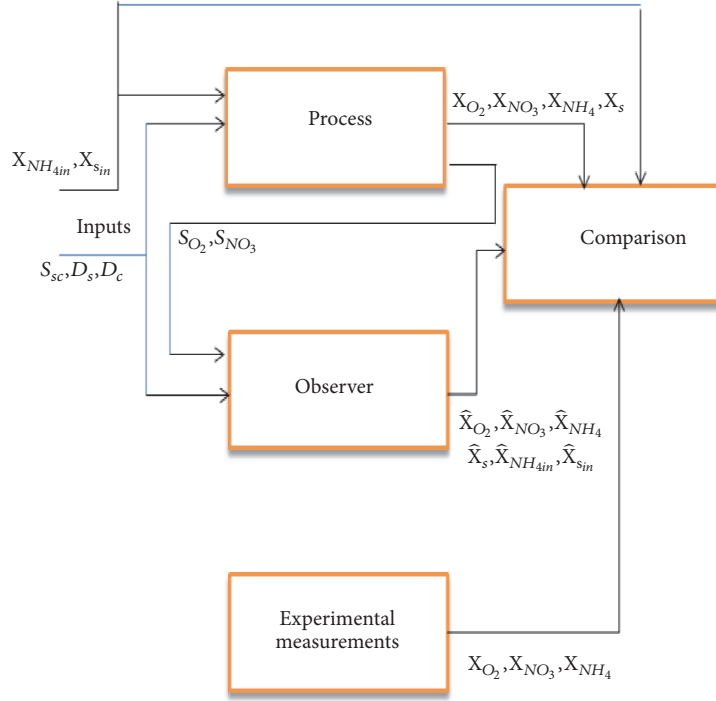


FIGURE 3: UIO diagram.

measured states  $x^1 = \begin{pmatrix} X_{O_2} \\ X_{NO_3} \end{pmatrix} \in \mathbb{R}^2$ , and the nonmeasured states  $x^2 = \begin{pmatrix} X_{NH_4} \\ X_S \end{pmatrix} \in \mathbb{R}^2$ .  $v = \begin{pmatrix} X_{NH_4in} \\ X_{Sin} \end{pmatrix} \in \mathbb{R}^2$  is the UIs vector and  $u = S_{Sc} \in \mathbb{R}$  is the known input.

The observer is given by system (34). So the appropriate

$$\begin{pmatrix} \dot{\hat{X}}_{O_2} \\ \dot{\hat{X}}_{NO_3} \end{pmatrix} = f^1(u, \hat{x}^1, \hat{x}^2) + g^1(u, \hat{x}^1, \hat{x}^2) - 3\theta e$$

with

$$f^1(u, x^1, x^2) = \begin{pmatrix} -(D_s + D_c)X_{O_2} + K_{La}(S_{O_2sat} - X_{O_2}) - \frac{1 - Y_H}{Y_H}\beta_1 - 4, 57\beta_3 \\ -(D_s + D_c)X_{NO_3} - \frac{1 - Y_H}{2, 86Y_H}\beta_2 + \beta_3 \end{pmatrix}$$

$$f^2(u, x^1, x^2) = \begin{pmatrix} -(D_s + D_c)X_{NH_4} - i_{NBM}(\beta_1 + \beta_2) - \beta_3 + \beta_4 \\ +D_sS_{Sc} - (D_s + D_c)X_S - \frac{1}{Y_H}(\beta_1 + \beta_2) + \beta_5 \end{pmatrix}$$

$$g^1(u, x^1, x^2) = 0;$$

$$g^2(u, x^1, x^2, v) = \begin{pmatrix} D_sX_{NH_4in} \\ D_sX_{Sin} \end{pmatrix}$$

$$e = \begin{pmatrix} \hat{X}_{O_2} - X_{O_2} \\ \hat{X}_{NO_3} - X_{NO_3} \end{pmatrix}$$

$$\begin{pmatrix} \dot{\hat{X}}_{NH_4} \\ \dot{\hat{X}}_S \end{pmatrix} = f^2(u, \hat{x}^1, \hat{x}^2) + g^2(u, \hat{x}^1, \hat{x}^2, v) - 3\theta^2\Lambda_{1,2}^+ e$$

$$\begin{pmatrix} \dot{\hat{X}}_{NH_4in} \\ \dot{\hat{X}}_{Sin} \end{pmatrix} = -\theta^3\Lambda_{1,3}^+ e$$

(37)

(38)

and

$$\Lambda_{1,2} = \begin{bmatrix} \frac{\partial f^1}{\partial (X_{NH_4})} & \frac{\partial f^1}{\partial (X_s)} \end{bmatrix}$$

$$\Lambda_{1,3} = \Lambda_{1,2} \begin{bmatrix} \frac{\partial g^2}{\partial (X_{NH_{4in}})} & \frac{\partial g^2}{\partial (X_{s_{in}})} \end{bmatrix}$$

$$\frac{\partial f^1}{\partial (X_{NH_4})} = \begin{pmatrix} -4,57\alpha_2 \frac{X_{O_2}}{X_{O_2} + K_{O_{2aut}}} \frac{K_{NH_{4aut}}}{(X_{NH_4} + K_{NH_{4aut}})^2} \\ \alpha_2 \frac{X_{O_2}}{X_{O_2} + K_{O_{2aut}}} \frac{K_{NH_{4aut}}}{(X_{NH_4} + K_{NH_{4aut}})^2} \end{pmatrix} \quad (39)$$

$$\frac{\partial f^1}{\partial (X_s)} = \begin{pmatrix} -\frac{1 - Y_H}{Y_H} \alpha_1 \frac{X_{O_2}}{X_{O_2} + K_{O_2H}} \\ -\frac{1 - Y_H}{2,86Y_H} \alpha_1 \frac{X_{NO_3}}{X_{NO_3} + K_{NO_3}} \frac{K_{O_2H}}{X_{O_2} + K_{O_2H}} \end{pmatrix}$$

and

$$\frac{\partial g^2}{\partial (X_{NH_{4in}})} = \begin{pmatrix} D_s \\ 0 \end{pmatrix};$$

$$\frac{\partial g^2}{\partial (X_{s_{in}})} = \begin{pmatrix} 0 \\ D_s \end{pmatrix} \quad (40)$$

**4.2. Validation of the UIO with Experimental Data.** We have taken advantage of the experiment done during the modeling and identification of the pilot unit [33] to highlight the performance of the studied observer.

The states issued from the process simulation model are compared to the estimated states issued from our observer model as well as their measured values (Figures 4 and 5). The real data (measured) was carried out for the ASWWTP over 6 hours and with a sampling period of 20 minutes [33]. In fact polluted water which comes from sanitary network in the city of Toulouse (France) feeds continuously the pilot unit in order to purify it. We obtained the measurement by taking samples every 20 minutes and analyze them in a biological laboratory to extract the three concentrations (oxygen, nitrate, and ammonia).

The real curves of the UIs are compared with their estimated ones. It is clear that the corresponding curves are almost superimposed. In addition, the UIs (the influent ammonia concentration  $X_{NH_{4in}}$  and the influent substrate concentration  $X_{s_{in}}$ ) are perfectly reconstructed by the UIO despite their variation. We have chosen a variable profile of the UIs to highlight the effectiveness of the UIO. Indeed, the proposed scenario reflects what is really happening in open-air treatment plants. For example, the increase in

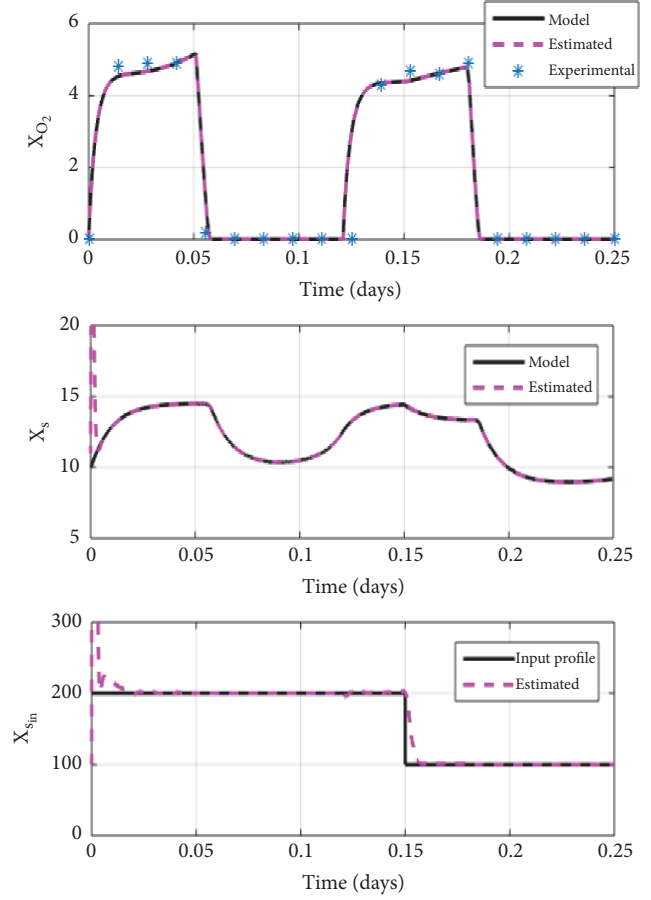


FIGURE 4: Estimation of dissolved oxygen, biodegradable substrate, and the influent biodegradable substrate concentration.

TABLE 4: Error quantification.

Error	$X_{O_2}$	$X_{NO_3}$	$X_{NH_4}$
$e_{max}$	0.268	1.29	0.24
$e_{max \text{ relative}} (\%)$	5.42	19.28	4.29

concentration of the “influent ammonia” is due to the arrival of water loaded with heavy mass caused by industrial discharges, while decreasing in concentration of the “influential biodegradable substrate” is due to important (continuous) reversals of rain. The found results evidently show a thorough compromise between estimated and real curves. Moreover, we can show that the state variables signals of the model and the observer are rallied with the experimental measurements. This is quantified by the relative error (Table 4). The unknown inputs estimation error converges to zero. The advantages of such observer are that it is relatively simple to design and it has only one adjustment parameter.

## 5. Conclusion

A large class of nonlinear MIMO systems that involves UIs has been studied in this paper in order to synthesize UIO. This observer permits jointly estimating UIs and state variables.

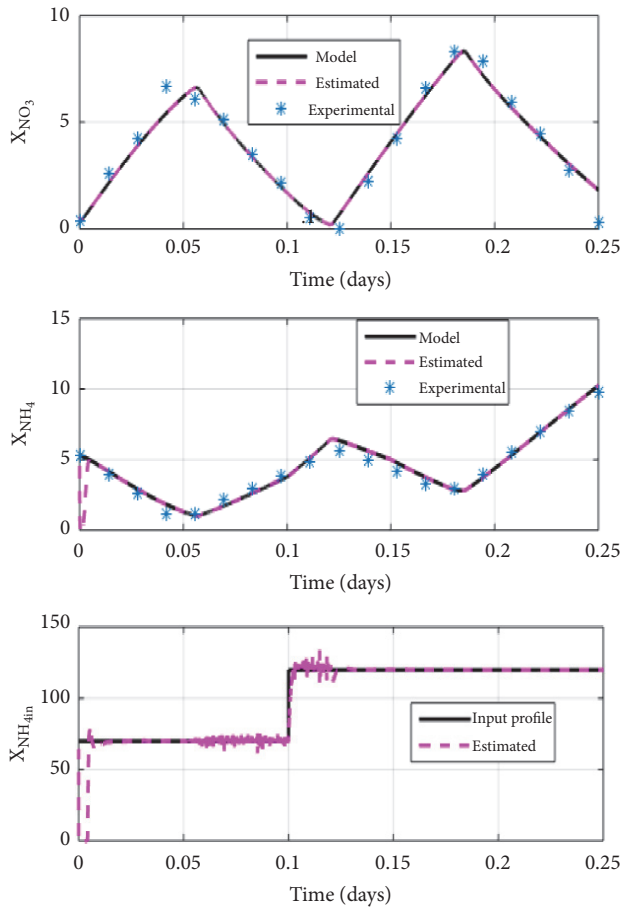


FIGURE 5: Estimation of nitrate, ammonia, and the influent ammonia concentration.

We have applied it to one complicated biochemical ASP. The latter is a reduced activated sludge model having switching anoxic and aerobic phases. By using only two measurements, we have achieved the reconstruction of two state variables ( $X_s$  and  $X_{NH_4}$ ) and two UI signals ( $X_{NH_{4in}}$  and  $X_{sin}$ ). Indeed, the obtained simulation results demonstrate quite estimation performances of the suggested observer compared to experimental data. Such observer should be combined with a state control law to ensure that the nitrogen concentration at the settler output does not exceed the standard European norm.

## Data Availability

The data supporting this study are from previously reported studies, which have been cited.

## Conflicts of Interest

The authors declare that they have no conflicts of interest.

## References

- [1] M. Henze, C. P. L. Grady, G. V. R. Marais, and T. Matsuo, "Activated sludge model no. 1," IAWQ Scientific and Technical Report 1, London, UK, 1987.

- [2] M. Henze, W. Gujer, T. Mino, T. Matsuo, M. C. M. Wentzel, and G. V. R. Marais, "Activated sludge model no. 2," IAWQ Scientific and Technical Report 3, London, UK, 1995.
- [3] M. Henze, W. Gujer, T. Mino et al., "Activated sludge model No. 2D, ASM2D," *Water Science and Technology*, vol. 39, no. 1, pp. 165–182, 1999.
- [4] W. Gujer, M. Henze, T. Mino, and M. Van Loosdrecht, "Activated Sludge Model No. 3," *Water Science and Technology*, vol. 39, no. 1, pp. 183–193, 1999.
- [5] U. Jeppsson and G. Olsson, "Reduced order models for on-line parameter identification of the activated sludge process," *Water Science and Technology*, vol. 28, no. 11-12, pp. 173–183, 1993.
- [6] M. A. Steffens, P. A. Lant, and R. B. Newell, "A systematic approach for reducing complex biological wastewater treatment models," *Water Research*, vol. 31, no. 3, pp. 590–606, 1997.
- [7] C. Gómez-Quintero, I. Queinnec, and J. Babary, "A reduced nonlinear model of an activated sludge process," *IFAC Proceedings Volumes*, vol. 33, no. 10, pp. 1001–1006, 2000.
- [8] B. Chachuat, N. Roche, and M. A. Latifi, "Reduction of the asm1 model for optimal control of small-size activated sludge treatment plants," *Journal of Water Science*, vol. 16, no. 1, pp. 05–26, 2003.
- [9] I. Y. Smets, J. V. Haegebaert, R. Carrette, and J. F. Van Impe, "Linearization of the activated sludge model ASM1 for fast and reliable predictions," *Water Research*, vol. 37, no. 8, pp. 1831–1851, 2003.
- [10] M. Mulas, S. Tronci, and R. Baratti, "Development of a 4-measurable states activated sludge process model deduced from the ASM1," *IFAC Proceedings Volumes*, vol. 40, no. 5, pp. 213–218, 2007.
- [11] R. Marquez, M. Blandria-Carvajal, C. Gómez-Quintero, and M. Ríos-Bolívar, "Average modeling of an alternating aerated activated sludge process for nitrogen removal," *IFAC Proceedings Volumes*, vol. 44, no. 1, pp. 14195–14200, 2011.
- [12] M. B. Khan, H. Nisar, C. A. Ng, P. K. Lo, and V. V. Yap, "Generalized classification modeling of activated sludge process based on microscopic image analysis," *Environmental Technology*, vol. 39, no. 1, pp. 24–34, 2017.
- [13] S. Caraman, M. Barbu, and E. Ceanga, "Robust multimodel control using qft techniques of a wastewater treatment process," *Control Engineering and Applied Informatics*, vol. 7, no. 2, pp. 10–17, 2005.
- [14] O. Gonzalez-Miranda, M. Rios-Bolivar, and C. Gomez-Quintero, "Adaptive output feedback regulation of an alternating activated sludge process," in *Proceedings of the 2009 European Control Conference (ECC)*, pp. 424–429, Budapest, Hungary, August 2009.
- [15] E. Petre, C. Marin, and D. Seliteanu, "Adaptive control strategies for a class of recycled depollution bioprocesses," *Control Engineering and Applied Informatics*, vol. 7, no. 2, pp. 25–33, 2005.
- [16] C. Vlad, M. Sbarciog, M. Barbu, S. Caraman, and A. Wouwer Vande, "Indirect control of substrate concentration for a wastewater treatment process by dissolved oxygen tracking," *Control Engineering and Applied Informatics*, vol. 14, no. 1, pp. 38–47, 2012.
- [17] C. Foscoliano, S. Del Vigo, M. Mulas, and S. Tronci, "Predictive control of an activated sludge process for long term operation," *Chemical Engineering Journal*, vol. 304, pp. 1031–1044, 2016.
- [18] O. K. Ogidan, C. Kriger, and R. Tzoneva, "Networked control with time delay compensation scheme based on a smith predictor for the activated Sludge Process," *Control Engineering and Applied Informatics*, vol. 19, no. 3, pp. 79–87, 2017.

- [19] C.-S. Gómez-Quintero and I. Queinnec, "State and disturbance estimation for an alternating activated sludge process," *IFAC Proceedings Volumes*, vol. 35, no. 1, pp. 447–452, 2002.
- [20] D. Dochain, "State and parameter estimation in chemical and biochemical processes: A tutorial," *Journal of Process Control*, vol. 13, no. 8, pp. 801–818, 2003.
- [21] N. R. Chiu, H. J. Navarro, and J. Picó, "A nonlinear observer for bioprocesses using LMI," *IFAC Proceedings Volumes*, vol. 40, no. 4, pp. 393–398, 2007.
- [22] B. Boukroune, M. Darouach, M. Zasadzinski, S. Gillé, and D. Fiorelli, "A nonlinear observer design for an activated sludge wastewater treatment process," *Journal of Process Control*, vol. 19, no. 9, pp. 1558–1565, 2009.
- [23] M. Triki, M. Farza, and Y. Koubaa, "Unknown inputs observers for a class of non triangular nonlinear systems," in *Proceedings of the 15th International Conference on Sciences and Techniques of Automatic Control and Computer Engineering (STA)*, pp. 259–266, Hammamet, Tunisia, December 2014.
- [24] H. Hammouri and Z. Tmar, "Unknown input observer for state affine systems: a necessary and sufficient condition," *Automatica*, vol. 46, no. 2, pp. 271–278, 2010.
- [25] K. Mohamed, M. Chadli, and M. Chaabane, "Unknown inputs observer for a class of nonlinear uncertain systems: An LMI approach," *International Journal of Automation and Computing*, vol. 9, no. 3, pp. 331–336, 2012.
- [26] F. J. Bejarano, W. Perruquetti, T. Floquet, and G. Zheng, "Observation of nonlinear differential-algebraic systems with unknown inputs," *Institute of Electrical and Electronics Engineers Transactions on Automatic Control*, vol. 60, no. 7, pp. 1957–1962, 2015.
- [27] K. C. Veluvolu, M. Defoort, and Y. C. Soh, "High-gain observer with sliding mode for nonlinear state estimation and fault reconstruction," *Journal of The Franklin Institute*, vol. 351, no. 4, pp. 1995–2014, 2014.
- [28] M. Farza, M. M'Saad, M. Triki, and T. Maatoug, "High gain observer for a class of non-triangular systems," *Systems & Control Letters*, vol. 60, no. 1, pp. 27–35, 2011.
- [29] S. H. Saïd, F. M'Sahli, and M. Farza, "Simultaneous state and unknown input reconstruction using cascaded high-gain observers," *International Journal of Systems Science*, vol. 48, no. 15, pp. 3346–3354, 2017.
- [30] B. Boukroune, M. Darouach, M. Zasadzinski, and S. Gille, "State and unknown input estimation for nonlinear singular systems: application to the reduced model of the activated sludge process," in *Proceedings of the Automation (MED 2008)*, pp. 1399–1404, Ajaccio, France, June 2008.
- [31] S. Methnani, J.-P. Gauthier, and F. Lafont, "Sensor fault reconstruction and observability for unknown inputs, with an application to wastewater treatment plants," *International Journal of Control*, vol. 84, no. 4, pp. 822–833, 2011.
- [32] I. Khoja, T. Lahdari, A. Sakly, and F. M'Sahli, "Unknown-input observer for disturbance and state estimation of an activated sludge waste water treatment process," in *Proceedings of the 17th International Conference on Sciences and Techniques of Automatic Control and Computer Engineering, STA 2016*, pp. 13–18, Sousse, Tunisia, December 2016.
- [33] C. Gomez-Quintero, *Modélisation et estimation robuste pour un procede boues actives en alternance de phases [Ph.D. thesis]*, Université Paul Sabatier, Laboratoire d'Analyse et d'Architecture des Systèmes, Toulouse, France, 2002.
- [34] S. Julien, *Modélisation et estimation pour le contrôle d'un procédé boues actives éliminant l'azote des eaux résiduaires urbaines [Ph.D. thesis]*, ENSEEIHT, UPS Toulouse, France, 1997.
- [35] F. Liu, M. Farza, and M. M'Saad, "Non-linear observers for state and unknown inputs estimation," *International Journal of Modelling, Identification and Control*, vol. 2, no. 1, pp. 33–48, 2007.